THE UNIVERSITY OF TEXAS AT AUSTIN

NASA CR-
141781

THE EFFECT OF SURFACE TEMPERATURE AND REYNOLDS NUMBER ON THE LEEWARD HEAT-TRANSFER FOR A SHUTTLE ORBITER

John J. Bertin, Gobporn Senalug,
Marilynn McBride, and R. Bruce Willman

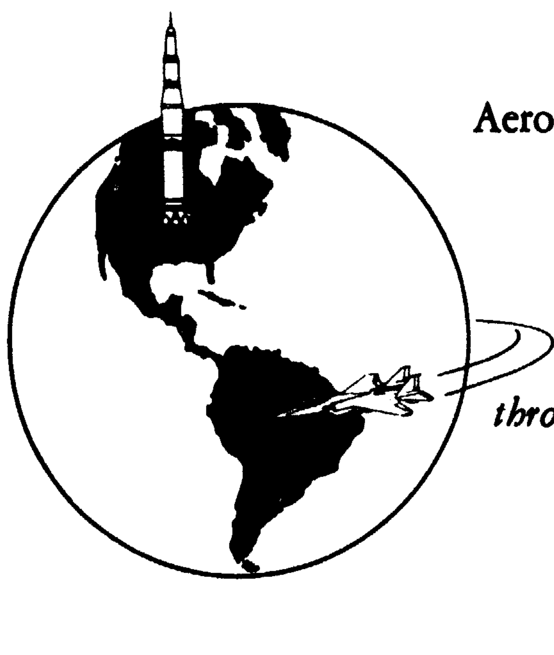

Aerospace Engineering Report 75002

This work supported in part
by the Johnson Space Center
through NASA Contract NAS 9–13707

April 1975

Department of Aerospace Engineering and Engineering Mechanics

THE EFFECT OF SURFACE TEMPERATURE AND REYNOLDS NUMBER ON THE LEEWARD HEAT-TRANSFER FOR A SHUTTLE ORBITER*

by

John J. Bertin, Gobporn Senalug
Marilynn McBride, and R. Bruce Willman

Aerospace Engineering Report 75002

*This work supported in part
by the Johnson Space Center
through NASA Contract NAS 9-13707

Department of Aerospace Engineering and
Engineering Mechanics

The University of Texas at Austin
April 1975

ACKNOWLEDGEMENTS

This research was supported in part by the Johnson Space Center (NASA) through Contract NAS 9-13707. The analysis of these data, which was supported primarily by University funds, was done in cooperation with personnel from Calspan where the tests were conducted. The authors acknowledge the considerable efforts of Mr. G. K. Mruk of Calspan. The interested reader is referred to Calspan Report No. ZC-5403-A-1 for a complete tabulation of the present data, which were obtained in the Calspan 96-Inch Hypersonic Shock Tunnel.

The authors would also like to thank Mrs. Pat Kleinert for cheerfully typing the numerous drafts of the manuscript.

TABLE OF CONTENTS

Pages

INTRODUCTION

In order to determine the convective heat-transfer distribution over the leeward surface of space shuttle entry configurations, one must describe a three-dimensional flow-field, which includes extensive regions of separated flow and complex viscous:inviscid interactions. Because of its complexity, the separated flow to the leeward of an entry configuration is a function of many variables. The variables to be considered include:

(1) the Reynolds number,

(2) the Mach number,

(3) the configuration (both forebody geometry and the afterbody geometry),

(4) the angle-of attack,

(5) the heat-shield material and mass-addition,

(6) the gas composition, and

(7) the surface temperature.

Numerous investigators have studied the effect of these parameters on the leeward flow-field for entry configurations at hypersonic speeds. A survey of the relevant literature has been completed as part of the present contractual effort. The interested reader is referred to Ref. 1 for the results of other investigations of the leeward flow-fields.

The present report discusses the experimental program which was conducted in the Calspan 96-Inch Hypersonic Shock Tunnel to investigate what effect the windward surface temperature had on the heat transfer to the leeward surface of the shuttle orbiter. Heat-transfer distributions, surface-pressure distributions, and schlieren photographs were obtained for an 0.01-scale model of the 37-0 shuttle orbiter at angles-of-attack of 30° and of 40°. Similar data were obtained for a fuselage-only configuration at angles-of-attack of 30° and of 90°. Data were obtained for Mach numbers from 10 to 19, for Reynolds numbers, $Re_{\infty,L}$, from 0.1×10^6

to 1.75 x 10^6, and for surface temperatures of $0.09\ T_t \leq T_{wwd} \leq 0.31\ T_t$ and of $0.09\ T_t \leq T_{lee} \leq 0.114\ T_t$.

NOMENCLATURE

F	dimensionless streamwise velocity function for the boundary layer (U/U_e)
h	local heat-transfer coefficient defined in eqn. 12
h	metric for three-dimensional boundary layer
$h_{t,ref}$	heat-transfer coefficient for the reference stagnation point heating rate
H_o	total enthalpy
L	axial model length, 1.075 ft
M_∞	free-stream Mach number
p	local static-pressure
p_b	base pressure
p_{t2}	stagnation pressure behind a normal shock wave
Pr	Prandtl number
$\dot{q}$	local heat-transfer rate
$\dot{q}_{t,ref}$	heat-transfer rate to the stagnation point of an 0.01-ft radius sphere (i.e., the reference radius reduced to model scale)
$\dot{q}_{t,\alpha=0°}$	stagnation-point heating rate for the zero angle-of-attack Apollo entry configuration
R	maximum body radius of the Apollo Command Module
$Re_{n\ell}$	Reynolds number behind a normal shock wave based on the wetted length from the stagnation point (see eqn. 25)
Re_{ns}	Reynolds number behind a normal shock wave (see eqn. 20)
Re_s	local Reynolds number integrated along a streamline, $Re_s = \frac{\int \rho_e U_e ds}{\mu e}$
$Re_{\infty,L}$	free-stream Reynolds number based on model length
s	wetted distance along a streamline
S	distance along the surface from the geometric center of the spherical heat shield of the Apollo
St	Stanton number (see eqn. 3)

$\overline{St}_{sig}$ Stanton number averaged over all the leeward gages downstream of the cockpit,

$$\overline{St}_{sig} = \frac{\int \dot{q}_w \, dA_{sig}}{\rho_{ns} U_{ns} (H_o - H_w) \int dA_{sig}}$$

(see shaded area of Fig. 38 for $\int dA_{sig}$)

$\overline{St}_{sep}$ Stanton number averaged over those leeward gages in the "separated" region,

$$\overline{St}_{sep} = \frac{\int \dot{q}_w \, dA_{sep}}{\rho_{ns} U_{ns} (H_o - H_w) \, dA_{sep}}$$

(see shaded area of Fig. 40 for $\int dA_{sep}$)

T local static-temperature

T_{lee} leeward-surface temperature

T_t stagnation temperature

T_{wwd} windward surface temperature

U streamwise velocity component

x axial coordinate

y coordinate measured normal to the model surface

α angle-of attack

δ boundary-layer thickness

θ momentum thickness (eqn. 16)

θ_H enthalpy thickness (eqn. 14)

μ viscosity

ρ **density**

ϕ angular coordinate of the leeward gages, measured as a rotation about waterline z400

Subscripts

e evaluated at the edge of the boundary layer

ns evaluated behind a normal shock wave

w evaulated at the wall

∞ evaluated at the free-stream conditions

NOTE: terms which are discussed only in the section, "Experimental Program", are not defined above. The interested reader is referred to a Calspan data report.

EXPERIMENTAL PROGRAM

The experimental program was conducted to investigate what effect the windward surface temperature has on heat transfer to the leeward surface of the shuttle orbiter. Heat-transfer distributions, surface-pressure distributions, and schlieren photographs were obtained in the Calspan 96-Inch Hypersonic Shock Tunnel using an 0.01-scale model of the 37-0 shuttle orbiter. A horizontal sheet of insulation, running the entire length of the model at waterline z350, physically divided the model into two sections: the "windward" section and the "leeward" section. The model was designed so that the temperature of the windward surface could be varied from 420°R (233°K) to 1440°R (800°K) while the temperature of the leeward surface could be varied from 420°R (233°K) to 530°R (294°K). The parameters of the experimental program included the free-stream Mach number, the free-stream Reynolds number, the angle of attack, and the temperature ratios: T_{wwd}/T_t and T_{wwd}/T_{lee}. The values of T_{wwd}/T_t used in the program were (nominally) 0.09, 0.18, and 0.31. The values for T_{wwd}/T_{lee} were (nominally) 1.00, 1.57, and 2.70. The values chosen for these parameters were intended to simulate, at one extreme, the temperature ratios obtained during atmospheric entry and, at the other extreme, values typical of those obtained in continuous-flow, supersonic wind-tunnels.

Model

As noted above, the 0.01-scale model of the 37-0 shuttle-orbiter was divided into a windward section and a leeward section. Sketches of the windward and of the leeward sections are presented in Fig. 1. The external body contours of the leeward section were constant in cross section aft of x = 0.334L. The model did not include either the engine pods or the tail surface. Since the principal objective of the program was to investigate parameters which af-

fect the heat transfer to the leeward surface, most of the instrumentation was concentrated there. Note that 43 of the 48 heat-transfer gages were located on the leeward surface. The locations of these gages are presented in Table 1 and in Fig. 1. For the present report, the angular coordinate of a heat-transfer gage is defined by a rotation with respect to an x-axis at the waterline z400 (see Fig. 1). Thus, $\phi = 0°$ for the leeward pitch-plane (which is also the plane-of-symmetry since all tests were conducted with zero yaw and zero roll).

Because the gage locations were identical at the stations $x = 0.335L$ and $x = 0.420L$, a single sketch is presented in Fig. 1b for these two stations. Although there was no gage at $\phi = 90°$ for $x = 0.500L$, the instrumentation both at $x = 0.500L$ and at $x = 0.600L$ were identical and one sketch is used for these two stations. An isometric sketch of the leeward surface of the orbiter illustrates the locations of these gages (Fig. 2). Two x-axes are shown in Fig. 2: (1) the waterline z400 which is the axis of rotation for the ϕ coordinate and (2) the waterline z338 which passes through the apex of the orbiter. A horizontal plane passing through the latter axis (i.e., z338) divides the windward surface from the leeward surface for the theoretical boundary-layer solutions. Furthermore, all five static-pressure orifices were located in the leeward pitch plane. See Table 2.

The locations of the five heat-transfer gages which were in the windward plane-of-symmetry, i.e., $\phi = 180°$, are also given in Fig. 1 and in Table 1.

For some of the runs, an Incaloy heater-element was placed in the windward section to generate the desired high surface temperature. For other runs, freon was passed through a cooling coil located in the windward section to obtain the desired low surface temperature. For all runs, freon was passed through the cooling coil located in the leeward section. By controlling the

mass-flow rate of the freon, the leeward surface could be maintained at approximately 530°R (294°K) for those runs where the windward surface was heated and at approximately 420°R (233°K) for those runs with a cooled windward surface. The coils can be seen exiting the aft end of the model and constrained to the model-support sting in the installation photographs of Fig. 3.

An insulator plate ran the length of the model at waterline z350 (i.e., the model split line) to limit heat transfer from the relatively hot windward section to the leeward section. The insulator plate consisted of a metal layer to serve as a radiation shield and an asbestos layer to inhibit conduction. The asbestos layer is clearly evident in both views of the model which are presented in Fig. 3. Illustrated in the photograph of Fig. 4 are the various components of the model, including the leeward section, the heat shield (without the asbestos gasket), and the windward section. Of special interest is the geometry and location of the cooling coil. The cross-section geometry of the fuselage-only configuration will be discussed in that section of the present report which discusses the fuselage-only data.

Instrumentation

Heat-transfer gages

The heat-transfer rates were determined from measurements of the transient surface temperature by means of thin-film resistance thermometers (Refs. 2 and 8). The standard gage consisted of a Pyrex blank with a substrate thickness of 0.0625 in. (0.1588 cm). This thickness is more than adequate to satisfy semi-infinite body requirements since the transient heat flux does not penetrate much beyond 0.01 in. (0.03 cm) in ten milliseconds. Using Hanovia-05X bright platinum solution, a strip of the solution is handpainted along a diameter of the substrate. Upon heating to about 1250°F in a ventilated furnace, the volatile constituents are driven off and a bright, specular, metallic film that

is firmly bonded to the Pyrex is obtained. Film planform dimensions are approximately 1 mm in width by 5 mm in length. Several thin coatings are generally fired consecutively to achieve a room temperature resistance in the range from 75 to 125 ohms. Optical techniques have been used to measure the film thickness which typically is less than 0.1 micron.

To insulate the metallic film, a thin dielectric coating of magnesium fluoride is deposited on the surface of the gage. As the heat capacity of the gage is negligible, the film temperature is a measure of the instantaneous surface temperature of the pyrex and is related to the heat transfer rate by the classical equation of heat transfer into a semi-infinite slab of known thermal characteristics. Analysis has shown this technique to be valid for 0.1-micron-thick gages during the short duration of a shock-tunnel test.

The heat-transfer gages are calibrated prior to tests to determine the change in resistance of the elements with temperature. Since calibrations at very high temperatures are not practical, the gage constant at room temperature ($K_{T = 70}$) is determined by measuring gage resistance at about 70°F and 150°F and calculating the gage sensitivity constant. Since $K_{T = 70}$ is applicable only to room temperature, a correction to appropriate ambient conditions is required. This conversion has been established by noting that for temperatures up to 1000°F, the resistance-temperature function is defined adequately by a second-degree equation.

$$R_{T = T} = a_o + b_oT - c_oT^2$$

Defining temperature T^* in the Fahrenheit scale, it is convenient to rewrite this equation in terms of a reference temperature of T = 70°F, i.e, room temperature.

$$R_{T = T} = a_1 + a_2(T - 70) - a_3(T - 70)^2$$

The constant a_1 is the value of gage resistance at $T = 70°F$.

$$R_{T = T} = R_{T = 70} + a_2(T - 70) - a_3(T - 70)^2$$

By differentiating this equation, the value of the slope K at any temperature is obtained.

$$K_{T = T} = \left(\frac{dR}{dT}\right)_{T = T} = a_2 - 2a_3(T - 70)$$

The constant a_2 is the value of K at $T = 70°F$, i.e., $a_2 = \left(\frac{dR}{dT}\right)_{T = 70} = K_{T = 70}$. Thus the last equation may be written as follows.

$$K_{T = T} = K_{T = 70}\,[1 - a_4(T - 70)]$$

where

$$a_4 = \frac{2a_3}{K_{T = 70}}$$

A relationship is available, therefore, to define heat-transfer gage sensitivity at any temperature T in terms of the room temperature calibration value, $K_{T = 70}$. For engineering purposes, a mean value for a_4 of 2.59×10^{-4} may be used for all gages. The resulting conversion is presented in graphical form in Figure 5.

These calibrations are then used to set the recording equipment for the expected temperature increases. Calibrations to determine the heat-transfer gage's temperature resistance characteristics are conducted with an error potential of one percent. Far more significant than this is the repeatability of the heat transfer gage during testing. A series of shock tunnel tests designed to determine repeatability of the heat transfer data has shown that the RMS deviation of the repeatability is ± 3 percent. A combination of these errors indicated that the relative RMS deviation of the heat transfer data is about ± 3.2 percent.

The leeward heat transfer rates were measured by "thin film" gages. This type of gage is a resistance thermometer which reacts to the local surface temperature of the model. The theory of heat conduction in a nonhomogeneous body is used to relate the surface temperature to the rate of heat transfer. Since the resistence element has negligible effect on the pyrex substrate surface temperature, the substrate can be characterized as being semi-infinite, homogeneous and isotropic. The general heat conduction equation is:

$$\rho c(T) \frac{\partial T}{\partial t} = \frac{\partial}{\partial x} \left(k(T) \frac{\partial T}{\partial x} \right) \tag{1}$$

where ρ, c and k are substrate density, specific heat and thermal conductivity, respectively, and x is the substrate depth.

If the substrate properties are independent of temperature; i.e., if the temperature change is less than 100°R, a closed-form solution is obtained for the heat transfer rate:

$$\dot{q}(t) = \frac{1}{2} \left(\frac{\pi \; \rho c k}{t} \right)^{1/2} \left(T(t) + \frac{1}{\pi} \int_0^t \frac{\lambda^{1/2} \; T(t) - t^{1/2} \; T(\lambda)}{(t - \lambda)^{3/2}} \, d\lambda \right) . \tag{2}$$

This equation is solved directly by use of q-meters, which are passive electrical analog networks, in conjunction with the heat-transfer gage. The analog is based on the fact that the equation for heat conduction in a semi-infinite solid is identical to that for a semi-infinite electrical transmission line with distributed series resistance and shunt capacitance. In practice, it has been found feasible to construct the analog of a finite number of circuit elements consisting of parallel resistor-capacitor elements in a series arrangement. For temperature changes greater than 100°F the variation of substrate properties and electrical properties of the resistance element with temperature causes a significant droop of the q-meter output which is corrected by a time and heat-transfer-rate dependent factor.

The heat-transfer data were normalized in terms of a Stanton number and heat-transfer coefficient based on free stream conditions. The relations used for the calculations are given by

$$St = \frac{778\ \dot{q}_w}{\rho_\infty U_\infty (r\ H_o - H_w)} = \frac{778\ \dot{q}_w}{\rho_{ns}\ U_{ns}\ (r\ H_o - H_w)} \tag{3}$$

$$h = 778(32.17)\ \frac{\dot{q}_w}{(r\ H_o - H_w)} \tag{4}$$

where the wall conditions are based on the appropriate initial model surface temperature. Heat transfer coefficients were generated for recovery factors of 1.0 and 0.85, whereas Stanton numbers were calculated for $r = 1.0$.

In addition, a theoretical stagnation heating rate for a 0.01 foot radius sphere was calculated for each run by the method of Fay and Riddell (Ref. 4) for the purpose of data normalization. The sphere temperature was that of the windward or leeward model wall depending on the location of the gage whose data were normalized.

Pressure

The model cavity and base pressures were measured by a system developed to meet the particular requirements of shock tunnel testing. The pressure transducers employ piezoelectric crystals, and their small size permits installation within the model. The transducers used in this test have a dual-element feature which reduces acceleration effects to an indicated pressure of .00015 psi/g. Pressures as low as .001 psi may be accurately measured by these transducers.

The pressure transducers measure the difference between the initial test section pressure and the applied local pressure. The initial pressure is of the order of 5 microns and is added to the measured pressure to obtain the absolute model pressure.

On the basis of calibration repeatability (see Fig. 6 for a calibration curve) and on the consistency and repeatability of past pressure data obtained with the type of transducer used to measure model pressure in this test, it is estimated that these data have an accuracy of ± 5%.

Schlieren System

The schlieren system used was of the double-pass collimated type with the knife edge horizontal. This system was used for the sensitivity needed to obtain photographs of shock wave during the low density runs. Schlieren photographs were taken on most of the runs.

Model Temperature

The model skin temperature was monitored by means of five Chromel-Alumel thermocouples which were operated with a room temperature reference function.

Model Attitude

The model attitude was set with an inclinometer at the desired angle of attack and these settings are estimated to be within ± 0.1°.

Data Acquisition

Forty-eight of the electrical outputs of heat transfer gages were sampled at 50-microsecond intervals and recorded on the magnetic storage drum of a Navigation Computer Corporation MCL-100 data acquisition system (NAVCOR). The stagnation-sphere heat-transfer gage and all pressures were recorded on oscilloscopes. The data stored on the magnetic drum were reproduced on a strip chart recorder for manual reading. The output from each heat-transfer gage, as recorded on the NAVCOR drum, was additionally processed by a "q-meter", which is a passive electrical analog network that converts the analog voltage representation of the gage element temperature into an analog voltage representation of heat-transfer rate. These results were also reproduced on the strip chart.

The electrical outputs of the remaining heat-transfer gage was first processed by a q-meter and the resultant signal was then recorded on Polaroid film from the oscilloscopes.

The 96-Inch Hypersonic Shock Tunnel

The basic components of the 96-inch leg are shown in Fig. 7. This leg consists of a chambered shock tube with an area ratio (driver/driven) of 1.56. The 5-inch (12.70 cm) I.D. driver is 16 ft. (4.87 m.) long and is externally heated to 1260°R (700°K). The 4-inch (10.16 cm) I.D. driven tube is 48.5 ft. (14.79 m.) long. A helium-air mixture was used as the driver gas. Air was used as the test gas in the present program.

The tailored-interface mode of operation was used to provide the longest possible steady-state reservoir conditions. Maximum driver pressure is 30,000 psi (2.07×10^8 N/m^2), which yields a maximum pressure behind the reflected shock of 20,000 psi (1.38×10^8 N/m^2).

All test conditions were obtained using the "D"-nozzle, which is a contoured, axisymmetric nozzle whose exit diameter is 4.0 ft (1.22 m.).

Test Program

The test conditions for the experimental program are presented in Table 3. Heat-transfer rates were measured over a range of free-stream Mach number from 10.0 to 18.6 and of free-stream Reynolds number from 0.1×10^6 per foot to 1.6×10^6 per foot (0.3×10^6 per meter to 5.3×10^6 per meter). For the complete orbiter configuration data were obtained at angles-of-attack of 30° and 40°. For the fuselage-only configuration, data were obtained at angles-of-attack of 30° and 90°. Note that, because of the irregular shape of the model, the surface temperature was not constant for either the leeward section or the windward section. Heat transfer from one part of the model to another

contributed to the temperature variations. Therefore, the surface temperatures presented in Table 3 merely represent a nominal value for a particular run.

Values of the freestream Mach number in the test section were determined from previous airflow calibrations in the nozzle. The test conditions of freestream pressure, temperature, and Reynolds number are computed by assuming isentropic expansion of the test gas from the conditions behind the reflected shock in the driven tube to the test section Mach number. The calculation of test section freestream parameters includes the effect of molecular vibration assuming a simple harmonic oscillator model for the diatomic constituents of air.

The stagnation enthalpy and temperature of the air behind the reflected shock are determined, respectively, from

$$H_o = H_1 \; (H_4/H_1) \tag{5}$$

and

$$T_o = T_1 \; (T_4/T_1) \tag{6}$$

where H_4/H_1 and T_4/T_1, are functions of U_i, the incident shock velocity (References 5-7). U_i is obtained by measuring the time taken by the shock wave to pass between two stations in the shock tube. H_1 is taken from Reference 8 and T_1 is measured prior to each run. Freestream static temperature is obtained from

$$T_\infty = \frac{H_o}{c_{p_\infty \, AV}} \left(1 + \frac{\gamma_\infty - 1}{2} \; \frac{c_{p_\infty}}{c_{p_\infty \, AV}} \; M_\infty^2 \right)^{-1} \tag{7}$$

where γ_∞ is a function of c_{p_∞}; c_{p_∞} and $c_{p_\infty \, AV}$ include vibrational heat capacity and are functions of T_∞, requiring an iteration between T_∞ and c_p. Freestream

pressure is calculated using

$$P_\infty = \frac{P}{P_p}\ P_o\left(1 + \frac{\gamma_\infty - 1}{2}\ M_\infty^2\right)^{-\frac{\gamma_\infty}{\gamma_\infty - 1}} \tag{8}$$

where $\frac{P}{P_p} = \frac{(P/P_o)\text{ real}}{(P/P_o)\text{ perfect}}$

is the real gas correction to the ideal static to total pressure ratio as described in Reference 9 but suitably modified to include vibrational specific heat in the test section, and P_o is the measured pressure behind the reflected shock. The source data used in this technique are References 8 and 10.

Freestream velocity, density and dynamic pressure are respectively calculated from

$$U_\infty = M_\infty\sqrt{\gamma_\infty R T_\infty} \tag{9}$$

$$\rho_\infty = P_\infty / \bar{R} T_\infty \tag{10}$$

$$q_\infty = \frac{1}{2}\rho_\infty U_\infty^2 \tag{11}$$

Values for absolute viscosity (μ) used to compute Reynolds numbers were obtained from Reference 11 for temperature below 500°R and from Reference 12 for temperature about 500°R.

Stagnation conditions behind a normal shock in the test section are based on the data of Reference 10.

The stagnation enthalpy and the test-section free-stream conditions were calculated, using the thermodynamic properties of real air, the incident shock wave velocity and the nozzle supply-pressure. The speed of the incident shock wave was measured to within ± 1 percent. Based on the agreement of pressure transducers, the nozzle supply pressure is considered accurate to within ± 2.6 percent. The test-section Mach number was determined from

airflow calibrations made prior to the test program. The computed values of free stream Mach number from a large number of airflow calibrations for each nozzle-throat combination were used to calculate variation coefficients in Mach number of ± 1.0 percent. Accordingly, the determination of free stream static pressure is considered to be accurate to within ± 7 percent of the true values.

DISCUSSION OF RESULTS

Theoretical Solutions

Theoretical solutions for the viscous boundary-layer of the orbiter model at an angle-of attack of 30° were generated to determine the effect of the test variables on the boundary-layer prior to separation. The theoretical solutions for the nonsimilar, laminar boundary-layer were computed using the code described in Ref. 13. Required as input for the code are the flow conditions at the edge of the boundary layer, the radius of the "equivalent" body-of-revolution, and the wall-temperature distribution.

The required inviscid solution was provided by Ken Houston of Lockheed (Houston) (Ref. 14) using a code based on Newtonian theory. Representative streamlines for an orbiter configuration, whose geometry is essentially that of the model used in the present program except for the absence of the canopy, are presented in Fig. 8 for an angle-of-attack of 30°. Parametric boundary-layer solutions were obtained along the streamline represented by the unbroken line, since this streamline encounters the free-vortex-layer separation downstream of the canopy but is upstream of the influence of the wing. Therefore, numerical solutions for a nonsimilar, laminar boundary-layer were generated along this streamline for six of the test conditions of the experimental program, i.e.,

Condition 1: $M_\infty = 11.80$, $Re_{\infty/ft} = 1.50 \times 10^6$

Condition 2: $M_\infty = 12.25$, $Re_{\infty/ft} = 0.55 \times 10^6$

Condition 3: $M_\infty = 11.68$, $Re_{\infty/ft} = 0.11 \times 10^6$

Condition 4: $M_\infty = 15.70$, $Re_{\infty/ft} = 0.57 \times 10^6$

Condition 5: $M_\infty = 10.10$, $Re_{\infty/ft} = 0.50 \times 10^6$

Condition 6: $M_\infty = 18.59$, $Re_{\infty/ft} = 0.13 \times 10^6$

For the numerical solutions, the windward and the leeward sections were assumed to be isothermal, though not necessarily of equal temperature. A horizontal plane passing through the x-axis (waterline z338) of Fig. 8 divided the windward

section from the leeward section. Solutions were obtained with values for the ratio of T_{wwd}/T_t equal to:

a: $T_{wwd} = 0.90\ T_t$ b: $T_{wwd} = 0.176\ T_t$ c: $T_{wwd} = 0.307\ T_t$

and with values for the ratio for T_{lee}/T_t of

i: $T_{lee} = 0.090\ T_t$ ii: $T_{lee} = 0.114\ T_t$

A summary of the conditions for which solutions were computed assuming that the fluid at the edge of the boundary layer had accelerated isentropically from a stagnation point behind a normal shock (NSE) is presented in Table 4. Typical results from these solutions are presented in Figs. 9 through 14 as well as in Table 4. Solutions were also generated assuming the fluid at the edge of the boundary layer had accelerated isentropically after passing through an oblique shock (PSE). A summary of the conditions for the PSE solutions is presented in Table 5. Typical results are presented in Figs. 15-16.

Attention is called to three points along the streamline which are of special interest (refer to Fig. 8). Since the first, at s = 0.201L (or 0.216 ft.), is a station just upstream of the section interface, the boundary-layer has been subjected to a uniform temperature wall. Since the second, at s = 0.221L (or 0.237 ft.), is just downstream of the section interface, the solution at this location illustrates the effect of a sudden change in surface temperature. The third, at s = 0.326L (or 0.351 ft.), is just upstream of the "assumed" separation location. The term "assumed" is used since, downstream of this location, the surface of the vehicle is inclined away from the free-stream. However, as will be discussed subsequently, the data indicate that the actual flow remained attached downstream of this location.

The Lockheed-generated solutions (Ref. 14) for the Newtonian pressure distribution and the associated metric describing the streamline divergence are presented in Fig. 9. The fluid properties were calculated assuming the flow

accelerated isentropically from the stagnation point behind a normal shock wave (NSE) in accordance with the pressure distribution of Fig. 9. Making the small-cross-flow approximation, the heat-transfer rate along a surface streamline of the inviscid flow can be calculated using the metric scale-factor (or "equivalent radius") to represent an equivalent body of revolution at zero angle-of-attack. The metric coefficients were calculated using the relations described by DeJarnette (Ref. 15) and Rakich and Mateer (Ref. 16).

Also presented in Fig. 9 is an alternate representation for the pressure distribution. As can be seen in Fig. 9b, there were significant differences between the pressure measured on the leeward section of the model (Ref. 17) and the Newtonian value. However, for most of the windward section the Newtonian values provided a suitable representation of the actual pressures. This was evidenced by the satisfactory agreement between the heat transfer to the windward surface as calculated using the Newtonian flow field and the measured value at $s \approx 0.1$ ft (Ref. 17). Thus, an "empirical" pressure distribution was constructed which represents a fairing from the windward Newtonian values to the measured value.

The boundary-layer profiles of the nondimensionalized streamwise velocity and of the nondimensionalized static temperature are presented in Fig. 10 for flow condition 2. Solutions are presented for three values of the windward surface temperature, i.e., (a) $T_{wwd} = 0.090\ T_t$ for case 2aii, (b) $T_{wwd} = 0.176\ T_t$ for case 2bii, and (c) $T_{wwd} = 0.307\ T_t$ for case 2cii. For all three cases the leeward surface temperature was (ii) $0.114\ T_t$. The corresponding solutions for the surface heat-transfer distributions along the streamline are presented in Fig. 11.

At $s = 0.201L$, which is just upstream of the section interface, the boundary-layer thickness increased by 20% with temperature over the range of surface temperatures considered (see Fig. 10a and Table 4b). Furthermore, as the wall

temperature increased, the temperature gradient at the wall and, therefore, the heat transfer decreased dramatically. At s = 0.201L, the heat transfer for $T_{wwd} = 0.307\ T_t$ was approximately 45% of the heat transfer for $T_{wwd} = 0.090\ T_t$ (see Fig. 11a). The magnitude of the decrease was much greater than would be predicted using the relation:

$$\dot{q} = h(T_r - T_w), \tag{12}$$

where

$$T_r = \sqrt{Pr}\,(T_t - T_e) + T_e \quad . \tag{13}$$

Using this relation the recovery temperature was approximately 0.86 T_t for all three cases. For this recovery temperature, $(T_r - T_w)$ for case 2cii was 72% of the value for $(T_r - T_w)$ for case 2aii. The decrease in $(T_r - T_w)$ for the two cases was much less than the decrease in the computed heat-transfer rate. Thus, either the local heat-transfer coefficient or the recovery temperature (or both) depend on the surface temperature for this highly accelerated flow. The computed displacement thickness at this location was small in magnitude and assumed both positive and negative values for these conditions. The values of the displacement thickness are, therefore, not presented in this report. The momentum thickness exhibits an inverse dependence on the surface temperature (see Table 4b).

The leeward surface temperature was the same for all three cases, i.e., $T_{lee} = 0.114\ T_t$. Thus, as the viscous flow passed from the windward section to the leeward section, it was subjected to an abrupt change in wall temperature. For cases 2bii and 2cii the wall temperature decreased from windward values of 0.176 T_t and 0.307 T_t, respectively. However, for case 2aii, the surface temperature increased slightly from the windward value of 0.090 T_t, as the viscous layer moved onto the leeward section. As noted previously, with the wall temperature at s = 0.201L equal to 0.307 T_t (i.e., case 2cii),

there was relatively little heat-transferred from the viscous layer to the surface. Thus, as the boundary layer passes onto the relatively cold, leeward section, there is a relative surplus of energy available for heat transfer. The temperature profile and the resultant increase in heat transfer are evident in Figs. 10b and 11a, respectively. A similar increase in heat transfer occurred for case 2bii. As would be expected, the heat transfer for case 2aii decreased abruptly as the boundary layer moved onto the leeward section. With all three viscous flows subjected to the same leeward surface temperature, the differences in the boundary-layer thicknesses for the three wall-temperature distributions quickly decreased. For example, note in Fig. 10b that the thickness of the boundary layer which had been subjected to the cold forebody (case 2aii) was 94% of that which had been subjected to the hot forebody. Substantial differences which continued to exist in the temperature profiles suggest the use of the enthalpy thickness to characterize the effect of the wall-temperature distribution on the boundary layer solutions. The enthalpy thickness is defined as (Ref. 18):

$$\theta_H = \int_0^\delta \frac{\rho u}{\rho_e u_e} \left(\frac{h}{h_e} - 1 \right) dy \quad , \tag{14}$$

which for a perfect gas is:

$$\theta_H = \int_0^\delta \frac{u}{u_e} \left(1 - \frac{T_e}{T} \right) dy \quad . \tag{15}$$

Value of the enthalpy thickness are presented in Table 4.

At the station just upstream of the separation location assumed for the theoretical solutions, i.e., s = 0.326L, the boundary-layer thickness was essentially the same for all three cases (refer to Fig. 10c and to Table 4). However, the average static temperature in the viscous layer was greatest for

the flow which has been exposed to the hottest windward surface (i.e., T_{wwd} = 0.307 T_t of case 2cii). This can be seen in the nondimensionalized temperature profiles of Fig. 10c. As a result, the enthalpy thickness and the heat transfer were greatest for case 2cii. At s = 0.326L, the computed heat-transfer for case 2cii was 1.13 times that for case 2bii and 1.23 times heat for case 2aii. Because the enthalpy thickness and the heat-transfer rate were greatest for the cases where the surface temperature of the windward section had been the greatest, one would expect the heat-transfer measurements for the downstream separated region to exhibit similar trends. Recall, however, that the wall-temperature distributions of the experimental program correspond to ratios of T_{wwd}/T_{lee} of (1) 0.090 T_t/0.090 T_t, which is combination ai, (2) 0.176 T_t/0.114 T_t, which is combination bii, and (3) 0.307 T_t/0.114 T_t, which is combination cii. Thus, the heat-transfer distribution for case 2ai (which is presented in Fig. 11b) would be more germaine to the analysis of the experimental data than that for case 2aii. For $0.206 \leq s \leq 0.326L$, the local heat-transfer rates computed for case 2ai were approximately equal to those computed for case 2bii. Thus, the difference in the theoretical heat-transfer at the last station before "separation" were of the order of 13% for the three most relevant cases.

The nondimensionalized streamwise velocity and the nondimensionalized temperature profiles for the boundary layer at s = 0.326L are presented in Fig. 12 for flow condition 4, M_∞ = 15.70, $Re_{\infty/ft} = 0.57 \times 10^6$. At this station, the difference in surface temperature of the windward section did not significantly affect the boundary-layer thickness. However, as was the case for flow condition 2, a significant difference remains in the average static temperature in the boundary layer, which is reflected in the enthalpy thickness.

The enthalpy thickness is presented in Fig. 13 as a function of the Reynolds number behind a normal shock wave. Note that, for these wind-tunnel

conditions, the enthalpy thickness can be correlated in terms of this single parameter, Re_{ns}, over the range of free-stream Reynolds numbers and free-stream Mach numbers considered. As has been discussed, the enthalpy thickness was greatest, i.e., least negative, for those cases where the windward surface temperature was greatest, i.e., $T_{wwd} = 0.307\ T_t$.

The momentum thickness

$$\theta = \int_0^\delta \frac{\rho u}{\rho_e u_e}\left(1 - \frac{u}{u_e}\right) dy, \tag{16}$$

which for a perfect gas is:

$$\theta = \int_0^\delta \frac{T_e}{T}\frac{u}{u_e}\left(1 - \frac{u}{u_e}\right) dy \tag{17}$$

is presented as a function of the Reynolds number behind a normal shock wave in Fig. 14. As would be expected from a comparison of eqn. (15) with eqn. (17), the momentum thickness can also be correlated in terms of this single parameter, Re_{ns}, over the range of free-stream Reynolds number and of free-stream Mach numbers considered. The momentum thickness was the smallest for those cases where the windward surface temperature was greatest.

For the PSE solutions, the procedure used to calculate the fluid properties at the edge of the boundary layer was as follows. (1) The static pressure, the Mach number, and the isentropic stagnation pressure was calculated for the flow downstream of a shock wave which was inclined 30° to the free-stream. (2) The location on the streamline at which this value for the static pressure and the value predicted using the NSE distribution (presented in Fig. 9) were equal was determined. (3) Downstream of this location, the flow was assumed to acclerate isentropically in accordance with the pressure distribution (p/p_{te}) given by the product of the pressure distribution of Fig. 9 (p/p_{t2}) and the ratio p_{t2}/p_{te}. Numerical solutions for a nonsimilar, laminar boundary-layer were generated for

three of the test conditions:

Condition II: $M_\infty = 12.25$, $Re_{\infty/ft} = 0.55 \times 10^6$

Condition IV: $M_\infty = 15.70$, $Re_{\infty/ft} = 0.47 \times 10^6$

Condition V: $M_\infty = 10.10$, $Re_{\infty/ft} = 0.50 \times 10^6$

Note that these free-stream conditions are identical to those for condition 2, 4, and 5. However, the shock strengths and, therefore, the local flow conditions at the edge of the boundary-layer are markedly different. It was found that the local heat-transfer rate and the local Reynolds number integrated along the streamline for a given free-stream condition was much larger for the PSE solutions (see Table 5) than the corresponding values for the NSE solutions. As a result, the boundary layer is thinner. The effects of the surface temperature distribution on the PSE solutions for the boundary-layer thickness and for the momentum thickness (see Table 5), for the boundary-layer profiles of the nondimensionalized streamwise velocity and of the nondimensionalized static temperature (see Fig. 15) and for the heat-transfer distribution (see Fig. 16) were similar to those observed for the NSE solutions.

Recall that nonsimilar, laminar boundary-layer solutions have been generated for the modified Newtonian pressure-distribution and for the empirical pressure distribution using the NSE relations and the PSE relations. The theoretical heat-transfer thus computed for $s = 0.326L$ (refer to Fig. 8) is presented in Fig. 17 as a function of Re_{ns}. The theoretical solutions for all four cases are correlated by:

$$St = A(Re_{ns})^{-0.5} \qquad (18)$$

The specific value of A depends on the pressure distribution, the metric-coefficient distribution, and the assumed expansion process. (Although solutions are presented only for the metric distribution of Fig. 9, the heat transfer differed significantly for solutions generated for other distributions of the metric co-

efficient). Note that, for a given pressure distribution, the PSE heat-transfer is approximately 1.2 times the NSE value. Note, however, that the pressure distribution had a more pronounced effect on the heat-transfer rate. The heat transfer calculated using the empirical pressure distribution was approximately 2.7 times that calculated using the modified Newtonian pressure distribution. Although the empirical pressure distribution was only very approximate and although it was not possible to calculate a metric-coefficient distribution based on experimental pressures, the theoretical heat-transfer values based on the empirical pressure distributions, i.e., curves 3 and 4, will be used for the subsequent comparisons with the heat-transfer data from gages T18, T23, and T33.

The Experimental Data for an Angle-of-Attack of 30°

The heat-transfer measurements are presented either as:

(1) a dimensionless ratio of heat-transfer coefficients, $h/h_{t,ref}$, which involves the ratio of the measured, local heat-transfer rate to the theoretical heat-transfer rate to the stagnation point of a 0.01-ft. radius sphere as calculated using the theory of Fay and Riddell (Ref. 4). For purposes of data presentation, the recovery factor r has been set equal to unity. Although the definition for the heat-transfer coefficient employed by Calspan for data reduction (see eqn. 4) differs from that used in the theoretical section (see eqn. 12), the magnitude of the dimensionless ratio is the same for both definitions.

(2) a Stanton number where

$$St = \frac{\dot{q}_w}{\rho_\infty U_\infty (H_o - H_w)} = \frac{\dot{q}_w}{\rho_{ns} U_{ns} (H_o - H_w)}$$

Other parameters used in the data correlations include the free-stream Reynolds number based on model length, $Re_{\infty,L}$, where

$$Re_{\infty,L} = \frac{\rho_\infty U_\infty L}{\mu_\infty} \qquad (19)$$

(L is the model length, 1.075 ft.) and the Reynolds number behind a normal shock, Re_{ns}, where

$$Re_{ns} = \frac{\rho_{ns} U_{ns} r_{ref}}{\mu_{ns}} \qquad (28)$$

(r_{ref} = 0.01 ft.).

Heat-transfer distributions. - Typical heat-transfer distributions are presented in the isometric projections of Fig. 18 for the $\phi = 0°$ plane, which is the leeward pitch-plane or plane-of-symmetry, and for the $\phi = 90°$ plane, for which the boundary-layer was attached foreward of the wing. A viscous interaction between the vortex shed from the wing leading-edge and the attached boundary layer on the fuselage produced locally high heating rates at gage T33 (which is the fourth gage in the $\phi = 90°$ plane). This viscous interaction apparently also affected the heat transfer in the separated region. Note the relatively high heat-transfer rate recorded at the gage at x = 0.70L in the $\phi = 0°$ plane (i.e., the next-to-last gage in the leeward pitch-plane) for the higher Reynolds number flow. Heat-transfer data reported by Zakkay et al (Ref. 19) also exhibited locally high, leeward heating rates near the aft-end of the orbiter (at x $\simeq$ 0.8L). The mechanism responsible for this heat-transfer perturbation is believed to be comparable to that of the present tests.

The heat-transfer distribution in the leeward plane of symmetry was similar to that observed during previous tests which were conducted in Tunnel B at AEDC (Ref. 20) of a model with a protuding cockpit. A shock-induced increase in the heating rate was recorded at the gages located on the canopy windshield. The shock-perturbed, nondimensionalized value for the heat transfer was greatest for the highest Reynolds number. Although the nose region geometry differed for the configurations tested in Tunnel B, the nondimensionalized heat-transfer coefficients for the windshield also increased with Reynolds number. The minimum heat-transfer occurred just downstream of the canopy.

At the lower Reynolds number (Fig. 18b) the downstream heat-transfer was essentially constant. However, at the higher Reynolds number, the heat-transfer increased markedly at $x \approx 0.4L$ and remained high at the downstream gages. This Reynolds-number-dependent behavior indicates that the increase was due to transition of the shear layer. A similar increase was evident in the heat-transfer distributions for all three Reynolds numbers of Ref. 20 ($1.6 \times 10^6 \leq Re_{\infty,L} \leq 7.8 \times 10^6$). Increased heating to the leeward surface due to transition of the shear layer was also reported by Zakkay et al (Ref. 19) and by Whitehead et al (Ref. 21).

The heat-transfer measurements for those leeward pitch-plane gages downstream of the cockpit are presented in Fig. 19 for those runs where the free-stream Mach number was approximately 12. The data are presented for the highest windward-surface-temperature ($0.31\ T_t$) in Fig. 19a, for the intermediate windward-surface-temperature ($0.18\ T_t$) in Fig. 19b, and for the lowest windward-surface-temperature ($0.09\ T_t$) in Fig. 19c. For a given Reynolds number, the heat-transfer distributions were essentially the same for the two higher surface temperatures (Fig. 19a and Fig. 19b). The phrase "essentially the same" was chosen because, although the distributions were qualitatively similar for a given Reynolds number, the magnitude of the heat-transfer did depend on the windward surface-temperature (as will be discussed for subsequent figures). At the lowest Reynolds number, the heat-transfer distribution indicated that the shear layer was laminar. At the intermediate and at the highest Reynolds number, the heat-transfer distributions indicated the onset of transition. When the shear layer was turbulent, the dimensionless heat-transfer coefficient at a given station was Reynolds-number dependent. This Reynolds-number dependence resulted because the numerator contains the experimental value of the local heat-transfer which resulted from a turbulent shear-layer while the denominator contains the theoretical laminar value. Since the

Reynolds-number dependence for the numerator differs from that for the denominator, the dimensionless ratio would not be expected to be independent of Reynolds number.

Significant differences were observed at the highest Reynolds number for those runs where $T_{wwd} \approx 0.09\ T_t$ (see Fig. 19c). The shear layer apparently was laminar at the lowest Reynolds number. At the intermediate Reynolds number, the data indicated transition occurred, with the turbulent heat-transfer measurements exhibiting only a weak dependence on streamwise position. However, at the highest Reynolds number, there were marked streamwise variations in the heat-transfer measurements downstream of transition. This was the only run for which such locally severe heating rates were observed for the vortical, turbulent flow. Note that heat-transfer rates were measured only at finite number of points. It is possible that similar peaks occurred for other runs but were not measured.

Circumferential heat-transfer distributions for those runs where the free-stream Mach number was essentially 12 are presented in Fig. 20. Distributions are presented for two axial-stations: $x = 0.335L$ and $x = 0.420L$ for each of the three surface-temperature combinations. Recall that $\phi = 0°$ (0.0 radians) corresponds to the leeward pitch-plane and that $\phi = 90°$ (1.571 radians) is the tangency point for the leeward arc. Based on the heat-transfer data, the boundary-layer separation occurred between 40° and 56° from the leeward plane-of-symmetry (at these two stations). At the forward station, i.e., $x = 0.335L$, the heat-transfer data indicated that both the attached boundary-layer and the shear layer were laminar. At the downstream station, i.e., $x = 0.420L$, the heat-transfer measurements reflect the complexity of the local flow. The Reynolds-number dependence of the heat-transfer measurments for gage T33 (at $\phi = 90°$) was due to the viscous interaction between the boundary layer and the vortical flow generated by the wing leading-edge. The onset of shear-layer

transition affected the heat-transfer measurements for the gage located in the leeward plane-of-symmetry at $x = 0.420L$ (which was gage T29). As noted when discussing the data of Fig. 19, the shear layer was laminar at the lowest Reynolds number, turbulent at the two higher Reynolds numbers. However, the heat-transfer measurements from the gages between $\phi = 90°$ and $\phi = 0°$ were independent of Reynolds number, indicating that the attached boundary-layer and the separated shear-layer were laminar.

The heat-transfer distributions for those leeward pitch-plane gages downstream of the canopy are presented in Fig. 21 for those runs where the free-stream Reynolds number based on model length, $Re_{\infty,L}$, was nominally 0.6×10^6. The controlled test-parameter which was varied for these runs was the free-stream Mach number. However, because the free-stream Mach number varied, the Reynolds number behind a normal shock wave,

$$Re_{ns} = \frac{\rho_{ns}\, U_{ns}\, r_{ref}}{\mu_{ns}} ,$$

($r_{ref} = 0.01$ ft) also varied. Specifically, the values were as follows:

Run	M_∞	$Re_{\infty,L}$	Rs_{ns}
15	10.05	0.525×10^6	704.9
10	12.26	0.566×10^6	528.9
13	15.71	0.613×10^6	354.0
38	10.16	0.610×10^6	770.1
34	12.28	0.600×10^6	557.9
37	15.70	0.619×10^6	357.5

Over the Mach number range of the present test program, Re_{ns} varied by a factor of two, although $Re_{\infty,L}$ was approximately constant.

Note that, if one considers the leeward viscous flow as characterized more by the Reynolds number behind a normal shock wave than by the free-

stream Reynolds number, the nondimensionalized values of the heat-transfer coefficient increased with Re_{ns}. As noted previously, this is not unexpected since the numerator would exhibit the Reynolds-number dependence of turbulent data, while the denominator would exhibit that for laminar theory. Thus, it is suggested that the data of Fig. 21 not be interpreted in terms of a Mach number effect but in terms of a Reynolds number effect. Further, the parameters used in correlations of the data should be evaluated using properties downstream of the shock wave rather than the free-stream conditions. The use of local flow conditions to correlate the separated-flow parameters is certainly not innovative (e.g., ref. 22).

Circumferential heat-transfer distributions are presented in Fig. 22 for those runs where the free-stream Reynolds number, $Re_{\infty,L}$, was nominally 0.6×10^6. The variation in heat transfer near the leeward plane-of-symmetry at x = 0.420L was due to the turbulent character of the shear layer. Thus, these data are believed to exhibit a Reynolds-number dependence (characterized for the present report by the parameter Re_{ns}) rather than a Mach-number dependence.

Data for individual gages. - So that the relation between the local flow characteristics and the local heat transfer can be better seen, the experimental Stanton numbers (St) for a particular gage are presented as a function of Re_{ns}. The sketches of Fig. 23 illustrate the locations of the gages for which heat-transfer data are presented. Similarly, experimental pressures for specific orifices are presented as a function either of $Re_{\infty,L}$ or Re_{ns}. The nondimensionalized pressure parameter is the local static-pressure measurements divided by either the calculated free-stream static-pressure (p/p_∞) or divided by the calculated stagnation pressure behind a normal shock wave (p/p_{t2}).

For the correlations of the measurements for a given gage (both pressure data and heat-transfer data), the symbols used are consistent from one figure

to another. Since the data are presented as a function of the Reynolds number, the symbols are used to identify the nominal values for the two remaining test parameters (Recall that α = 30° for this section). For the free-stream Mach numbers:

$$\bigcirc\ M_\infty \approx 10\ ;\quad \square\ M_\infty \approx 12\ ;\quad \diamond\ M_\infty \approx 16\ ;\quad \nabla\ M_\infty \approx 18$$

For the temperature combinations:

$$\text{open: } T_{wwd} \approx 0.31\ T_t,\ T_{lee} \approx 0.11\ T_t$$
$$\text{half-filled: } T_{wwd} \approx 0.18\ T_t,\ T_{lee} \approx 0.11\ T_t$$
$$\text{filled: } T_{wwd} \approx 0.09\ T_t,\ T_{lee} \approx 0.09\ T_t$$

This symbol logic was not used in figures where the experimental measurements are presented as a distribution rather than data for a particular gage, e.g., Figs. 27 and 28.

(a) Gages located on the lateral surface of the fuselage where the boundary layer is attached. - The experimentally-determined Stanton numbers for gages T18, T23, and T33 are compared with the theoretical values in Fig. 24a, 24b, and 24c, respectively. The theoretical values are those for s = 0.326L (see Fig. 8) as calculated using the "empirical" pressure distribution and the Newtonian metric coefficient distribution of Fig. 9. Thus, the theoretical values correspond to correlations 3 and 4 of Fig. 17. Note that for these flow-field assumptions, the theoretical values did not provide even rough estimates for the experimental values. Based on a telephone conversation with Dr. Goodrich, it is believed that the correlation between theory and data would be significantly improved if the actual pressure distribution and a metric coefficient distribution based on the actual pressures were to be used.

However, a comparison between the measurements and the laminar, theoretical values indicates that the boundary layer was laminar for gages T18 and T23. For gage T33 (see Fig. 24c), the experimentally-determined Stanton numbers indicated the flow was laminar for some runs. However, for other runs the

data were correlated by the turbulent correlation

$$St = B(Re_{ns})^{-0.2} \tag{21}$$

This turbulent behavior is attributed to the interaction between the vortical flow generated by the wing leading-edge and the boundary layer. With the exception of these turbulent data, the experimental heat-transfer values for gages T18. T23, and T33 were usually highest for those runs where $T_{wwd} \approx 0.31\ T_t$. This is consistent with the correlation between wall-temperature distributions and the theoretical, laminar heat-transfer calculations presented in Figs. 11 and 16.

(b) Gages located on the nose upstream of the cockpit. - Oil-flow patterns for the nose region of the orbiter indicate the existence of a free-vortex layer type of separation. The oil-flow pattern obtained using a partial model of the current orbiter configuration exposed to a hypersonic flow ($M_\infty \approx 8$, $Re_\infty/ft \approx 1 \times 10^6$) in Tunnel B of AEDC is presented in Fig. 25. At $x \approx 0.12L$, the circumferential component of the flow which was initially directed toward the leeward plane of symmetry reversed direction. At the separation line, oil accumulated and proceeded to travel down the separation line toward the rear of the orbiter. The oil near the leeward plane-of-symmetry continued to flow from the attached region into the vortex region indicating that the longitudinal component of the skin friction was also finite.

Also included in the photograph, which was provided by Dr. Goodrich, are the "approximate" locations of the gages whose data will be discussed subsequently. The locations may be slightly inaccurate because of the difficulty of locating specific coordinates in a photograph of a three-dimensional configuration. Furthermore, it should be noted that the oil-flow pattern of Fig. 25 was obtained in another tunnel at different test conditions. Nevertheless, there was good correlation between the heat-transfer and the surface-pressure measurements

from the Calspan tests and the flow field phenomena depicted in the oil-flow pattern. Thus, T4 and PS2 were located upstream of the free-vortex separation. The scrubbed oil pattern near the plane-of-symmetry indicates relatively high shear forces existed at T8 and T9.

The dimensionless pressure parameter p/p_∞ is presented as a function of Re_{ns} in Fig. 26a. Note that, for a given Mach number, this parameter was approximately constant (except for one apparently erroneous measurement). Thus, the experimental value of p/p_∞ was a function of the free-stream Mach number but not of the Reynolds number. As might now be expected, the pressure ratio p/p_{t2} for the orifice in this attached flow region was essentially constant, independent both of Mach number and of Reynolds number. The pressure measurements for PS2, thus nondimensionalized, are presented in Fig. 26b.

The pressure distribution for the leeward plane-of-symmetry is presented in Fig. 27. Included are data from the present tests and from the Ames Research Center as provided by Dr. Goodrich (Ref. 17). For the lower Mach number of the Ames tests, the unit Reynolds number was 6.5×10^6 per foot. Upstream of the cockpit, the nondimensionalized pressures from the Ames tests were independent of the test condition. The streamwise pressure decrease in the static pressure indicates the rapid acceleration of the flow over the nose. Note that the measured pressure was a minimum at x = 0.10L then increased for the next orifice, which was also upstream of the cockpit. Using data for a different orbiter configuration, Bertin et al (Ref. 20) found that 30° was the lowest angle-of-attack at which the cockpit-generated perturbation caused the heat-transfer to increase at thermocouples upstream of the canopy. The cockpit-generated shock-wave produced a sharp increase in the pressure measurements for those orifices located on the windshield. For the data of Fig. 27, the maximum windshield pressure was approximately 3.0 times the upstream minimum. Using the experimental pressures and the normal shock expansion (NSE) assumption

to define the upstream Mach number, a conical shock-wave (Ref. 23) generated by the cockpit deflection would cause the pressure to increase by a factor of 3.26, while a wedge shock-wave would produce a pressure increase of 4.37. Downstream of the cockpit, the pressure data were not independent of the test conditions.

The heat-transfer distribution for the nose-region/cockpit-windshield is presented in Fig. 28. Upstream of the windshield, the nondimensionalized heat-transfer coefficient was essentially independent of Reynolds number. As the flow expands over the nose, the heat transfer decreases monotonically until the flow encounters the windshield ($x > 0.15L$). Note that these heat-transfer data did not exhibit an upstream influence of the cockpit. This is attributed to a Reynolds-number dependence, since the Calspan heat-transfer measurements of Fig. 28 were obtained at lower Reynolds numbers than the ($M_\infty = 7.32$) Ames pressure data of Fig. 27 or the heat-transfer data of Ref. 20. Thus, the Reynolds number (or, equivalently, the shear layer thickness) is an important parameter in deciding whether or not the presence of the cockpit perturbs the upstream flow for a given geometry. Note also that, at the lowest Reynolds number of Fig. 28, the heat-transfer rates measured on the windshield were not much greater than the minimum value measured on the upstream nose. Thus, the abrupt change in the surface contour had a relatively small effect on the heat transfer for the relatively thick shear layer of the lowest Reynolds-number flow. The heat transferred to the windshield increased markedly with Reynolds number. Furthermore, the heat transfer in this region was very sensitive to position. Gage T11 ($x = 0.170L$), which recorded the highest of the leeward heating rates on runs 4 and 5, did not operate after run 5. As the flow expands past the cockpit, the heat transfer decreases rapidly. The fact that the nondimensionalized heat-transfer coefficient at $x = 0.213L$ was independent of Reynolds number indicates that the large favorable pressure gradient produced

relaminarization of the viscous layer.

Theoretical solutions for the nose-region boundary-layer in the leeward plane-of-symmetry were generated using the code of Ref. 13. The local fluid properties at the edge of the boundary layer were evaluated assuming the inviscid flow expanded isentropically from the stagnation point behind a normal shock wave (NSE) in accordance with the pressures measured at the Ames Research Center (Fig. 27). Solutions were generated for a two-dimensional boundary-layer and for a three-dimensional boundary-layer with small cross-flow. For the three-dimensional solutions, the Newtonian values for the metric-coefficient distribution provided by Houston (Ref. 14) were used.

The theoretical values for the nose-region heat-transfer are compared with the experimental values for T4 ($x = 0.100L$) and for T8 ($x = 0.125L$) in Fig. 29. The theoretical solutions for three-dimensional flow underpredicted the heat transfer by (typically) one-third. Thus, the data indicate that, although they free-vortex separation of the boundary layer has occurred in this region away from the plane of symmetry, there was a strong axial flow component near the plane of symmetry. The resultant shearing force can be seen in oil-flow photograph of Fig. 25 and in the heat-transfer data of Fig. 29. Improved correlation between data and theory would be expected if the effect of the entropy gradients on the fluid properties at the edge of the boundary layer were to be included and if a metric-coefficient distribution based on the actual flow field were to be used. Nevertheless, the similarity between the Reynolds number dependence of the data and of the theoretical, laminar values indicates that the flow was laminar at both stations for all conditions. Note also that the experimental heat-transfer rates were greatest for those runs where the windward surface-temperature was greatest ($T_{wwd} \simeq 0.31\ T_t$). Thus, as noted in the theoretical section, since there was less heat transferred from the boundary layer to the relatively hot wall, there was a "surplus" of energy available for heat transfer

to the leeward section.

(c) A gage located on the cockpit windshield. - A shock wave was generated as the supersonic flow of the nose region encountered the cockpit windshield. The interaction between the viscous layer and the cockpit-generated shock wave significantly perturbed the flow field. The experimentally-determined Stanton numbers for a gage on the cockpit windshield, gage T10, are presented in Fig. 30 as a function of the Reynolds number behind a normal shock wave. For relatively low values of Re_{ns} (i.e., $Re_{ns} < 130$), the St:Re_{ns} relationship was that for a laminar flow. For $Re_{ns} > 300$, the experimentally determined Stanton numbers were essentially constant, i.e., independent of Reynolds number.

The heat transfer to a gage on the cockpit windshield T10 divided by that to a gage on the nose T8 is presented in Fig. 31 as a function of Re_{ns}. Note that, for $\alpha = 30°$, the minimum upstream heat-transfer was measured not at T8 but at T9. Furthermore, the maximum windshield heating rate was measured at T11, which (unfortunately) did not operate after run 5. The ratio of $\dot{q}_{T10}/\dot{q}_{T8}$ was selected to represent the cockpit-induced heat-transfer perturbation since both gages functioned during the entire program and since one could use the pressure distribution of Fig. 27 to calculate a theoretical value for $\dot{q}_{T8}$ (i.e., the reference heating). For $Re_{ns} < 130$, the ratio $\dot{q}_{T10}/\dot{q}_{T8}$ was essentially constant. As noted when discussing the heating data of Fig. 28, the perturbation due to the presence of the cockpit was relatively small at the low Reynolds number. For $Re_{ns} > 300$, the experimental value of $\dot{q}_{T10}/\dot{q}_{T8}$ varied approximately as $(Re_{ns})^{0.64}$. Two calculated values of $\dot{q}_{T10}/\dot{q}_{T8}$ are included in Fig. 31 for comparison with the data. Both used the empirical relation suggested by Markarian (Ref. 24) for a laminar interaction:

$$\frac{\dot{q}_{PK}}{\dot{q}_{ref}} = \left(\frac{P_{PK}}{P_{ref}}\right)^{1.29} \tag{22}$$

Using the theoretical pressure ratio for a conical shock wave, the heat-transfer ratio is 4.59 (see the white arrow labeled 1). Using the experimental pressure ratio (which was obtained at Re_{ns} = 7600), the heat-transfer ratio is 3.88 (see the black arrow labeled 2). Although these calculated values are roughly equal to the maximum experimental values, the correlation is not necessarily satisfactory, since the experimental values are for relatively low values of Re_{ns}.

(d) Gages located in the separated region downstream of the cockpit where the shear layer was laminar. - The heat-transfer measurements for T19 and for T21 are presented in Fig. 32. The oil-flow pattern of Fig. 25 indicates that these gages were located near the boundary of the separated region. The reader is reminded that, as noted previously, the relative location of the gages with respect to the oil-flow pattern is only approximate. Thus, when a gage is on the fringe of a region in Fig. 25, it may have actually been in an adjacent region. However, Hefner and Whitehead (Ref. 25) noted that, whereas there was a "threshold" Reynolds number (based on body length) below which the peak heating decreased abruptly, the "featherlike" reattachment regions existed at low and high Reynolds numbers. For a given test condition, the heat-transfer rates were essentially equal for these two gages and were approximately one-sixth the heat-transfer rates measured at T23, which was subjected to the attached, laminar boundary-layer at this axial station. Note that, for gages T19 and T21, the experimentally-determined Stanton numbers varied as $(Re_{ns})^{-0.5}$, as did the data for T23. Thus, it is concluded that the shear layer was laminar for all test conditions at this station. Note that the heat transfer was usually greatest for those runs where the windward surface-temperature was greatest, i.e., $T_{wwd} = 0.31\ T_t$.

(e) Gages located in the separated region downstream of the cockpit where the shear layer was transitional. - The heat-transfer measurements for T29 and for

T31 are presented in Fig. 33. These gages were located in the separated region downstream of the cockpit at $x = 0.420L$. Based on Fig. 25, T31 was subjected to the "fully" separated flow between the free-vortex separation and the vortex-induced feather pattern along the lee meridian (where T29 was located). Note that the relation between the experimentally-determined Stanton number and the Reynolds number differed significantly for these two gages. For gage T29, the measurements followed a laminar correlation, $(Re_{ns})^{-0.5}$, for $Re_{ns} < 130$. For $Re_{ns} > 300$, the data for gage T29 followed a turbulent correlation, $(Re_{ns})^{-0.2}$. Over the entire Reynolds number range, the experimentally-determined Stanton number for gage T31 varied roughly as $(Re_{ns})^{-0.5}$. For $Re_{ns} < 130$, i.e., where the shear layer was laminar for both locations, the heat-transfer rates were approximately equal for the two gages and were roughly one-sixth of the values measured at T33. Referring to Fig. 24c, the boundary layer for T33 was laminar and attached. For $Re_{ns} > 300$, the heat-transfer rates for gage T29 were significantly greater than those for gage T31 but significantly less then the attached values for gage T33.

The static-pressure measurements for PS4 are presented in Fig. 34. The static pressures which have been divided either by the free-stream value (p/p_∞) or by the stagnation pressure behind a normal shock wave (p/p_{t2}) are presented as a function either of Re_{ns} or of $Re_{\infty,L}$. The presentation of the data in terms of the parameter p/p_{t2} as a function of Re_{ns} appears to provide the best correlation. The static pressure at this location in the separated region decreased as the Reynolds number increased. The Reynolds-number dependence of these data corresponded to the second of the four regions described by Crocco and Lees (Ref. 26) to characterize the correlation between base pressure and Reynolds number, see Fig. 35. The decrease in base pressure as the Reynolds number increased occurred because transition in the shear layer moved upstream from the throat (with a corresponding order-of-magnitude increase in the local mixing rate). The increased mixing rate was more important than the accompany-

ing increase in the thickness of the mixing layer which, by itself, would have caused the base pressure ratio to decrease.

(f) Gages located in the separated region downstream of the cockpit where the shear layer was turbulent. - Heat-transfer measurements for gages T37, T39, and T41 are presented in Fig. 36. For all three gages, the experimentally determined Stanton number varied as $(Re_{ns})^{-0.2}$, the correlation for a turbulent shear layer. Note, however, that the measurements for gage T41 exhibited significant scatter. Recall that this gage was located in the region affected by the flow-field perturbation created by the interaction between the viscous flow and the vortex shed from the wing leading-edge.

The highest heat-transfer rates recorded at T37 were those runs where $T_{wwd} \approx 0.31\ T_t$. (Unfortunately, the gage was inoperative for the runs where $T_{wwd} \approx 0.09\ T_t$). Thus, although the shear layer was turbulent, the correlation between the local heating rate and the windward surface temperature is similar to that observed for gages where the shear layer was laminar. For gages T39 and T41, there was no clear correlation between the local heat-transfer rate and the windward surface-temperature. The mixing due to the interaction with the vortical flow apparently eliminated the effect of the windward surface-temperature.

The static-pressure measurements for PS5 are presented in Fig. 37 as a function of Re_{ns}. The Reynolds-number dependence of the pressure corresponds to Region 3 and/or the beginning of Region 4 of the Crocco-Lees model (see Fig. 35). Thus, the mixing rate is relatively unaffected by the change in Reynolds number and the thickening of the boundary layer produced increased pressure. Since the pressures measured at PS4 (see Fig. 34) were less than the values obtained in PS5, it is concluded that the flow at PS4 corresponds to the end of region 2. The relation between the data for PS4 and PS5 and the Crocco-Lees model is not obvious, since the data are presented herein as a func-

tion of Re_{ns}, which depended only on the flow condition and not the gage location. Thus, the correlation parameters do not contain a characteristic length which would define the effect of the length from the separation location or of the shear layer thickness.

The experimentally-determined Stanton numbers were averaged for gages located on the leeward surface. $\overline{St}_{sig}$, the Stanton number averaged over all the leeward gages downstream of the cockpit (see Fig. 38) are presented as a function of Re_{ns} in Fig. 39. $\overline{St}_{sep}$, the Stanton number averaged only for those gages in the "separated" region (see Fig. 40) are presented as a function of Re_{ns} in Fig. 41. The separated region was determined using the circumferential heat-transfer distributions (e.g., Fig. 20). The average value of the Stanton number varied as $(Re_{ns})^{-0.37}$ for both averages. Specifically,

$$\overline{St}_{sig} = 0.00463\ (Re_{ns})^{-0.37} \tag{23a}$$

and

$$\overline{St}_{sep} = 0.00282\ (Re_{ns})^{-0.37} \tag{23b}$$

Note that the average value over the "entire" leeward region (including gages where the boundary layer was attached) was 1.64 times that for the separated region.

Note that the correlations for the leeward Stanton numbers in equation 23 do not account for the effect that the windward surface-temperature had on the leeward heating. As noted when discussing the theoretical results and the heat-transfer measurements for individual gages, the leeward heat-transfer was greatest when the windward surface-temperature was greatest. To obtain a measure of the wall-temperature effect, $\overline{St}_{sep}$ for a particular run has been divided by $0.00282\ (Re_{ns})^{-0.37}$ for that run and is presented in Fig. 42 as a function of T_{wwd}/T_t. As would be expected, the heat-transfer parameter increased as the temperature of the windward surface increased. If one assumes a linear

correlation of the data, a least squares fit yields the relation:

$$\frac{\overline{St}_{sep}}{0.00282(Re_{ns})^{-0.37}} = 1.067 \left(\frac{T_{wwd}}{T_t}\right) + 0.7905 \tag{24}$$

Thus, the experimentally-determined Stanton numbers increased by approximately 26% over the range $0.09\ T_t < T_{wwd} < 0.31\ T_t$, i.e., the range for the present test program.

The Experimental Data for an Angle-of-Attack of 40°

Of the twenty-nine runs using the orbiter configuration, eight were for $\alpha = 40°$ (see Table 3). Since the experimental program concentrated on the $\alpha = 30°$ configuration, the theoretical flow-field solutions were limited to the $\alpha = 30°$ conditions. Because of the limited amount of data from the $\alpha = 40°$ runs, conclusions regarding trends will often be influenced by the results for $\alpha = 30°$.

(a) Gages located on the lateral surface where the boundary layer was attached. - The experimentally-determined Stanton numbers for gages T18, T23, and T33 are presented in Fig. 43. Since the experimental values varied as $(Re_{ns})^{-0.5}$, the viscous flow was laminar. Note that the magnitude of the Stanton numbers for $\alpha = 40°$ were approximately equal to the corresponding values for $\alpha = 30°$, where the boundary layer was attached. Thus, it is concluded that the laminar boundary-layer for these three gages was also attached for $\alpha = 40°$. The experimental heat-transfer values were usually highest for those runs where $T_{wwd} \approx 0.31\ T_t$. However, there were only a limited number of points at the lower temperature and the observation is influenced by the experience with the $\alpha = 30°$ data.

(b) Gages located on the nose upstream of the cockpit or on the cockpit windshield. - The static-pressure measurements for PS2, which were divided either by P_∞ or by P_{t2}, are presented in Fig. 44. It is believed that the shear layer was separated at this higher angle-of-attack. Furthermore, the measurements

were very sensitive to the windward surface temperature. Because the temperature-dependent variation was so extreme and was not exhibited to a similar degree in the other pressure and the heat-transfer data, the possibility exists that the temperature affected the validity of these measurements.

The nose-region heat transfer distributions for the leeward pitch-plane are presented in Fig. 45 for those runs where $M_\infty \simeq 12$. Note that, at the highest Reynolds number, the cockpit-induced perturbation extended well upstream of the windshield. At the lowest Reynolds number, the pitch-plane heat transfer was essentially constant over the nose region and increased relatively little as the flow encountered the windshield. That the magnitude and the extent of the heat-transfer perturbation was greatest at the highest Reynolds number is consistent with the heat-transfer and pressure measurements for $\alpha = 30°$.

The experimentally-determined Stanton numbers for gages T4, T8, and T10 are presented in Fig. 46 as a function of Re_{ns}. There were no simple correlations, since the heating rates in this region were affected by the cockpit-generated flow-field perturbation, whose magnitude and extent were Reynolds-number dependent. Note that the experimentally-determined Stanton numbers were greatest for gages T4 and T8. Such was not the case for the measurements at T10.

The heat-transfer ratio $\dot{q}_{T10}/\dot{q}_{T8}$ is presented in Fig. 47 as a function of Re_{ns}. The correlation was qualitatively similar to that observed when alpha was 30°. For (the one condition where) $Re_{ns} < 130$, $\dot{q}_{T10}/\dot{q}_{T8}$ was of order unity. For $Re_{ns} > 300$, the ratio increased with Re_{ns}. Because of the limited data available, it is not possible to determine whether the considerable variation evident in the data of Fig. 47 was due to experimental error or to undefined flow mechanisms.

(c) Gages located in the leeward separated region downstream of the cockpit. - The heat-transfer distributions from the leeward pitch-plane downstream of the cockpit are presented in Fig. 48 for runs where $M_\infty \simeq 12$. The heat-transfer was

a minimum just aft of the cockpit. Downstream, the heat transfer increased, being constant for $0.42L \leq x \leq 0.60L$. Note that the nondimensionalized heat-transfer coefficient in this region did not vary appreciably with Reynolds number, as had been the case with the higher Reynolds-number measurements for $\alpha = 30°$ when the shear layer was turbulent (see Fig. 19). Referring to Fig. 23, it can be seen that gage T29 (which was at $x = 0.42L$, i.e., at the upstream end of the increased heating of Fig. 48) was in the "shadow" of the wing leading-edge. Thus, the local plateau in heating is attributed to effect of the wing on the leeward flow. For $x \geq 0.7L$, the nondimensionalized heat-transfer coefficients increased markedly and varied with Reynolds number. At the corresponding test condition ($M_\infty = 11.81$, $Re_{\infty,L} = 1.676 \times 10^6$, $T_{wwd} \approx 0.31\ T_t$), the heat-transfer measurements indicated the onset of transition by $x = 0.42L$ for $\alpha = 30°$ (see Fig. 19a). The differences in the flow field at the higher angle-of-attack may have substantially altered the onset of shear-layer transition. Thus, it appears that transition occurred further downstream for a given free-stream Reynolds number when alpha was 40°.

Heat-transfer distributions for the leeward pitch-plane are presented in Fig. 49 for runs where $Re_{\infty,L} \approx 0.6 \times 10^6$. The distributions for all four runs were qualitatively similar to those discussed in Fig. 48. The experimentally-determined heat-transfer coefficients were essentially equal for runs 19, 39, and 40. The dimensionless heat-transfer coefficients for run 21 were significantly higher than those from the other three runs. Referring to the circumferential distributions of Fig. 50, the relatively high heating rates for run 21 were limited to gages in or near the leeward plane-of-symmetry.

The Stanton number is presented for T19 and T21, which were located at $x = 0.279L$, and for T29 and T31, which were located at $x = 0.420L$, in Figs. 51 and 52, respectively. There was considerable scatter in the data for the two pitch-plane gages, i.e., T19 and T29. Referring to the data presented in Figs.

49 and 50, the heat-transfer measurements for run 21 were found to be significiently high. Although the cause of the deviation is not understood, let us eliminate the measurements for run 21 (◇) and for run 22 (○) from consideration in Figs. 51a and 51b. Having eliminated these measurements, the Stanton number for all four gages varied as $(Re_{ns})^{-0.5}$, the laminar correlation.

The static-pressure measurements for PS4 and for PS5 are presented as a function of Re_{ns} in Figs. 53 and 54. For a particular run, the pressure for PS5 was consistently higher than the value for PS4. Based on this observation, one would conclude that the pressure at PS4 was dominated by an increased mixing rate as transition in the shear layer moved upstream, while the pressure at PS5 was affected by the changes in the viscous layer thickness.

The Stanton number for gages T37, T39, and T41 are presented in Fig. 55 as a function of Re_{ns}. Although there was significant scatter in the few measurements available, the Stanton number varied (approximately) as $(Re_{ns})^{-0.5}$ for gages T37 and T39 and as $(Re_{ns})^{-0.2}$ for gage T41. Locating transition between 0.6L and 0.7L is consistent with the comments made when discussing the heat-transfer distribution.

The experimentally-determined Stanton numbers were averaged for gages located on the leeward surface. $\overline{St}_{sig}$ (see Figs. 38 and 56) varied as $(Re_{ns})^{-0.28}$. $\overline{St}_{sep}$ (see Figs. 40 and 57) varied as $(Re_{ns})^{-0.45}$. Because of the paucity of data available, these correlations are merely crude approximations. As would be expected, since transition occurred near the aft end of the vehicle, the exponent of the Reynolds-number correlation was between the laminar and the turbulent values.

A Reconsideration of Apollo Data

The determination of the reentry heating environment for the Apollo program made extensive use of wind-tunnel data. The local heat-transfer rates obtained in the wind tunnel were divided by the heating rate measured at the

stagnation point of the entry configuration at zero angle-of-attack, $\dot{q}/\dot{q}_{t,\alpha = 0°}$. This nondimensionalized ratio was assumed to define the relative heating rate at entry velocities (with consideration given to the character of the boundary layer). Heat-transfer data for the leeward pitch-plane of the reentry configuration at $\alpha = 33°$ as presented in Ref. 27 are reproduced in Fig. 58. It was noted in Ref. 27 that "none of the heating rates measured between an S/R of -1.1 and an S/R or -2.0 exceeded 1/40 of the heating rate at the zero angle-of-attack stagnation point. The agreement between the different measurements is considerable reasonable. The heat-transfer data in this region are slightly dependent on the free-stream Reynolds number".

Let us reexamine these data in terms of the parameters used in the present report. The experimentally-determined Stanton numbers for $S < -1.5R$ are presented in Fig. 59 as a function of $Re_{n\ell}$

$$Re_{n\ell} = \frac{\rho_{ns} U_{ns} \ell}{\mu_{ns}} \tag{25}$$

where ℓ was the wetted pitch-plane distance from the stagnation point to the thermocouple location. The wetted distance ℓ was used in an attempt to represent the effect of shear-layer development on the heating to different thermocouples for a particular run. Although there were significant run-to-run experimental variations, there was an approximate correlation between ℓ and the heat-transfer measurements for the relatively simple leeward flow of the Apollo configuration. For $Re_{n\ell} > 10^4$, the Stanton number varied as $(Re_{n\ell})^{-0.2}$ indicating that the shear layer was turbulent for most of the runs. For the one, very low-Reynolds-number flow, the shear layer was apparently laminar. Dr. Goodrich observed a similar effect of transition on the leeward heating rates measured during the Apollo flight-test program.

CONCLUDING REMARKS

The present effort studied the effect of the surface temperature distribution on the heat transfer to the leeward surface of the shuttle orbiter. The parameters of the experimental program included the free-stream Mach number, the free-stream Reynolds number, the angle-of-attack, and the temperature ratios: T_{wwd}/T_t and T_{lee}/T_t. For the range of flow conditions considered by the present program, the following conclusions are made.

(1) The data from the runs where $Re_{\infty,L}$ was constant but M_∞ varied exhibited significant variations in the nondimensionalized leeward heating rates (see Fig. 21). However, the variation was a Reynolds-number-dependent effect, as could be seen when Re_{ns} was used as the correlation parameter. Thus, it is possible to misinterpret the effect of a given parameter on the data correlation, if the parameter is evaluated using the free-stream properties. For the present report, the measured heating rates were nondimensionalized using fluid properties evaluated downstream of a normal shock wave and were presented as a function of Re_{ns}, which also used the static-fluid properties downstream of a normal shock wave. However, Re_{ns} used a single characteristic length (i.e., 0.01 ft., which was the reference radius reduced to model scale) for all gage locations. A Reynolds number which used local fluid properties and a length characterizing the development of the viscous flow to the point of interest would be a more appropriate correlation parameter.

(2) The surface-temperature distribution had a measurable effect on the heating rates in the separated region, as was predicted by the theoretical boundary-layer solutions and verified by the experimental measurements. The leeward heating rates were greatest for those runs where the windward surface temperature was greatest. This resulted since there was less heat transferred from the boundary layer to the relatively hot windward-surface and, thus, there was a "surplus" of energy available for heat transfer to the leeward section.

(3) For the range of flow conditions considered in the present experimental program, shear-layer reattachment and transition appeared to have the most significant effect on the local heating rates. Although the effect was not clearly defined, the surface-temperature distribution apparently affected the onset of turbulence in some instances (see Fig. 19c).

(4) Whether or not the presence of the cockpit perturbed the upstream flow (and the magnitude and the extent of the perturbation for a given configuration) was a function of the Reynolds number. For $\alpha = 30°$, the heat-transfer data from the present program (which were obtained at relatively low Reynolds numbers) did not exhibit an upstream influence of the cockpit, whereas pressure and heat-transfer data obtained higher Reynolds numbers (in other programs) did exhibit an upstream influence.

REFERENCES

1. Bertin, J.J.: "A Study of Parameters Which Influence Surface Pressure and Heat-Transfer In Separated Regions - A Literature Review", Aerospace Engineering Report 74004, September 1974, The University of Texas at Austin.

2. Bogdan, L.: "Instrumentation Techniques for Short-Duration Test Facilities", CAL Report No. WTH-030, March 1967, Cornell Aeronautical Laboratory.

3. Vidal, R.J.: "Transient Surface Temperature Measurements", CAL Report No. 114, March 1962, Cornell University Laboratory.

4. Fay, J.A. and Riddell, F.R.: "Theory of Stagnation Point Heat Transfer in Dissociated Air", Journal of the Aeronautical Sciences, Vol. 25, No. 2, February 1958, pp. 73-85, 121.

5. Reece, J.W.: "Shock Tube Theory for Real Air with Applications to Wind Tunnel Testing and to Flight Simulation", CAL Experimental Facilities Division, WTH-003, October 1958 (Revised August 1959).

6. Wittliff, C.: Unpublished Normal Shock Calculations Using Duff's Computing Procedure, Aerodynamics Research Department, CAL about 1963.

7. Lewis, Clark H. and Burgess, E.G.: "Charts of Normal Shock Wave Properties in Imperfect Air", AEDC-TDR-64-43, March 1964.

8. Hilsenrath, J.; Beckett, C.W.; et al.: "Tables of Thermal Properties of Gases", National Bureau of Standards Circular 564, November 1965.

9. Reece, J.W.: "Test Section Conditions Generated in the Supersonic Expansion of Real Air", Reader's Forum, Journal of Aerospace Sciences, Vol. 29, No. 5, May 1962, pp. 617-618.

10. Neel, C.A. and Lewis, Clark H.: "Interpolations of Imperfect Air Thermodynamic Data, II, at Constant Pressure", AEDC-TDR-64-184, September 1964.

11. Hirschfelder, J.O.; Curtis, C.F.; and Bird, R.G.: Molecular Theory of Gases and Liquids, J. Wiley and Sons, 1954.

12. Hansen, C.F.: "Approximations for Thermodynamic and Transport Properties of High Temperature Air", NACA-TN-4150, March 1958 (Revised NASA TR-50, 1959).

13. Bertin, J.J., and Byrd, O.E., Jr.: "The Analysis of a Nonsimilar Boundary Layer - A Computer Code (NONSIMBL)" Aerospace Engineering Report 70002, August 1970, The University of Texas at Austin.

14. Houston, K.: Private transmittal, Dec. 23, 1974.

15. DeJarnette, F.R.: "Calculation of Inviscid Surface Streamlines and Heat Transfer on Shuttle Type Configurations", CR-11921, August 1971, NASA (prepared by North Carolina State University).

16. Rakich, J.V., and Mateer, G.G.: "Calculation of Metric Coefficients for Streamline Coordinates", AIAA Journal, Vol. 10, No. 11, November 1972, pp. 1538-1540.

17. Goodrich, W.D.: Data from tests conducted at the Ames Research Center, as transmitted on February 6, 1975.

18. Schlichting, H., Boundary-Layer Theory, Chapter 15, McGraw-Hill Book Company, 1960, New York.

19. Zakkay, V., Miyazawa, M., and Wang, C.R.: "Lee Surface Flow Phenomena Over Space Shuttle at Large Angles of Attack at $M_\infty = 6$", AIAA Paper 75-148, presented at AIAA 13th Aerospace Sciences Meeting, Pasadena, Calif., January 1975 (Also NASA CR-132501 from New York University).

20. Bertin, J.J., Faria, H.T., Goodrich, W.D., and Martindale, W.R.: "Effect of Nose Geometry on the Aerothermodynamic Environment of Shuttle Entry Configurations", Journal of Spacecraft and Rockets, May 1974, Vol. 11, No. 5, pp. 275-281.

21. Whitehead, A.H., Jr., Hefner, J.N., and Rao, D.M.: "Lee-Surface Vortex Effects Over Configurations in Hypersonic Flow", AIAA Paper No. 72-77, Presented at the AIAA 10th Aerospace Sciences Meeting, San Diego, Calif., January 1972.

22. Cassanto, J.M.: "A Base Pressure Experiment for Determining the Atmospheric Pressure Profile of Planets", Journal of Spacecraft and Rockets, April 1973, Vol. 10, No. 4, pp. 253-261.

23. Ames Research Staff: "Equations, Tables, and Charts for Compressible Flow", Report 1135, 1953, NACA.

24. Markarian, C.F.: "Heat-Transfer in Shock Wave - Boundary Layer Interaction Regions", NWC TP4485, November 1968, Naval Weapons Center.

25. Hefner, J.N., and Whitehead, A.H., Jr.: "Lee-Side Flow Phenomena on Space Shuttle Configurations at Hypersonic Speeds, Part II - Studies of Lee-Side Heating at Hypersonic Mach Numbers", Space Shuttle Aerothermodynamics Technology, Volume II - Heating, TM X 2507, February 1972, NASA.

26. Crocco, L. and Lees, L.: "A Mixing Theory for the Interaction Between Dissipative Flows and Nearly Isentropic Streams", Journal of the Aeronautical Sciences, October 1952, Vol. 19, No. 10, pp. 649-676.

27. Bertin, J.J.: "Wind-Tunnel Heating Rates for the Apollo Spacecraft", TMX-1033C, January 1965, NASA.

Table 1. - Location of heat-transrer gages

Gage No.	Model Station (in/cm)	x (in/cm)	$\frac{x}{L}$	ϕ (°)
1	2.767/7.028	0.387/0.983	0.030	0
2	3.154/8.011	0.774/1.966	0.060	0
3	3.541/8.994	1.161/2.282	0.090	0
4	3.670/9.322	1.290/3.277	0.100	0
5	3.670/9.322	1.290/3.277	0.100	41
6	3.670/9.322	1.290/3.277	0.100	69
7	3.670/9.322	1.290/3.277	0.100	90
8	3.993/10.142	1.613/4.097	0.125	0
9	4.315/10.960	1.935/4.915	0.150	0
10	4.445/11.290	2.065/5.245	0.160	0
11	4.574/11.617	2.194/5.573	0.170	0
12	4.703/11.945	2.323/5.900	0.180	0
13	5.130/13.030	2.750/6.985	0.213	0
14	5.130/13.030	2.750/6.985	0.213	17.5
15	5.130/13.030	2.750/6.985	0.213	35
16	5.130/13.030	2.750/6.985	0.213	52.5
17	5.130/13.030	2.750/6.985	0.213	70
18	5.130/13.030	2.750/6.985	0.213	90
19	5.980/15.189	3.600/9.144	0.279	0
20	5.980/15.189	3.600/9.144	0.279	22
21	5.980/15.189	3.600/9.144	0.279	44
22	5.980/15.189	3.600/9.144	0.279	66
23	5.980/15.189	3.600/9.144	0.279	90
24	6.700/17.018	4.320/10.973	0.335	0
25	6.700/17.018	4.320/10.973	0.335	20
26	6.700/17.018	4.320/10.973	0.335	40
27	6.700/17.018	4.320/10.973	0.335	56
28	6.700/17.018	4.320/10.973	0.335	90
29	7.799/19.809	5.419/13.764	0.420	0
30	7.799/19.809	5.419/13.764	0.420	20
31	7.799/19.809	5.419/13.764	0.420	40
32	7.799/19.809	5.419/13.764	0.420	56
33	7.799/19.809	5.419/13.764	0.420	90

Table 1. - Continued

Gage No.	Model Station (in/cm)	x (in/cm)	$\frac{x}{L}$	ϕ (°)
34	8.832/22.433	6.452/16.388	0.500	0
35	8.832/22.433	6.452/16.388	0.500	30
36	8.832/22.433	6.452/16.388	0.500	56
37	10.122/25.709	7.742/19.665	0.600	0
38	10.122/25.709	7.742/19.665	0.600	30
39	10.122/25.709	7.742/19.665	0.600	56
40	10.122/25.709	7.742/19.665	0.600	90
41	11.412/28.986	9.032/22.941	0.700	0
42	11.412/28.986	9.032/22.941	0.700	90
43	12.702/32.263	10.322/26.218	0.800	0
44	2.380/6.045	0.000/0.000	0.000	180
45	3.670/9.321	1.290/3.277	0.100	180
46	5.130/13.030	2.750/6.985	0.213	180
47	6.700/17.018	4.320/10.973	0.335	180
48	12.702/32.263	10.322/26.218	0.800	180

Table 2. - Location of static-pressure orifices

Gage No.	Model Station (in/cm)	x (in/cm)	$\frac{x}{L}$	ϕ (°)
1	3.348/8.503	0.968/2.459	0.075	0
2	3.799/9.649	1.419/3.604	0.110	0
3	5.468/13.888	3.088/7.8435	0.239	0
4	8.056/20.462	5.676/14.417	0.440	0
5	11.692/29.697	9.312/23.652	0.722	0

Table 3. - Run schedule

(a) English units

(i) Fuselage Only

Run	α (°)	M_∞	Re_∞/ft ($\times 10^{-6}$)	p_{t2} (psia)	T_t (°R)	T_{wwd} (°R)	T_{lee} (°R)
1	30	12.26	0.5648	4.311	4626	420	420
2	90	12.26	0.5643	4.307	4626	420	420
3	90	11.87	1.629	13.24	4644	420	420
26	90	12.32	0.5389	3.639	4336	860	530
27	90	11.81	1.589	13.61	4758	1430	530
28	90	12.24	0.5103	3.872	4605	1440	530
29	90	11.66	0.1091	0.898	4564	1440	530
30	90	15.70	0.5790	2.786	4643	1440	530
31	90	11.83	1.613	13.94	4792	860	530
32	30	12.26	0.5737	4.305	4578	1460	530

(ii) Orbiter

Run	α (°)	M_∞	Re_∞/ft ($\times 10^{-6}$)	p_{t2} (psia)	T_t (°R)	T_{wwd} (°R)	T_{lee} (°R)
4	30	11.80	1.516	12.98	4751	833	530
5	30	12.24	0.5272	4.103	4675	820	530
6	30	11.67	0.1155	0.983	4658	820	530
7	30	15.71	0.5722	2.772	4670	830	530
8	30	11.81	1.559	13.24	4734	1460	530
9	30	11.61	1.045	9.139	4729	1420	530
10	30	12.26	0.5263	4.003	4623	1410	530
11	30	11.64	0.1078	0.905	4603	1420	530
12	30	16.01	0.8793	4.094	4657	1440	530
13	30	15.71	0.5701	2.721	4631	1420	530
14	30	10.16	0.9917	1.092	4717	1430	530
15	30	10.05	0.4883	5.340	4641	1430	530
16	30	15.81	0.1123	0.681	5299	1430	530
17	40	12.24	0.5476	4.219	4640	830	530
18	40	11.82	1.578	13.57	4776	1440	530
19	40	12.23	0.5530	4.288	4763	1430	530
20	40	11.68	0.1069	0.884	4714	1440	530
21	40	15.70	0.5789	2.767	4770	1430	530

Table 3. - Continued.

(a) English units

(ii) Orbiter

Run	α (°)	M_∞	Re_∞/ft ($\times 10^{-6}$)	p_{t2} (psia)	T_t (°R)	T_{wwd} (°R)	T_{lee} (°R)
22	40	10.01	0.4808	5.545	4821	1440	530
23	30	18.26	0.1349	0.442	4423	1430	530
24	30	18.59	0.2210	0.790	4727	1420	530
33	30	11.80	1.560	13.39	4758	430	430
34	30	12.28	0.5577	4.206	4607	430	430
35	30	11.70	0.1074	0.886	4597	420	420
36	30	16.09	0.9186	4.038	4539	420	420
37	30	15.70	0.5759	2.736	4613	420	420
38	30	10.16	0.5678	5.433	4342	420	420
39	40	12.23	0.5622	4.262	4590	425	425
40	40	15.70	0.5859	2.825	4651	430	430

Table 3. - Run schedule

(b) Metric units

(i) Fuselage Only

Run	α (°)	M_∞	Re_∞/m ($\times 10^{-6}$)	P_{t2} ($N/m^2 \times 10^{-4}$)	T_t (°K)	T_{wwd} (°K)	T_{lee} (°K)
1	30	12.26	1.853	2.972	2570	233.4	233.4
2	90	12.25	1.851	2.970	2570	233.4	233.4
3	90	11.87	5.345	9.129	2580	233.4	233.4
26	90	12.32	1.768	2.509	2409	477.8	294.5
27	90	11.81	5.213	9.384	2643	794.[illegible]	294.5
28	90	12.24	1.674	2.670	2558	800.0	294.5
29	90	11.66	0.358	0.619	2536	800.[illegible]	294.5
30	90	15.70	1.900	1.920	2579	800.0	294.5
31	90	11.83	5.292	9.734	2662	477.8	294.5
32	30	12.26	1.882	2.968	2543	811.1	294.5

(ii) Orbiter

Run	α (°)	M_∞	Re_∞/m ($\times 10^{-6}$)	P_{t2} ($N/m^2 \times 10^{-4}$)	T_t (°K)	T_{wwd} (°K)	T_{lee} (°K)
4	30	11.80	4.974	8.950	2639	462.8	294.5
5	30	12.23	1.730	2.830	2597	455.6	294.5
6	30	11.67	0.379	0.678	2588	455.6	294.5
7	30	15.71	1.877	1.911	2594	461.1	294.5
8	30	11.81	5.115	9.129	2630	811.1	294.5
9	30	11.61	3.428	6.301	2627	788.9	294.5
10	30	12.26	1.727	2.760	2568	783.3	294.5
11	30	11.64	0.354	0.624	2557	788.9	294.5
12	30	16.01	2.885	2.823	2587	800.0	294.5
13	30	15.71	1.870	1.876	2573	788.9	294.5
14	30	10.16	3.254	0.753	2621	794.5	294.5
15	30	10.05	1.602	3.682	2578	794.5	294.5
16	30	15.81	0.368	0.469	2944	794.5	294.5
17	40	12.24	1.797	2.909	2578	461.1	294.5
18	40	11.82	5.177	9.357	2653	800.0	294.5
19	40	12.23	1.814	2.957	2646	794.5	294.5
20	40	11.68	0.351	0.610	2619	800.0	294.5
21	40	15.70	1.899	1.908	2650	794.5	294.5
22	40	10.01	1.577	3.823	2678	800.0	294.5

Table 3. - Continued

(b) Metric units

(ii) Orbiter

Run	α (°)	M_∞	Re_∞/m ($\times 10^{-6}$)	P_{t2} ($N/m^2 \times 10^{-4}$)	T_t (°K)	T_{wwd} (°K)	T_{lee} (°K)
22	40	10.01	1.577	3.823	2678	800.0	294.5
23	30	18.26	0.443	0.305	2457	794.5	29[illegible]
24	30	18.59	0.725	0.545	2626	768.9	294.5
33	30	11.80	[illegible].118	9.232	2643	238.9	238.9
34	30	12.28	1.830	2.900	2559	238.9	238.9
35	30	11.70	0.352	0.611	2554	233.4	233.4
36	30	16.09	3.014	2.784	2522	233.4	233.4
37	30	15.70	1.889	1.886	2563	233.4	233.4
38	30	10.16	1.863	3.746	2412	233.4	233.4
39	40	12.23	1.845	2.939	2550	236.1	236.1
40	40	15.70	1.922	1.948	2584	238.9	238.9

Table 4. - Theoretical solution for a nonsimilar, laminar boundary-layer assuming the air at the edge of the boundary layer has accelerated isentropically from the stagnation point (NSE).

(a) Identification of cases

Case I.D.	M_∞	Re_∞/ft ($\times 10^6$)	p_{t2} (psia)	T_t (°R)	$\frac{T_{wwd}}{T_t}$	$\frac{T_{lee}}{T_t}$
1ai	11.80	1.50	13.0	4750	0.090	0.090
1aii	↓	↓	↓	↓	↓	0.114
1bii	↓	↓	↓	↓	0.176	↓
1cii	↓	↓	↓	↓	0.307	↓
2ai	12.25	0.55	4.1	4650	0.090	0.090
2aii	↓	↓	↓	↓	↓	0.114
2bii	↓	↓	↓	↓	0.176	↓
2cii	↓	↓	↓	↓	0.307	↓
3ai	11.68	0.11	0.9	4650	0.090	0.090
3aii	↓	↓	↓	↓	↓	0.114
3bii	↓	↓	↓	↓	0.176	↓
3cii	↓	↓	↓	↓	0.307	↓
4ai	15.70	0.57	2.8	4650	0.090	0.090
4aii	↓	↓	↓	↓	↓	0.114
4cii	↓	↓	↓	↓	0.307	↓
5ai	10.10	0.50	5.3	4650	0.090	0.090
5aii	↓	↓	↓	↓	↓	0.114
5cii	↓	↓	↓	↓	0.307	↓
6ai	18.59	0.13	0.4	4400	0.090	0.090
6aii	↓	↓	↓	↓	↓	0.114
6cii	↓	↓	↓	↓	0.307	↓

Table 4. - Continued.

(b) Boundary-layer parameters

Case I.D.	At s = 0.216 ft (which is just upstream of the section interface) δ (ft) $\times 10^2$	θ (ft) $\times 10^3$	θ_H (ft) $\times 10^2$	$Re_s \times 10^{-4}$	At s = 0.351 ft (which is just upstream of the "assumed" separation) δ (ft) $\times 10^2$	θ (ft) $\times 10^3$	θ_H (ft) $\times 10^2$	$Re_s \times 10^{-4}$
1ai	.436	.911	—	6.933	1.597	3.506	—	8.190
1aii	.436	.911	-.200		1.648	3.496	-.863	
1bii	.470	.876	-.185		1.634	3.385	-.831	
1cii	.520	.824	-.163		1.633	3.246	-.796	
2ai	.769	1.604	—	2.186	2.810	6.178	—	2.593
2aii	.769	1.604	-.354		2.900	6.160	-1.527	
2bii	.828	1.544	-.327		2.877	5.965	-1.468	
2cii	.916	1.451	-.288		2.875	5.721	-1.406	
3ai	1.642	3.424	—	0.480	5.948	13.19	—	0.569
3aii	1.642	3.424	-.755		6.189	13.15	-3.257	
3bii	1.767	3.296	-.715		6.140	12.73	-3.132	
3cii	1.954	3.098	-.613		6.136	12.21	-3.001	
4ai	.931	1.941	—	1.493	3.400	7.476	—	1.771
4aii	.931	1.941	-.428		3.509	7.454	-1.847	
4cii	1.108	1.756	-.348		3.479	6.923	-1.701	
5ai	.677	1.411	—	2.826	2.471	5.434	—	3.351
5aii	.677	1.411	-.311		2.550	5.418	-1.342	
5cii	.805	1.277	-.253		2.528	5.032	-1.237	
6ai	2.396	4.988	—	.218	8.722	19.22	—	.260
6aii	2.396	4.988	-1.106		9.000	19.17	-4.767	
6cii	2.848	4.518	-.899		8.929	17.80	-4.668	

Table 5. - Theoretical solution for a nonsimilar, laminar boundary-layer assuming the air of the edge of the boundary layer accelerates isentropically after passing through a shock wave parallel to the surface (PSE).

(a) Identification of cases

Case I.D.	M_∞	Re_∞/ft ($\times 10^{-6}$)	P_{te} (psia)	T_t (°R)	$\frac{T_{wwd}}{T_t}$	$\frac{T_w}{T_t}$
II ai	12.25	0.55	95.505	4650	0.090	0.090
II bi	12.25	0.55	95.505	4650	0.176	0.090
II ci	12.25	0.55	95.505	4650	0.307	0.090
IV ai	15.70	0.57	70.692	4650	0.090	0.090
IV bi	15.70	0.57	70.692	4650	0.176	0.090
IV ci	15.70	0.57	70.692	4650	0.307	0.090
V ai	10.10	0.50	110.208	4650	0.090	0.090
V bi	10.10	0.50	110.208	4650	0.176	0.090
V ci	10.10	0.50	110.208	4650	0.307	0.090
II aii	12.25	0.55	95.505	4650	0.090	0.114
II bii	12.25	0.55	95.505	4650	0.176	0.114
II cii	12.25	0.55	95.505	4660	0.307	0.114
IV aii	15.70	0.57	70.692	4650	0.090	0.114
IV bii	15.70	0.57	70.692	4650	0.176	0.114
IV cii	15.70	0.57	70.692	4650	0.307	0.114
V aii	10.10	0.50	110.208	4650	0.090	0.114
V bii	10.10	0.50	110.208	4650	0.176	0.114
V cii	10.10	0.50	110.208	4650	0.307	0.114

Table 5. - Continued

(b) Boundary-layer parameters

	At s = 0.216 ft (which is just upstream of the section interface)			At s = 0.351 ft (which is just upstream of the "assumed" separation)		
Case I.D.	δ (ft) $\times 10^2$	θ (ft) $\times 10^3$	$Re_s \times 10^{-5}$	δ (ft) $\times 10^2$	θ (ft) $\times 10^3$	$Re_s \times 10^{-5}$
II ai	0.563	0.636	1.1481	2.046	2.439	1.3541
II bi	0.616	0.603	1.1481	2.052	2.339	1.3541
II ci	0.714	0.561	1.1481	2.140	2.237	1.3541
IV ai	0.679	0.746	0.8173	2.488	2.858	0.9641
IV bi	0.743	0.707	0.8173	2.498	2.741	0.9641
IV ci	0.862	0.657	0.8173	2.602	2.610	0.9641
V ai	0.497	0.588	1.3994	1.824	2.240	1.6507
V bi	0.544	0.554	1.3994	1.831	2.149	1.6507
V ci	0.630	0.517	1.3994	1.906	2.053	1.6507
II aii	0.563	0.636	1.1481	2.152	2.417	1.3541
II bii	0.616	0.603	1.1481	2.165	2.313	1.3541
II cii	0.714	0.561	1.1481	2.210	2.225	1.3541
IV aii	0.679	0.746	0.8173	2.582	2.842	0.9641
IV bii	0.743	0.707	0.8173	2.585	2.723	0.9641
IV cii	0.862	0.657	0.8173	2.686	2.596	0.9641
V aii	0.497	0.588	1.3994	1.893	2.227	1.6507
V bii	0.544	0.554	1.3994	1.895	2.135	1.6507
V cii	0.630	0.517	1.3994	1.967	2.043	1.6507

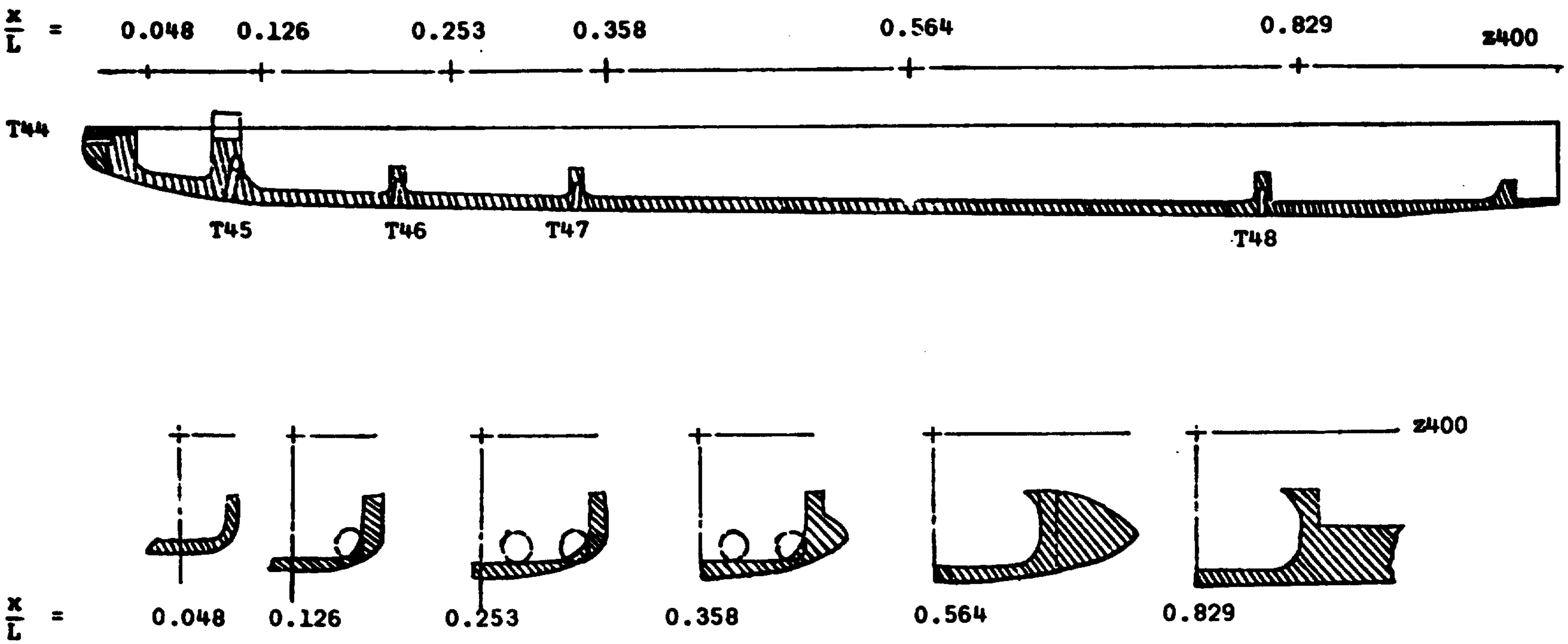

(a) Windward Section for orbiter model.

Figure 1. - Sketch of the 0.01-scale 37-0 shuttle orbiter model.

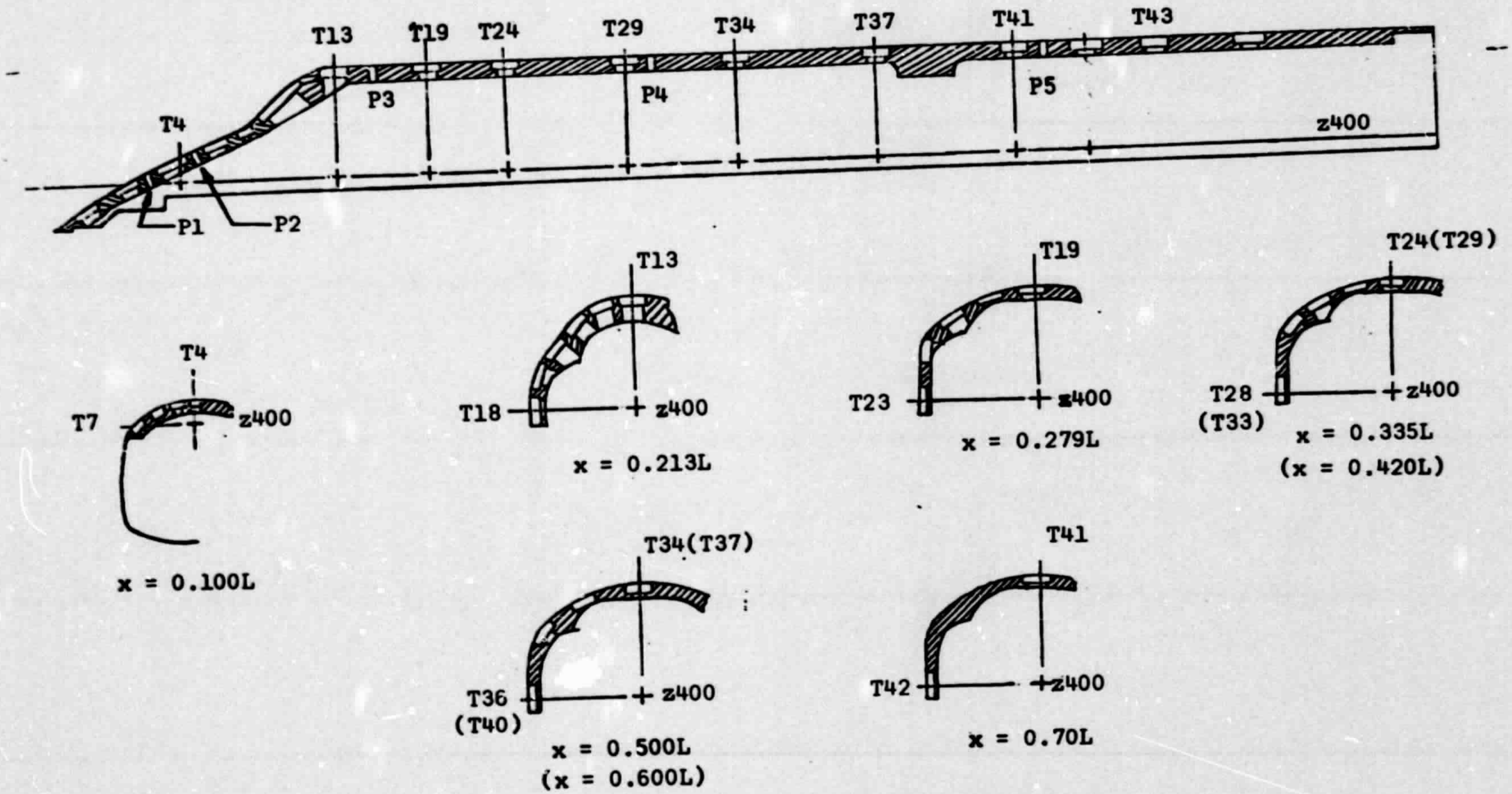

(b) Common leeward section.

Figure 1. - Concluded.

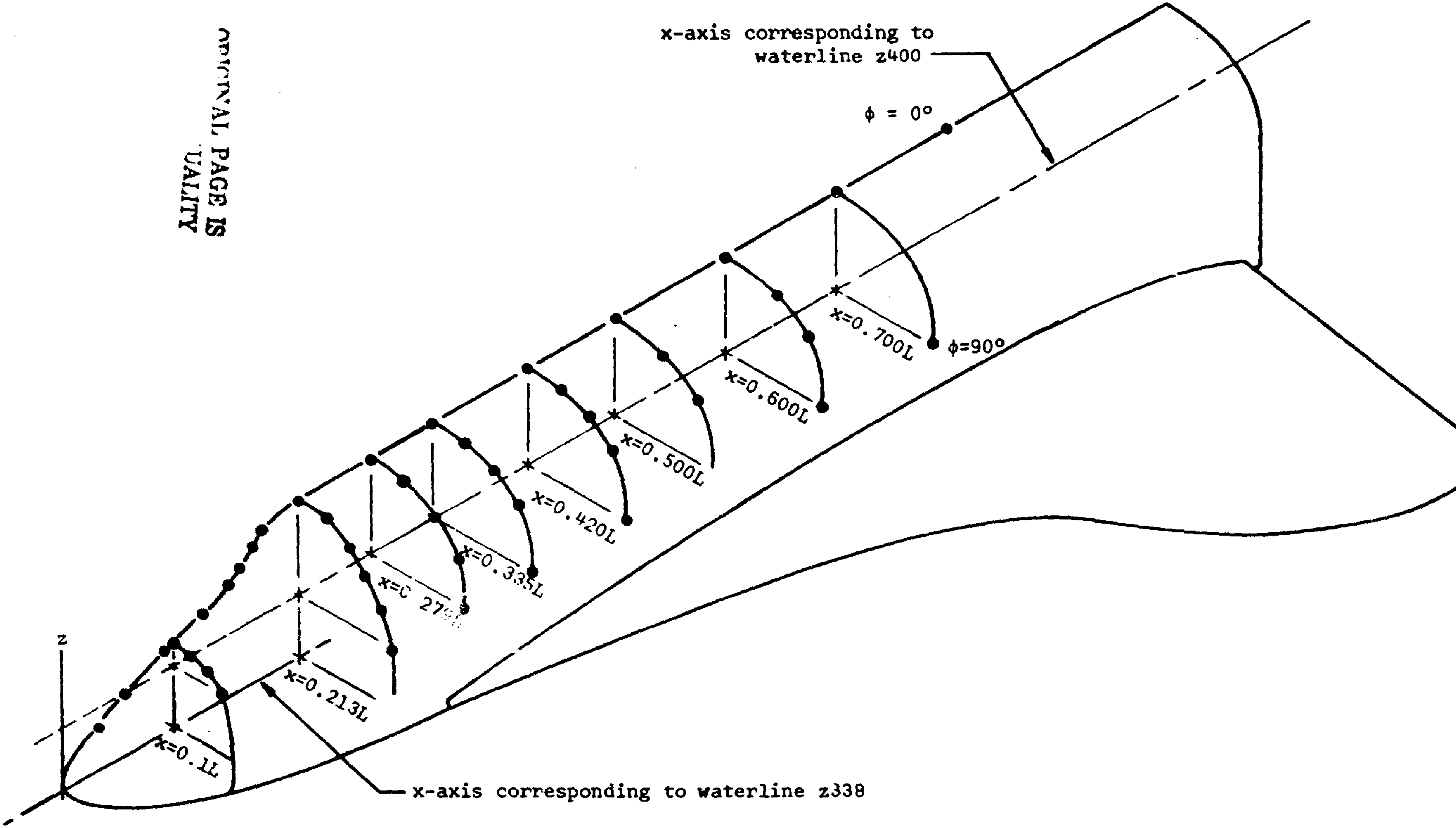

Figure 2. - An isometric sketch of the shuttle orbiter model illustrating the locations of the leeward heat-transfer gages.

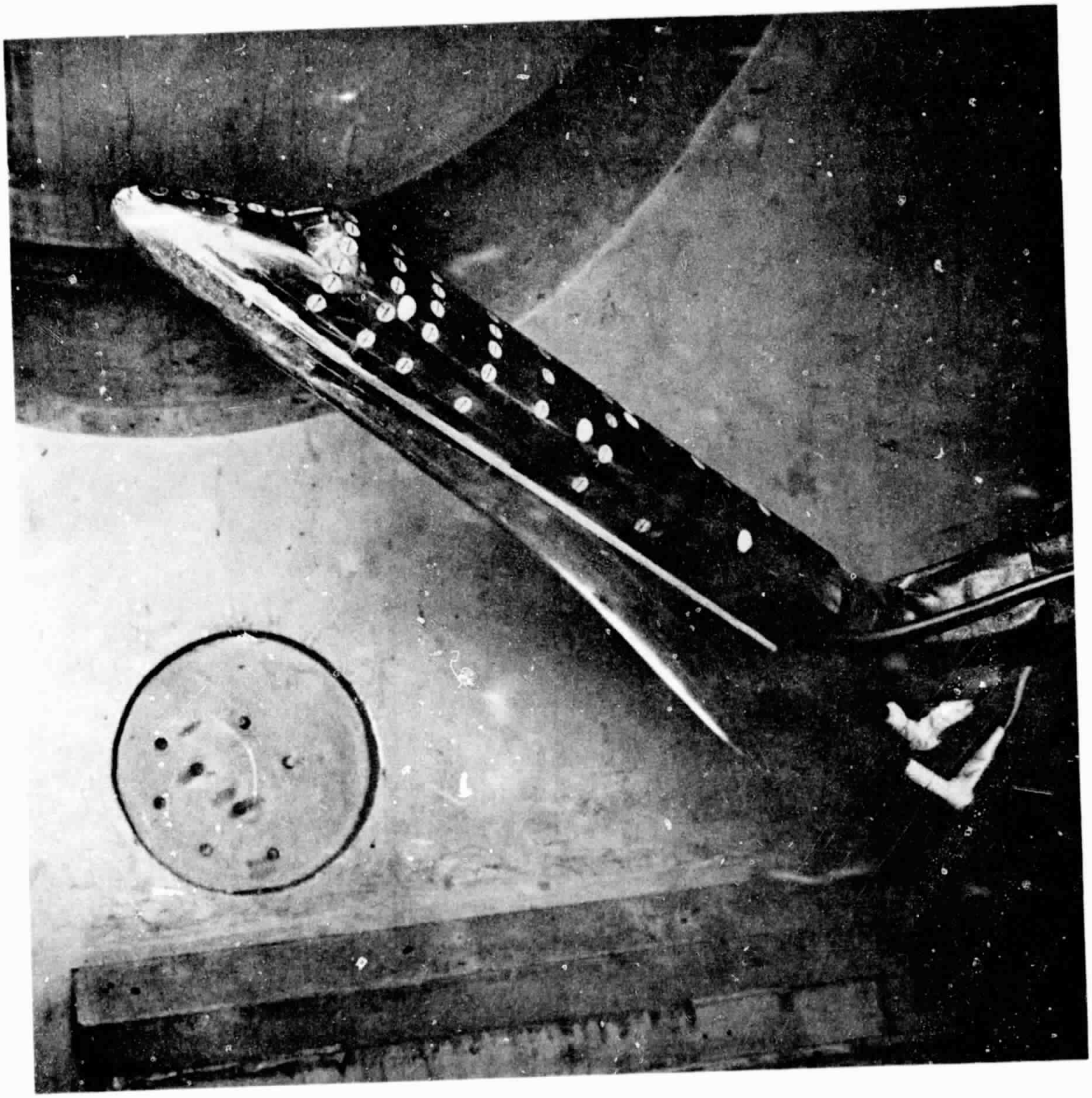

(a) Side view

Figure 3. - Photographs of the 0.01-scale shuttle orbiter model in the Calspan 96-Inch Hypersonic Shock Tunnel.

ORIGINAL PAGE IS
[illegible]LITY

(b) View of leeward surface

Figure 3. - Concluded.

ORIGINAL PAGE IS OF POOR QUALITY

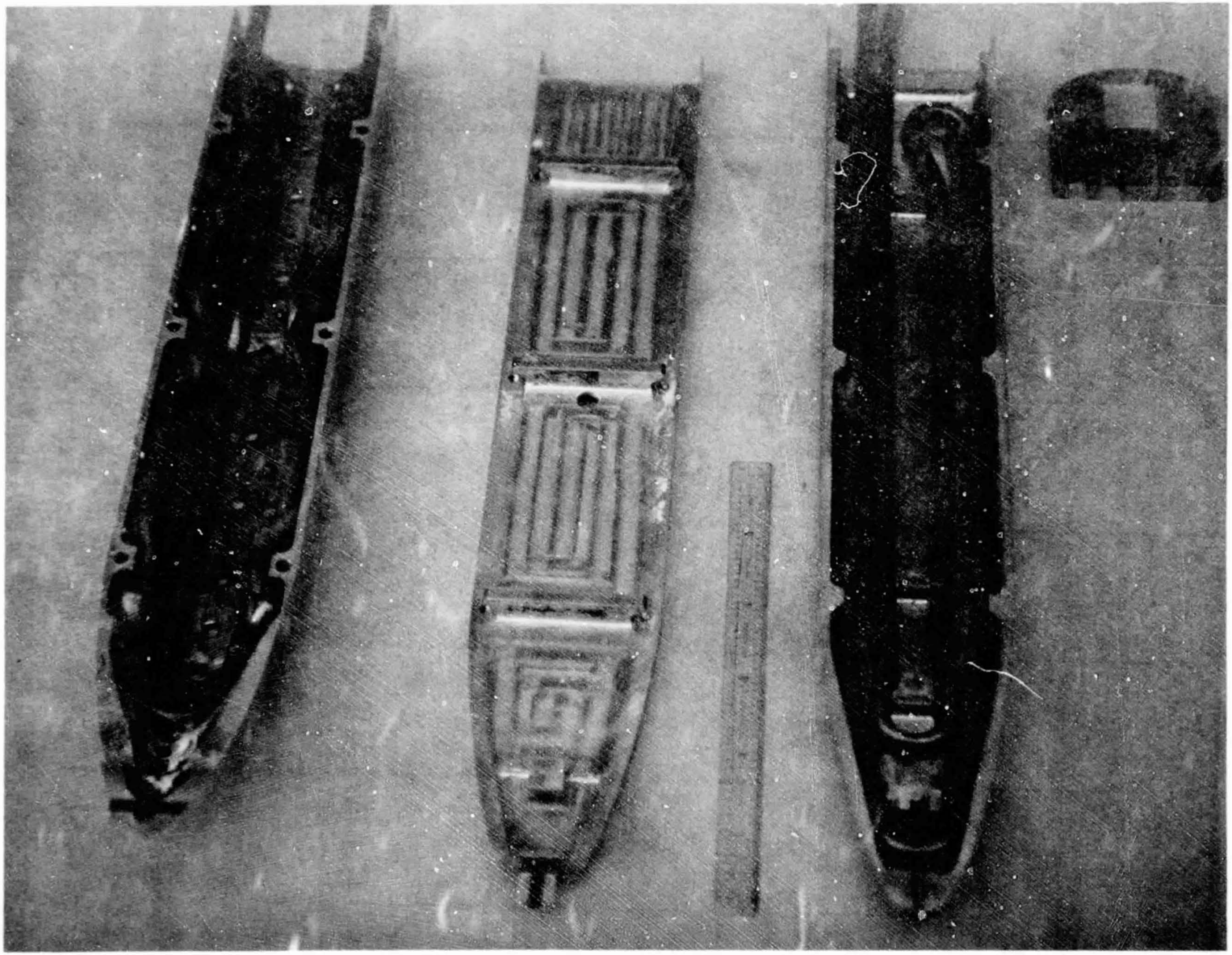

Figure 4. - Photograph of the fuselage only configuration disassembled to illustrate the windward section, leeward section, insulation sheet, and cooling coils.

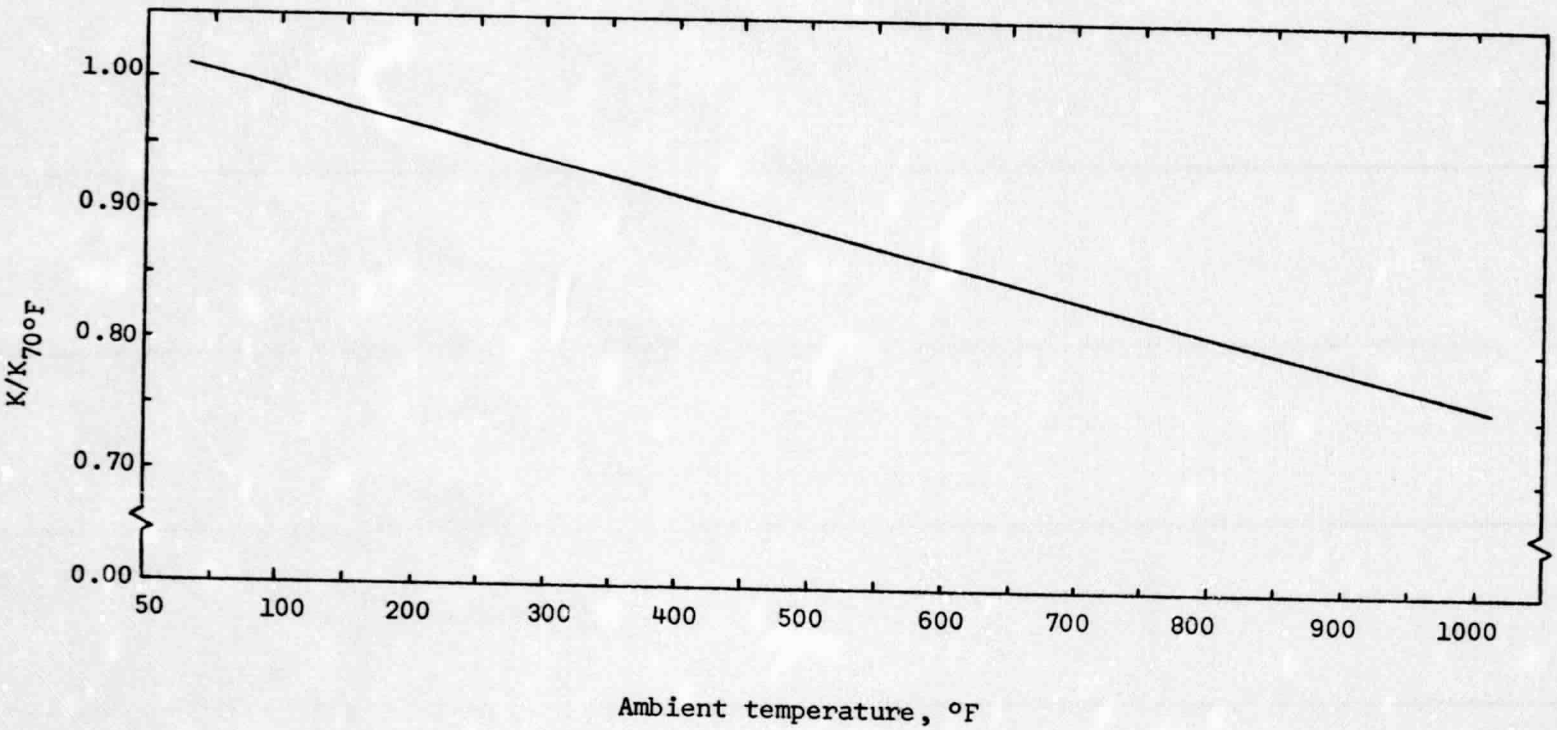

Figure 5. - Variation of heat transfer gage sensitivity with temperature.

ORIGINAL PAGE IS
OF POOR QUALITY

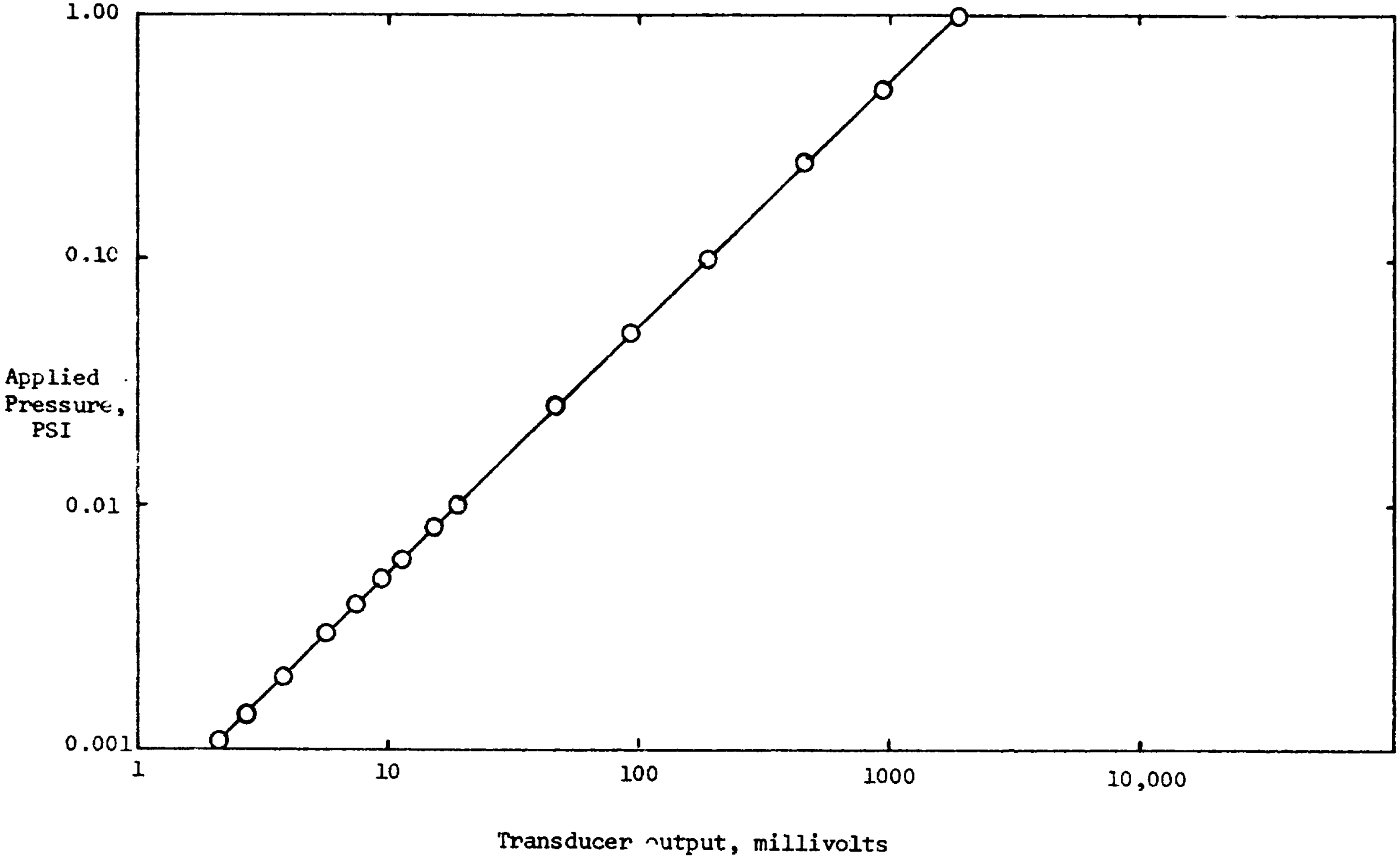

Figure 6. - Transducer calibration curve.

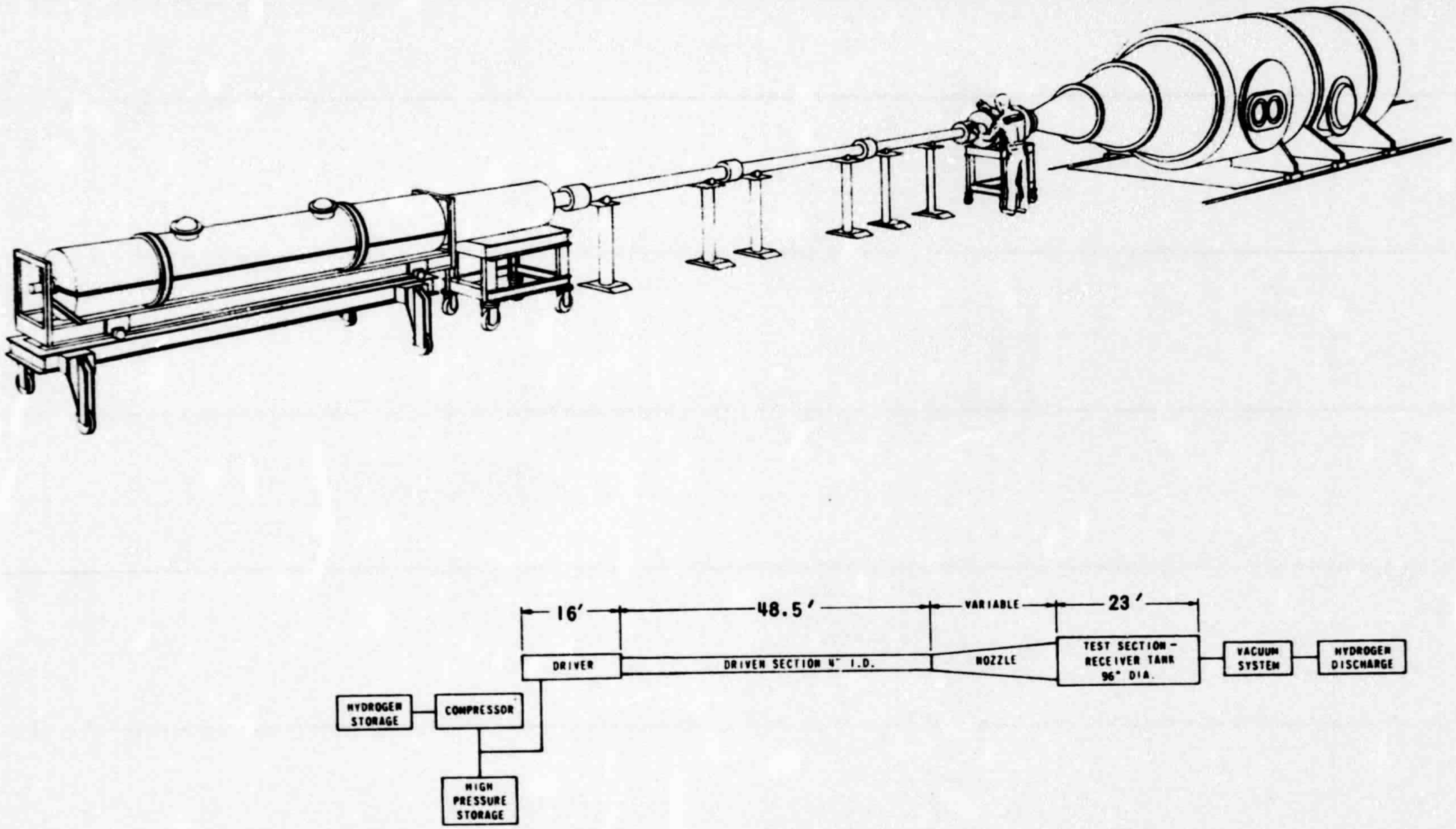

Figure 7. - Basic components of the Calspan 96" Hypersonic Shock Tunnel

ORIGINAL PAGE IS
OF POOR QUALITY

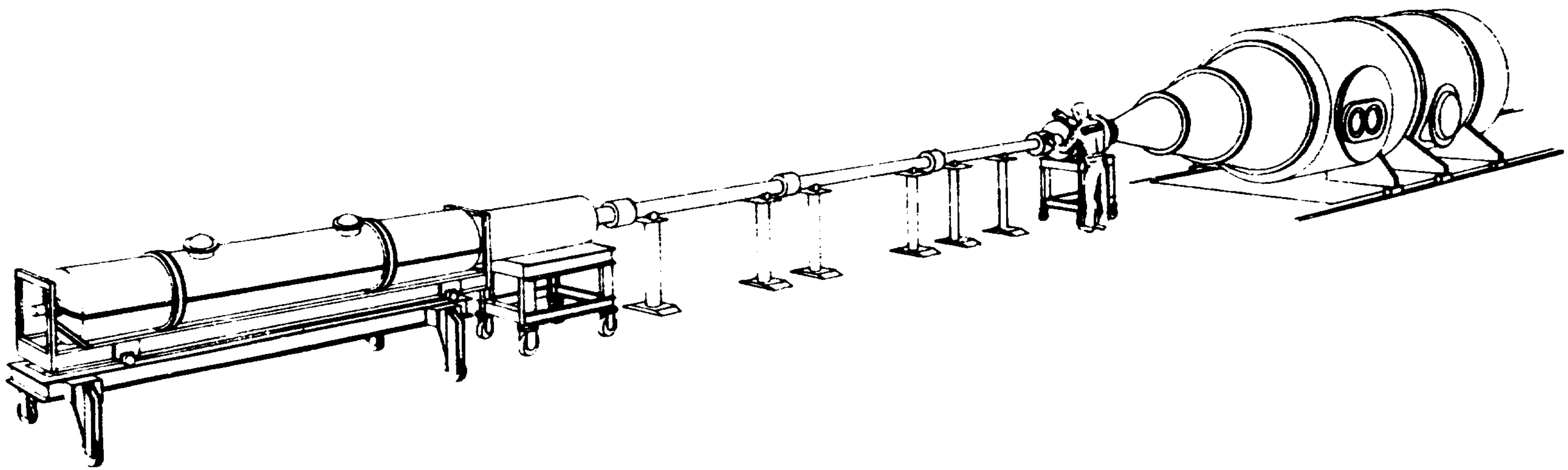

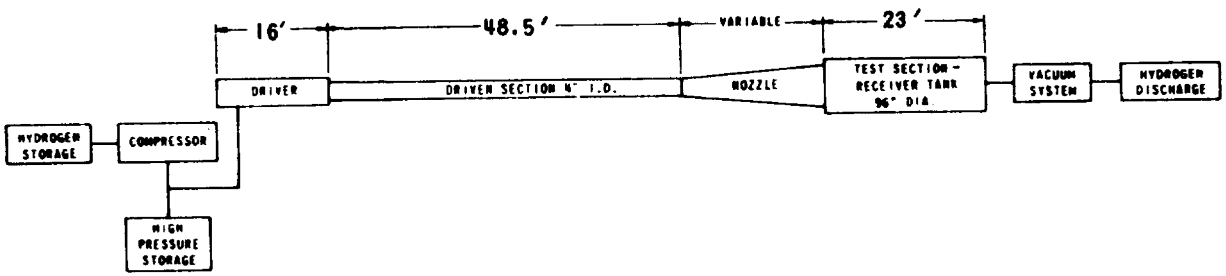

Figure 7. - Basic components of the Calspan 96" Hypersonic Shock Tunnel

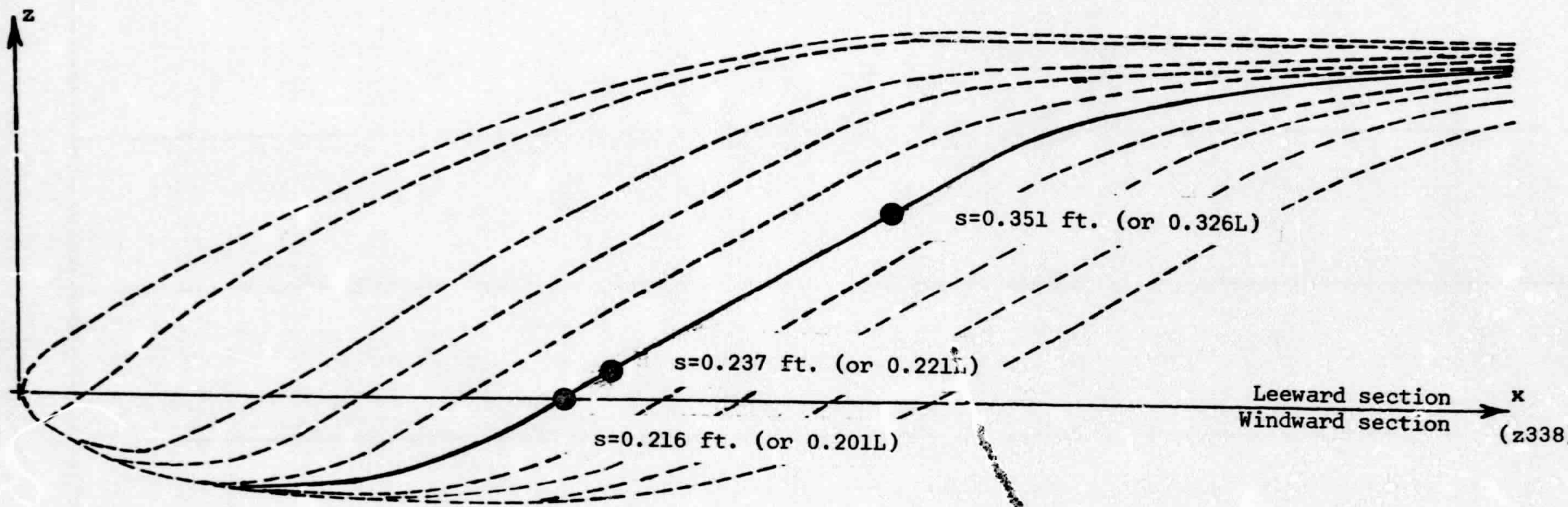

Figure 8. - A sideview sketch of the Newtonian streamlines calculated for a representative orbiter geometry (without a canopy), $\alpha = 30^\circ$.

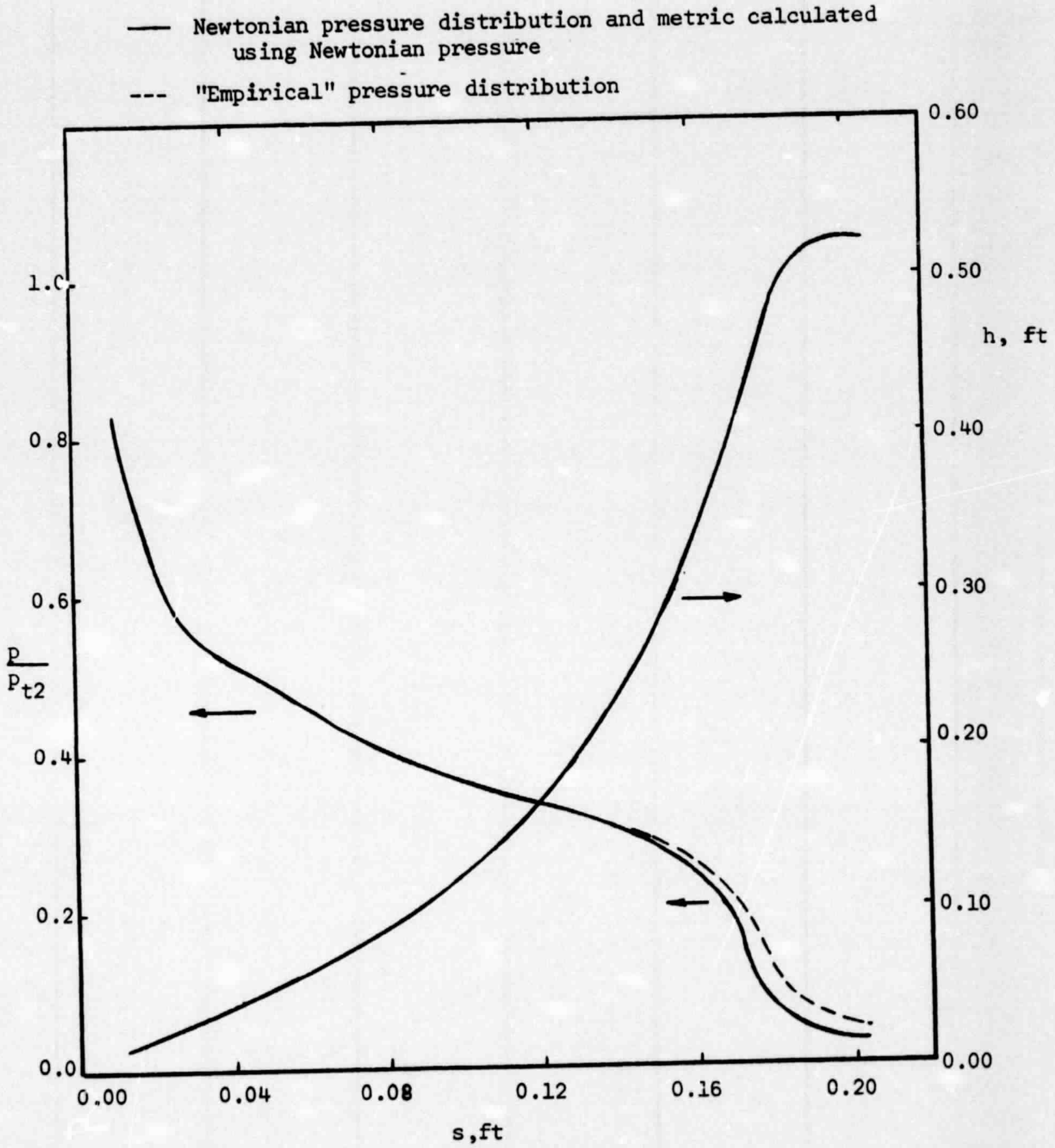

(a) Windward section

Figure 9. - The theoretical flow-characteristics along a streamline as determined for a Newtonian pressure distribution using the Lockheed program (NSE, α = 30°).

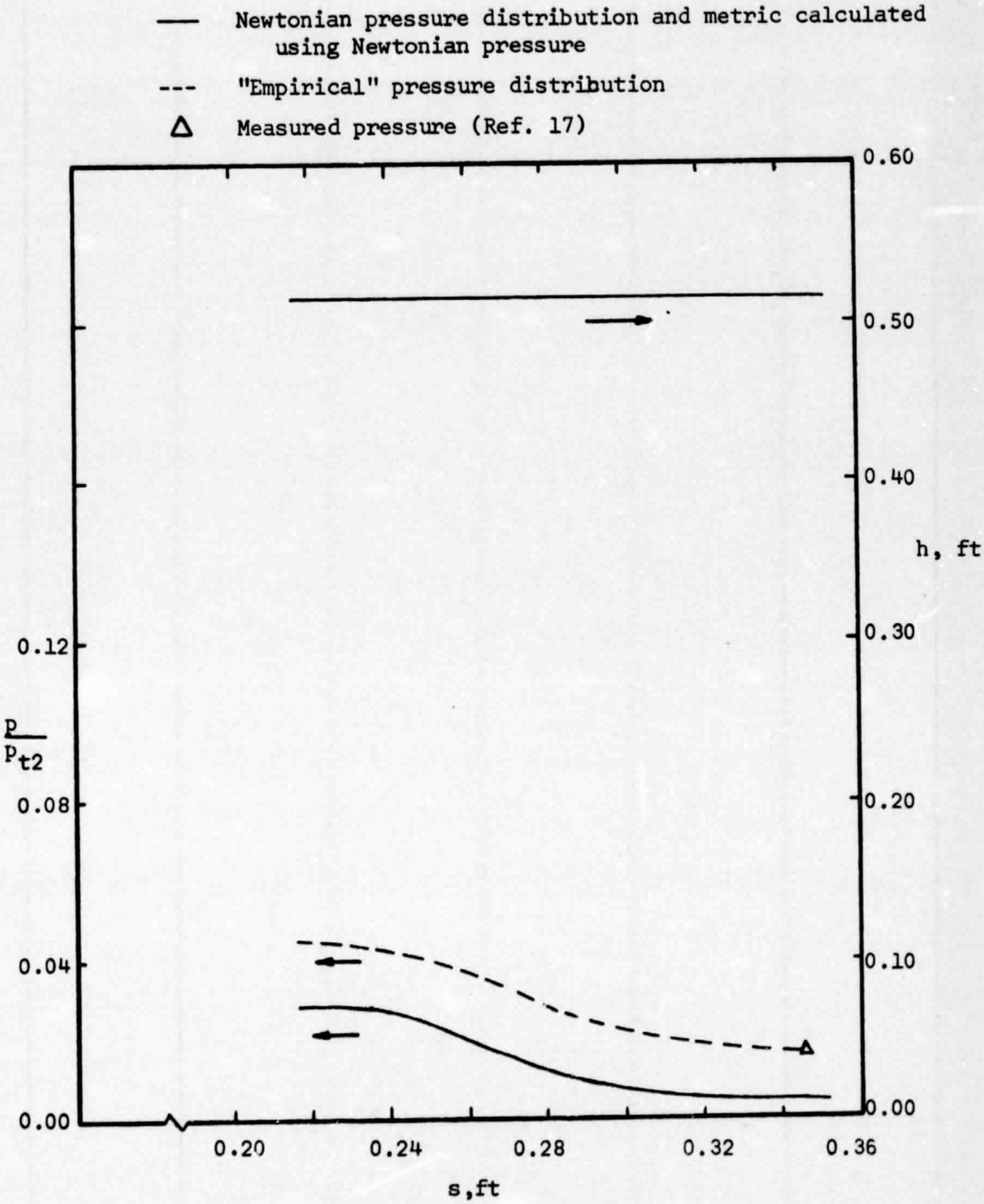

(b) Leeward section

Figure 9. - Concluded.

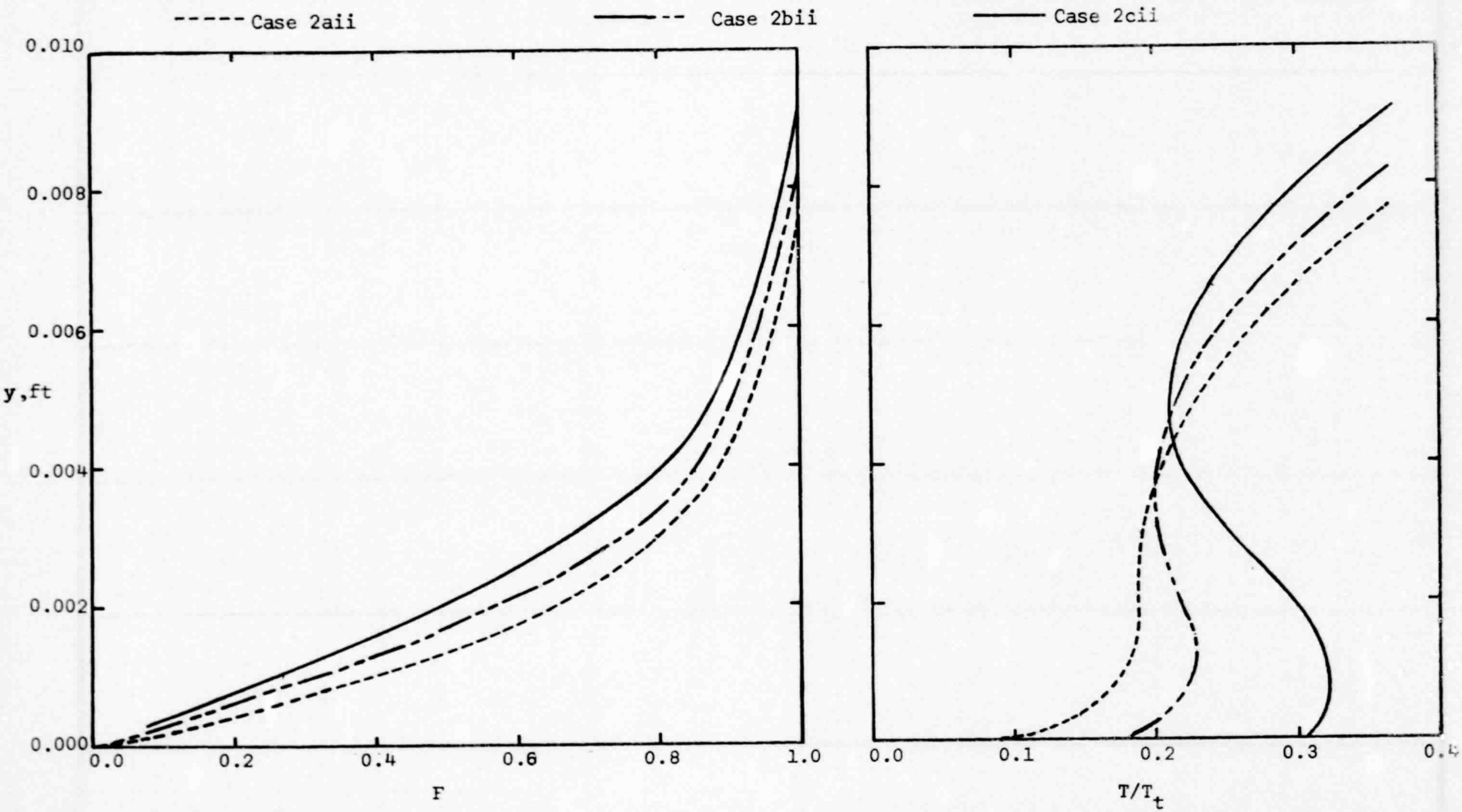

(a) s = .216 ft (i.e., s = 0.201 L, which is just upstream of the section interface)

Figure 10. - The effect of surface temperature on the theoretical, laminar boundary-layer (NSE for α = 30°), M_∞ = 12.25, $Re_{\infty,L}$ = 0.59 x 10^6.

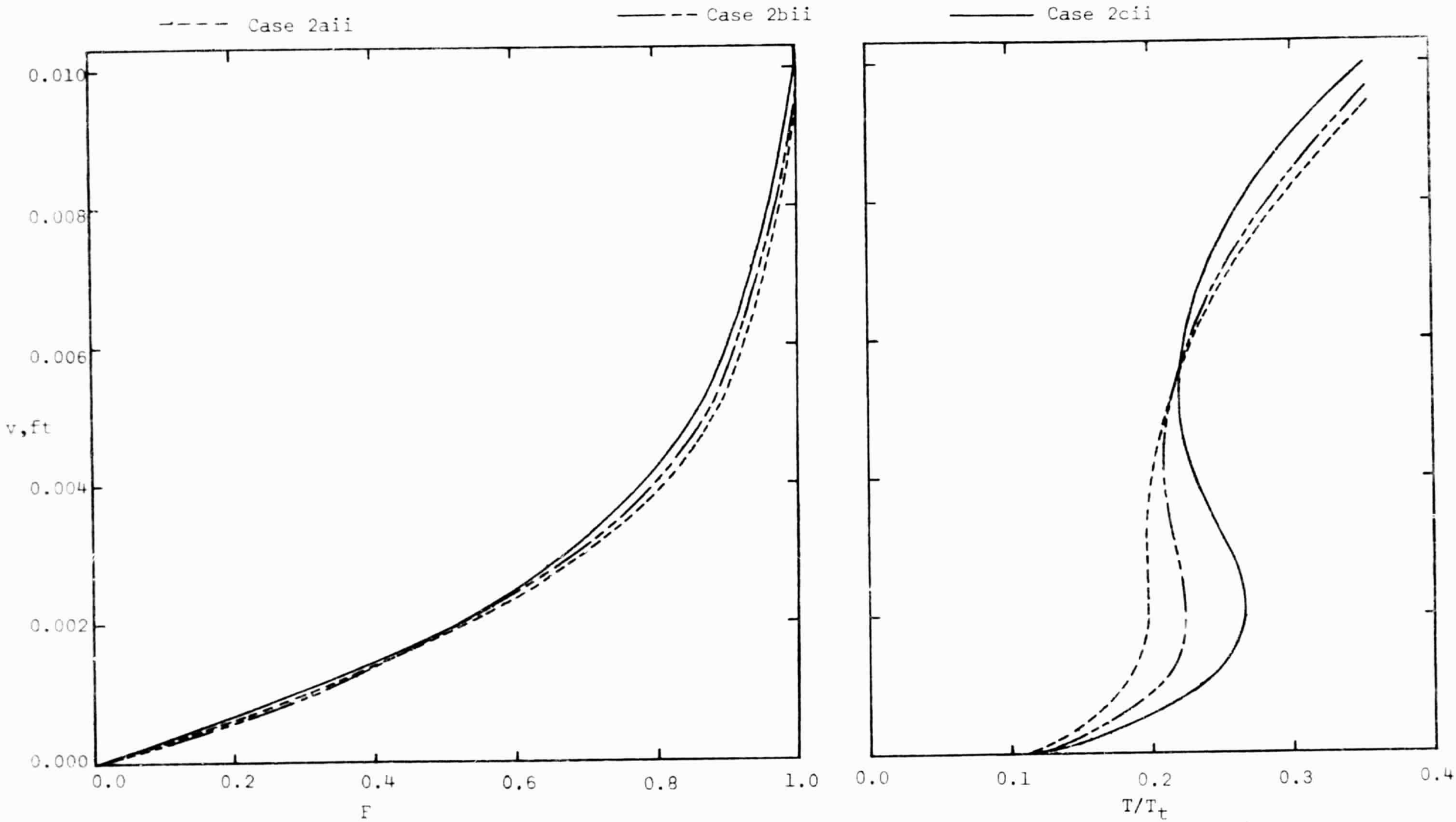

(b) s = 0.237 ft (i.e., s = 0.221 L, which is just downstream of the section interface)

Figure 10. - Continued.

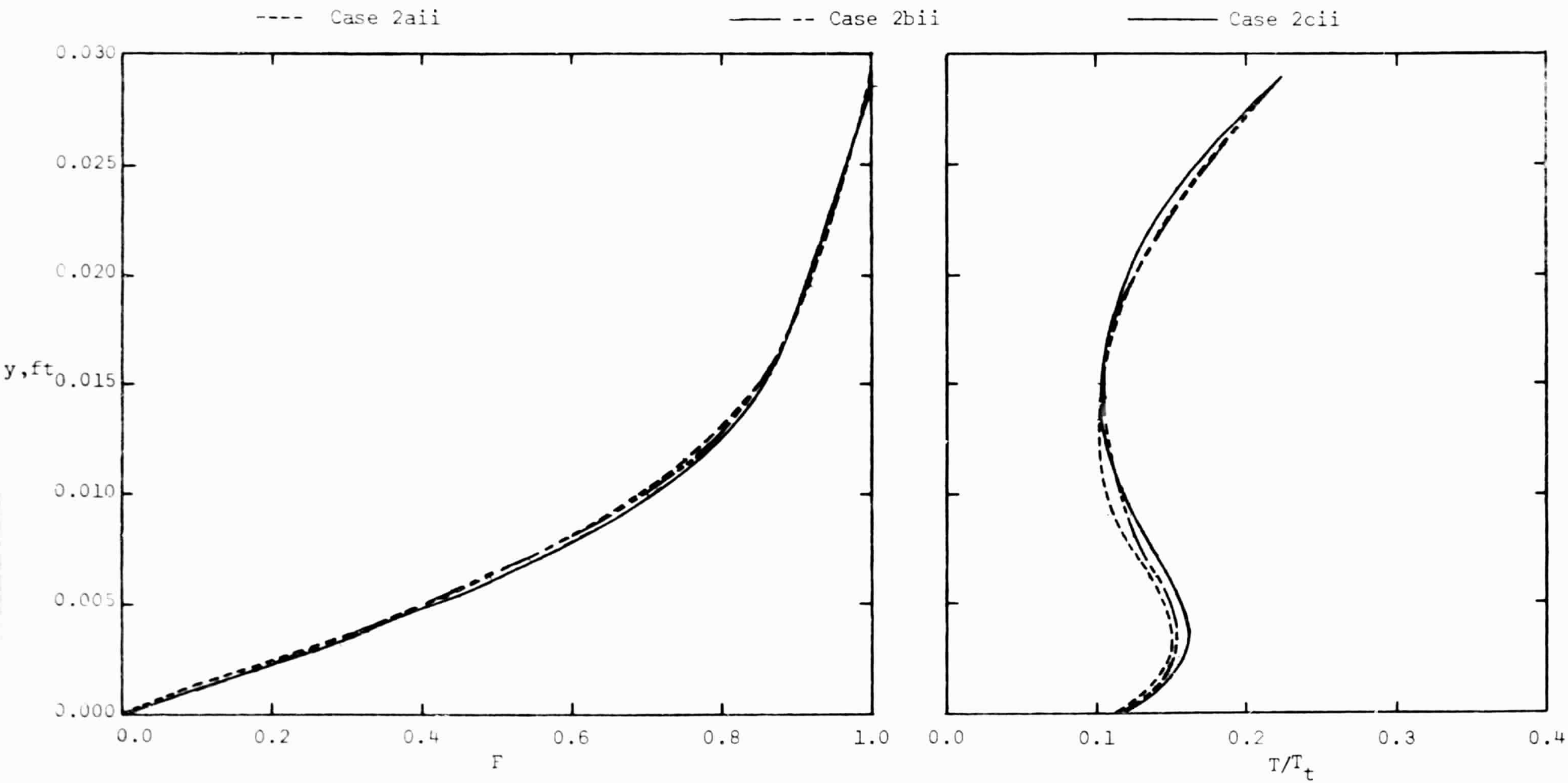

(c) s = 0.351 ft (i.e., s = 0.326L, which is just upstream of the "assumed" separation).

Figure 10. - Concluded.

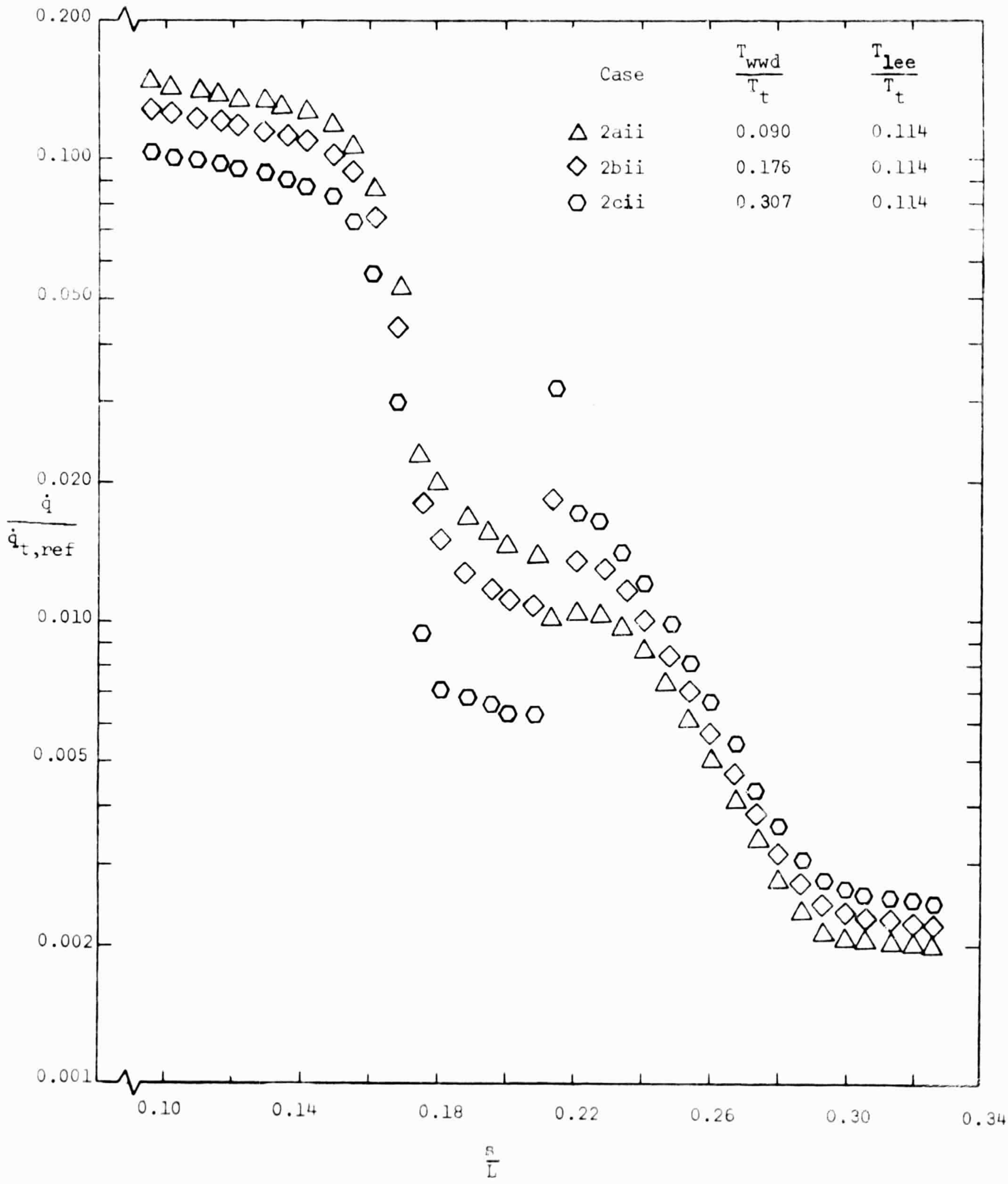

(a) The effect of the windward-section temperature.

Figure 11.- The effect of the surface temperature distribution on the streamwise heat-transfer distribution for flow condition 2, $M_\infty = 12.25$, $Re_{\infty/ft} = 0.55 \times 10^6$ (NSE for $\alpha = 30°$).

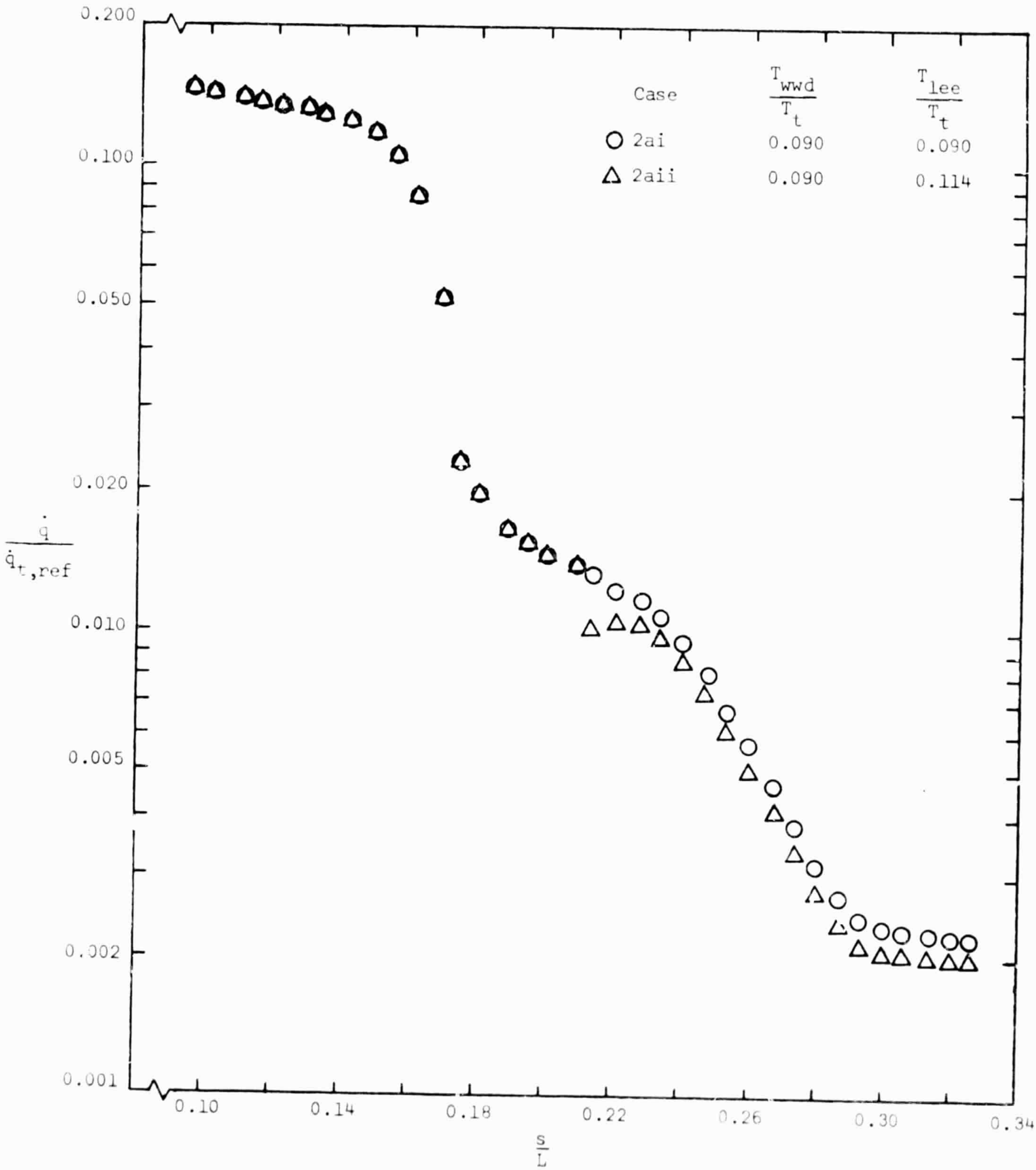

(b) The effect of the leeward-section temperature

Figure 11. - Concluded.

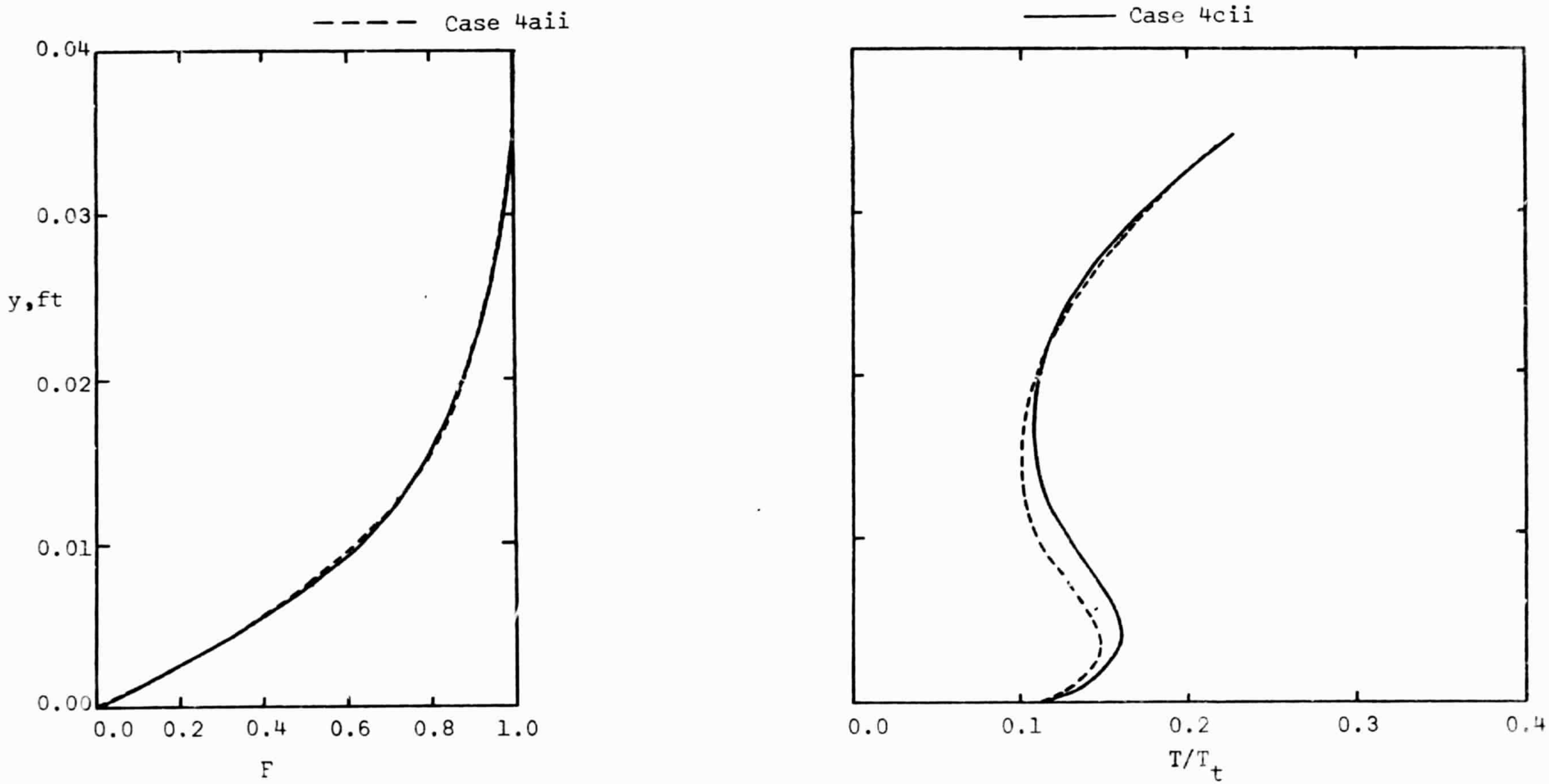

s = 0.351 ft (i.e., s = 0.326 L, which is just upstream of the "assumed" separation)

Figure 12. - The effect of surface temperature on the theoretical, laminar boundary-layer (NSE for $\alpha = 30°$), $M_\infty = 15.70$, $Re_{\infty,L} = 0.61 \times 10^6$.

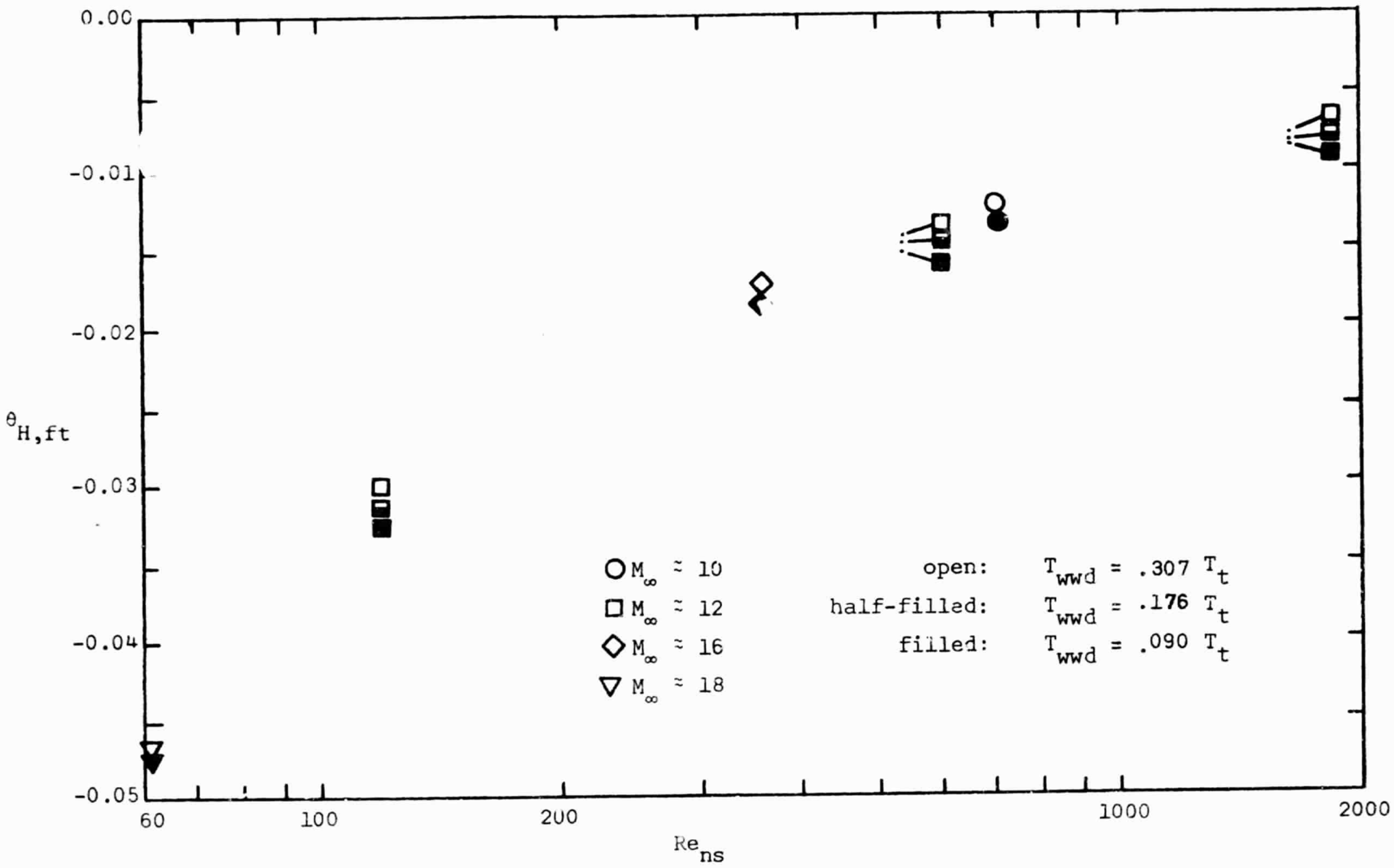

Figure 13. - The computed enthalpy thickness at the "assumed" separation location as a function of the Reynolds number behind a normal shock wave (NSE for $\alpha = 30°$).

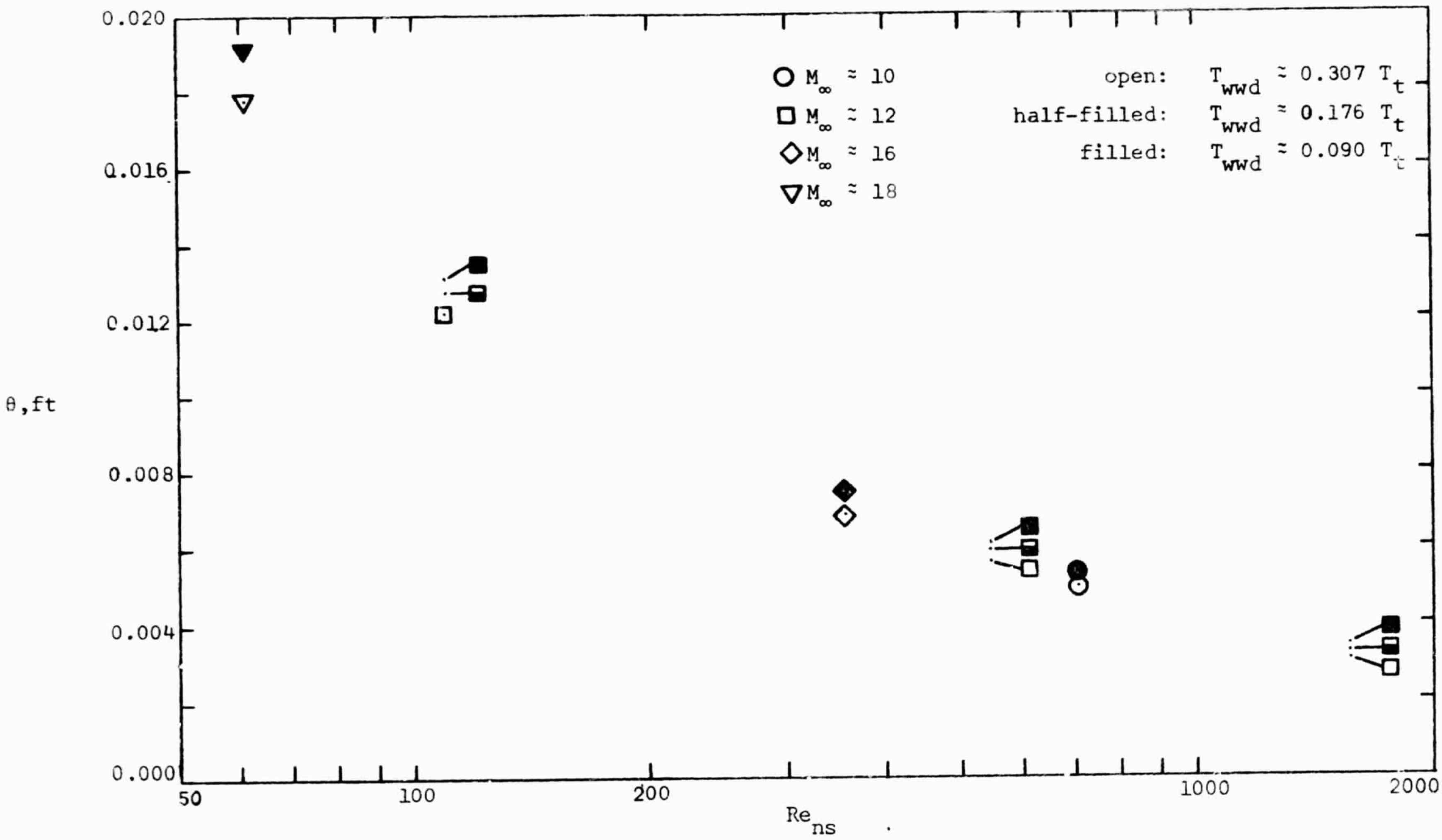

Figure 14. - The computed momentum thickness at the "assumed" separation location as a function of the Reynolds number behind a normal shock wave (NSE for α = 30°).

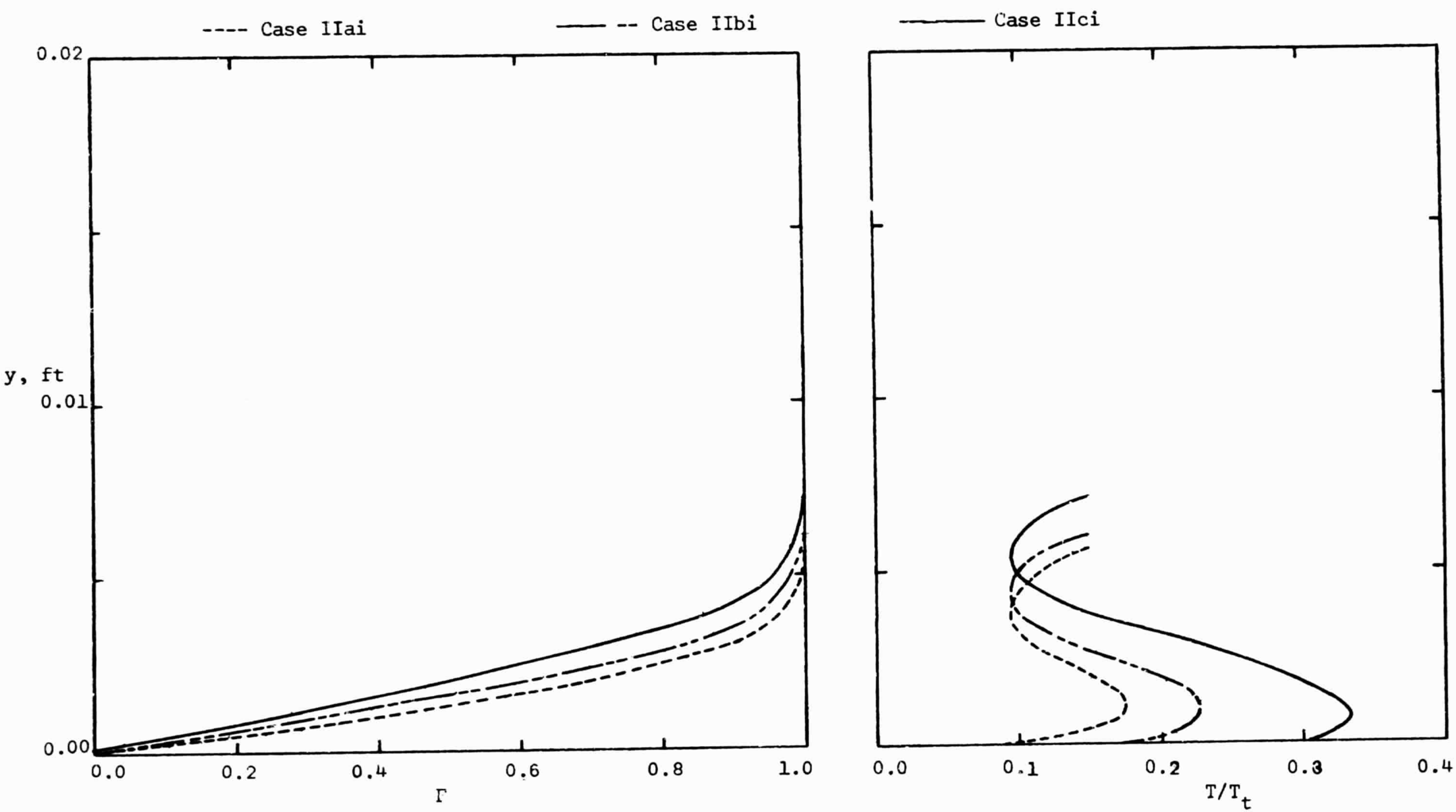

(a) s = 0.216 ft (i.e., s = 0.201L, which is just upstream of the section interface)

Figure 15. - The effect of surface temperature on the theoretical, laminar boundary-layer (PSE for α = 30°) M = 12.25, $Re_{\infty,L}$ = 0.59 x 10^6.

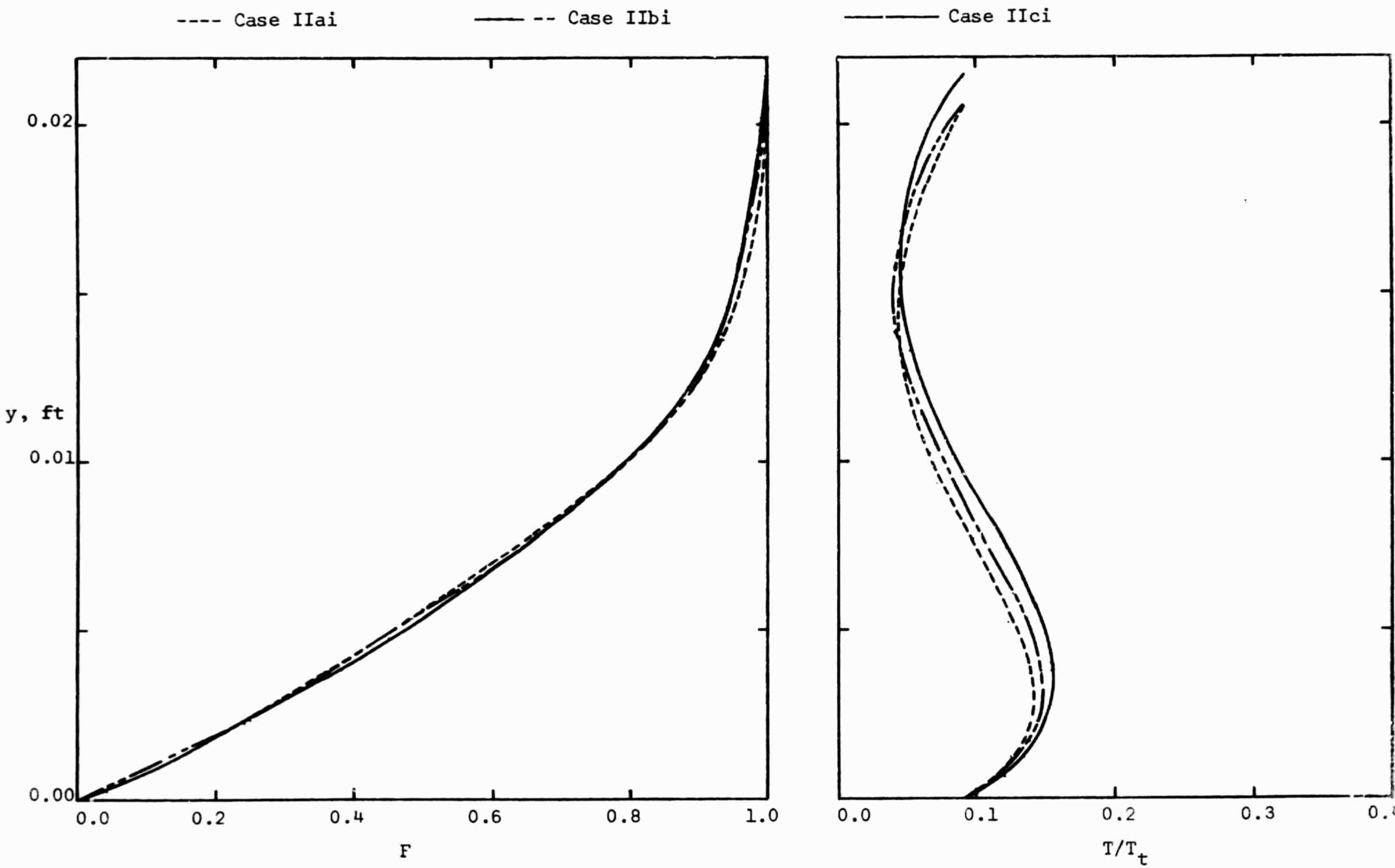

(b) s = 0.351 ft (i.e., s = 0.326L, which is just upstream of the "assumed" separation)

Figure 15. - Concluded.

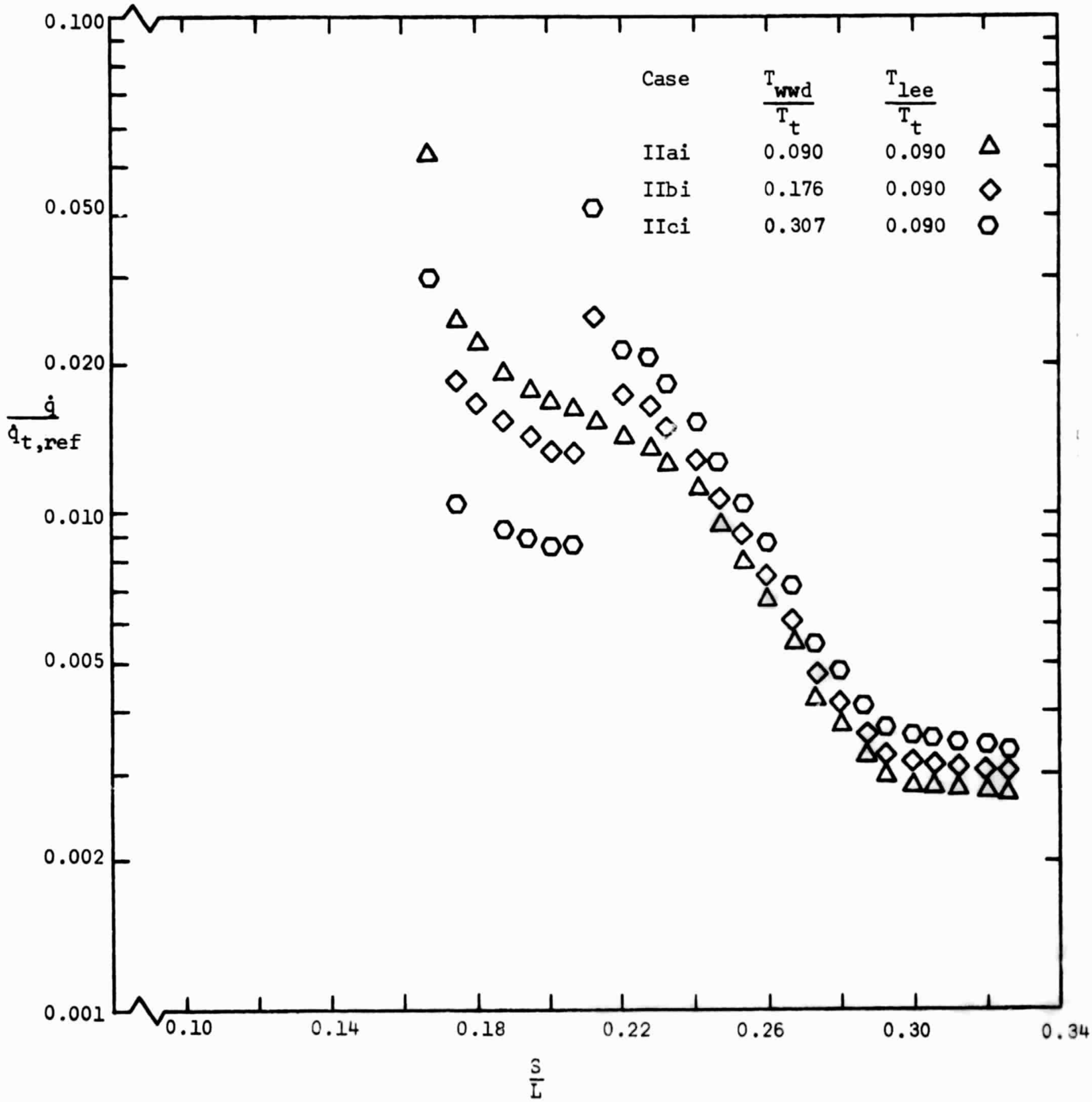

Figure 16. - The effect of the windward-section surface temperature distribution on the streamwise heat-transfer distribution for flow condition II, $M_\infty = 12.25$, $Re_{\infty,L} = 0.59 \times 10^6$ (PSE for $\alpha = 30°$).

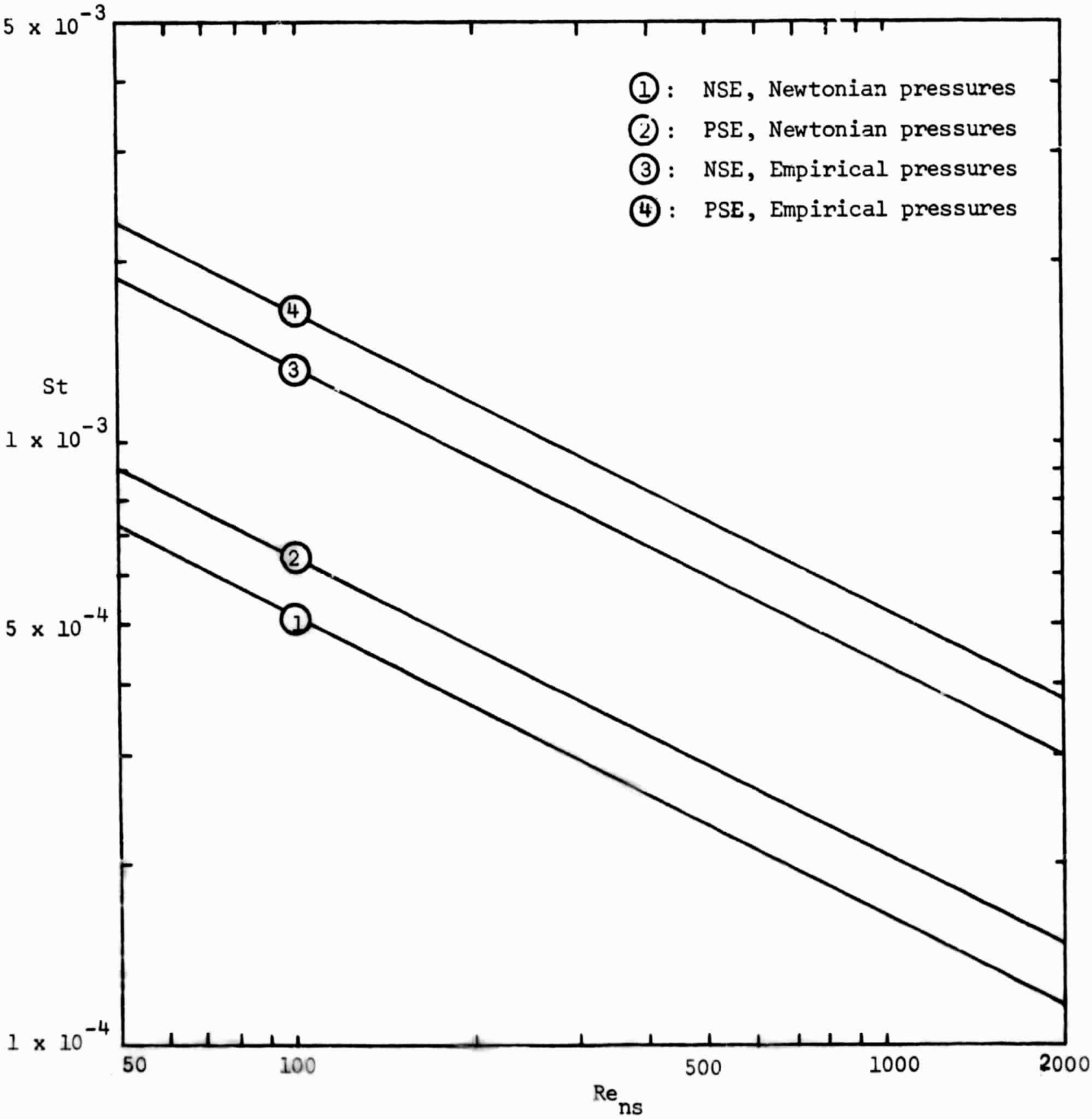

Figure 17. - The effect of inviscid flow model on the theoretical heat-transfer at s = 0.351 ft (s = 0.326L), α = 30°.

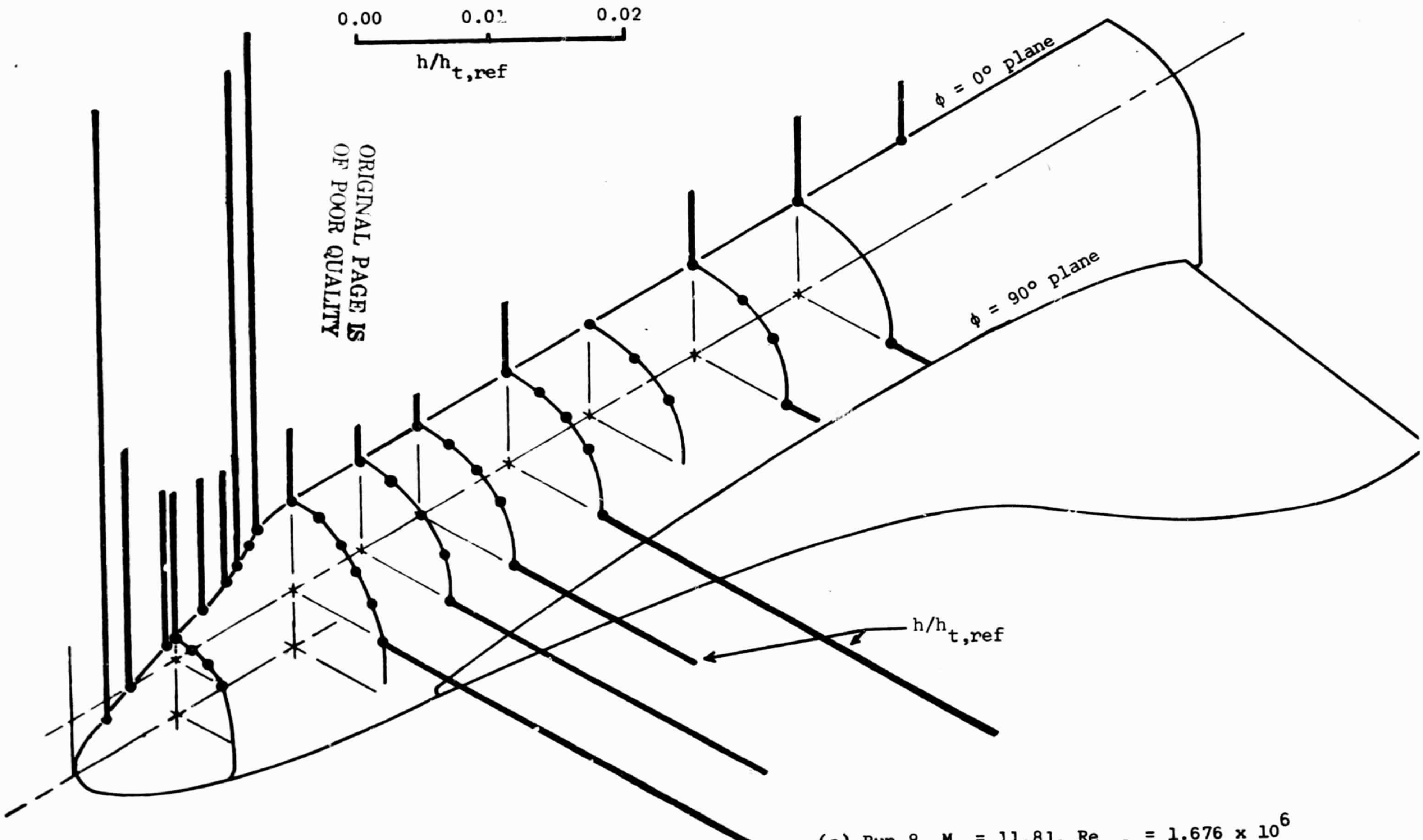

(a) Run 8, $M_\infty = 11.81$, $Re_{\infty,L} = 1.676 \times 10^6$

Figure 18. - Typical heat-transfer distributions in the $\phi = 0°$ plane and in the $\phi = 90°$ plane, $\alpha = 30°$.

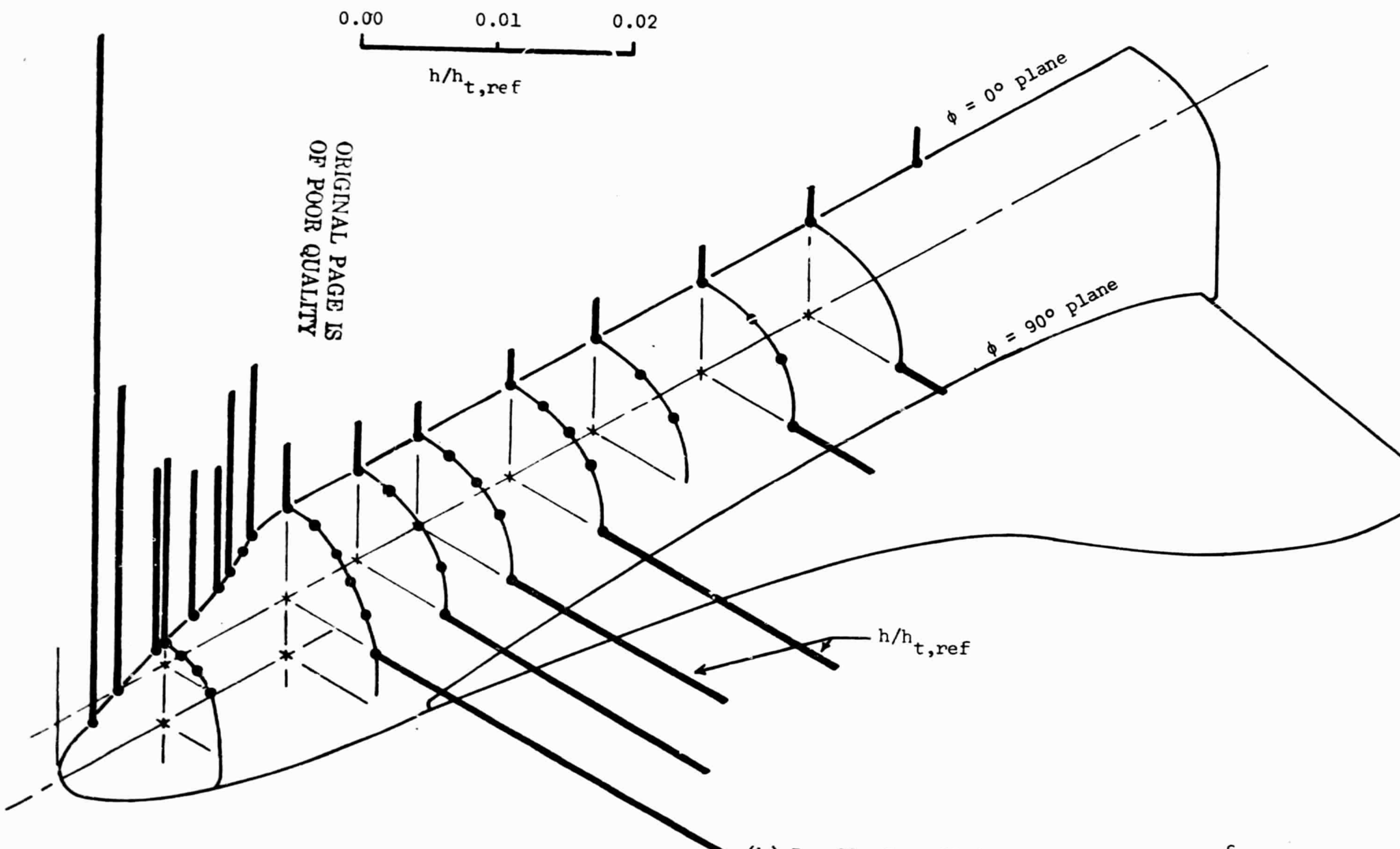

ORIGINAL PAGE IS OF POOR QUALITY

(b) Run 11, $M_\infty = 11.64$, $Re_{\infty,L} = 0.116 \times 10^6$

Figure 18. - Concluded.

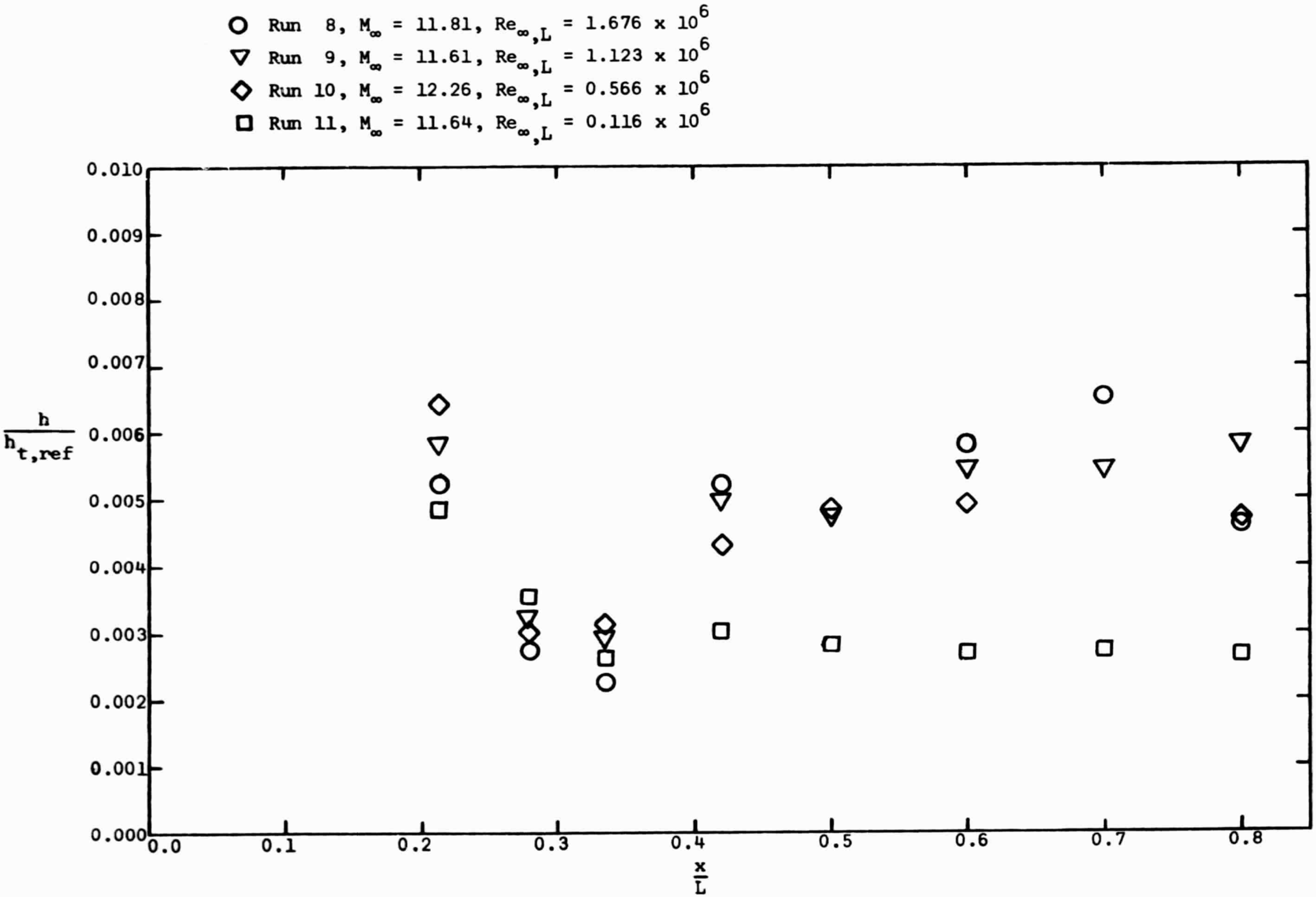

(a) $T_{wwd} \approx 0.31\ T_t$, $T_{lee} \approx 0.11\ T_t$

Figure 19. - The effect of Reynolds number on the heat-transfer distribution in the leeward pitch plane for the nominal Mach 12 flows, α = 30°.

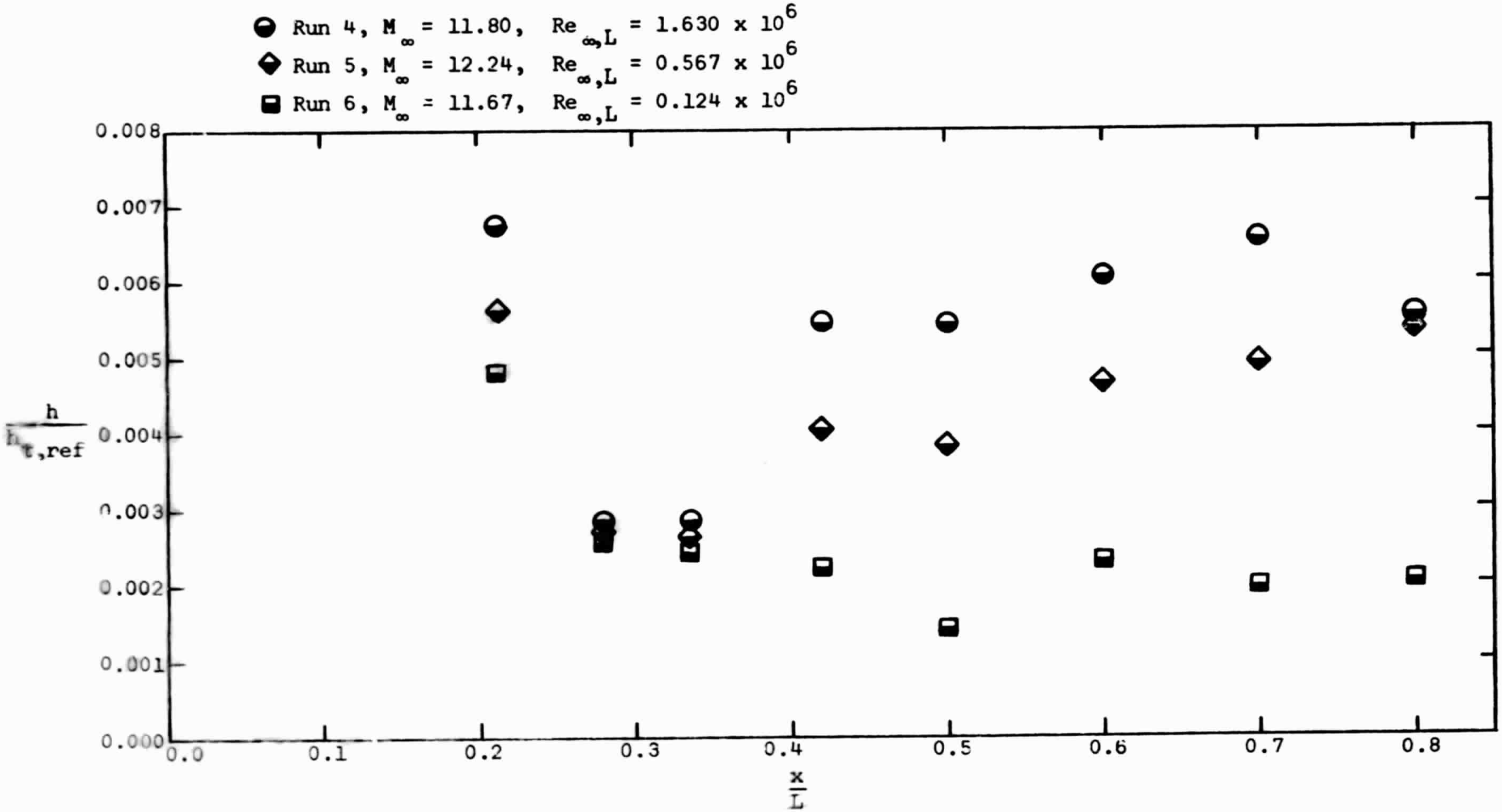

(b) $T_{wwd} \approx 0.18\ T_t$, $T_{lee} \approx 0.11\ T_t$

Figure 19. - Continued.

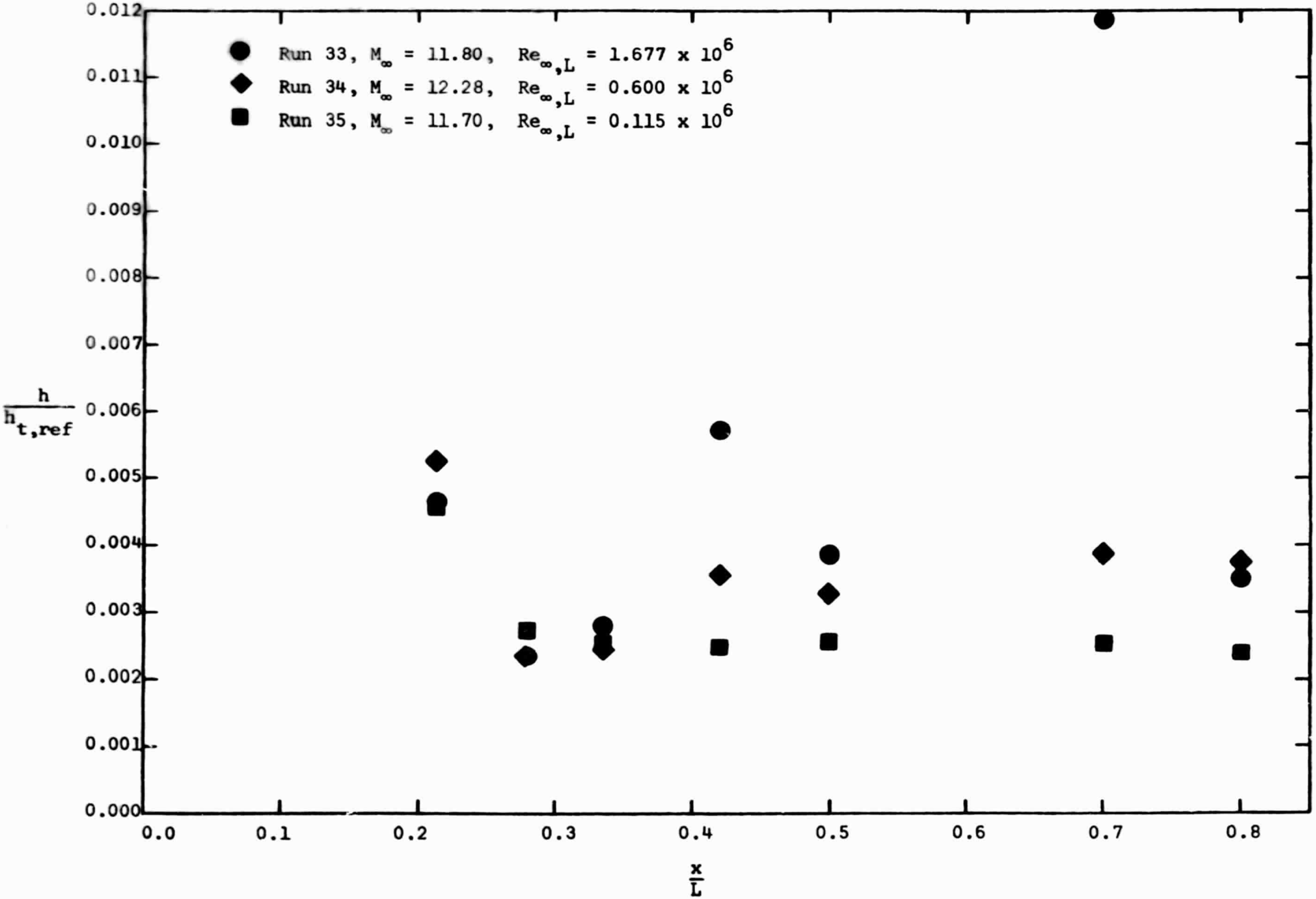

(c) $T_{wwd} \approx 0.09\ T_t$, $T_{lee} \approx 0.09\ T_t$

Figure 19. - Concluded.

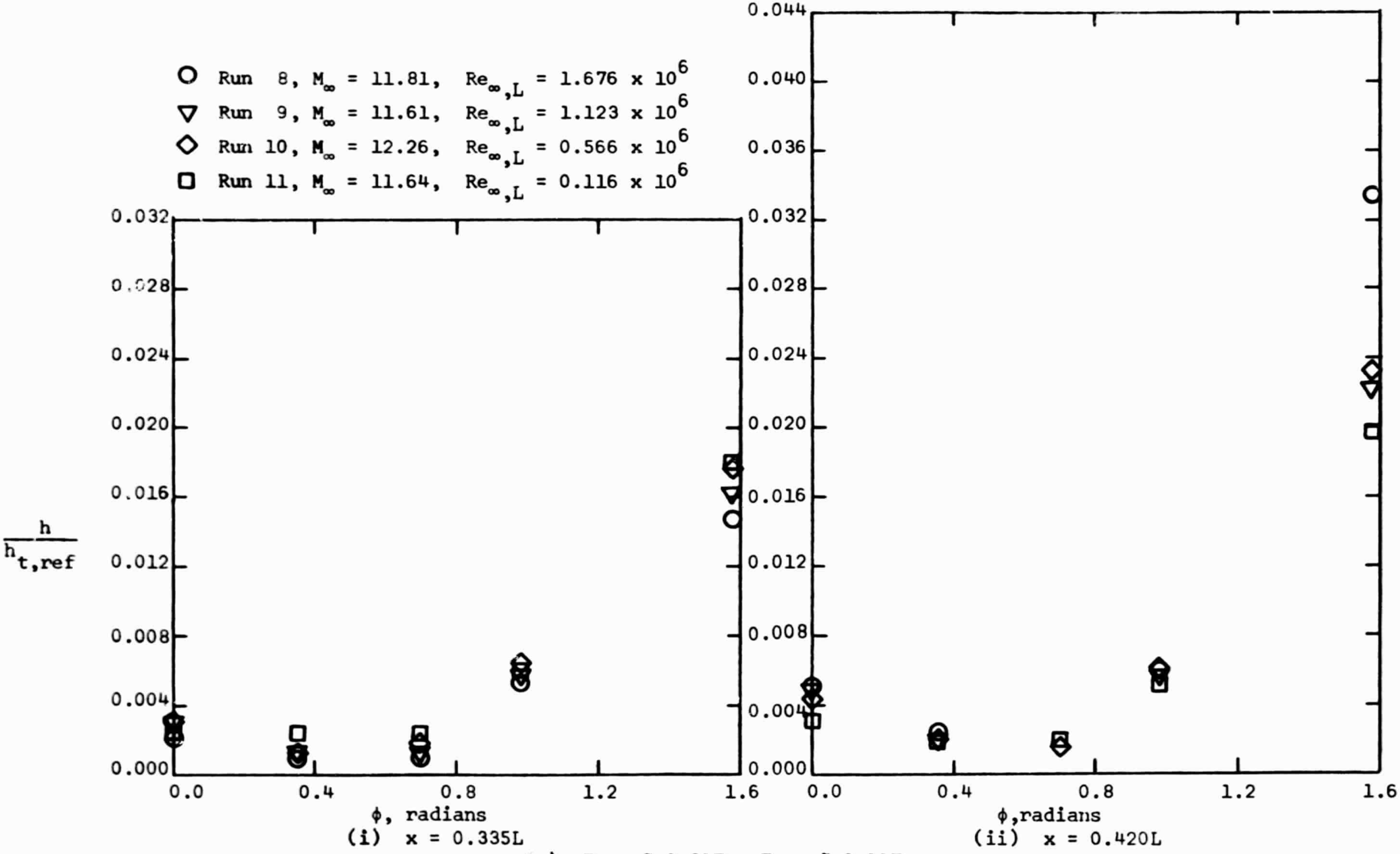

(a) $T_{wwd} \approx 0.31T_t$, $T_{lee} \approx 0.11T_t$

Figure 20. - The effect of Reynolds number on the circumferential heat-transfer distribution for the nominal Mach 12 flow, α = 30°.

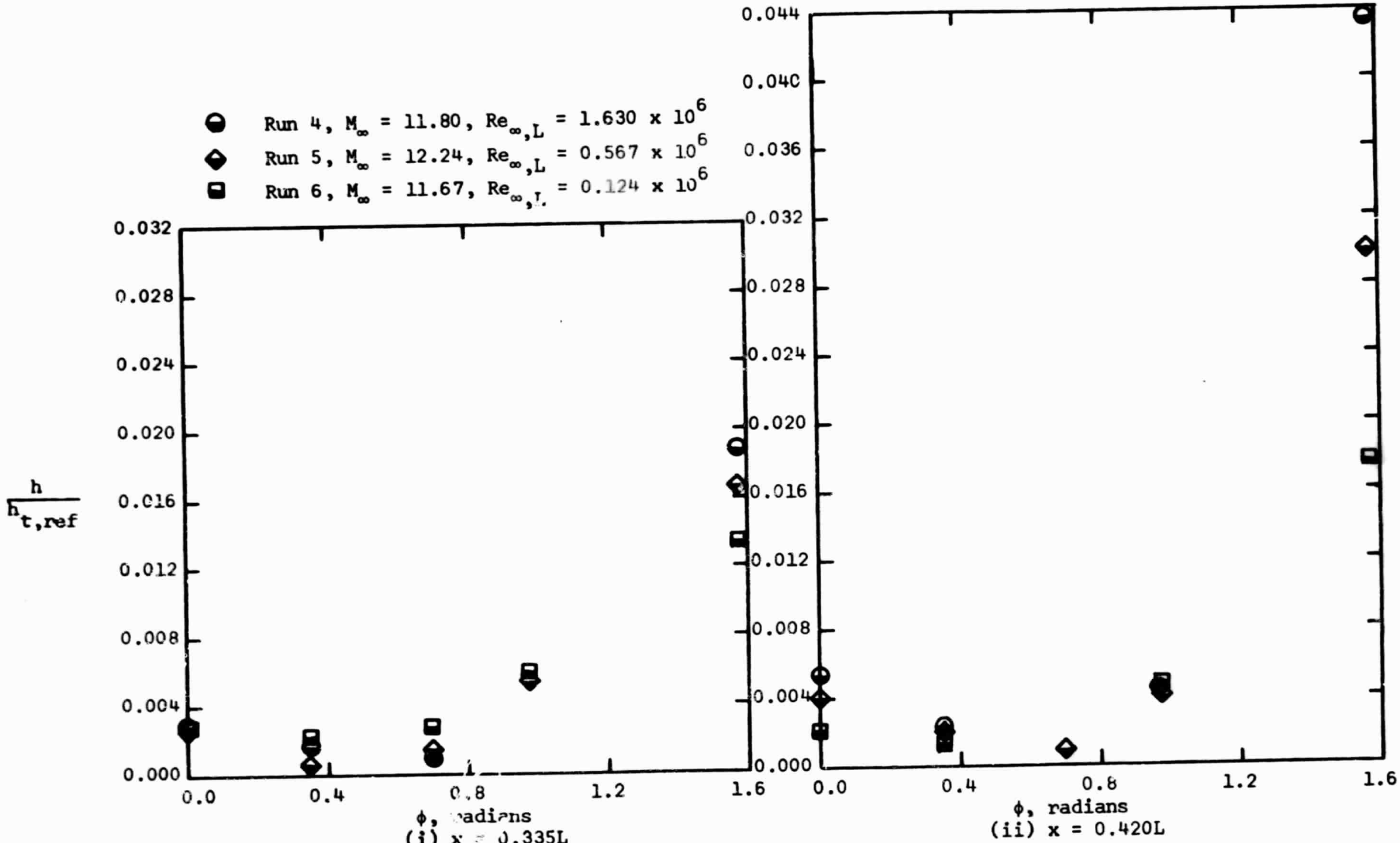

(b) $T_{wwd} \approx 0.18T_t$, $T_{lee} \approx 0.11T_t$

Figure 20. - Continued.

C2

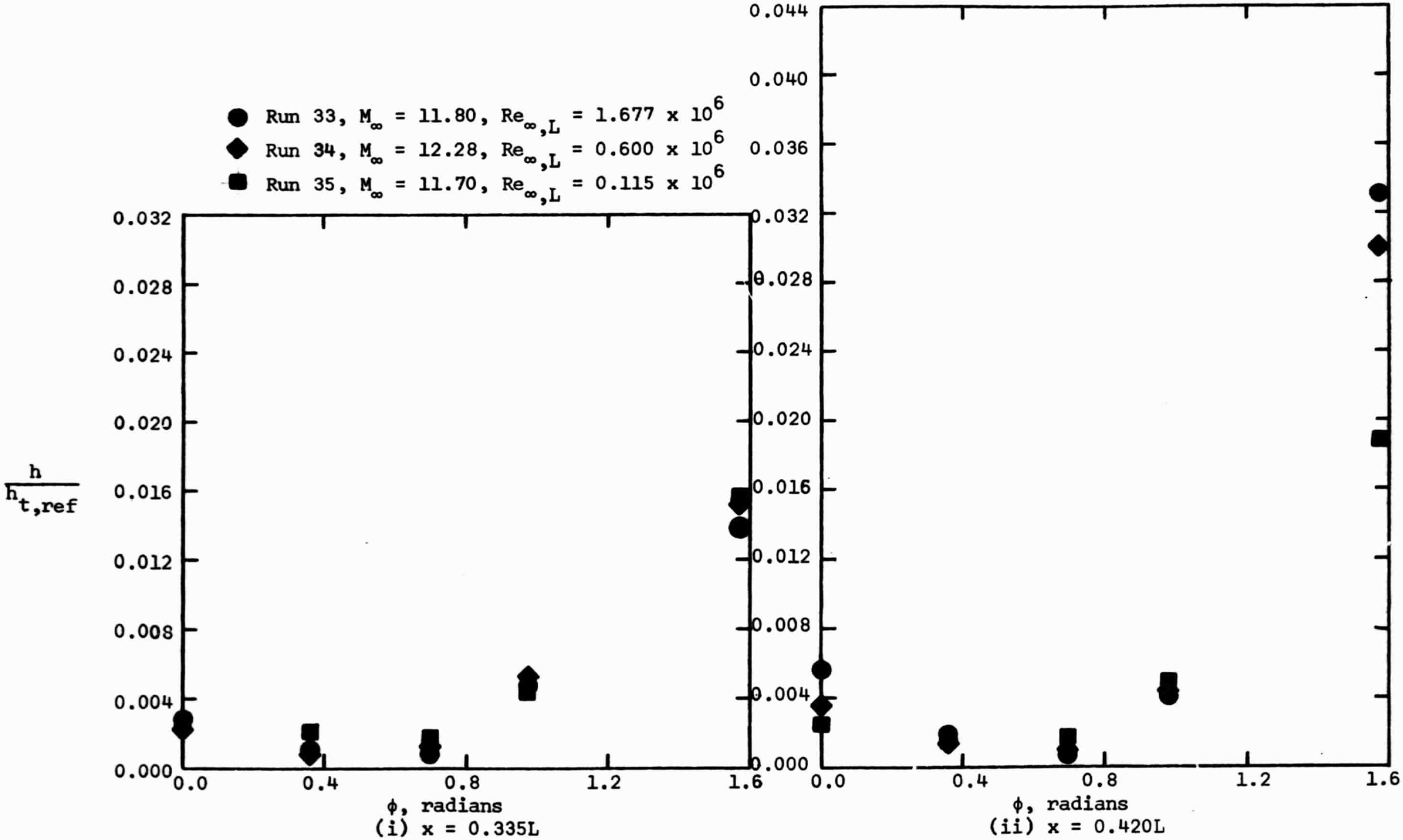

(c) $T_{wwd} \approx 0.09\ T_t$, $T_{lee} \approx 0.09\ T_t$

Figure 20. - Concluded.

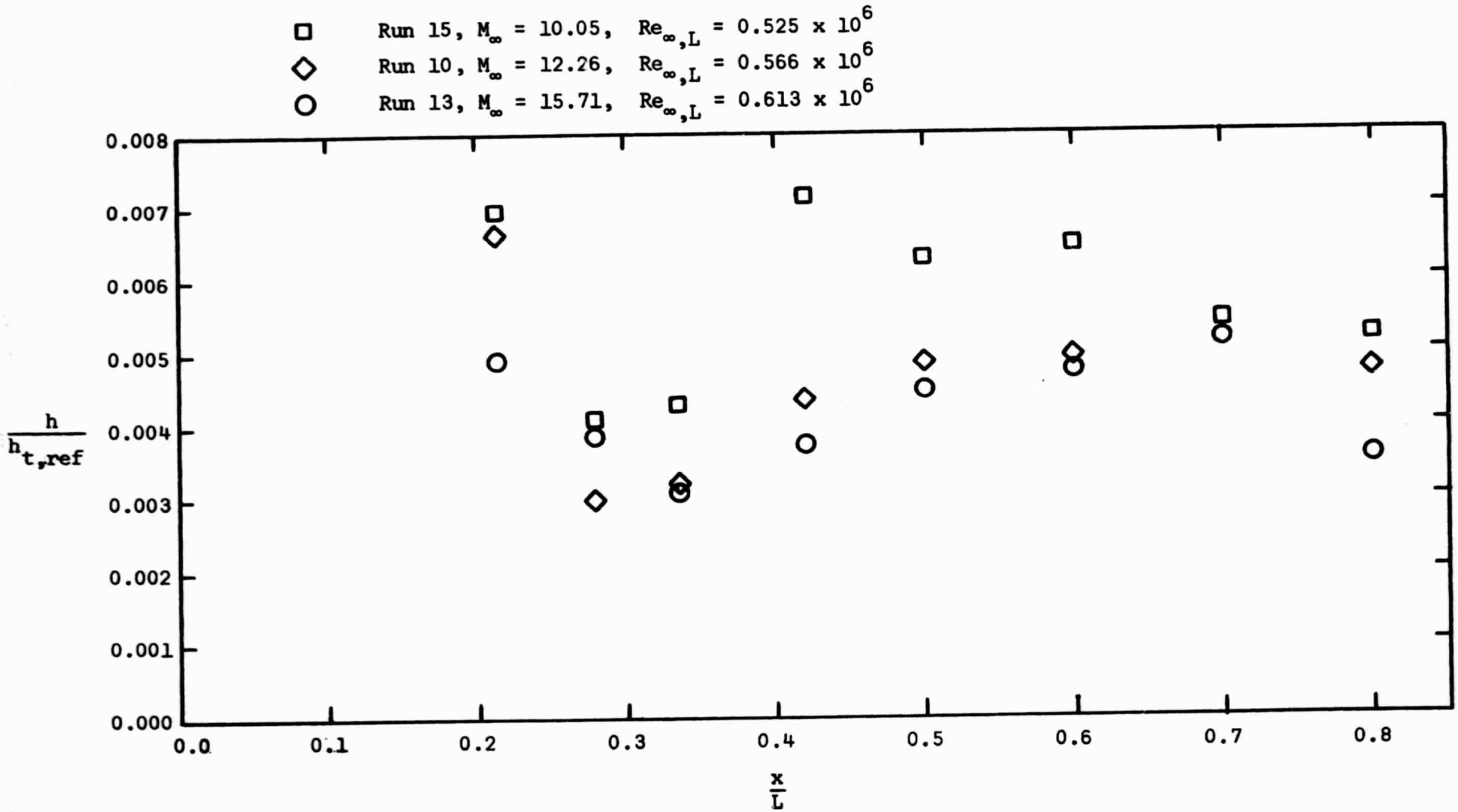

(a) $T_{wwd} \approx 0.31\ T_t$, $T_{lee} \approx 0.11\ T_t$

Figure 21. - The heat-transfer distribution in the leeward pitch plane for those runs with the nominal $Re_{\infty,L}$ of 0.6 x 10^6, $\alpha = 30°$.

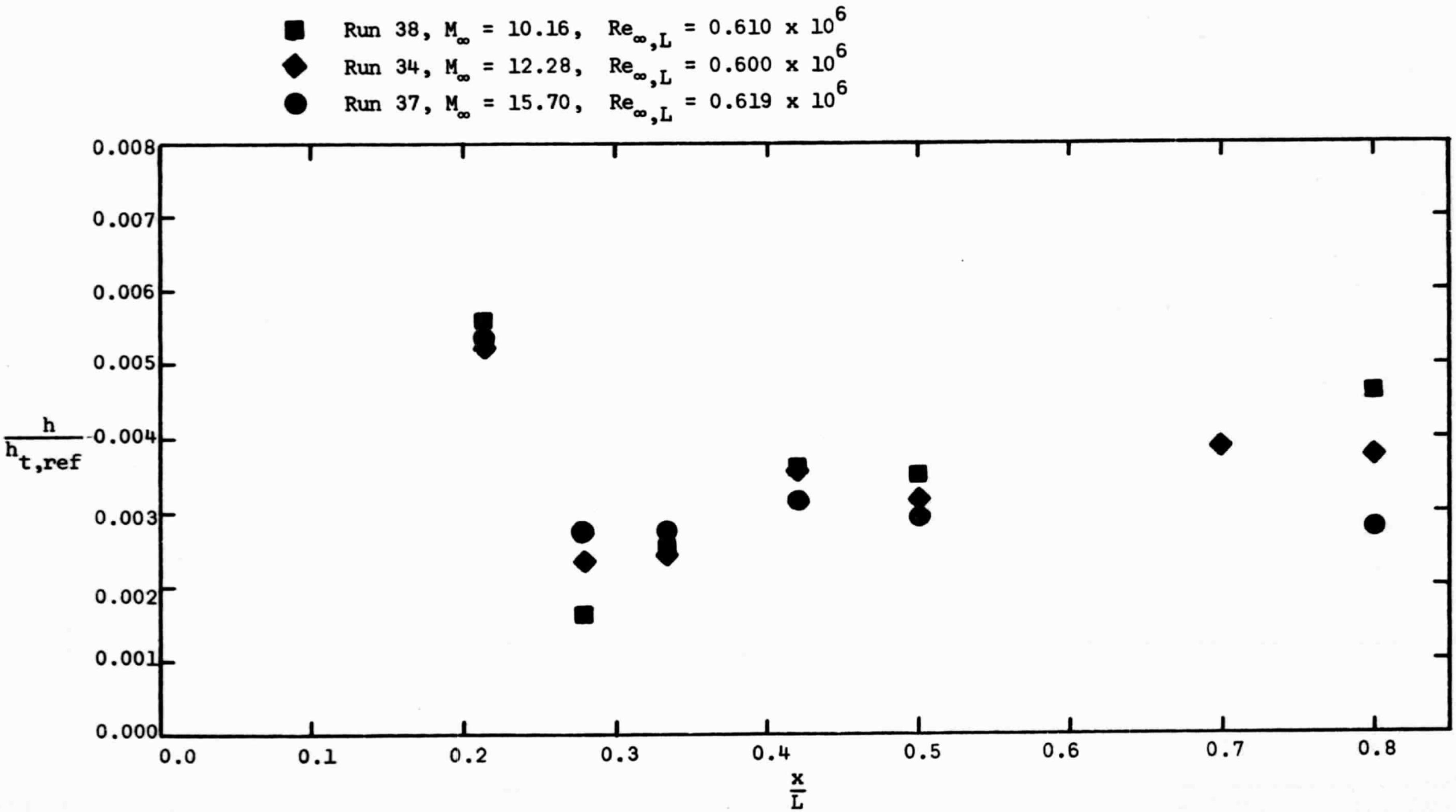

(b) $T_{wwd} \approx 0.09\ T_t$, $T_{lee} \approx 0.09\ T_t$

Figure 21. - Concluded.

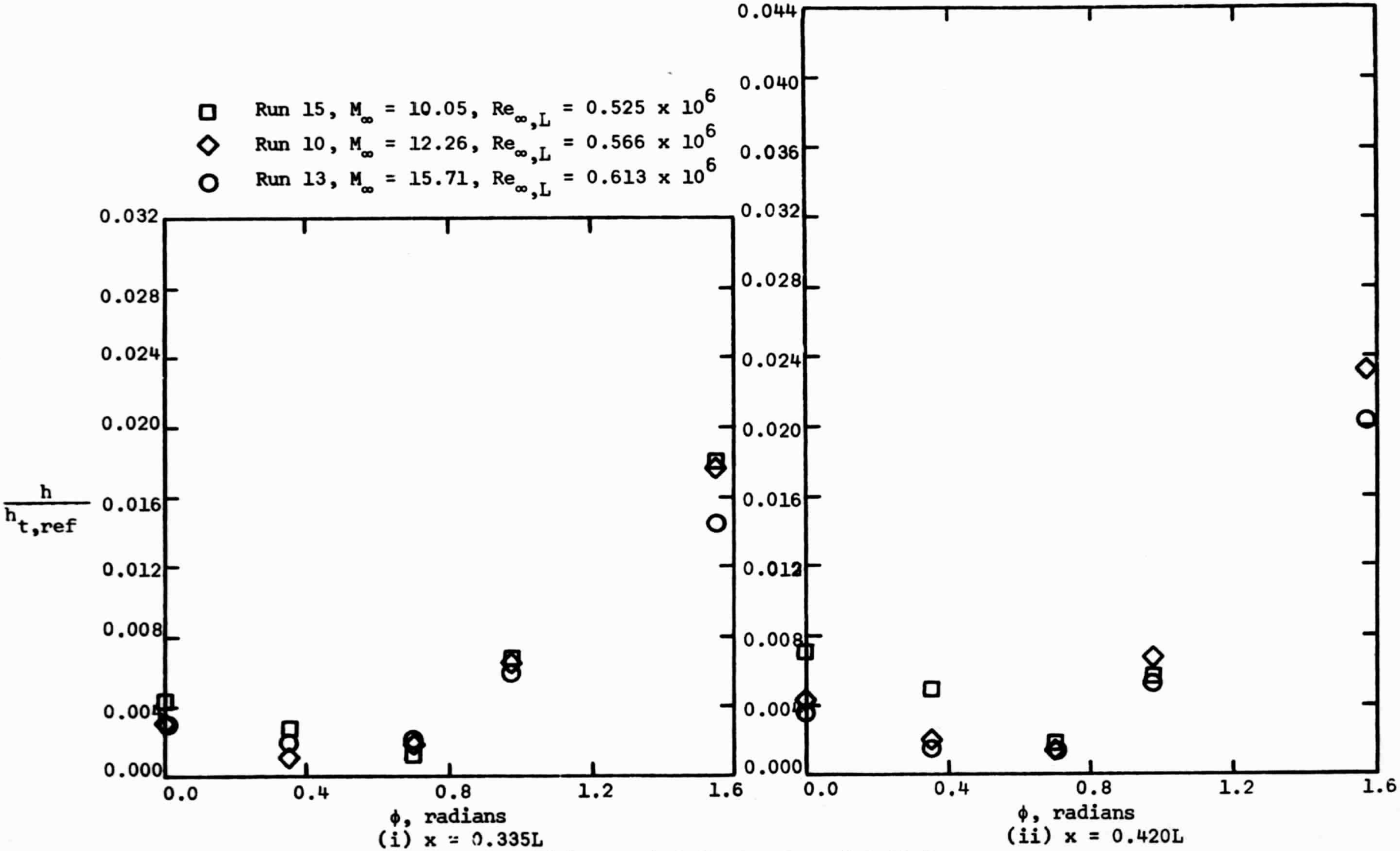

(a) $T_{wwd} \approx 0.31\ T_t$, $T_{lee} \approx 0.11\ T_t$

Figure 22. - The circumferential heat-transfer distribution in the leeward pitch plane for those runs

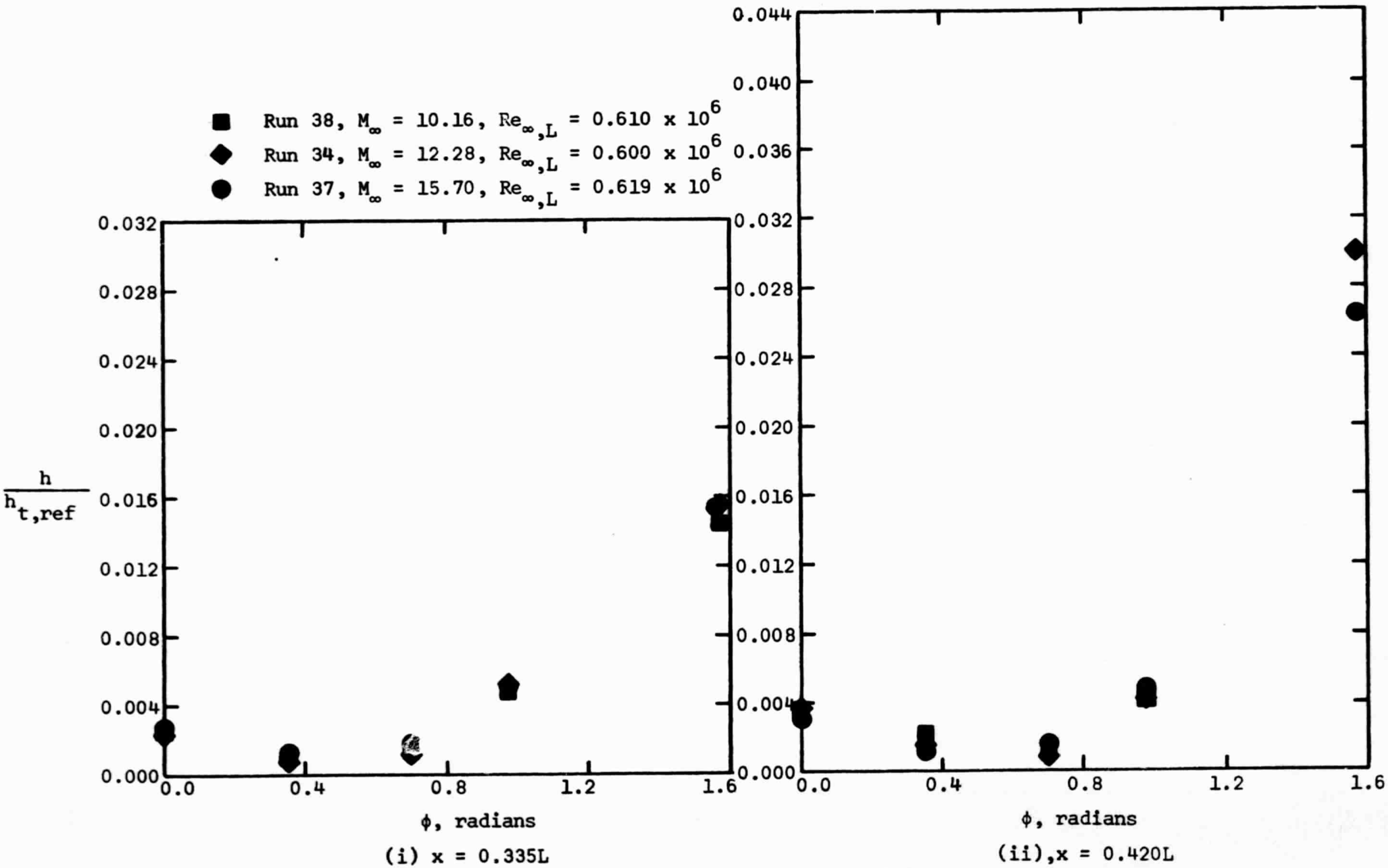

(b) $T_{wwd} \approx 0.09\ T_t$, $T_{lee} \approx 0.09\ T_t$

Figure 22. - Concluded.

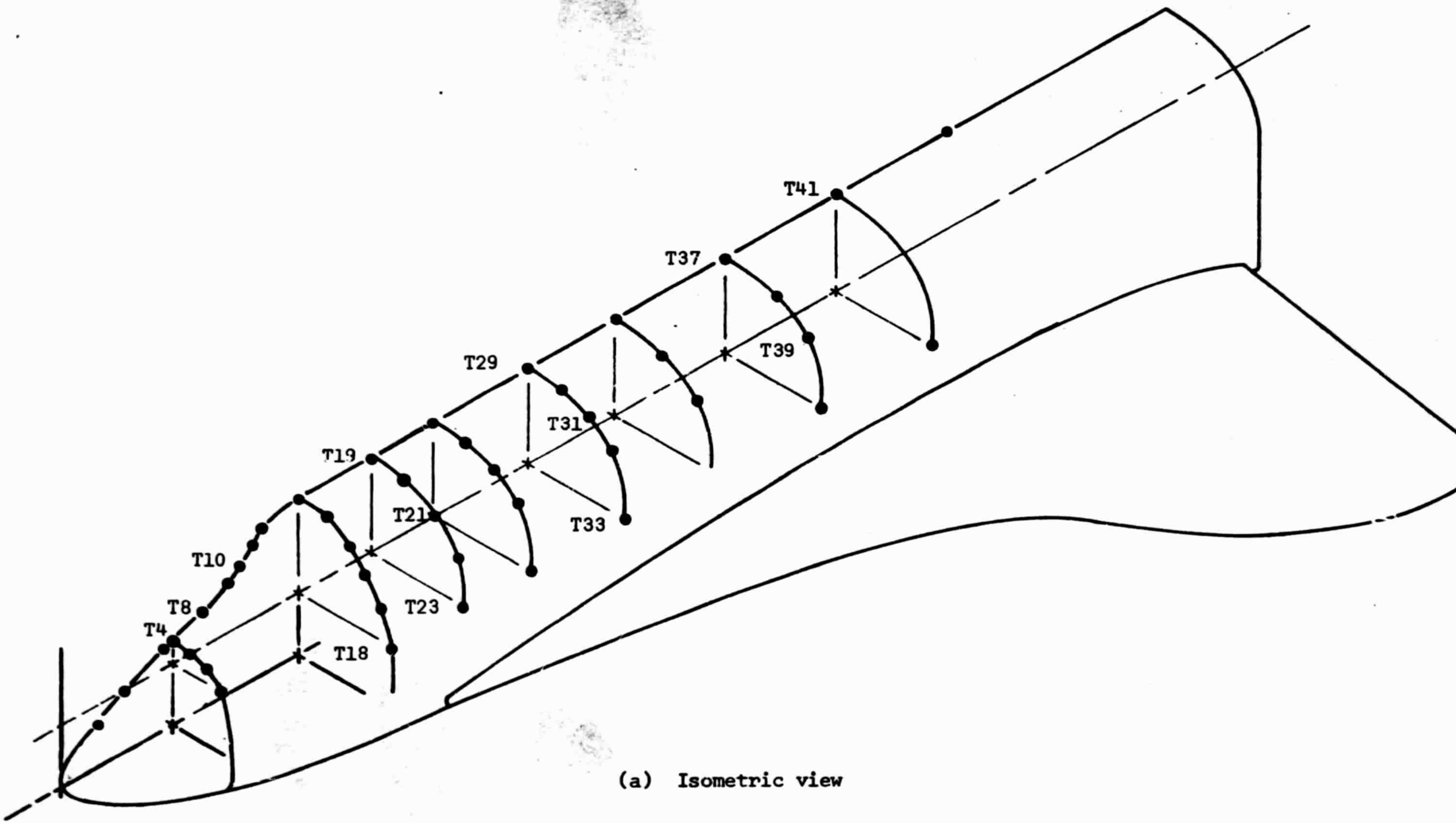

(a) Isometric view

Figure 23. - Location of the gages for which heat-transfer data are presented as a function of Re_{ns}.

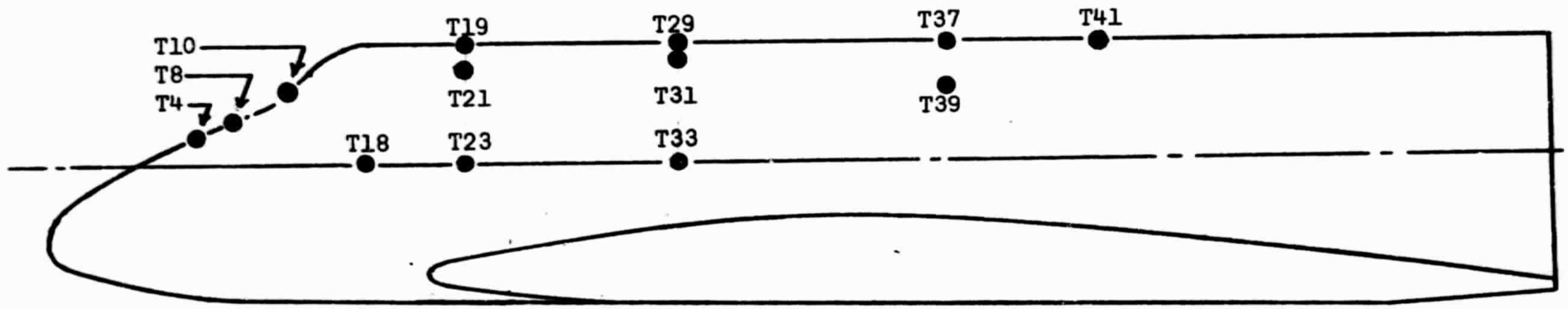

(b) Side view

Figure 23. - Concluded.

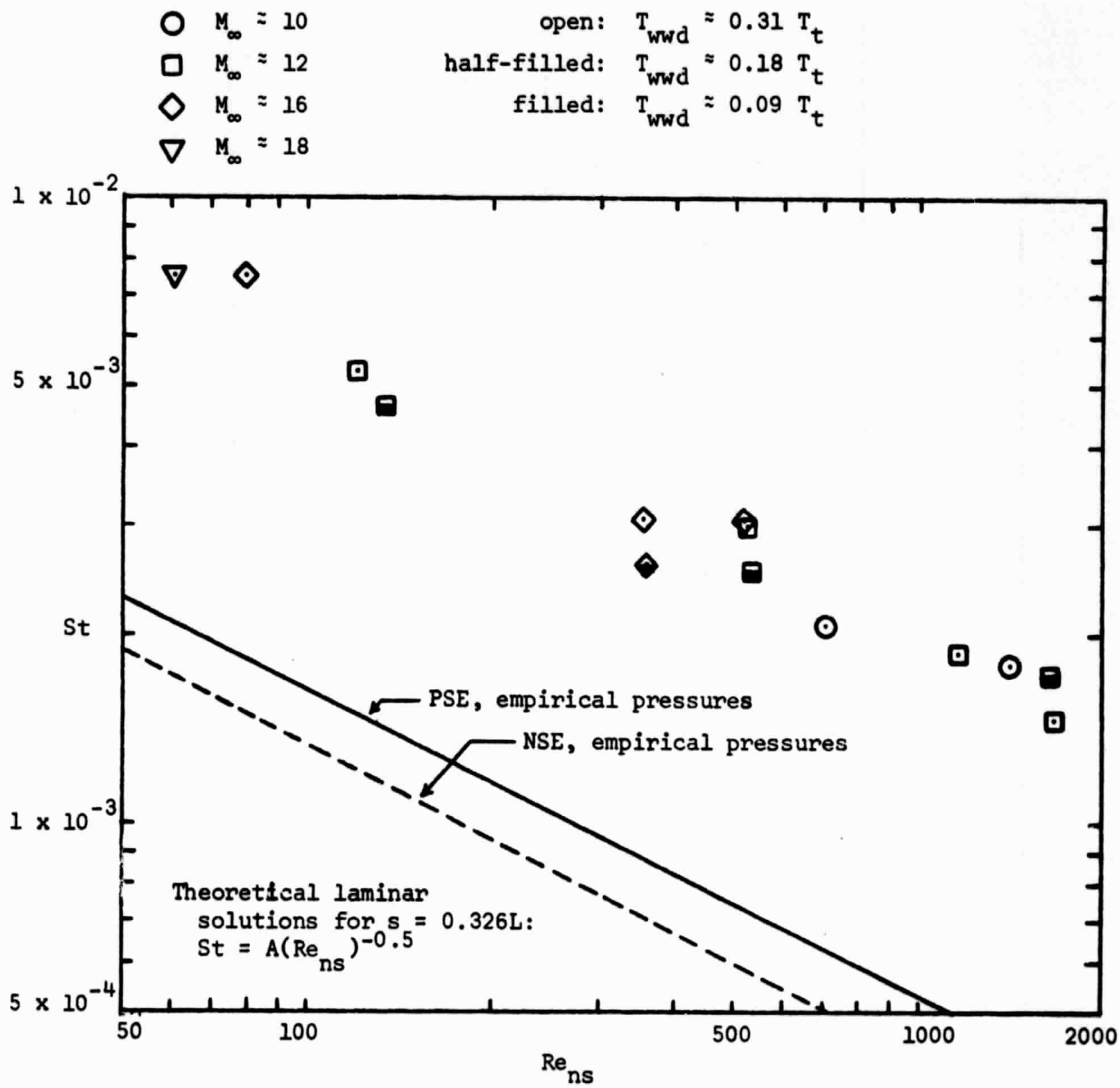

(a) Gage T18, x = 0.213L, ϕ = 90°

Figure 24. - The Stanton number as a function of the Reynolds number behind a normal shock wave for gages on the lateral surface of the fuselage (where the boundary-layer is attached), α = 30°.

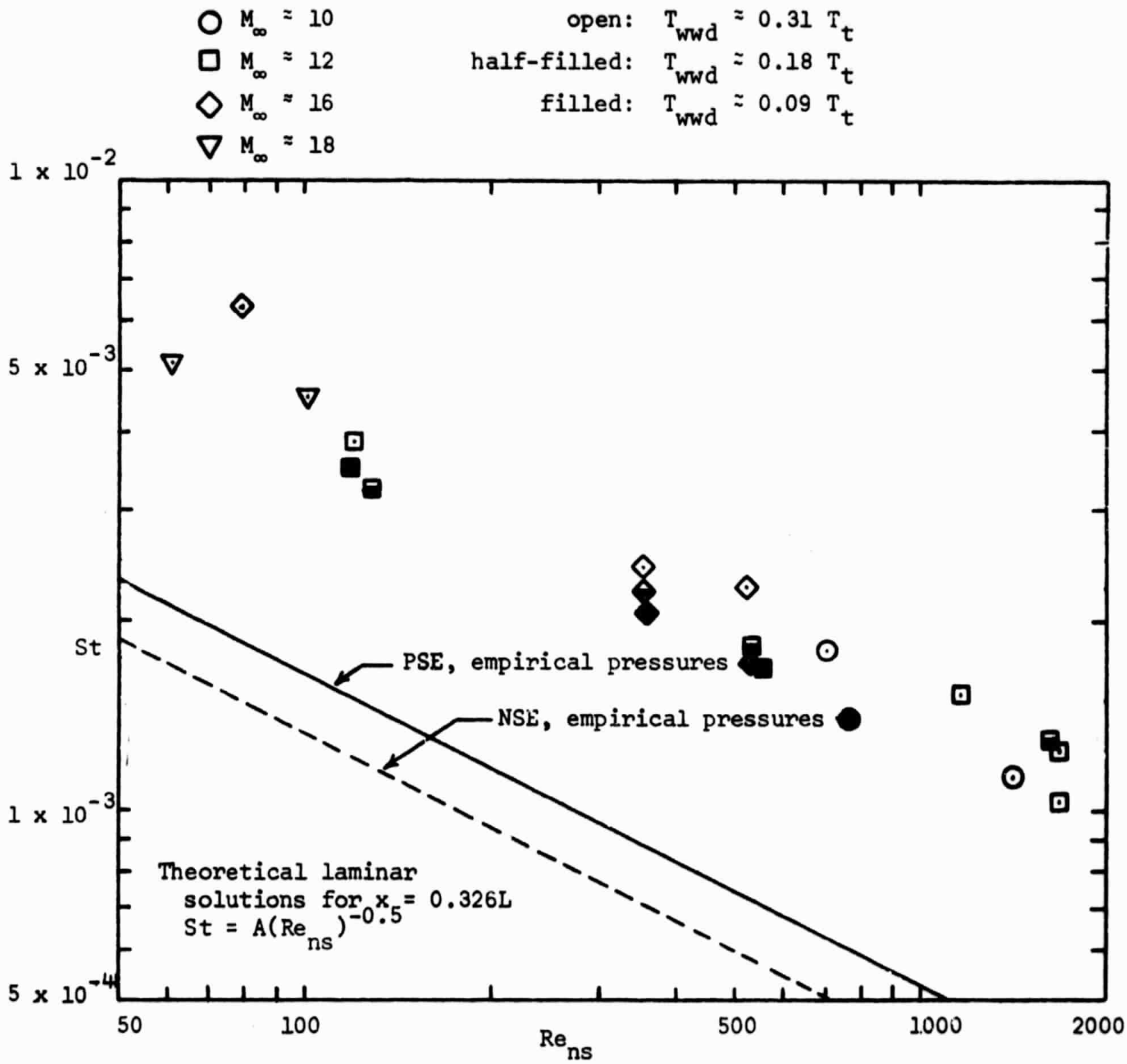

(b) Gage T23, $x = 0.279L$, $\phi = 90°$

Figure 24. - Continued.

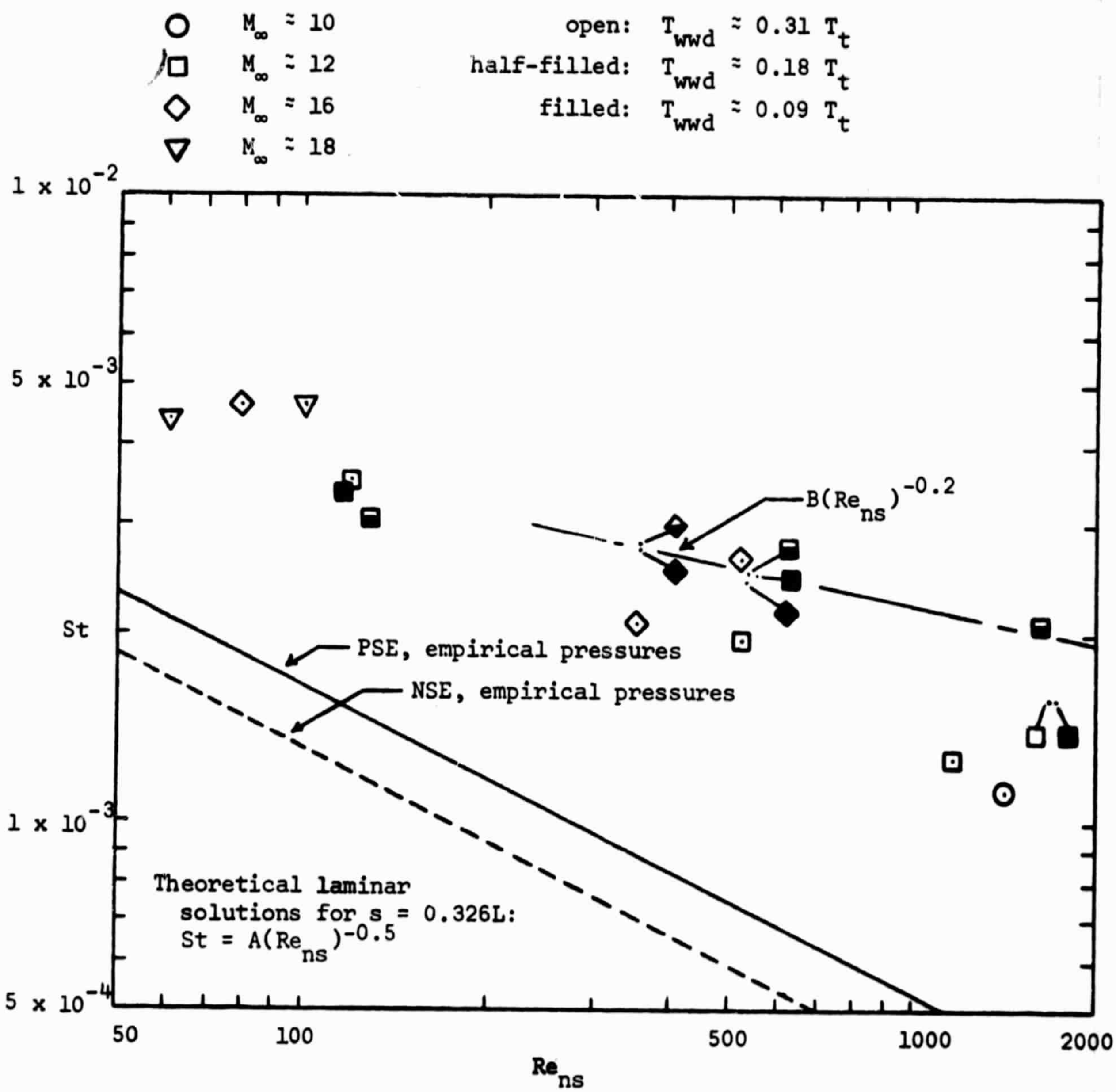

(c) Gage T33, $x = 0.420L$, $\phi = 90°$.

Figure 24. - Concluded.

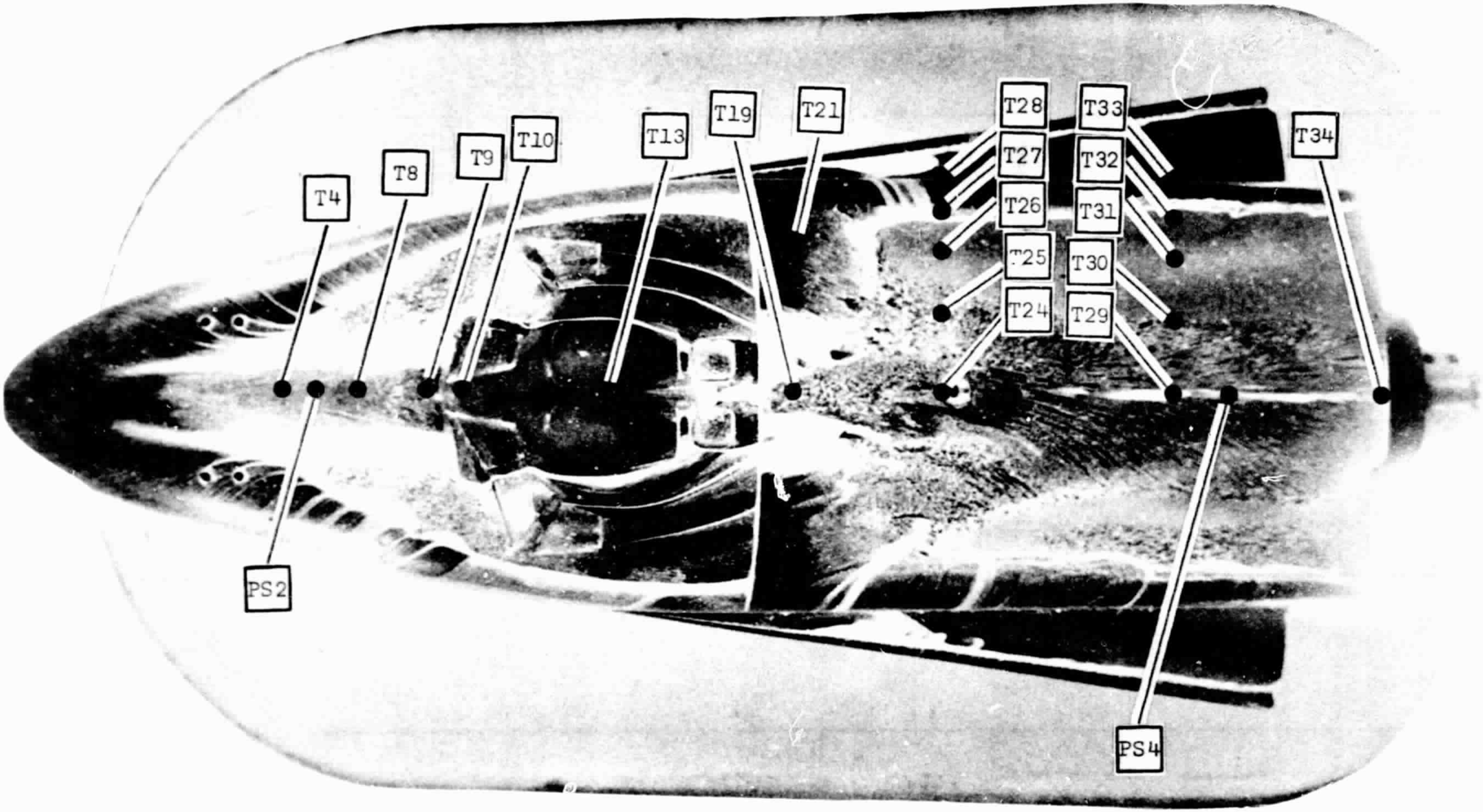

Figure 25. - Photograph of the oil-flow pattern obtained in Tunnel B of AEDC, $Re_{\infty/ft} \approx 1 \times 10^6$.

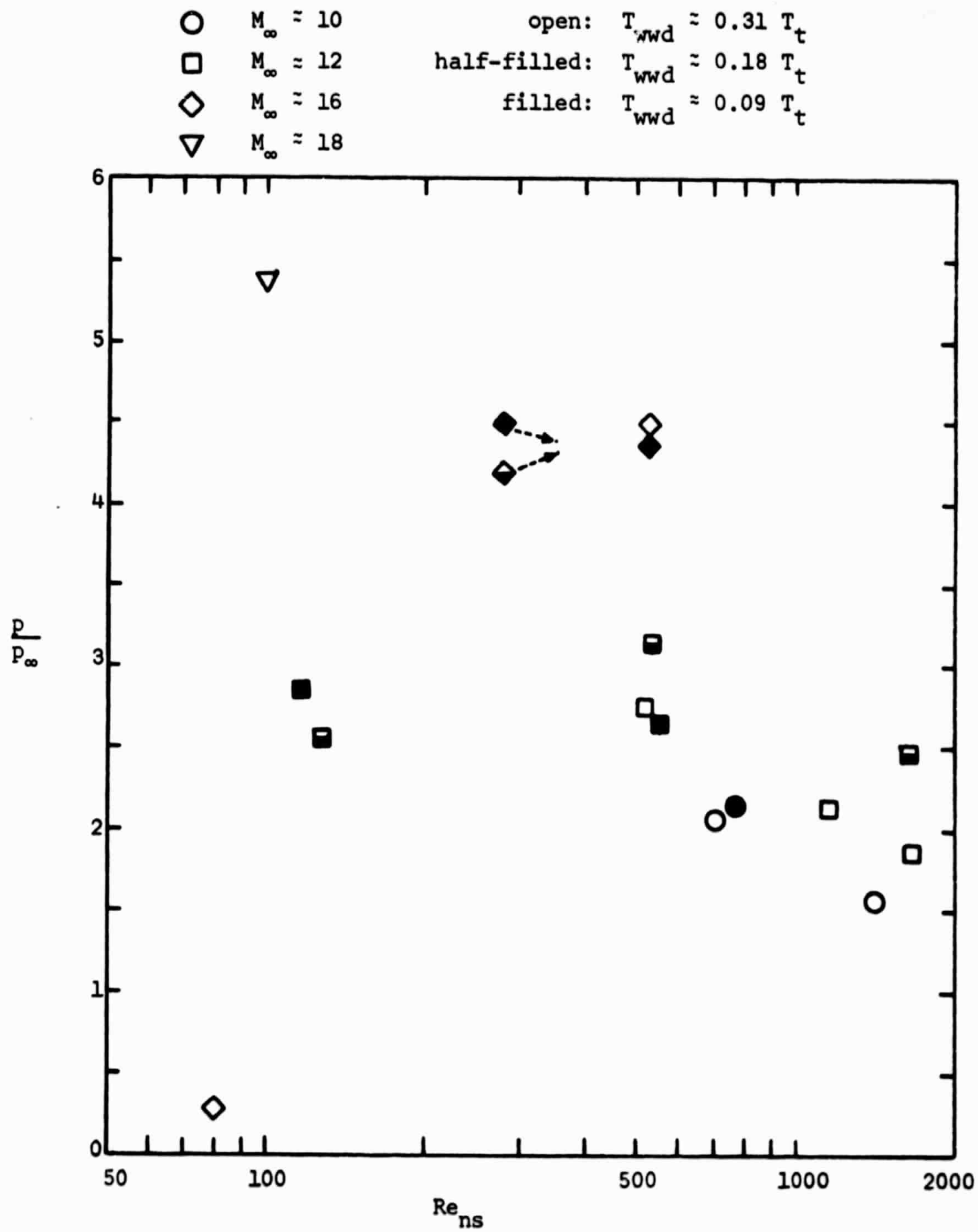

(a) The parameter p/p_∞

Figure 26. - The pressure measurements as a function of Reynolds number for an orifice on the nose upstream of the cockpit (PS2, x = 0.110L, ϕ = 0°), α = 30°.

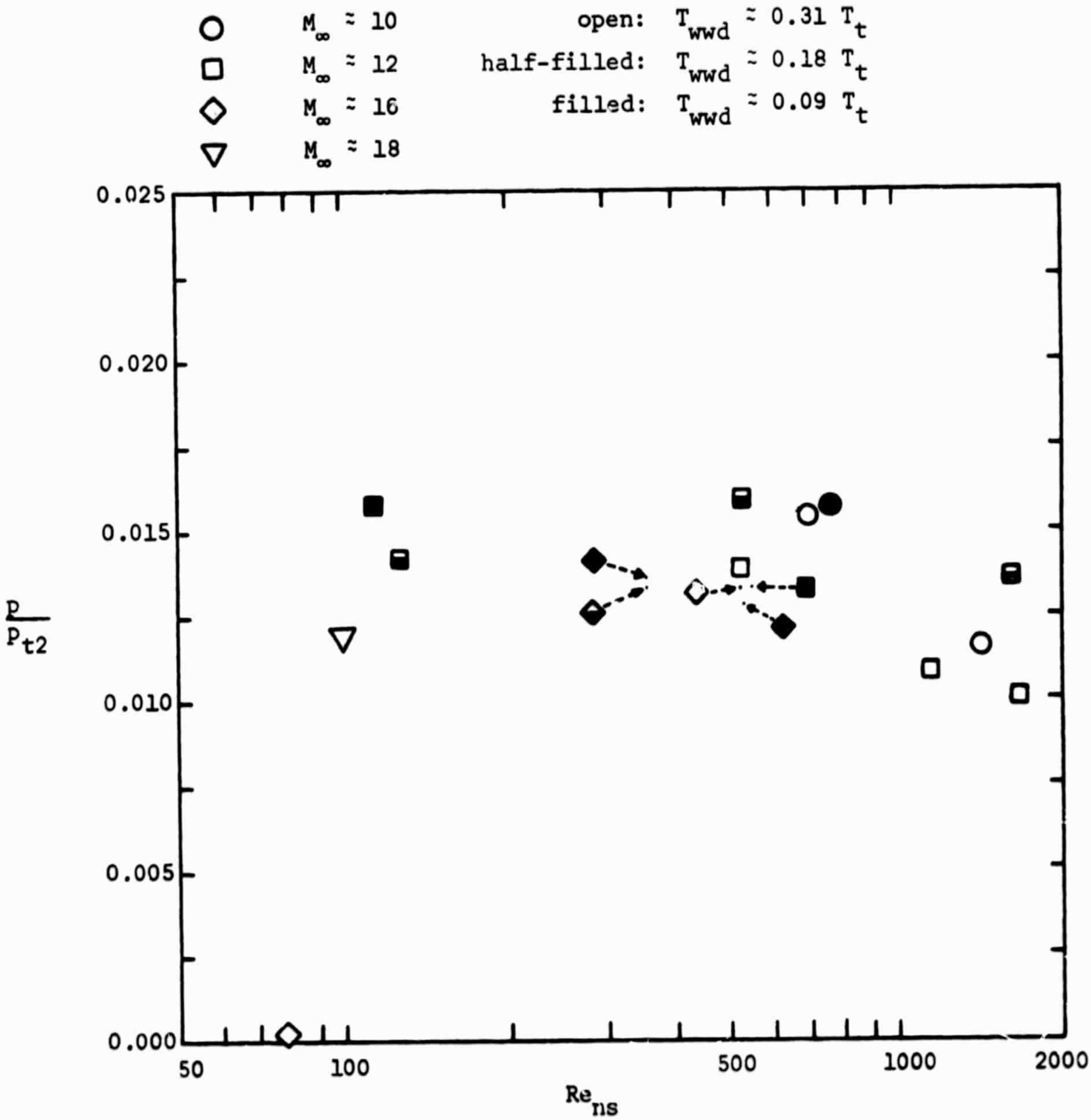

(b) The parameter p/p_{t2}

Figure 26. - Concluded.

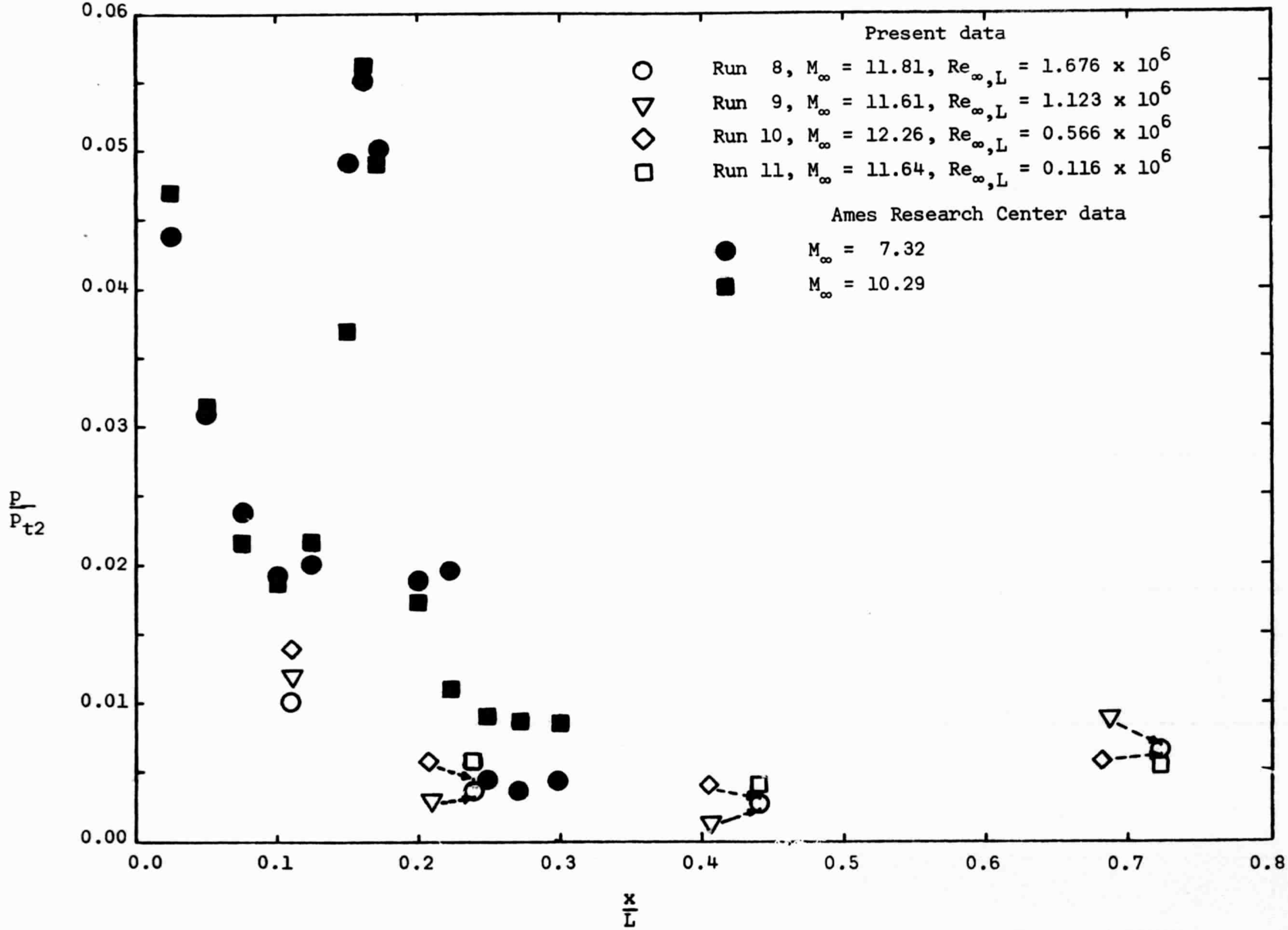

Figure 27. - Pressure distribution for the leeward plane-of-symmetry, α = 30°.

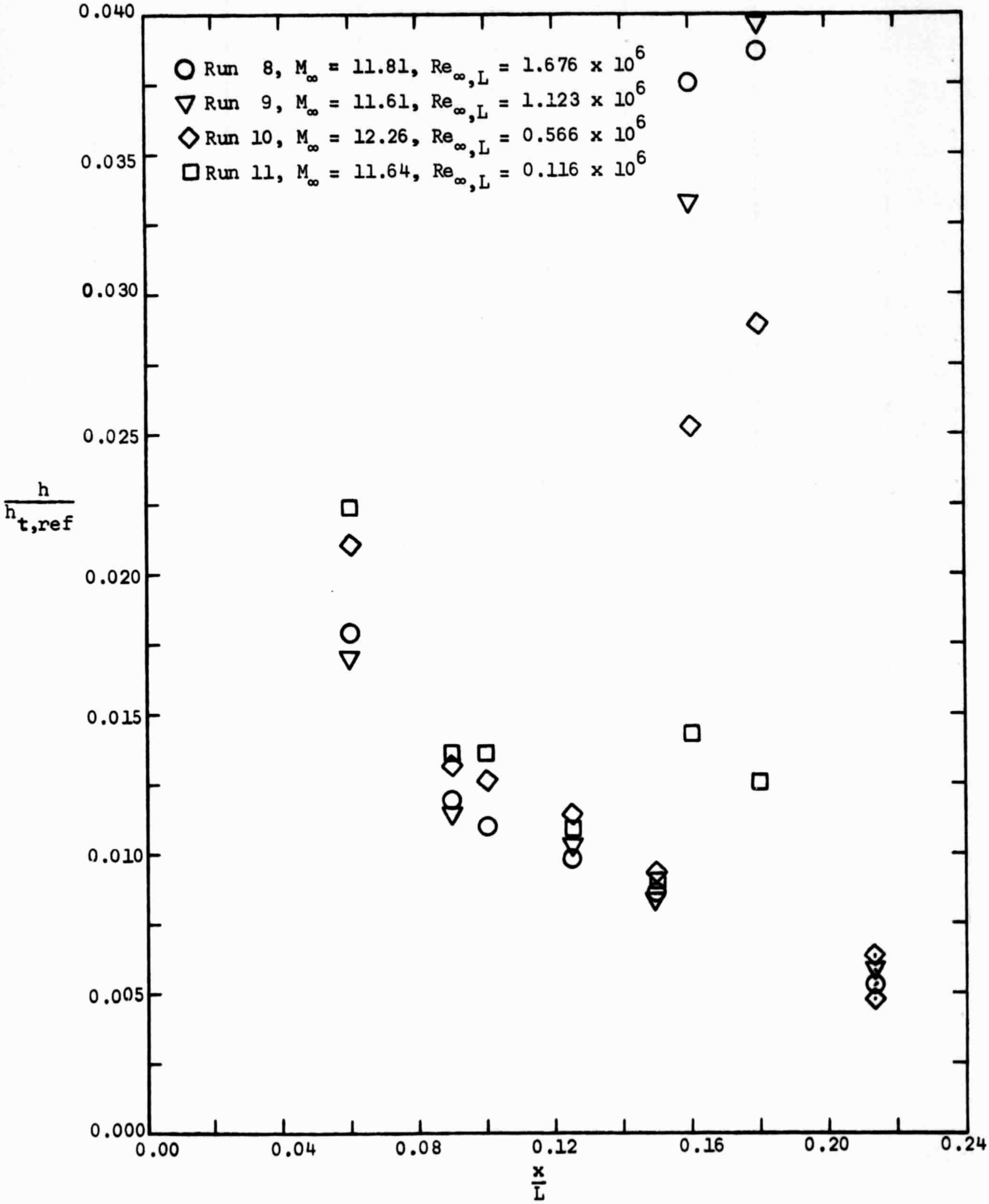

Figure 28. - The nose-region/cockpit heat-transfer distribution for the leeward plane-of-symmetry for $M_\infty \approx 12$, $\alpha = 30°$.

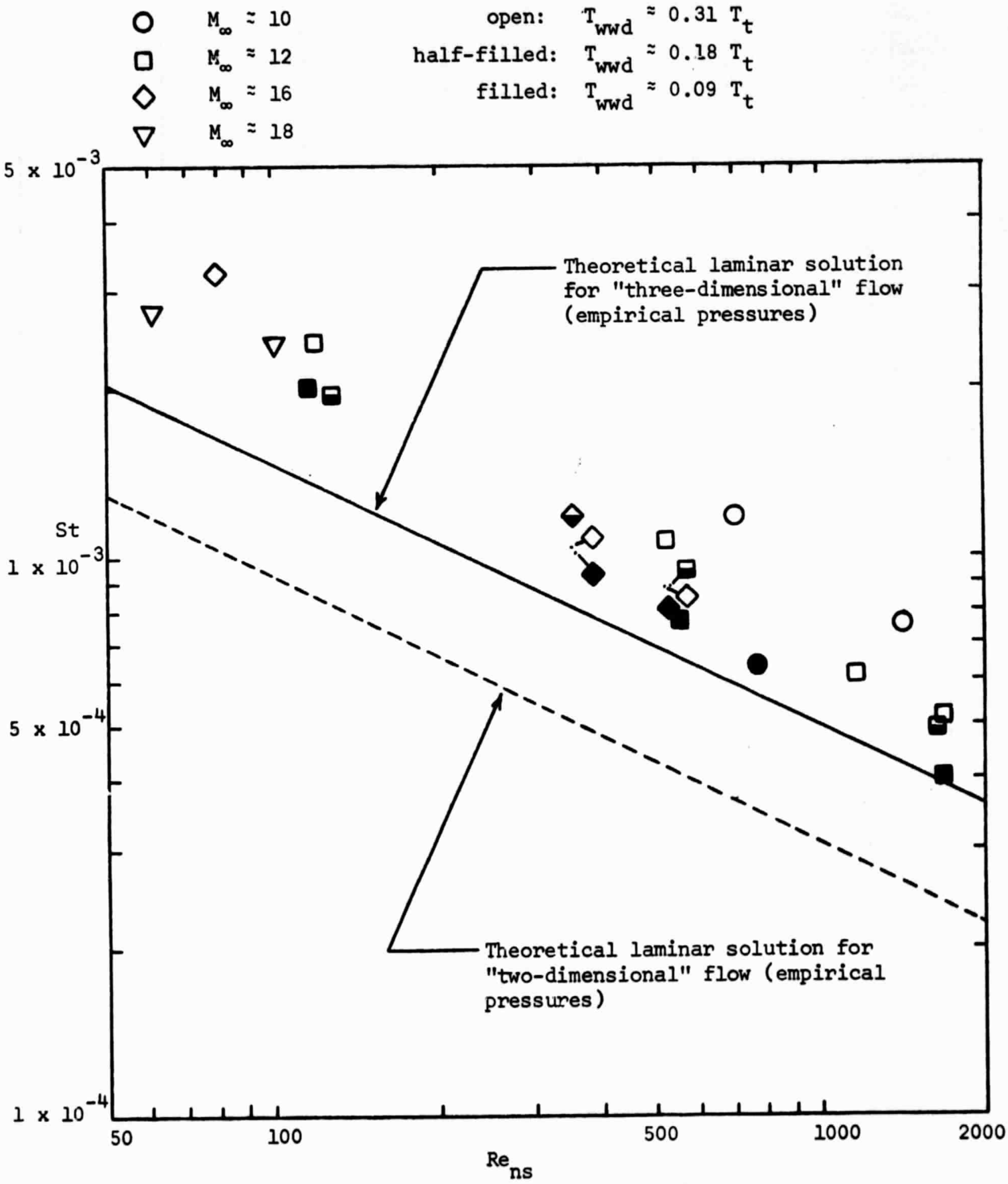

(a) Gage T4, x = 0.100L, ϕ = 0°

Figure 29. - The Stanton number as a function of the Reynolds number behind a normal shock wave for gages on the nose-region (upstream of the cockpit), α = 30°.

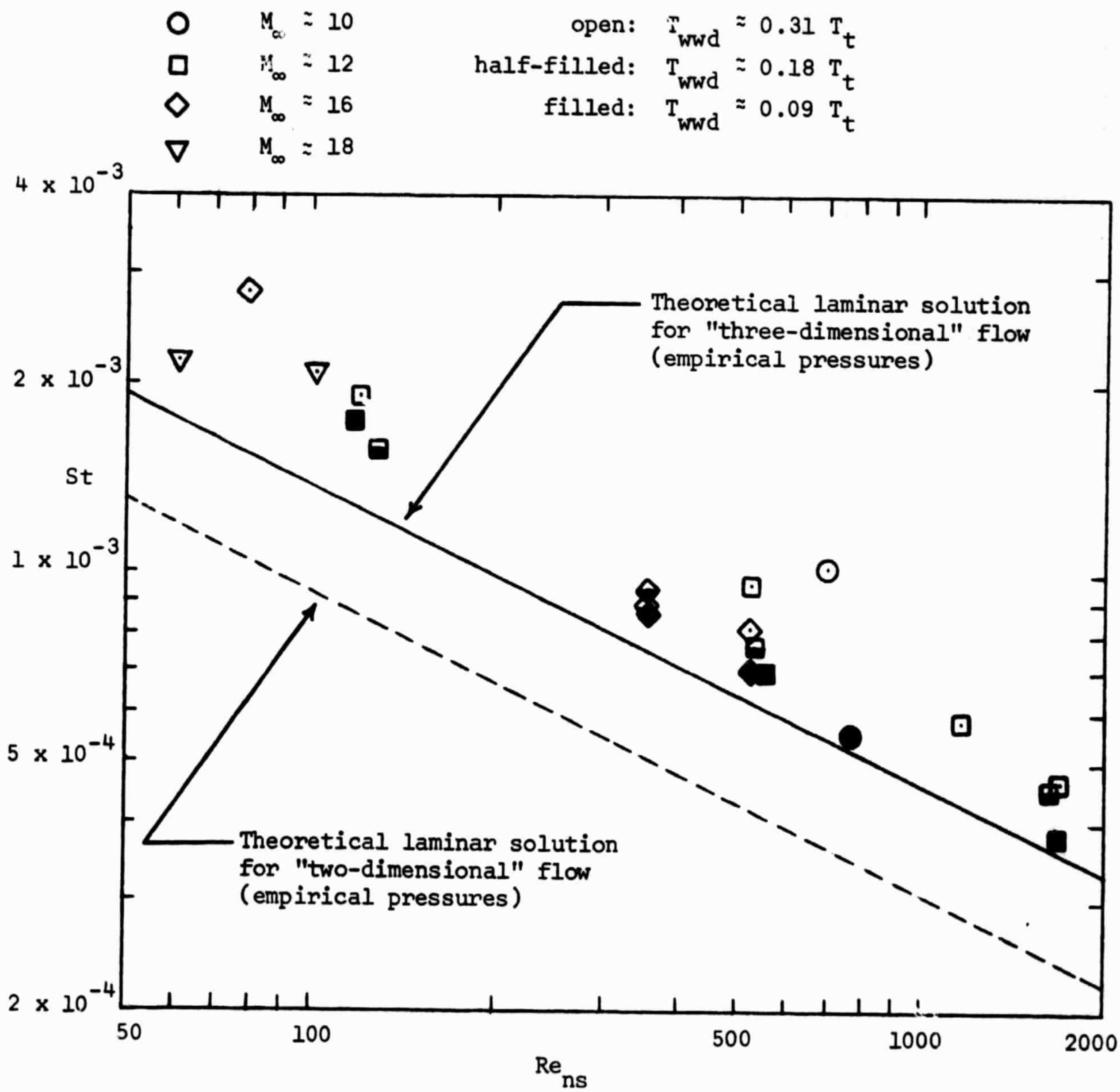

(b) Gage T8, x = 0.125L, ϕ = 0°.

Figure 29. - Concluded.

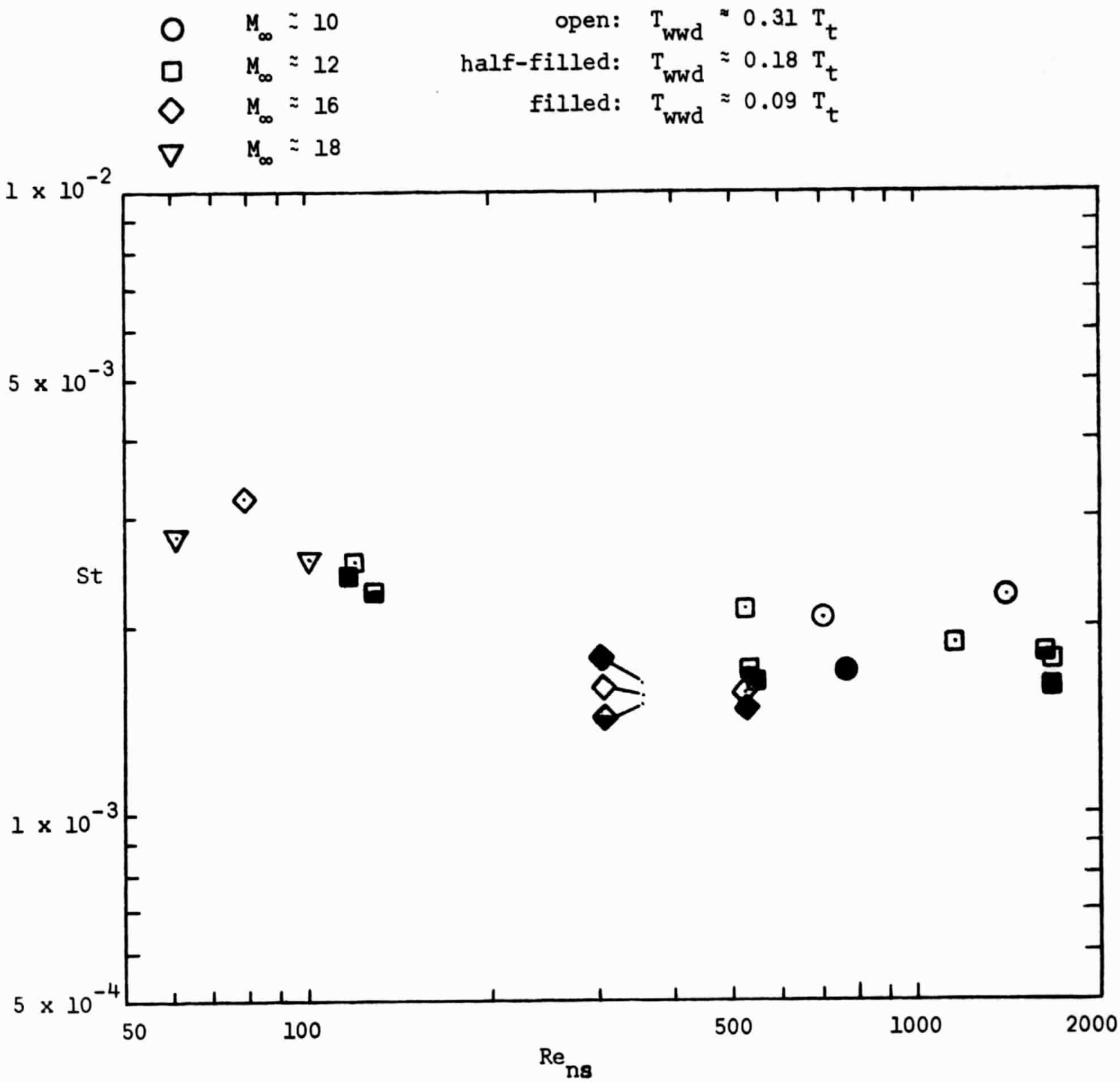

Gage T10, x = 0.160L, ϕ = 0°.

Figure 30. - The Stanton number as a function of the Reynolds number behind a normal shock wave for a gage on the cockpit windshield, α = 30°.

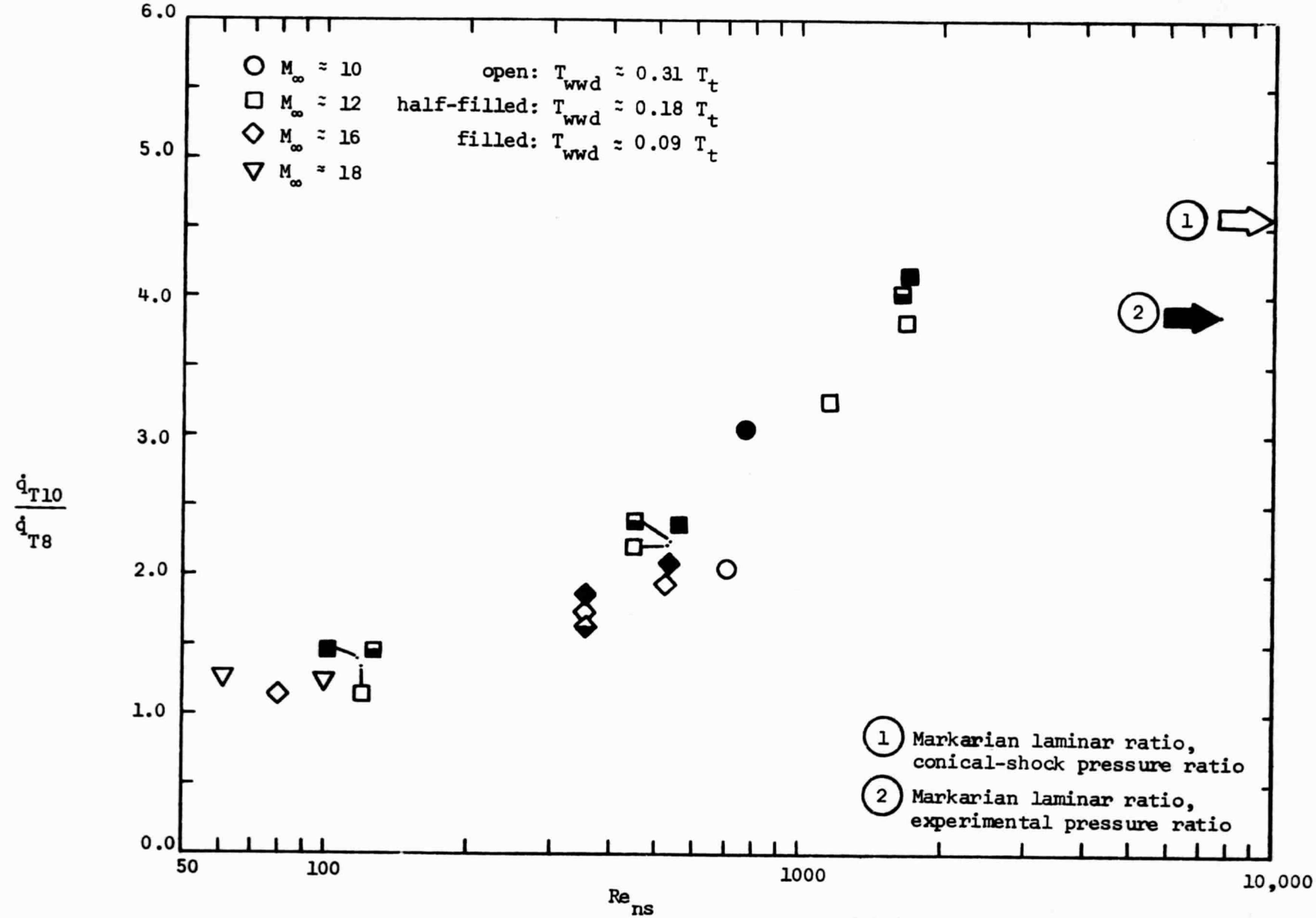

Figure 31. - The heat transfer to a gage on the cockpit windshield (T10) divided by that to a gage on the nose (T8) as a function of Re_{ns}, $\alpha = 30°$.

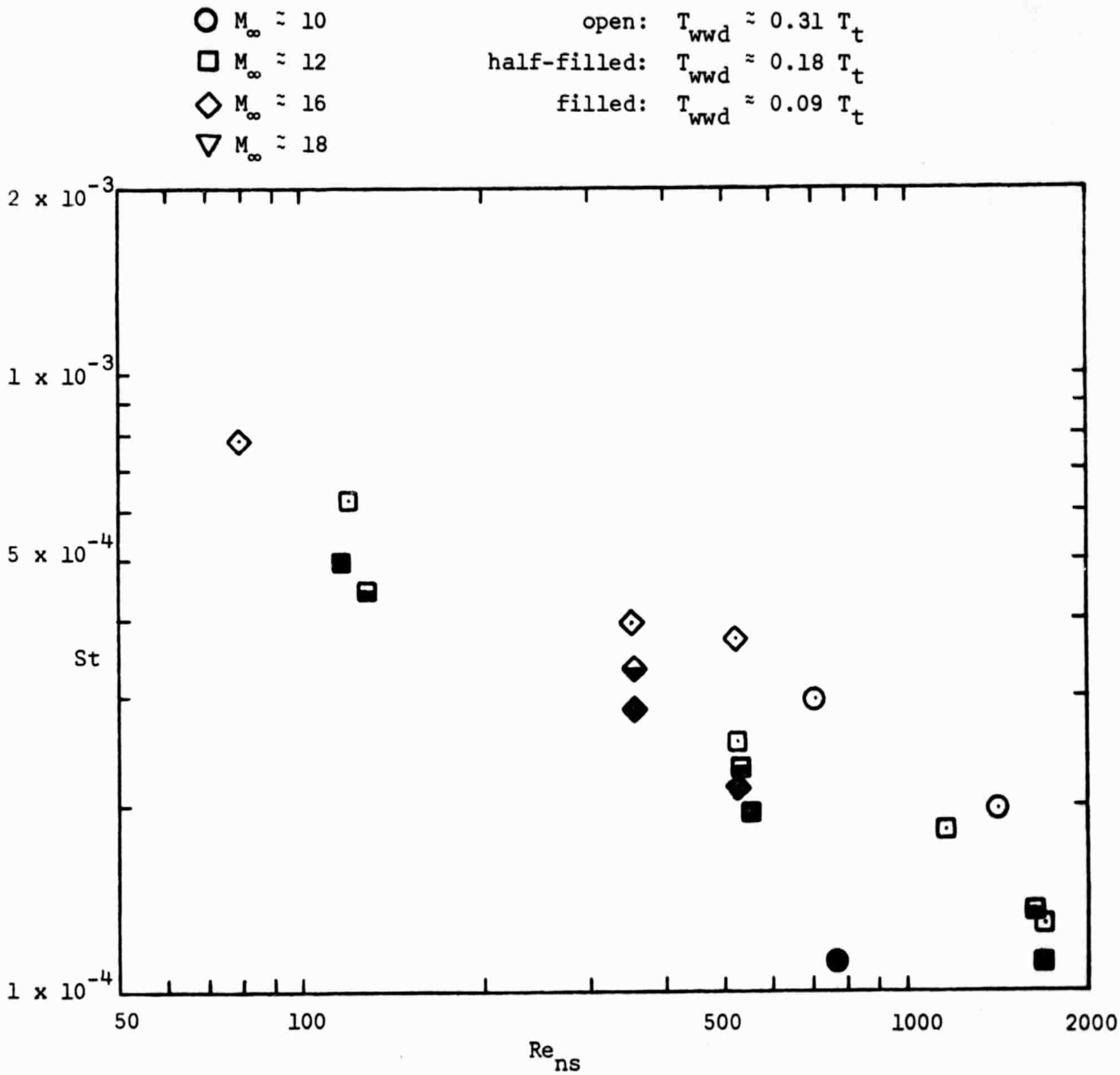

(a) Gage T19, $x = 0.279L$, $\phi = 0°$

Figure 32. - The Stanton number as a function of the Reynolds number behind a normal shock wave for gages aft of the cockpit where the shear layer was laminar, $\alpha = 30°$.

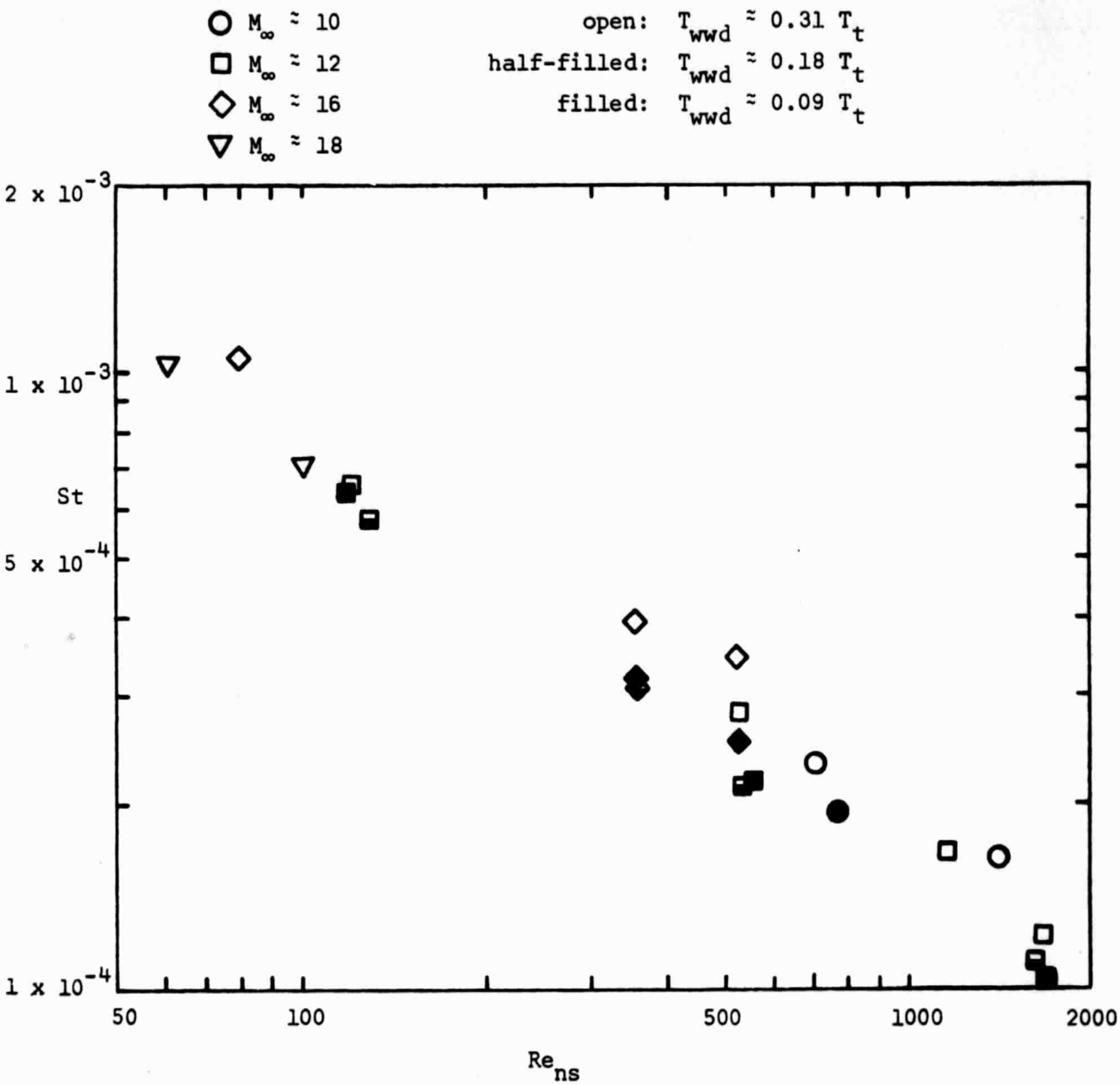

(b) Gage T21, x = 0.279L, ϕ = 44°.

Figure 32. - Concluded.

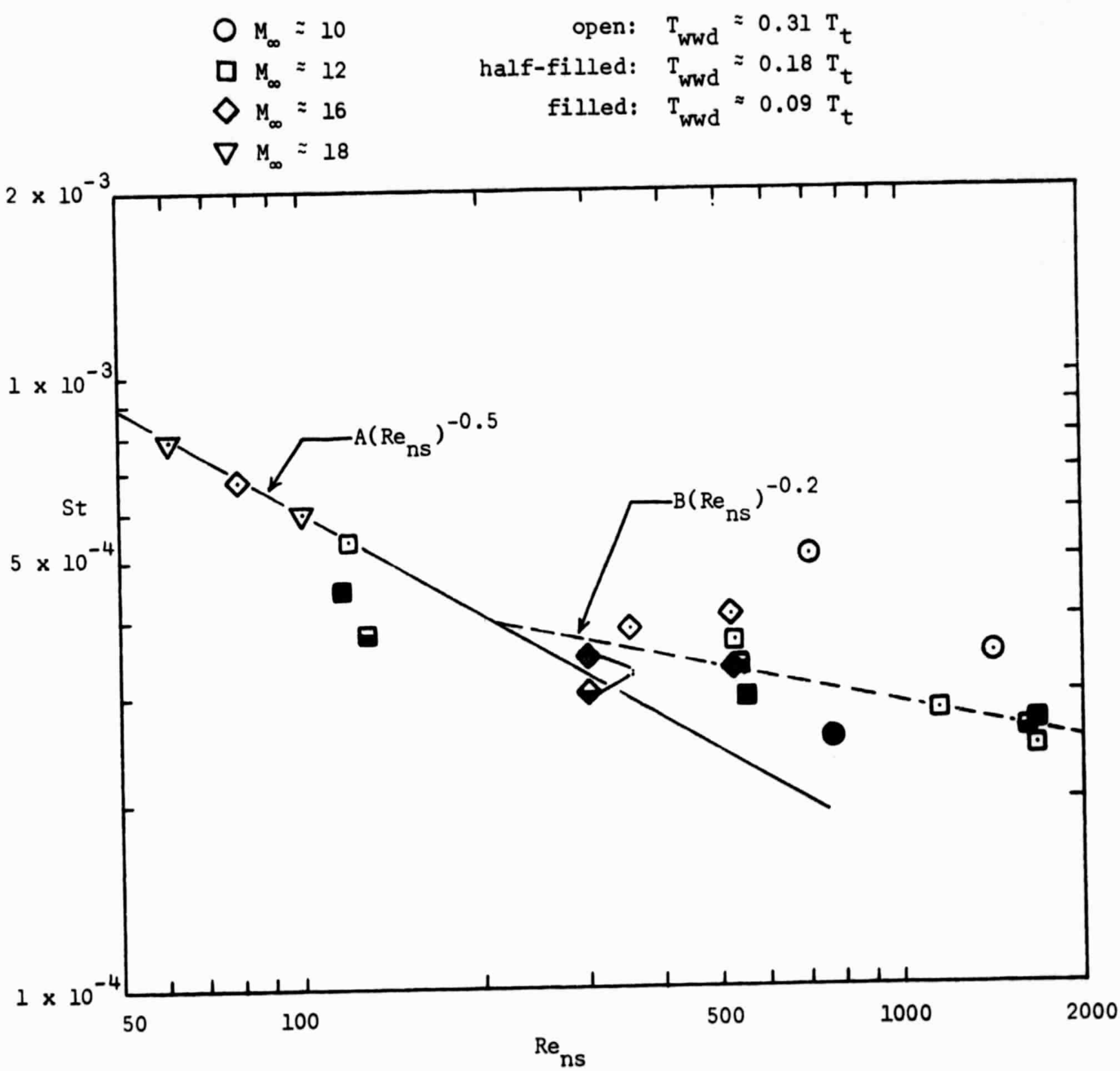

(a) Gage T29, x = 0.420L, $\phi = 0°$

Figure 33. - The Stanton number as a function of the Reynolds number behind a normal shock wave for gages aft of the cockpit where the shear layer was transitional, $\alpha = 30°$.

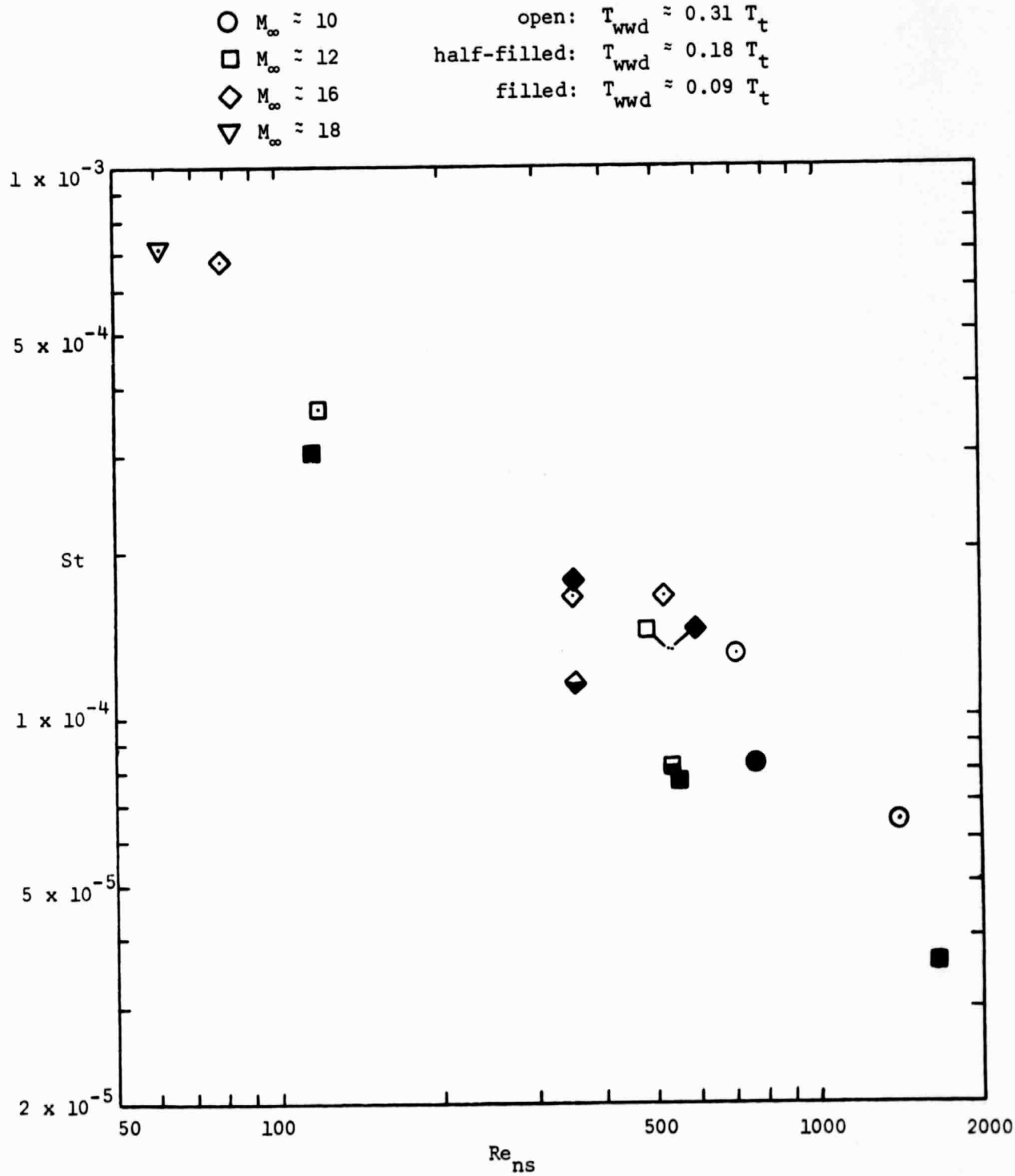

(b) Gage T31, x = 0.420L, ϕ = 40°

Figure 33. - Concluded.

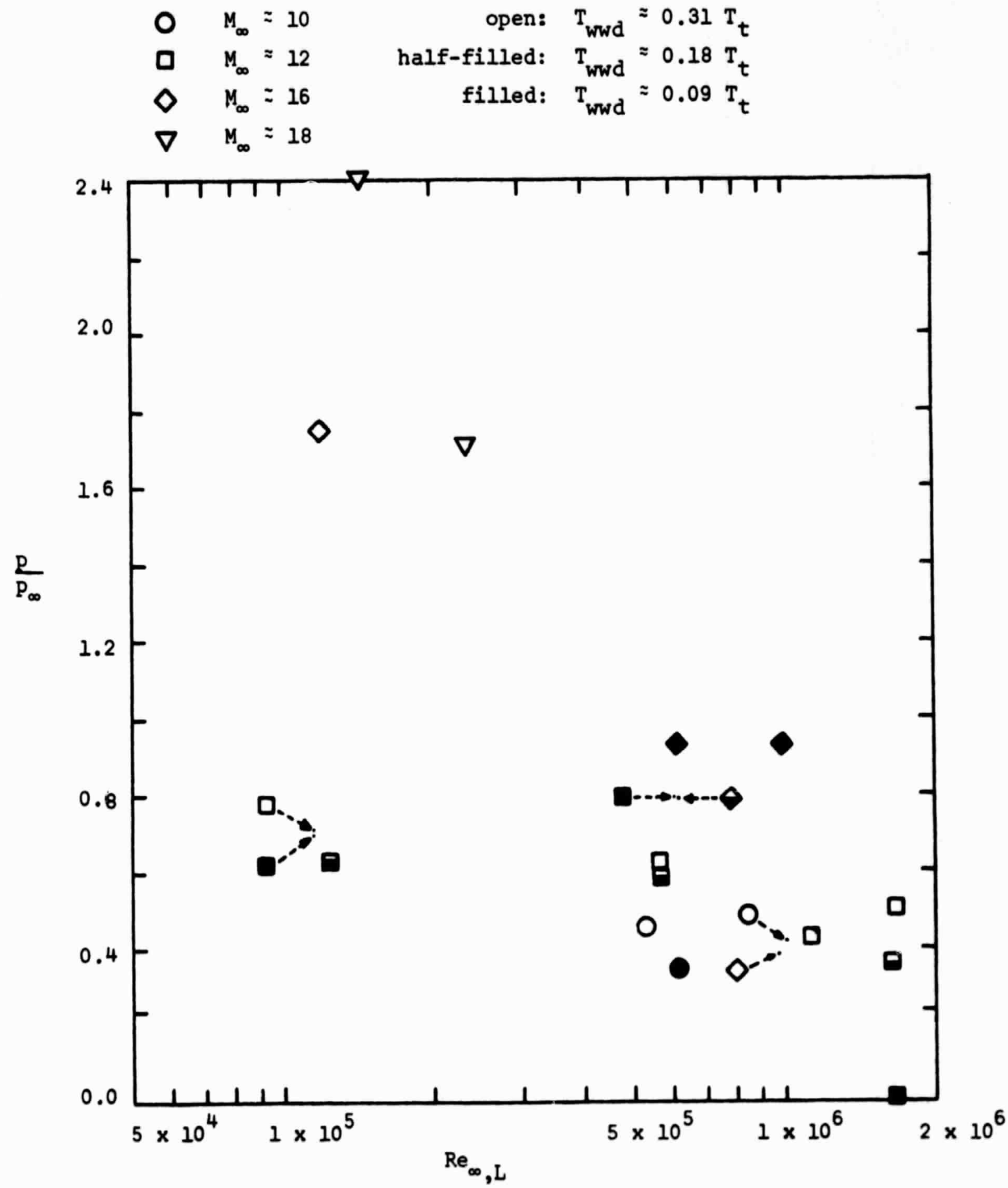

(a) p/p_∞ as a function of $Re_{\infty,L}$

Figure 34. - The pressure measurements as a function of Reynolds number for PS4, $x = 0.440L$, $\phi = 0°$, $\alpha = 30°$.

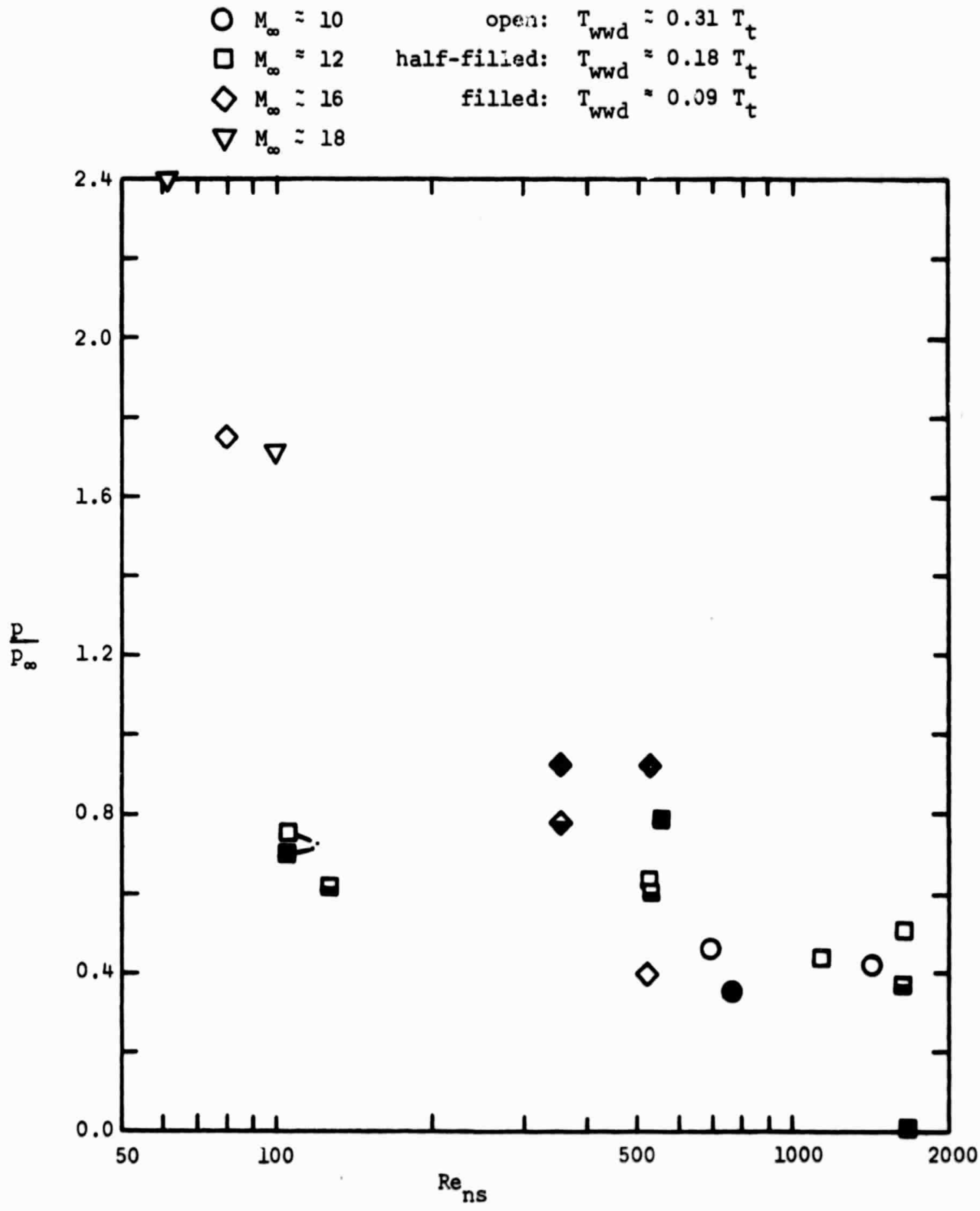

(b) p/p_∞ as a function of Re_{ns}

Figure 34. - Continued

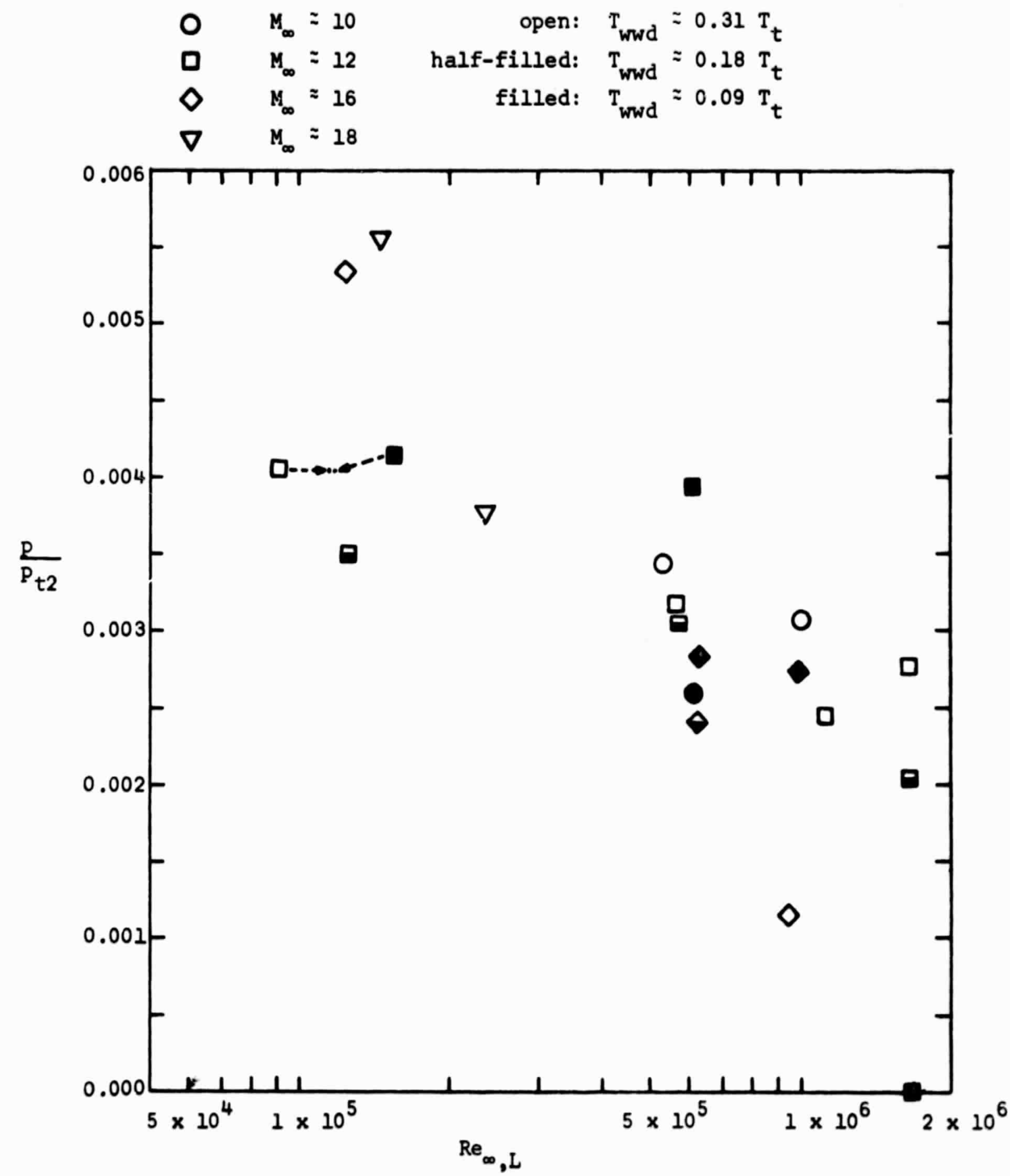

(c) p/p_{t2} as a function of $Re_{\infty,L}$

Figure 34. - Continued.

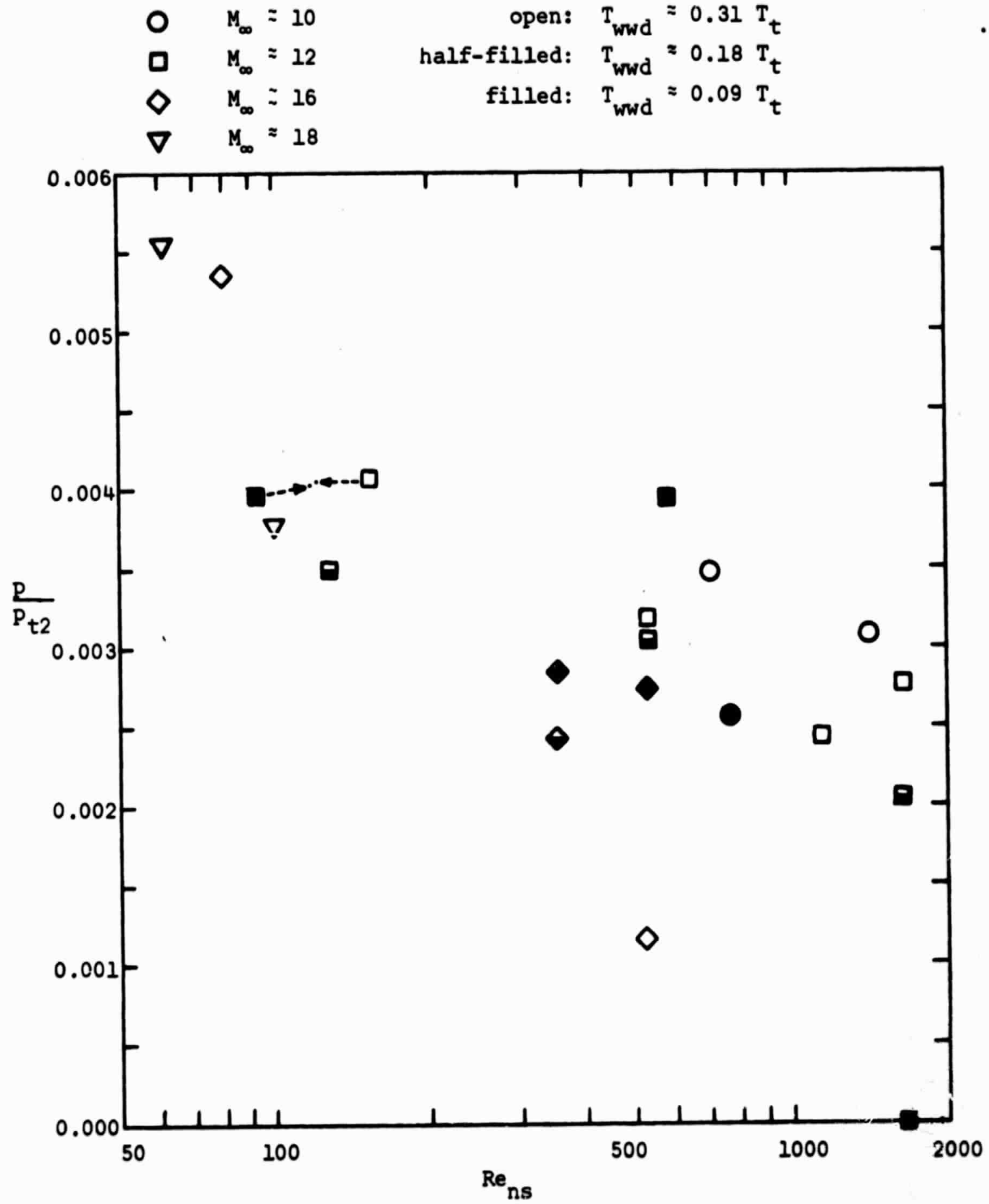

(d) p/p_{t2} as a function of Re_{ns}

Figure 34. - Concluded.

Region 1: The decrease in mixing rate dominates the laminar shear layer flow.

Region 2: As the Reynolds number is increased, transition moves upstream from the throat. The increased mixing rate causes the base pressure to decrease.

Region 3: Transition of the vehicle's boundary layer occurs, thickening the boundary layer and increasing the base pressure.

Region 4: The base pressure decreases as the boundary layer thickness decreases.

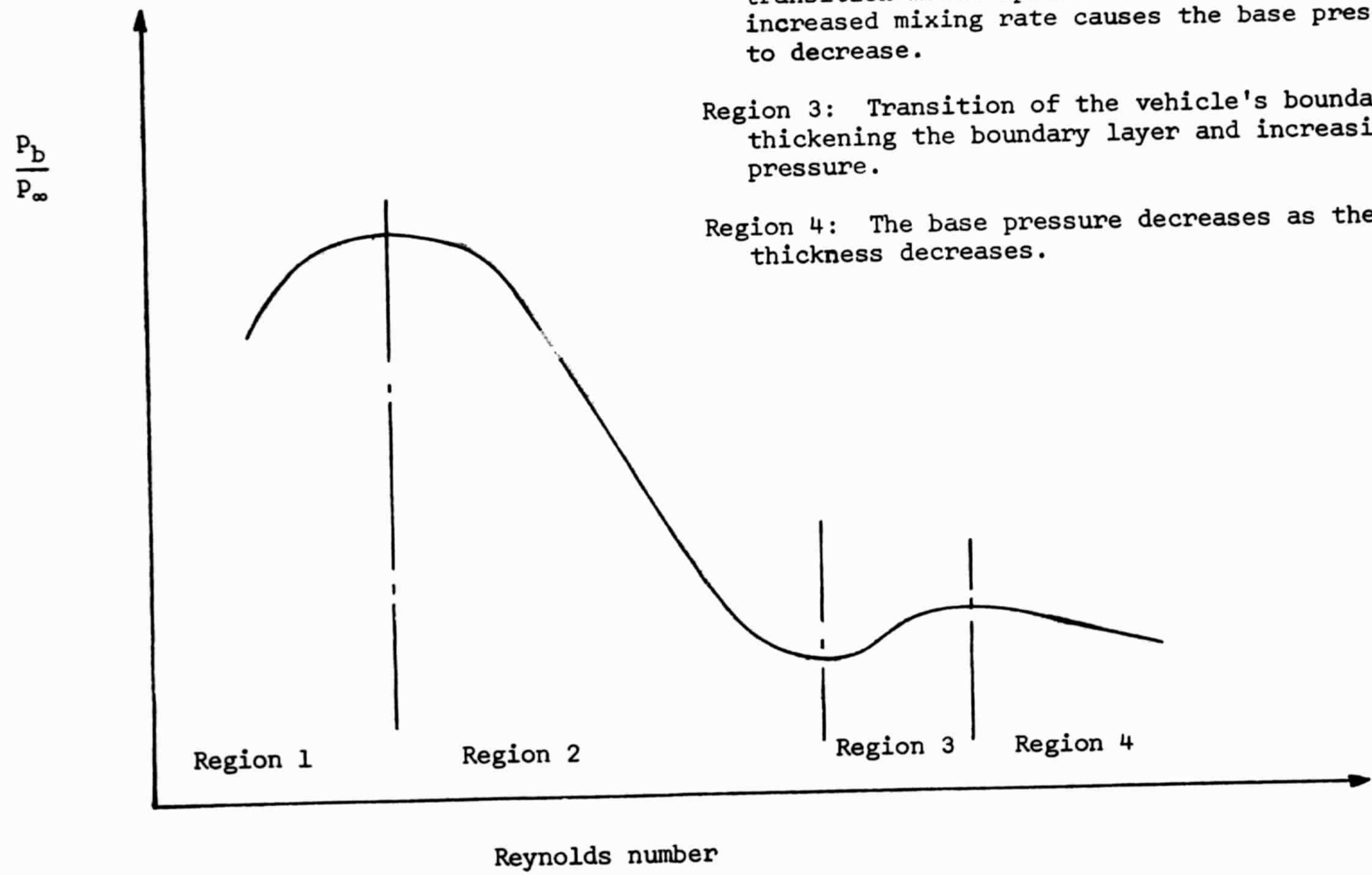

Figure 35. - The effect of Reynolds number on the base pressure.

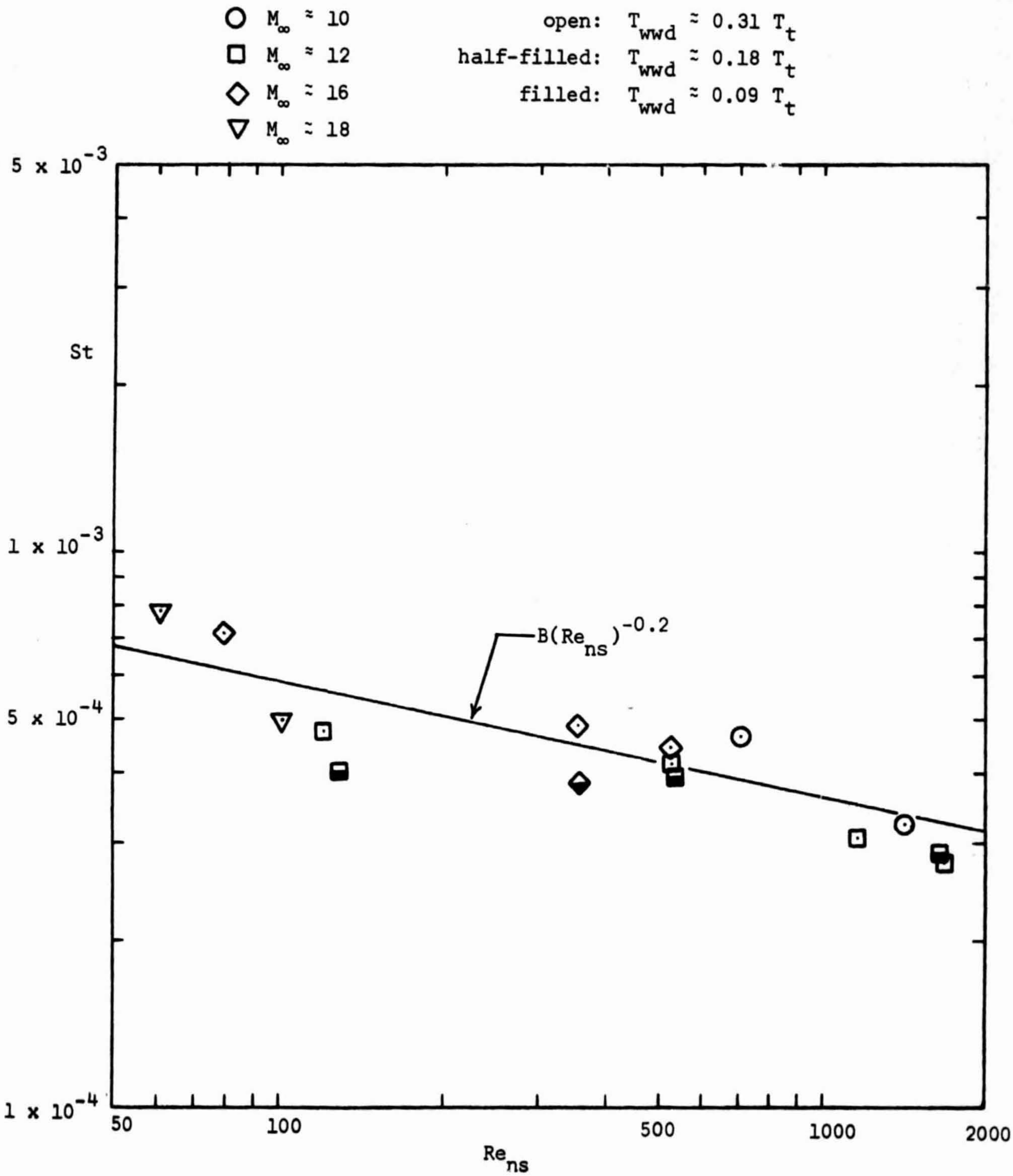

(a) Gage T37, x = 0.600L, ϕ = 0°

Figure 36. - The Stanton number as a function of the Reynolds number behind a normal shock wave for gages aft of the cockpit where the shear layer was turbulent, α = 30°.

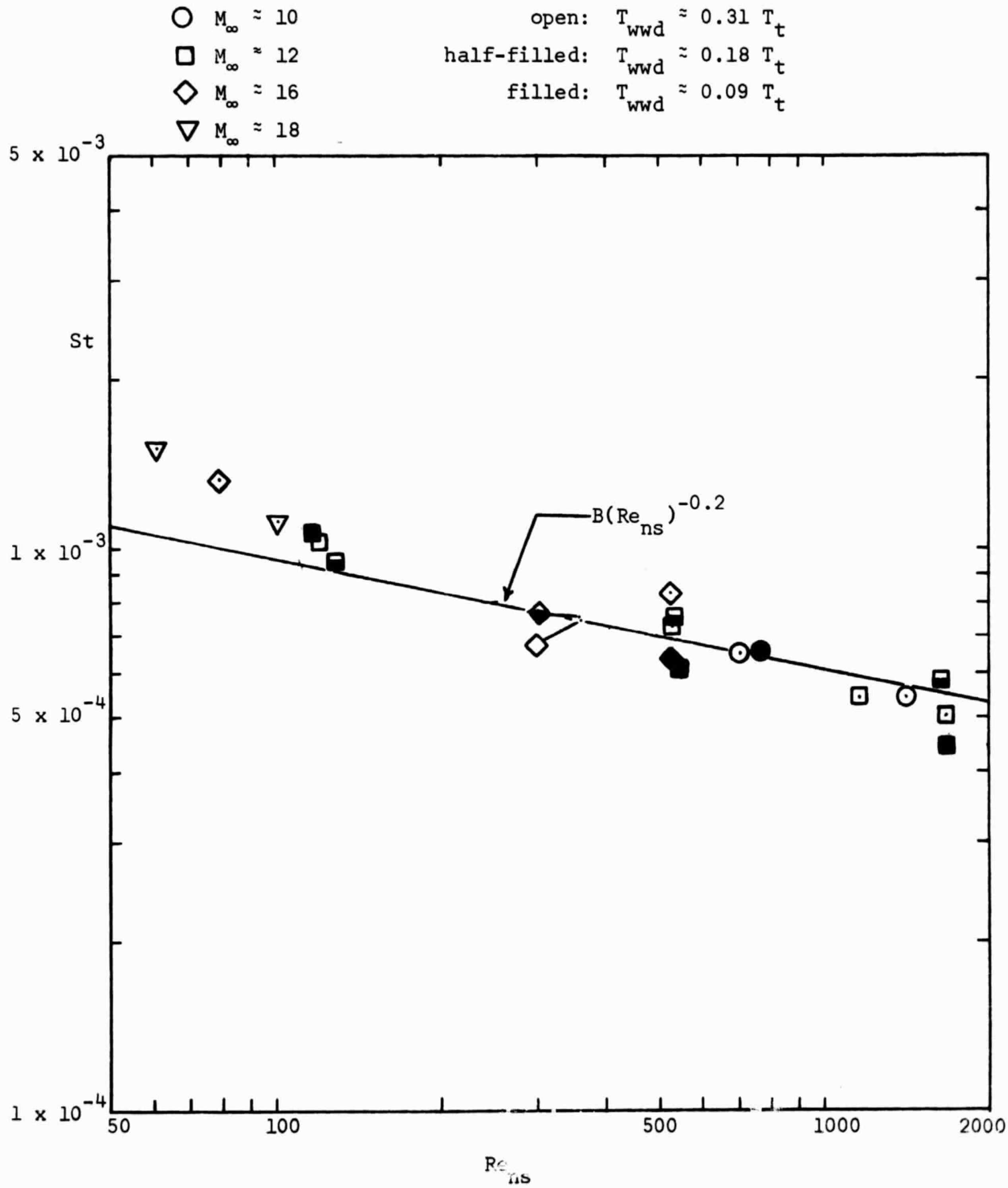

(b) Gage T39, x = 0.600L, ϕ = 56°

Figure 36. - Continued.

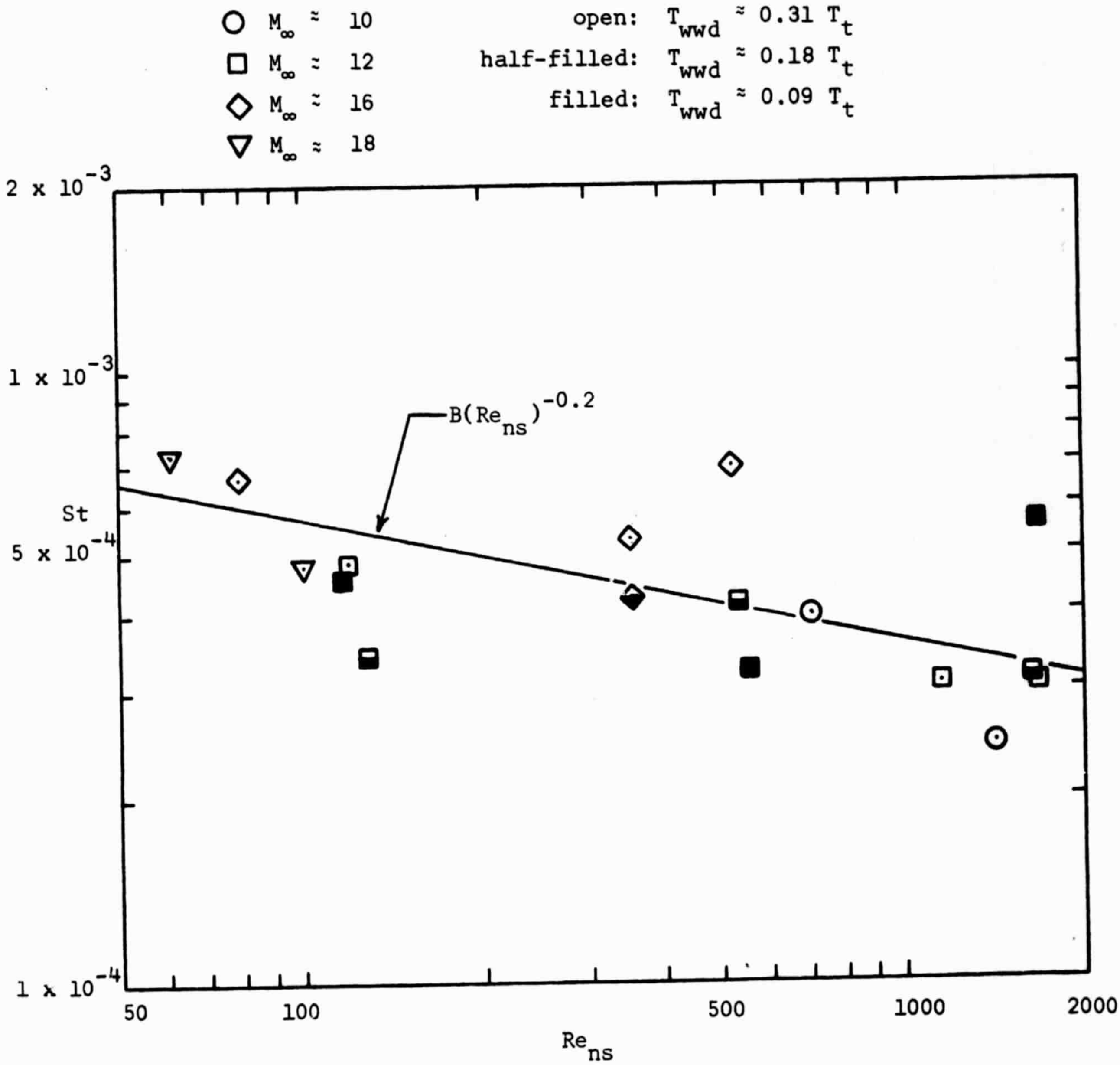

(c) Gage T41, x = 0.700L, $\phi = 0°$

Figure 36. - Concluded.

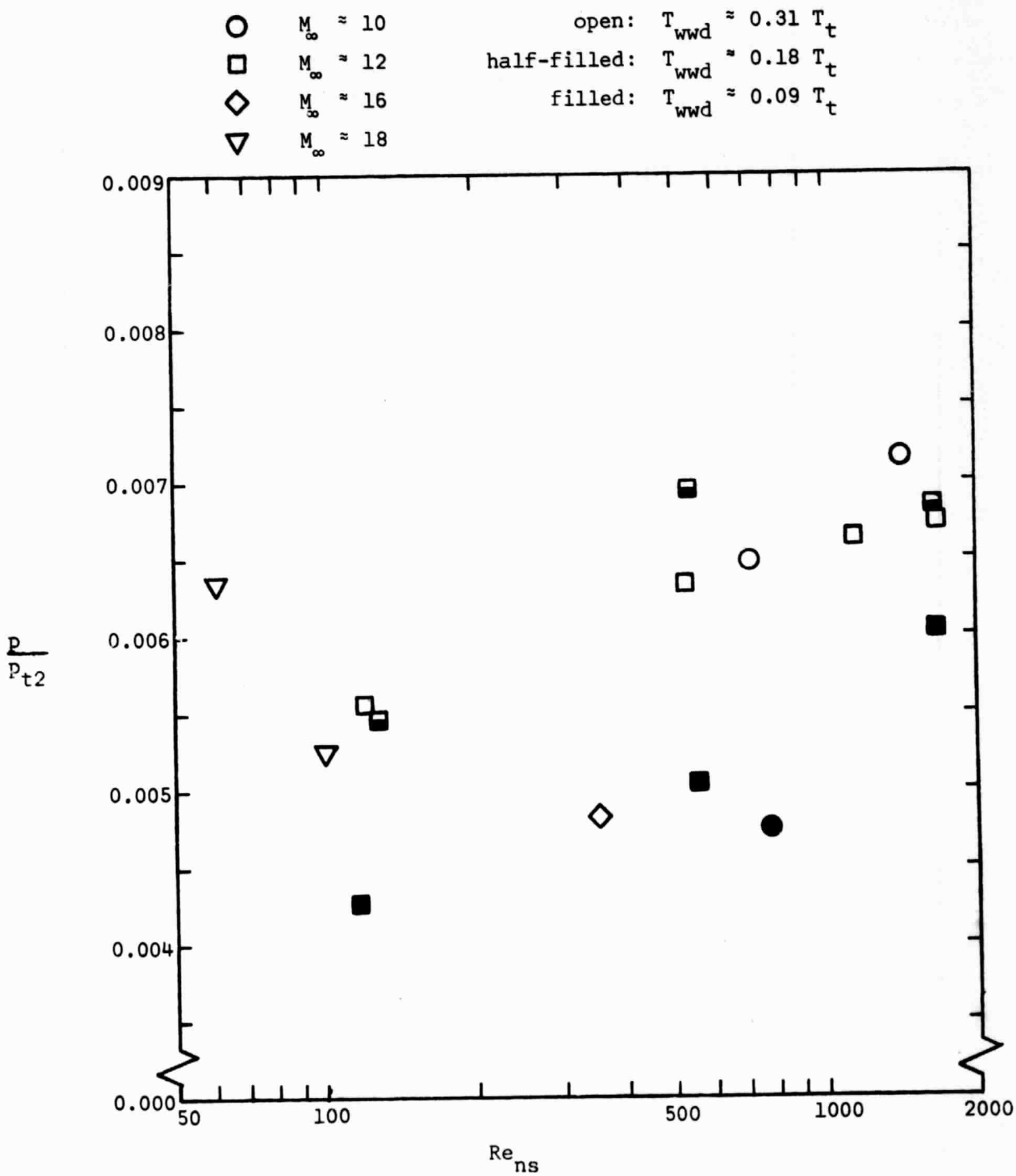

Figure 37. - The pressure measurements as a function of Reynolds number for PS5 ($x = 0.722L$, $\phi = 0°$), $\alpha = 30°$.

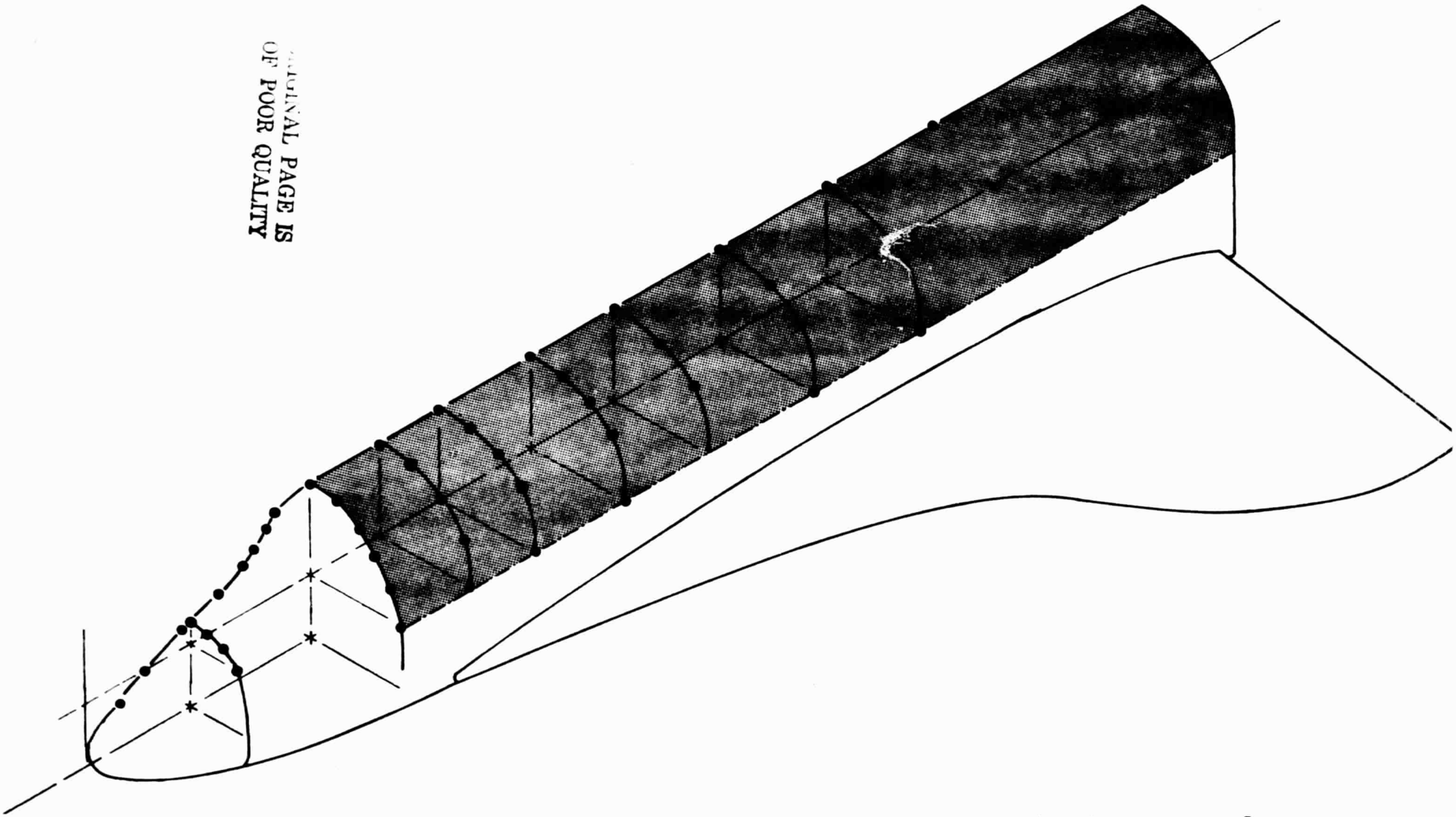

Figure 38.- Isometric sketch of orbiter showing leeward surface area over which the heat-transfer measurements were averaged to obtain $\overline{St}_{sig}$.

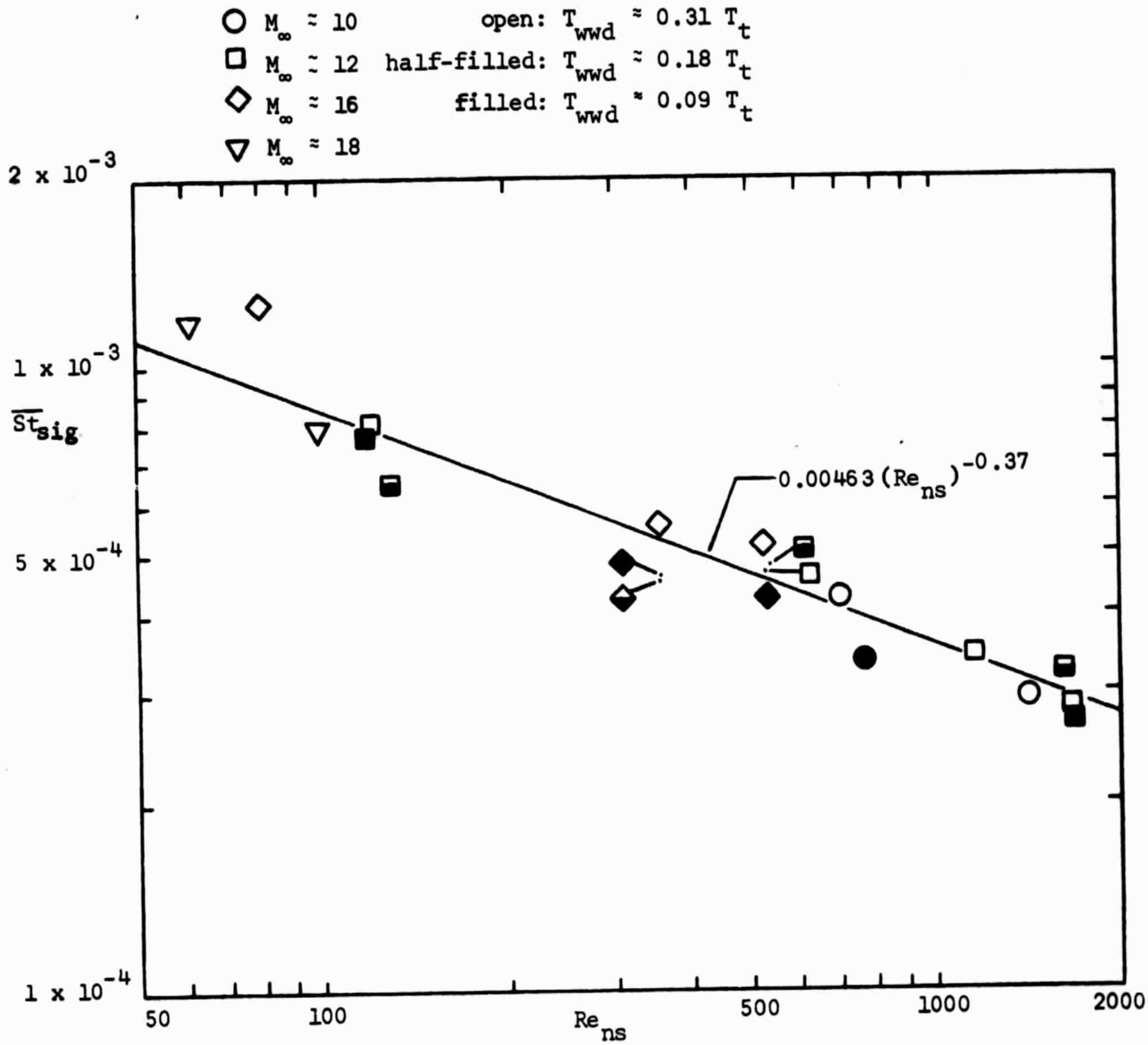

Figure 39. - The Stanton number averaged over all the leeward gages downstream of cockpit as a function of Re_{ns}, $\alpha = 30°$.

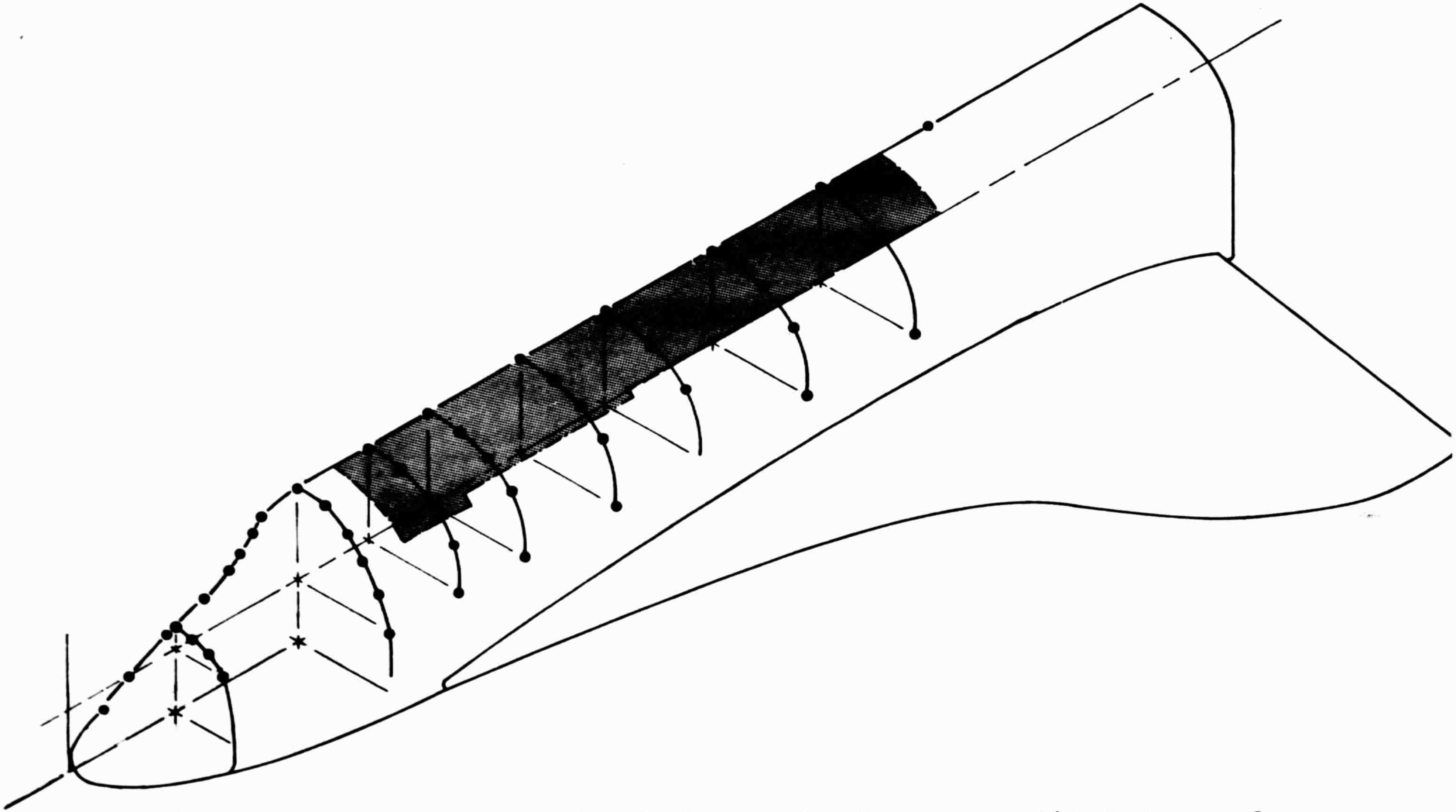

Figure 40 - Isometric sketch of orbiter showing leeward surface area over which the heat-tranfer measurement were averaged to obtain $\overline{St}_{sep}$.

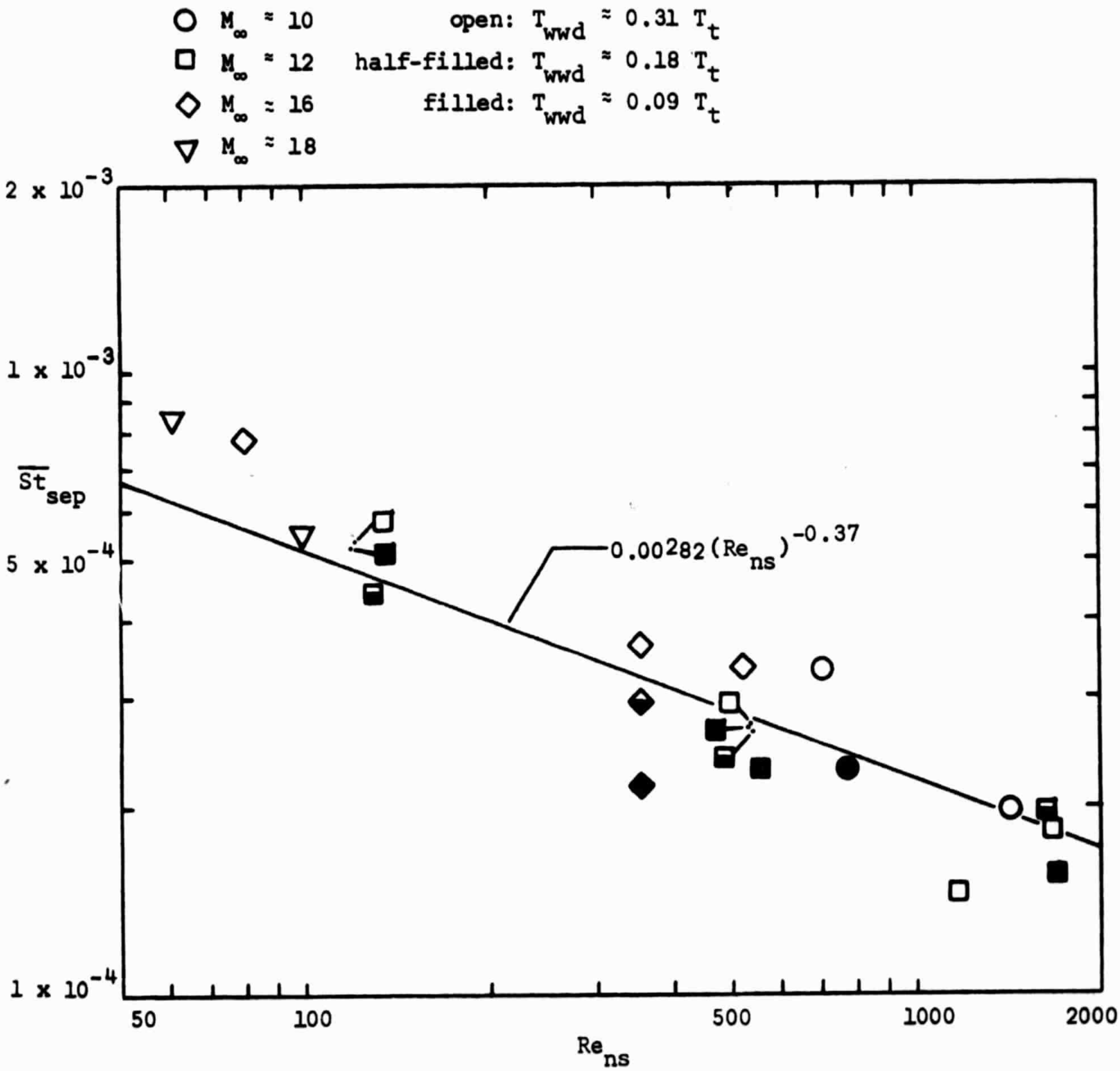

Figure 41 - The Stanton number averaged over those gages in the leeward "separated" region as a function of Re_{ns}, $\alpha = 30°$.

. PAGE IS
.OR QUALITY

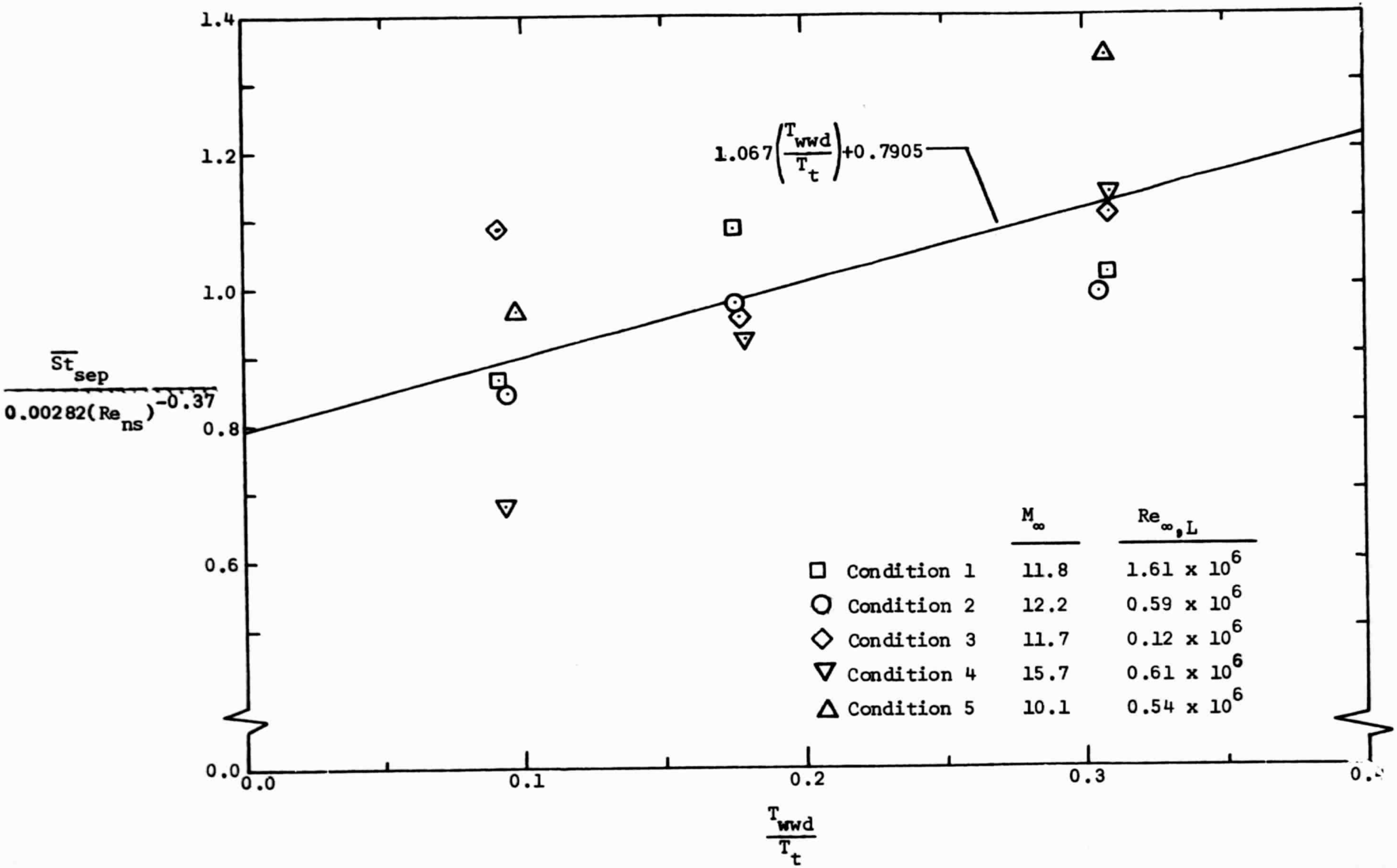

Figure 42. - The effect of the windward surface-temperature on the average heating in the leeward "separated" region.

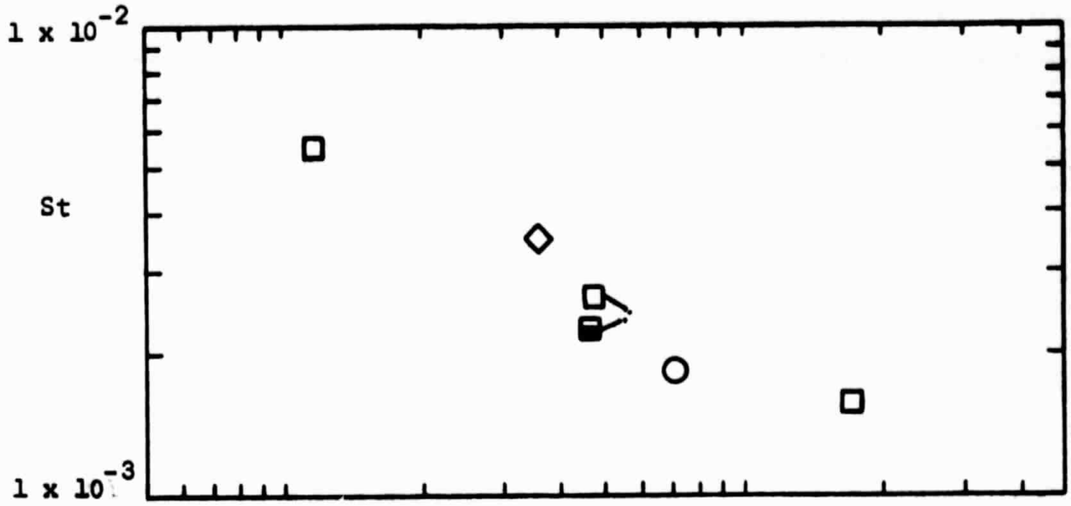

(a) Gage T18, x = 0.213L, ϕ = 90°

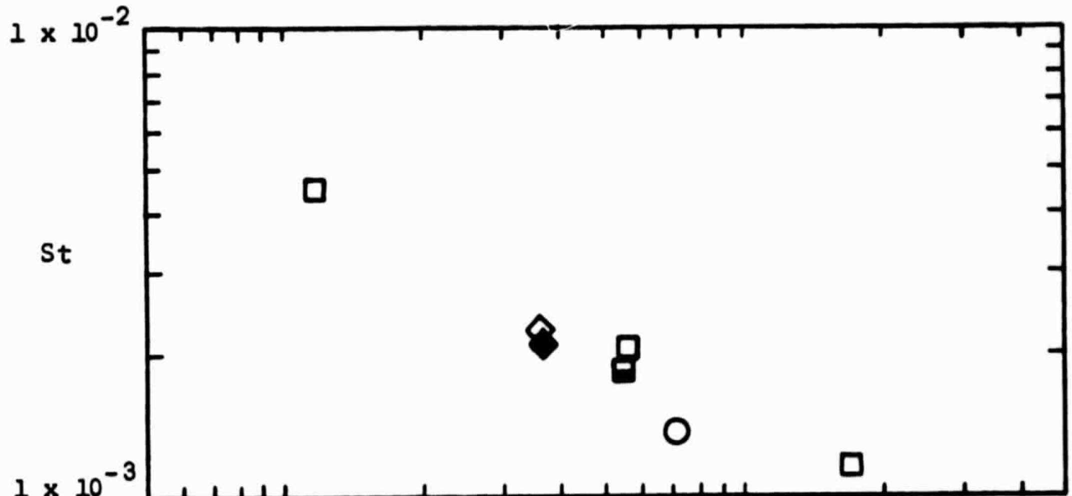

(b) Gage T23, x = 0.279L, ϕ = 90°

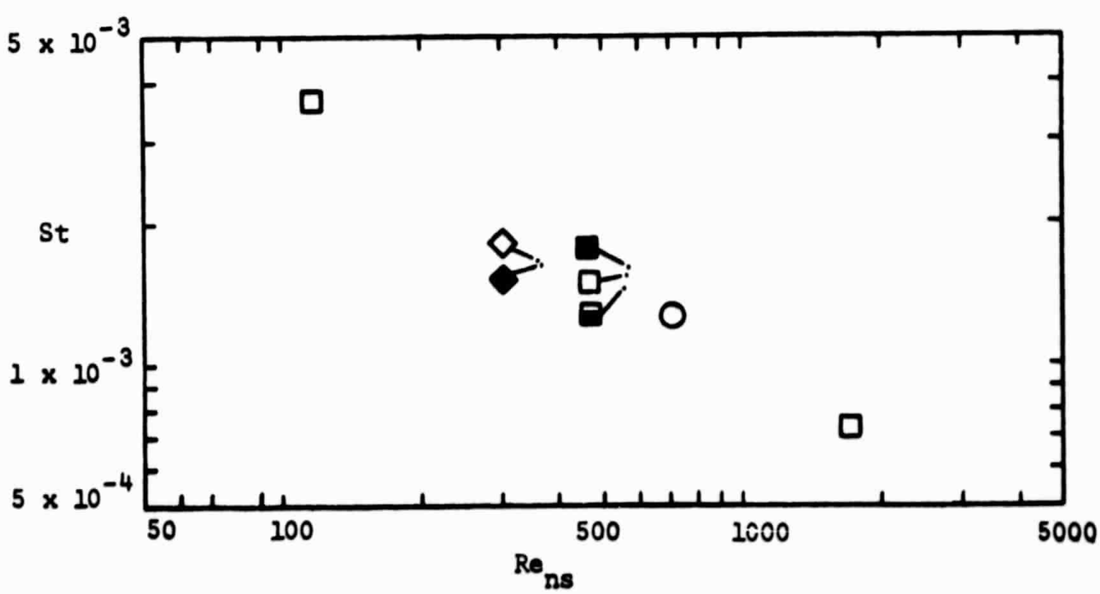

(c) Gage T33, x = 0.420L, ϕ = 90°

Figure 43. - The Stanton number as a function of Re_{ns} for gages on the lateral surface of the fuselage, α = 40°.

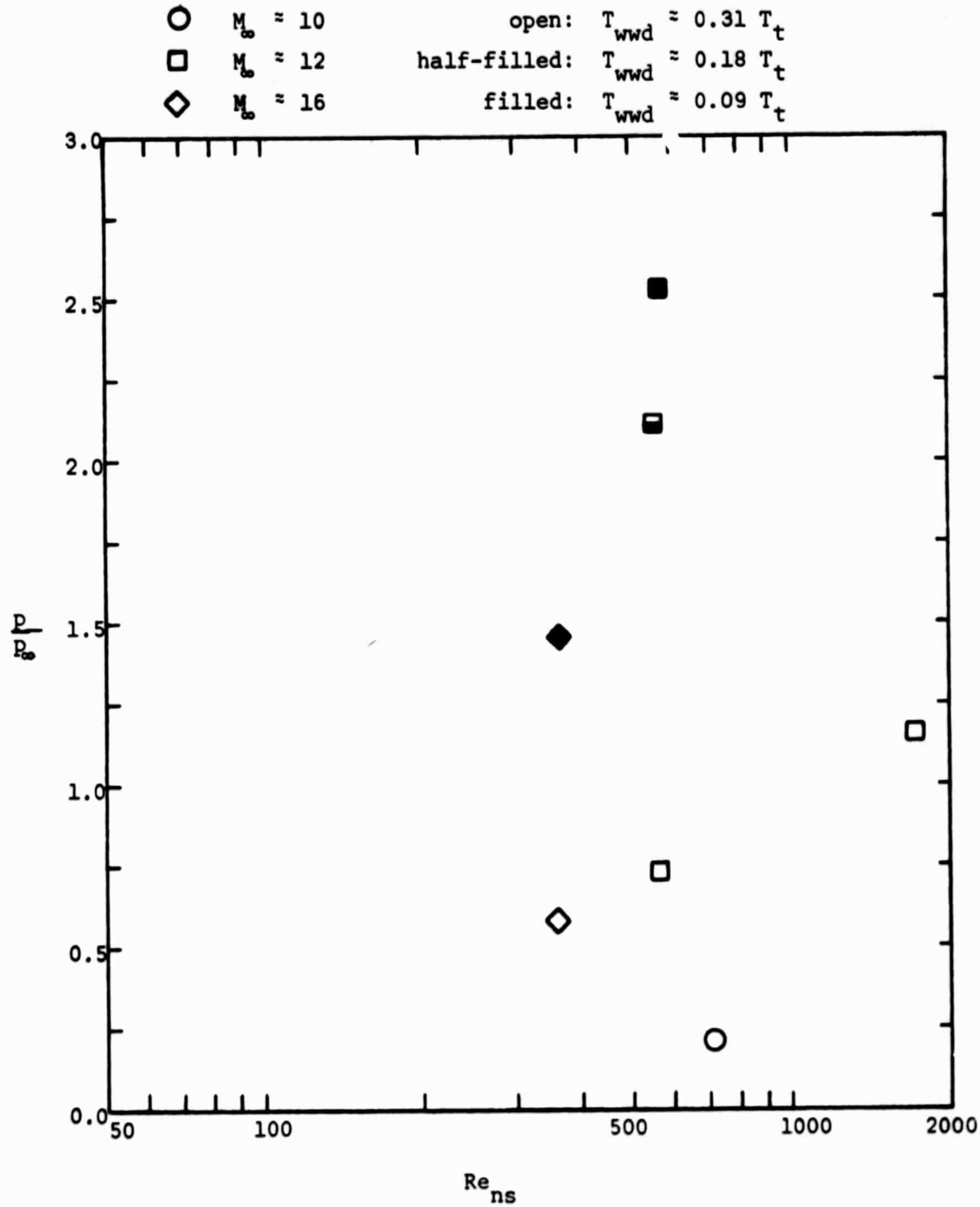

(a) The parameter p/p_∞

Figure 44. - The pressure measurements as a function of Reynolds number for an orifice on the nose upstream of the cockpit (PS2, x = 0.110L, ϕ = 0°), α = 40°.

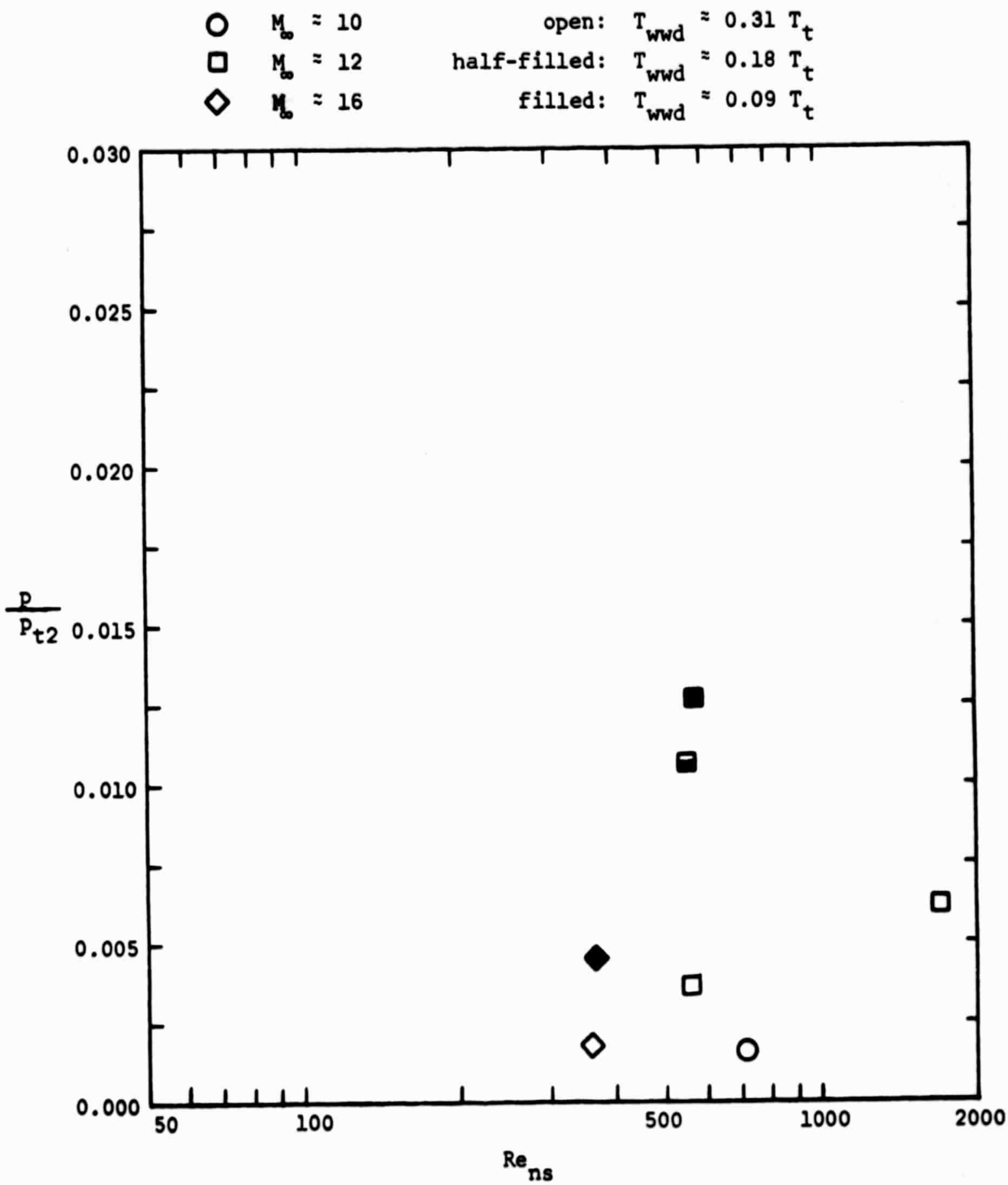

(b) The parameter p/p_{t2}

Figure 44. - Concluded.

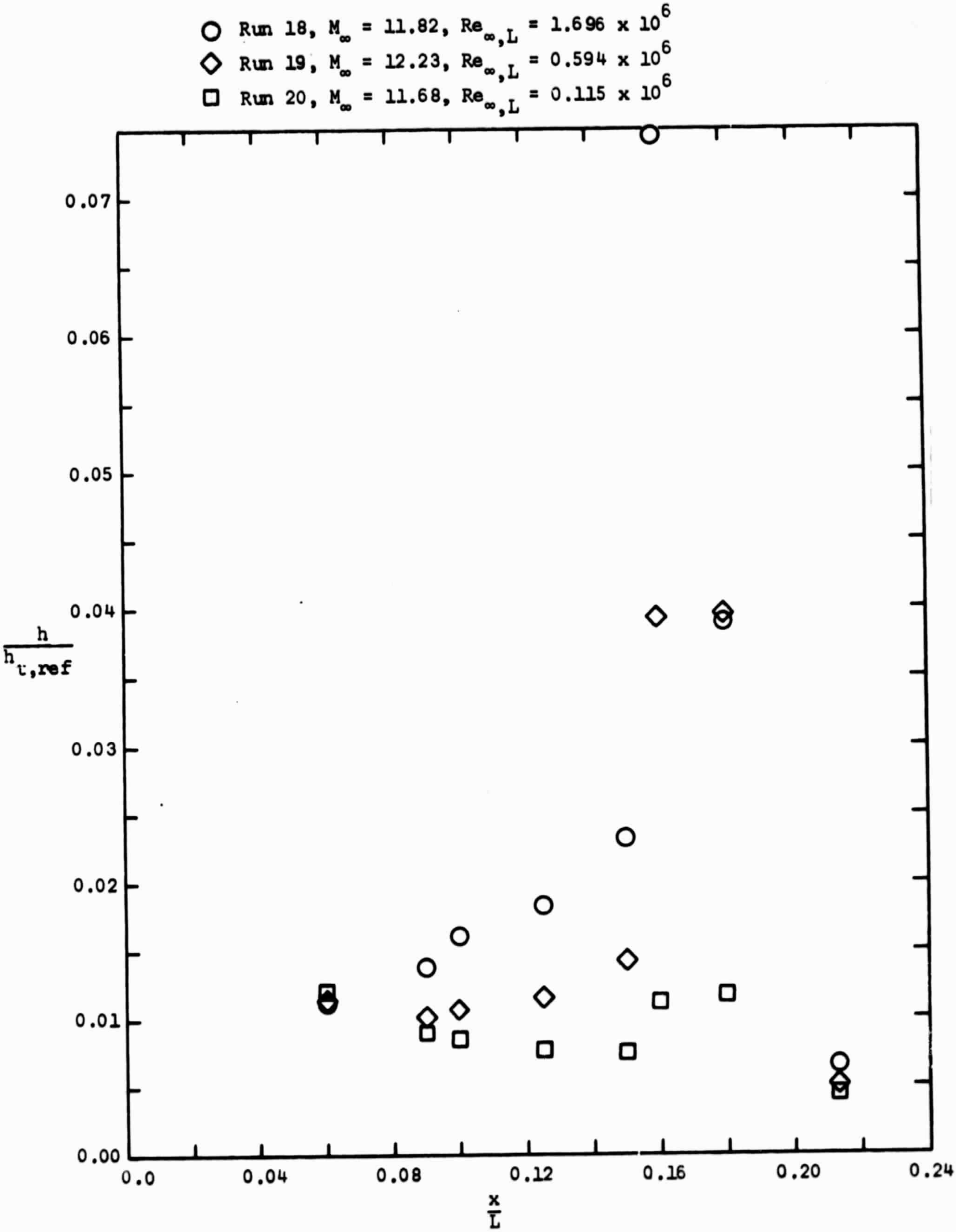

Figure 45. - The nose-region/cockpit windshield heat-transfer distribution for the leeward plane of symmetry $M_\infty \simeq 12$, $\alpha = 40°$.

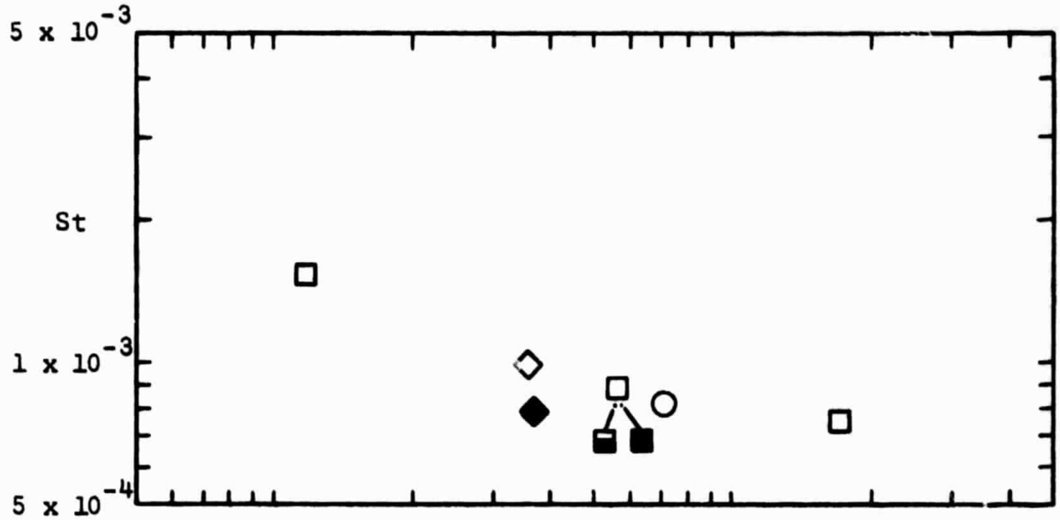

(a) Gage T4, $x = 0.100L$, $\phi = 0°$

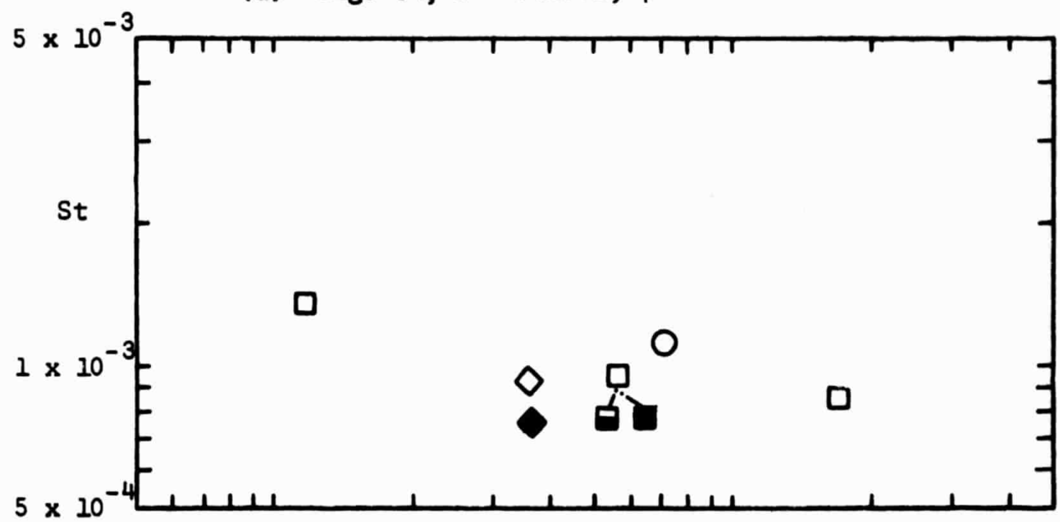

(b) Gage T8, $x = 0.125L$, $\phi = 0°$

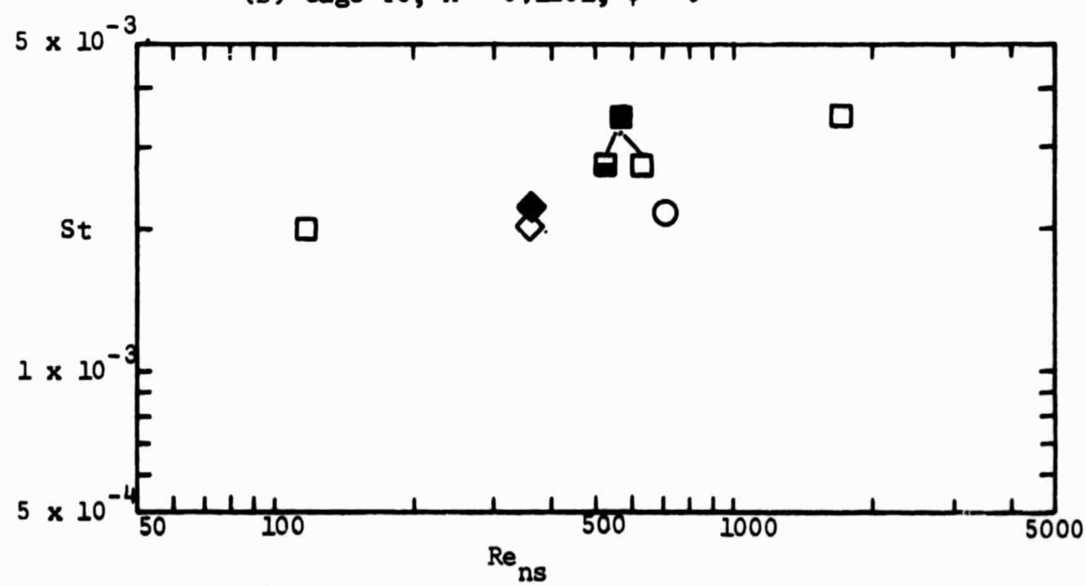

(c) Gage T10, $x = 0.160L$, $\phi = 0°$

Figure 46. - The Stanton number as a function of Re_{ns} for gages on the nose and on the cockpit windshield, $\alpha = 40°$.

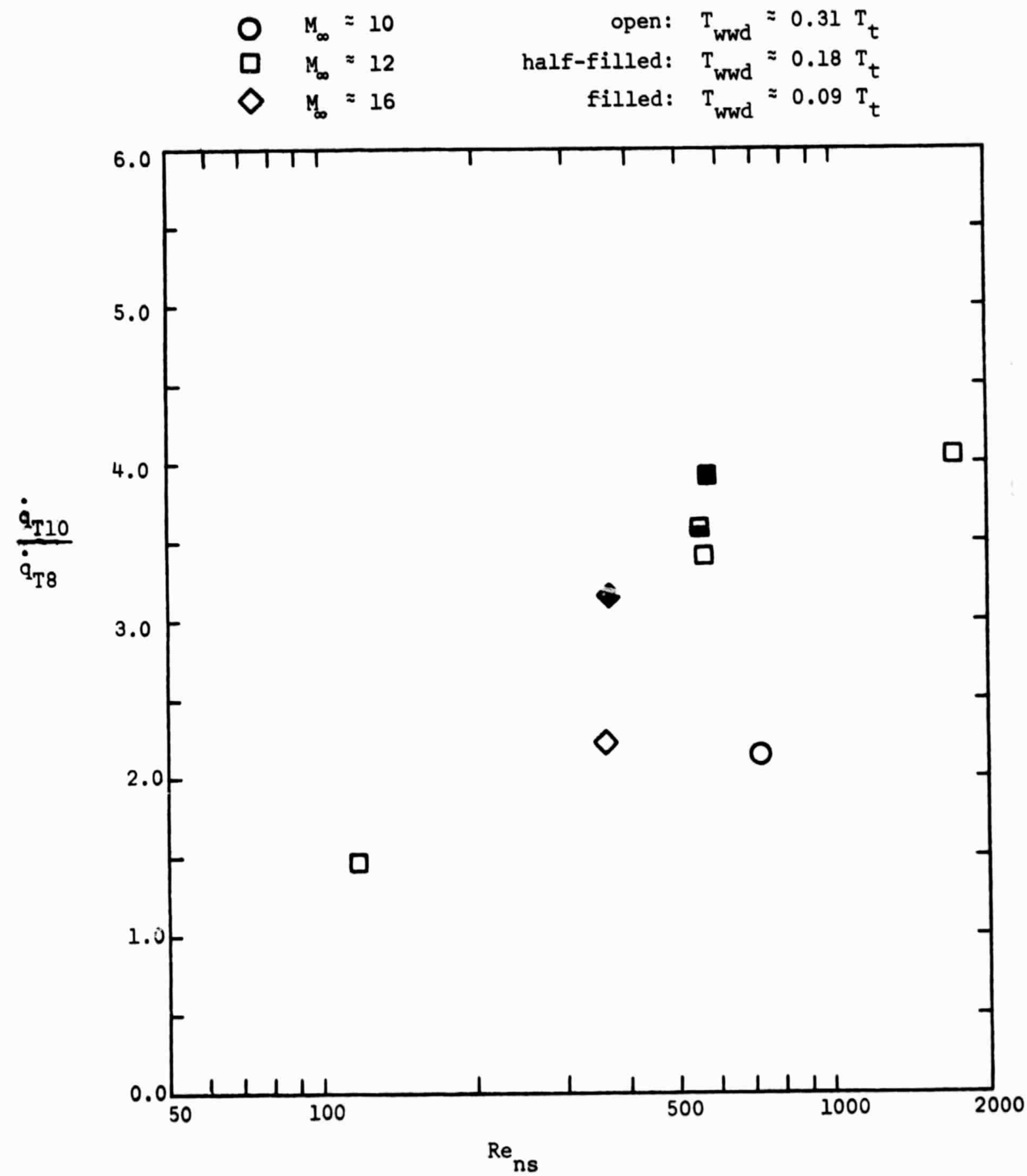

Figure 47. - The heat transfer to a gage on the cockpit windshield (T10) divided by that to a gage on the nose (T8) as a function of Re_{ns}, $\alpha = 40°$.

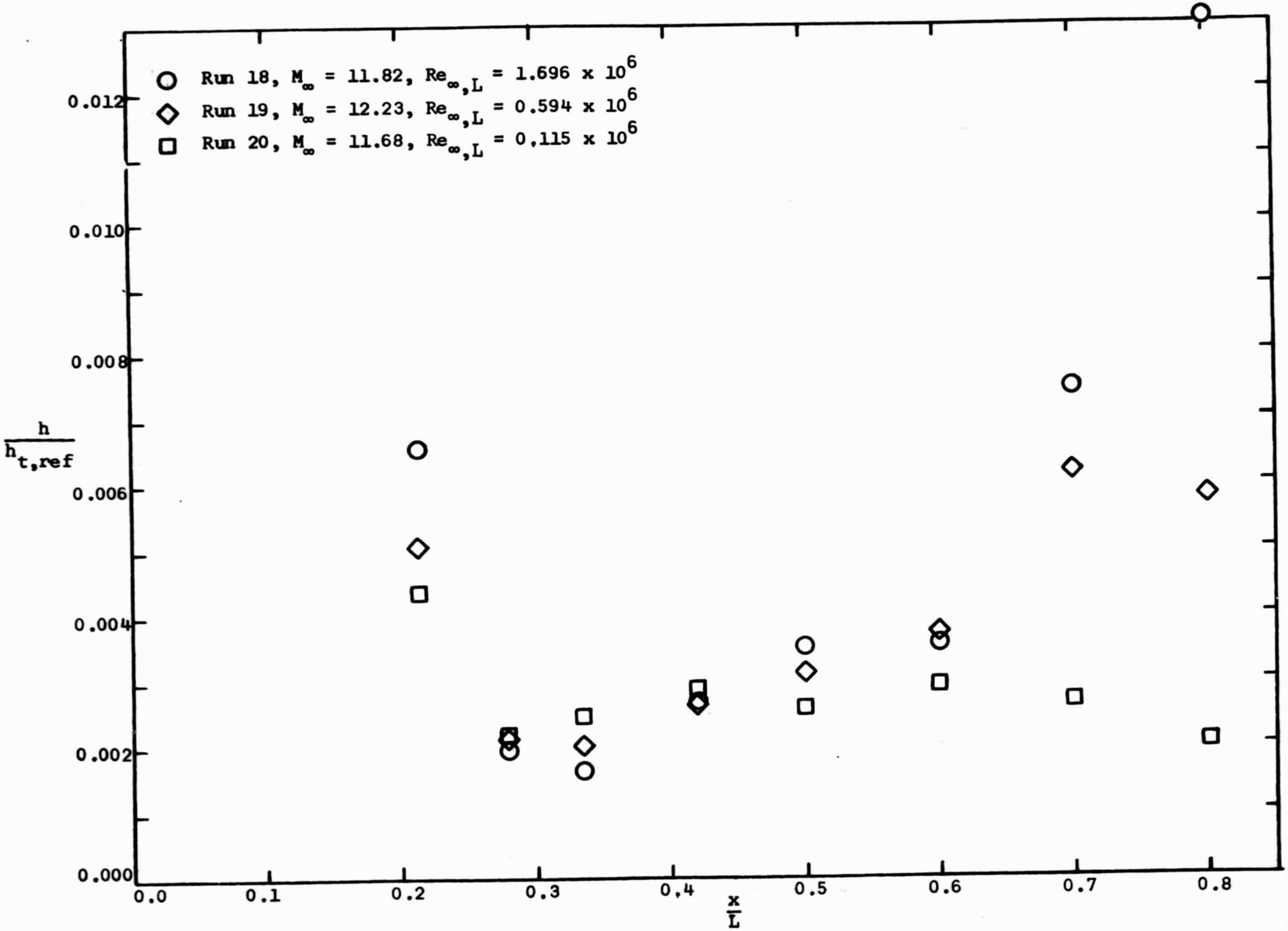

Figure 48. - The effect of Reynolds number on the heat-tranfer distribution in the leeward pitch plane for the nominal Mach 12 flows, $T_{wwd} \approx 0.31\ T_t$, $\alpha = 40°$.

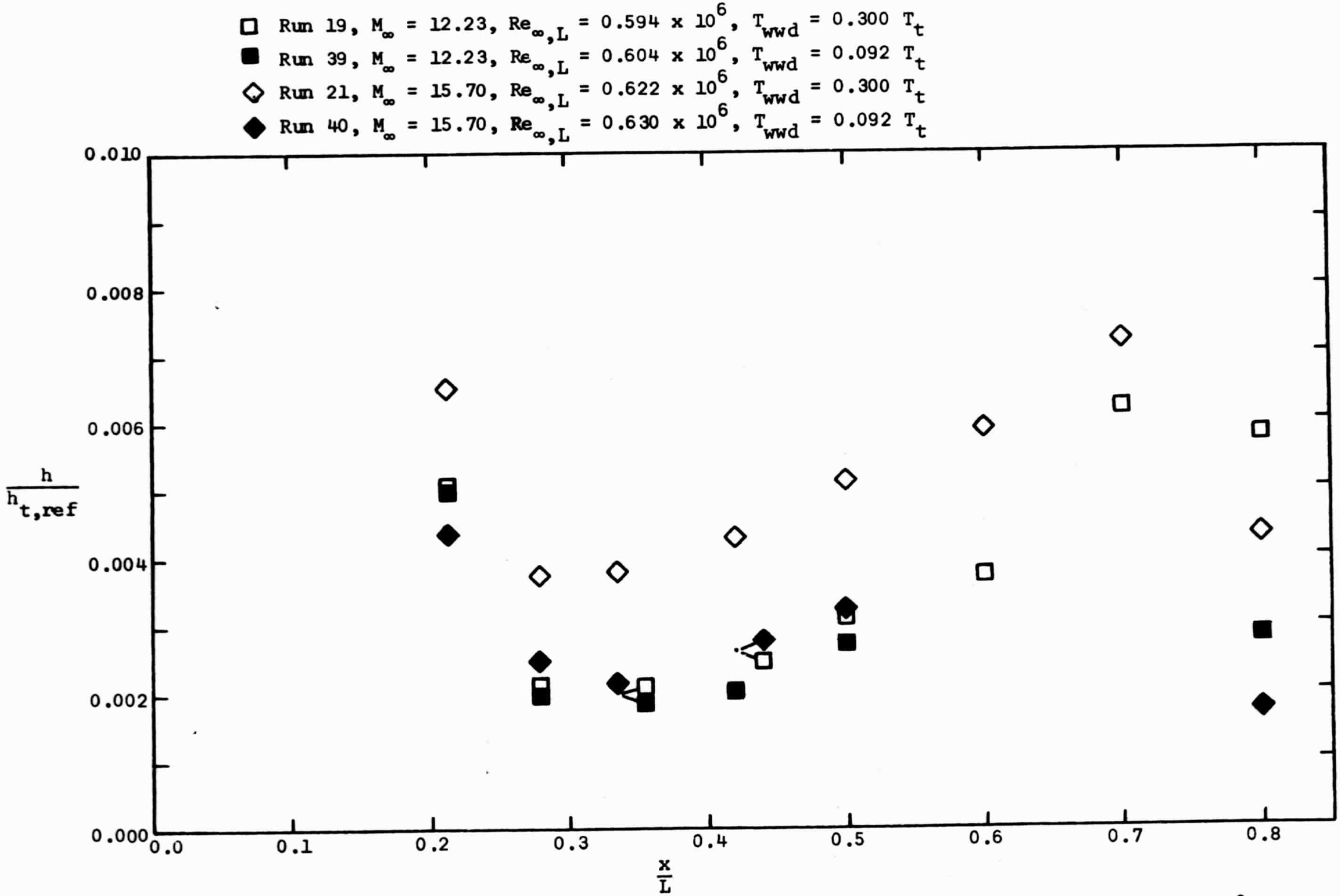

Figure 49. - The heat-transfer distribution in the leeward pitch plane for $Re_{\infty,L} \approx 0.6 \times 10^6$, $\alpha = 40°$

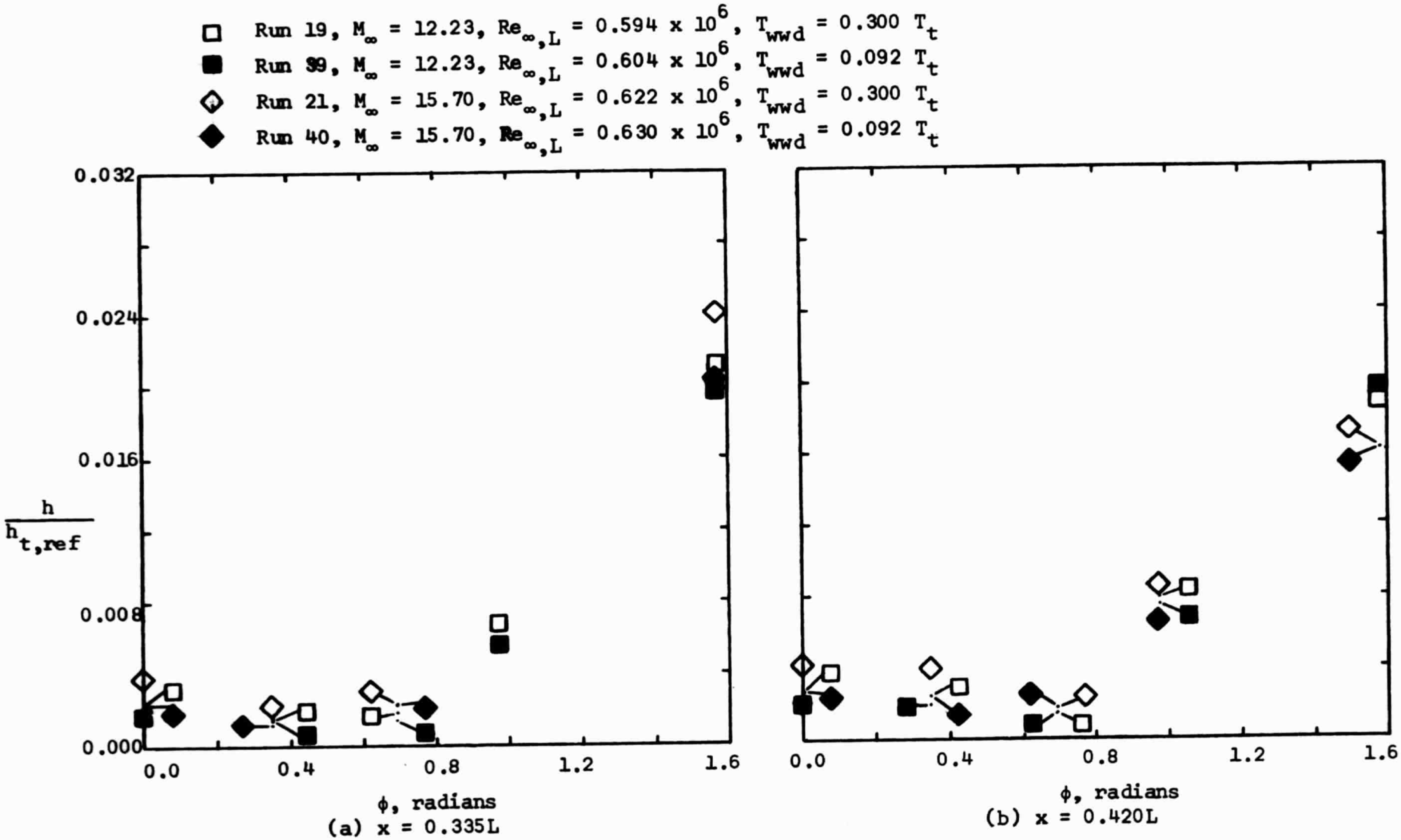

Figure 50. - The circumferential heat-transfer distributions for a nominal $Re_{\infty,L} \approx 0.6 \times 10^6$, $\alpha = 40°$.

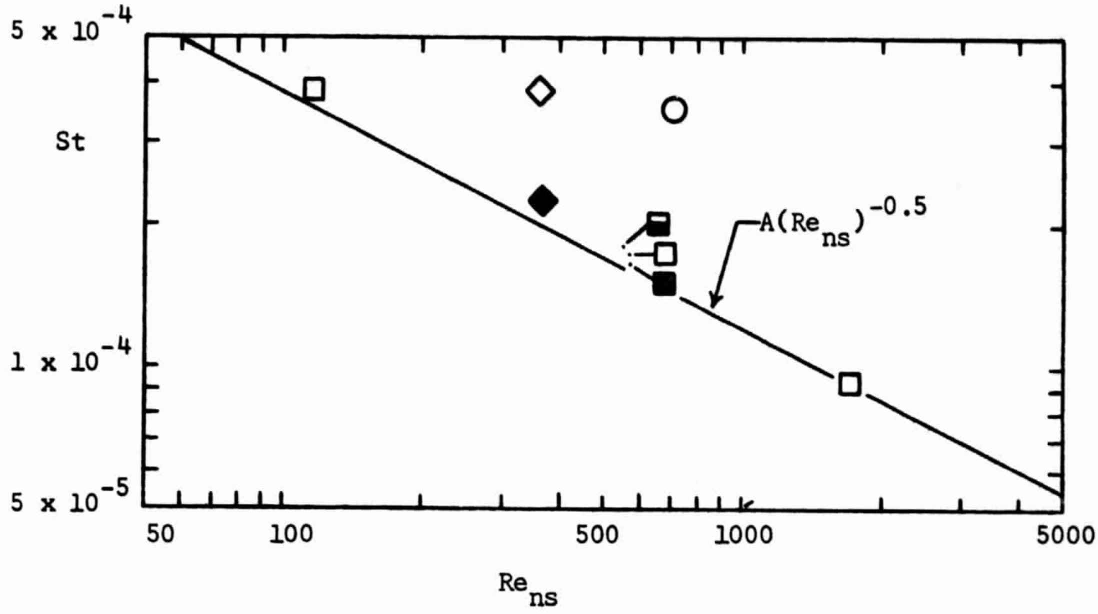

(a) Gage T19, $x = 0.279L$, $\phi = 0°$

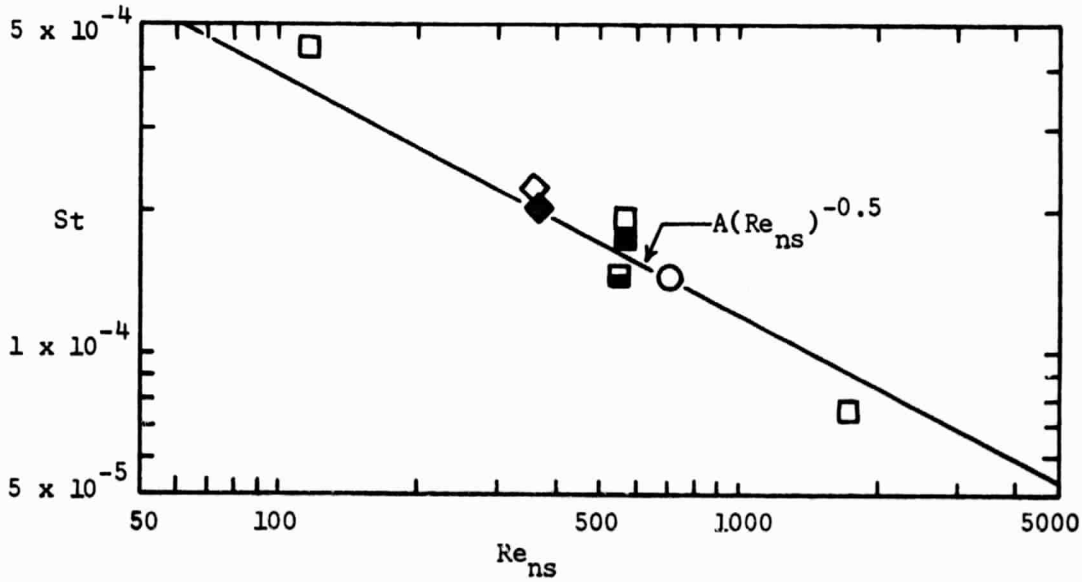

(b) Gage T21, $x = 0.279L$, $\phi = 44°$

Figure 51. - The Stanton number as a function of Re_{ns} for gages at $x = 0.279L$, $\alpha = 40°$.

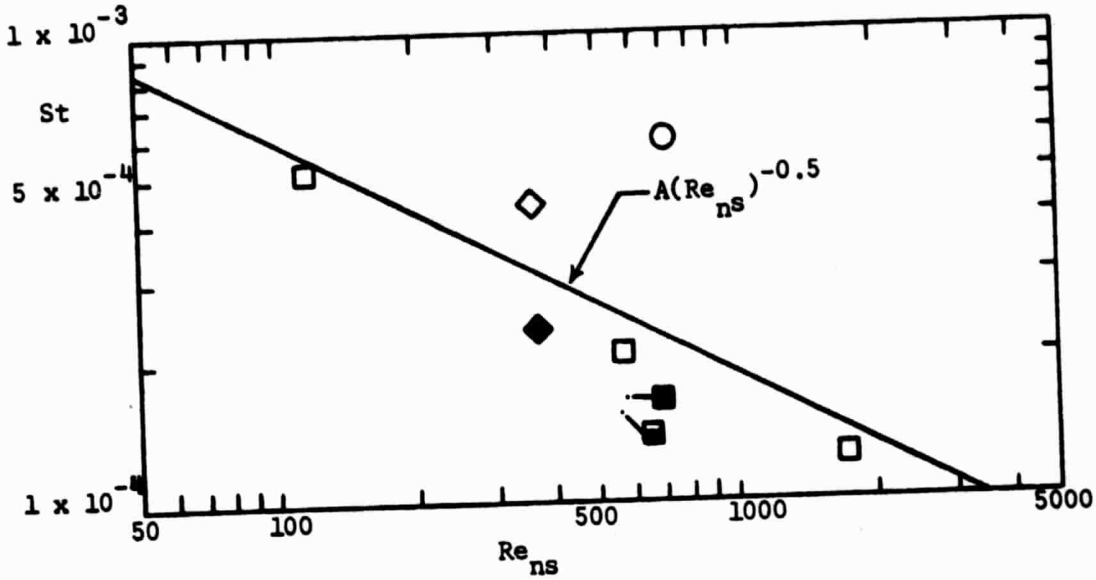

(a) Gage T29, $x = 0.420L$, $\phi = 0°$

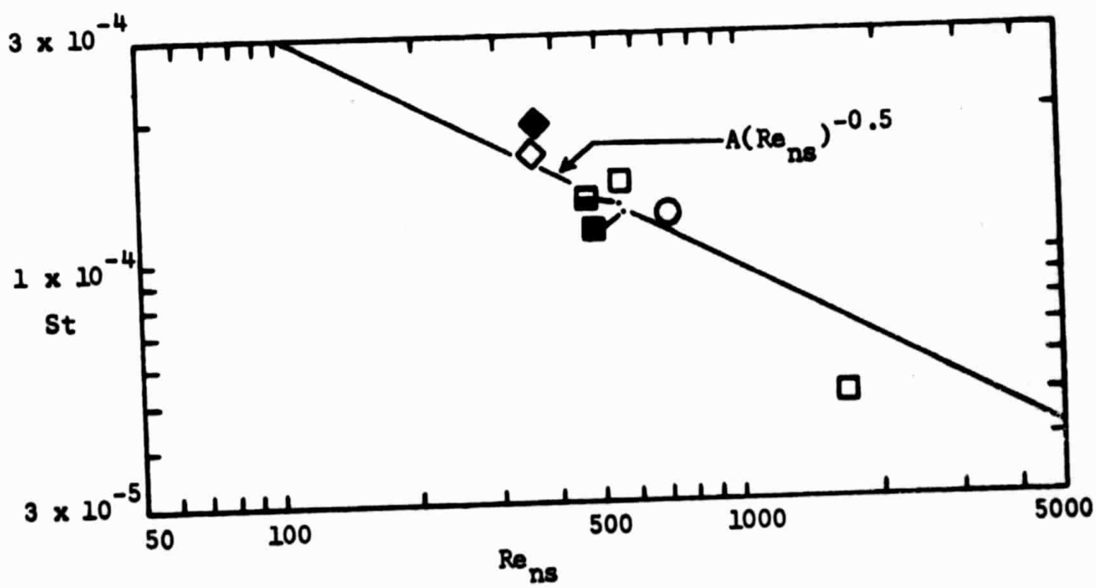

(b) Gage T31, $x = 0.420L$, $\phi = 40°$

Figure 52. - The Stanton number as a function of Re_{ns} for gages at $x = 0.420L$, $\alpha = 40°$.

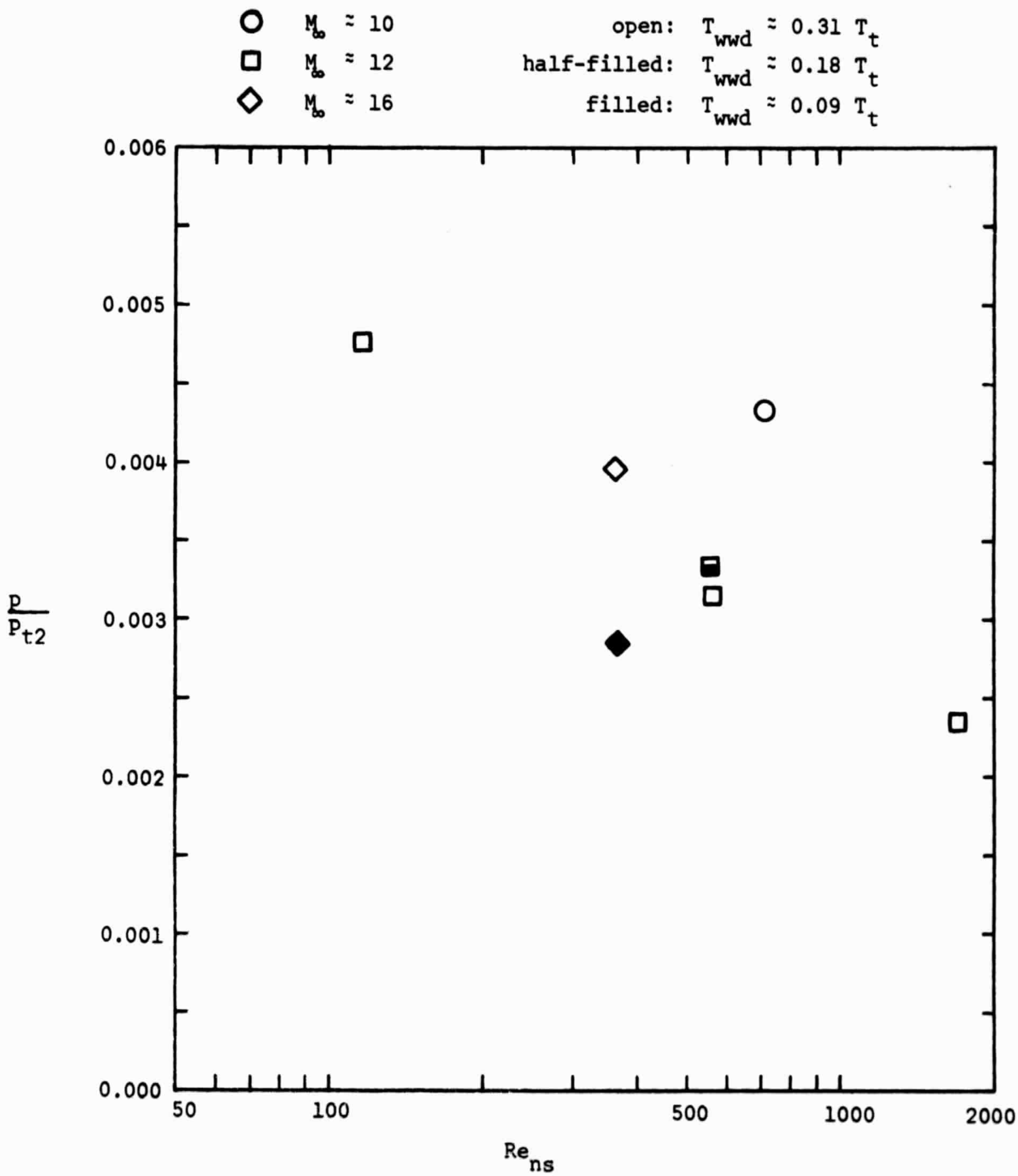

Figure 53. - The pressure measurements as a function of Reynolds number for PS4 ($x = 0.440L$, $\phi = 0°$), $\alpha = 40°$.

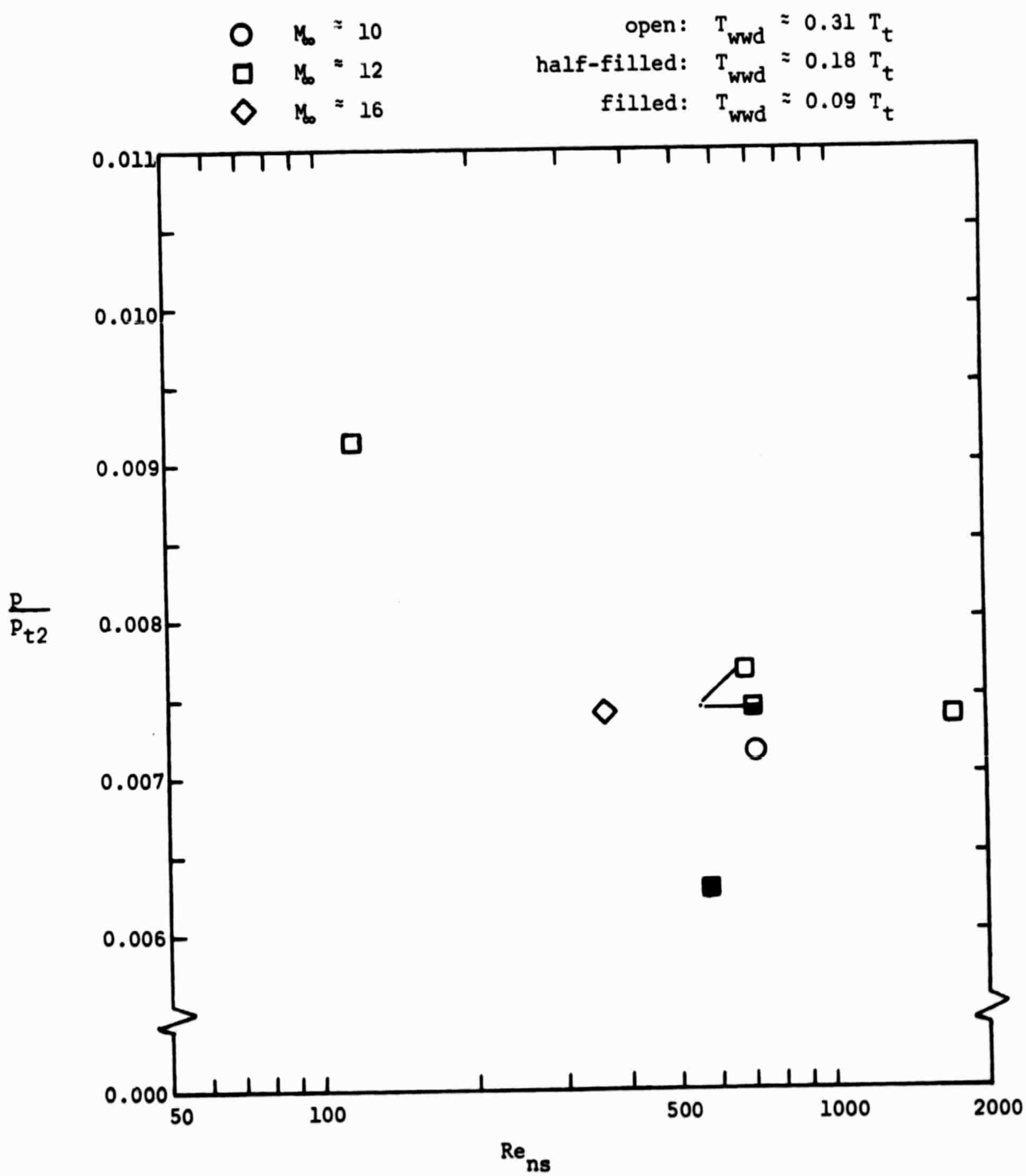

Figure 54. - The pressure measurements as a function of Reynolds number for PS5 ($x = 0.722L$, $\phi = 0°$), $\alpha = 40°$.

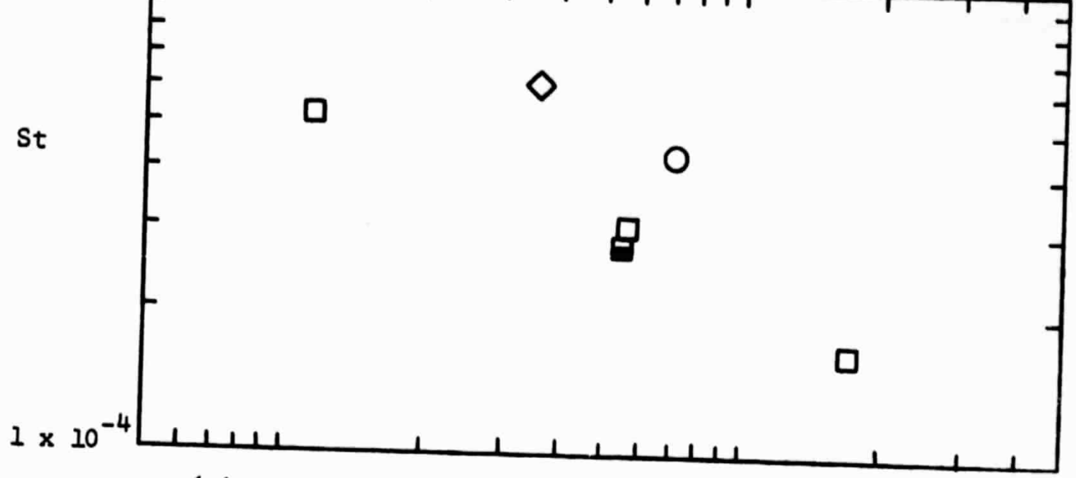

(a) Gage T37, x = 0.600L, ϕ = 0°

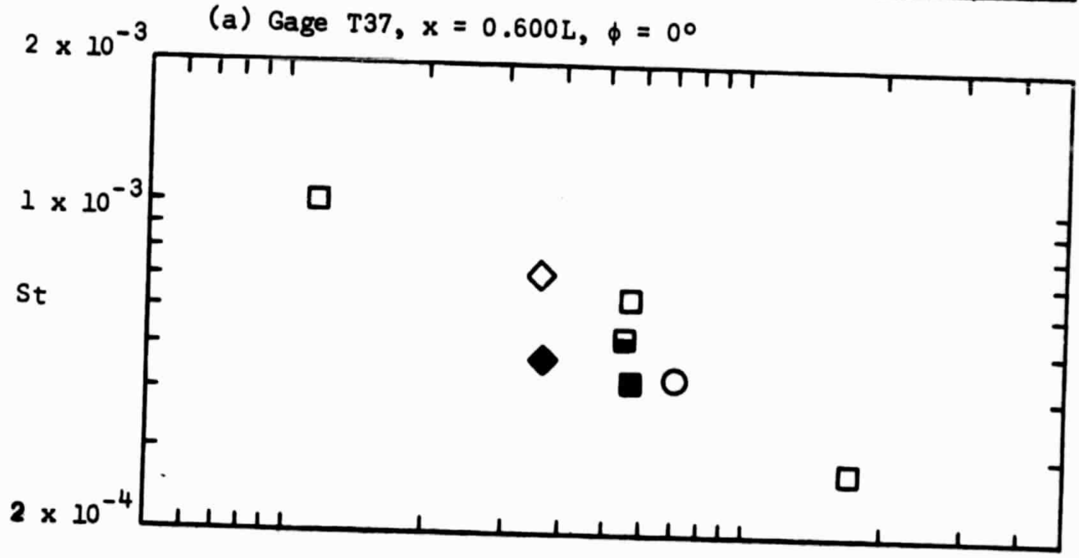

(b) Gage T39, x = 0.600L, ϕ = 56°

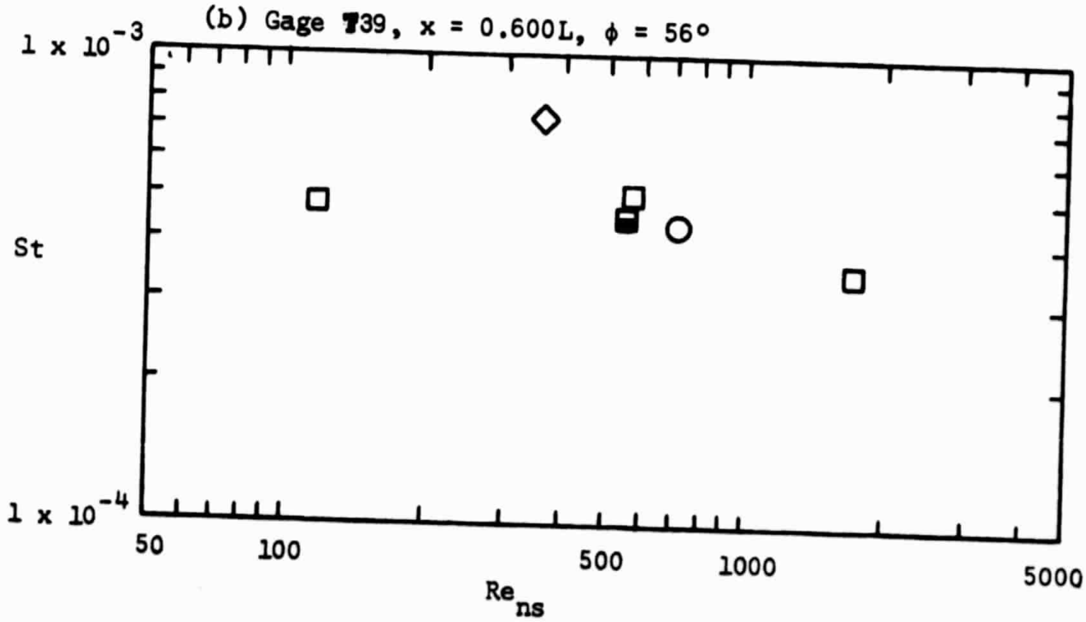

(c) Gage T41, x = 0.700L, ϕ = 0°

Figure 55. - The Stanton number as of function of the Reynolds number behind a normal shock wave for gages near the aft end of the orbiter, α = 40°.

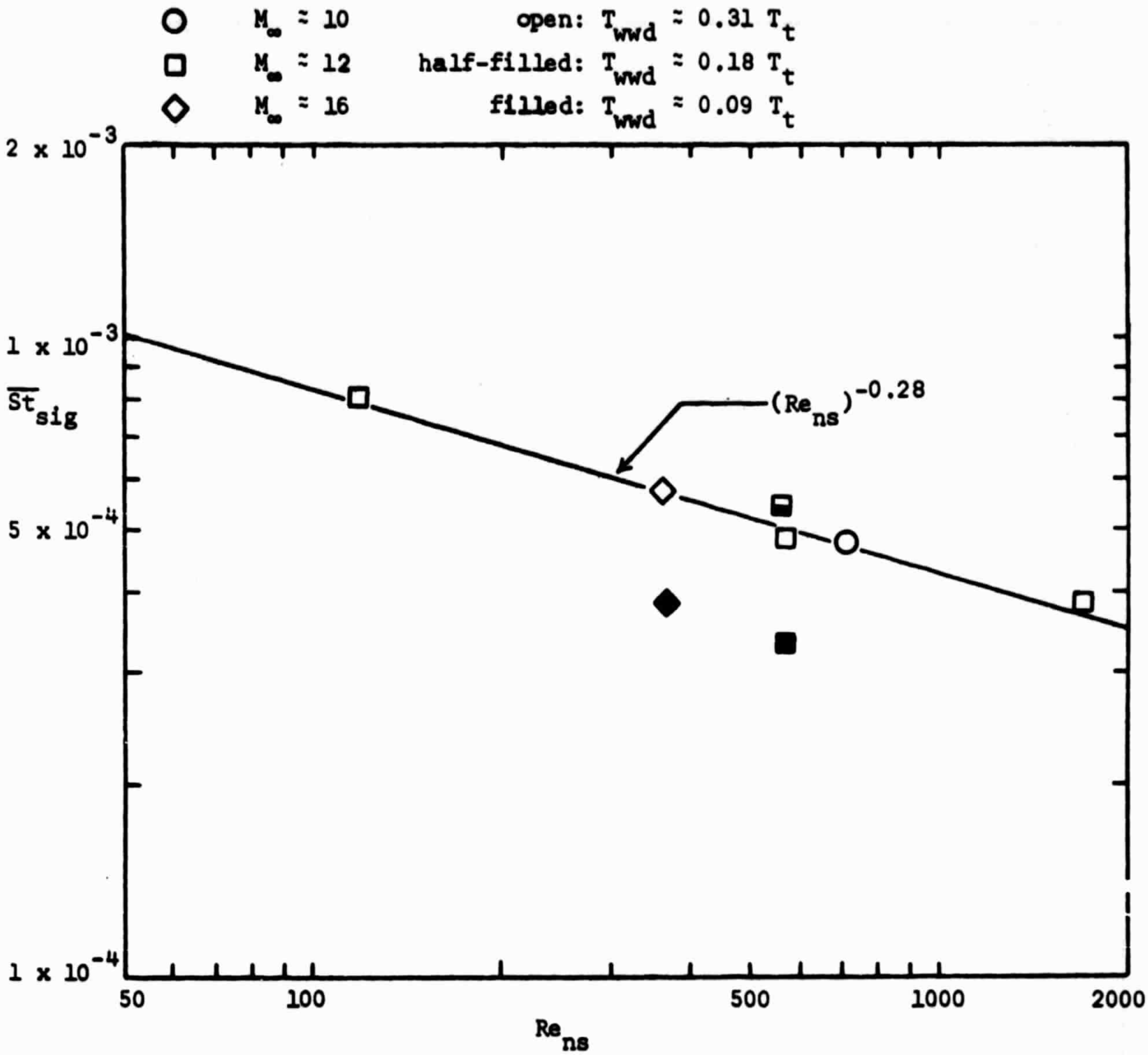

Figure 56. - The Stanton number averaged over all the leeward gages downstream of the cockpit as a function of Re_{ns}, $\alpha = 40°$.

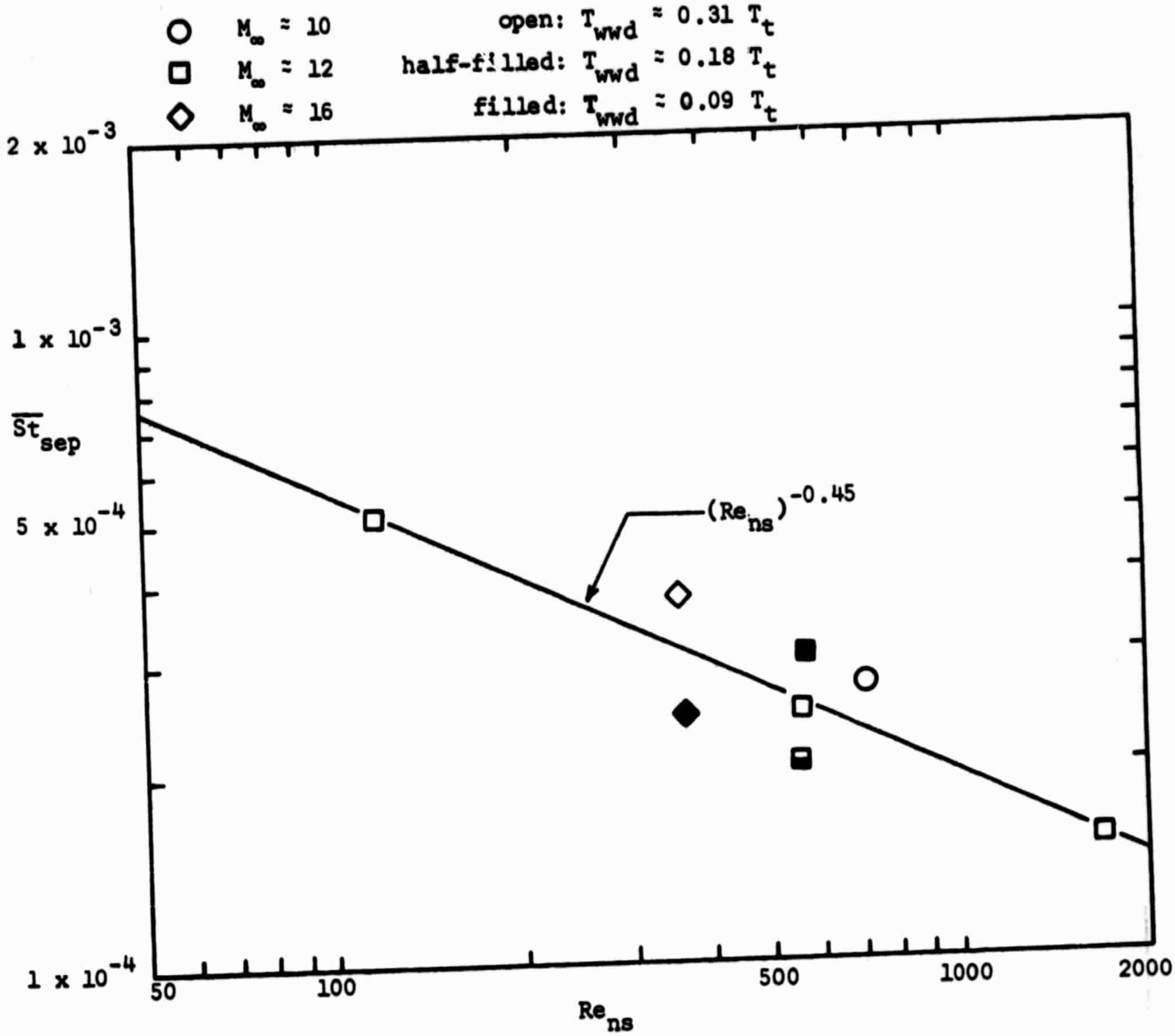

Figure 57. - The Stanton number averaged over these gages in the leeward "separated" region as a function of Re_{ns}, $\alpha = 40°$.

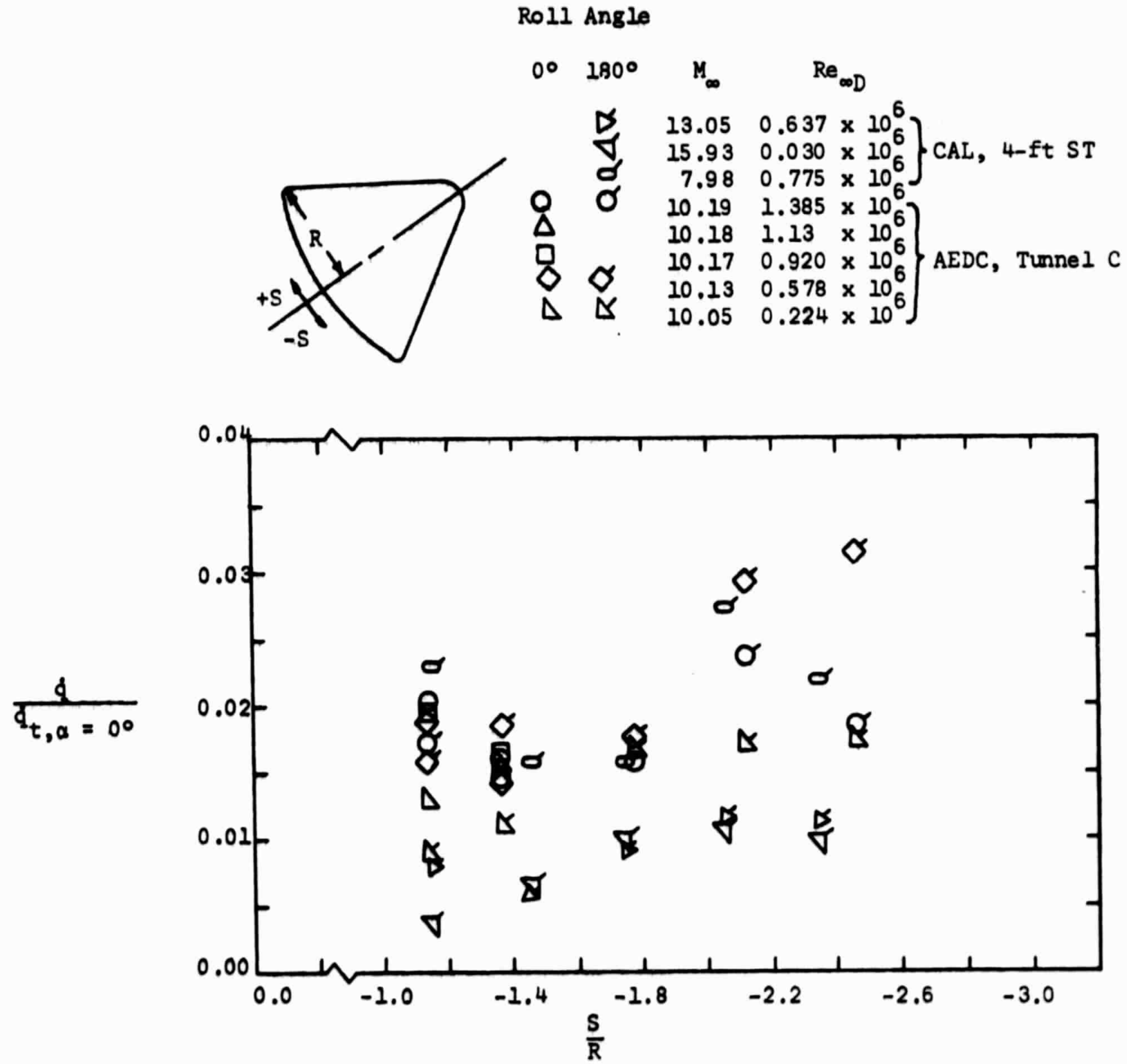

Figure 58. - Heat-transfer-rate distribution in the leeward pitch plane of the Apollo entry configuration, $\alpha = 33°$.

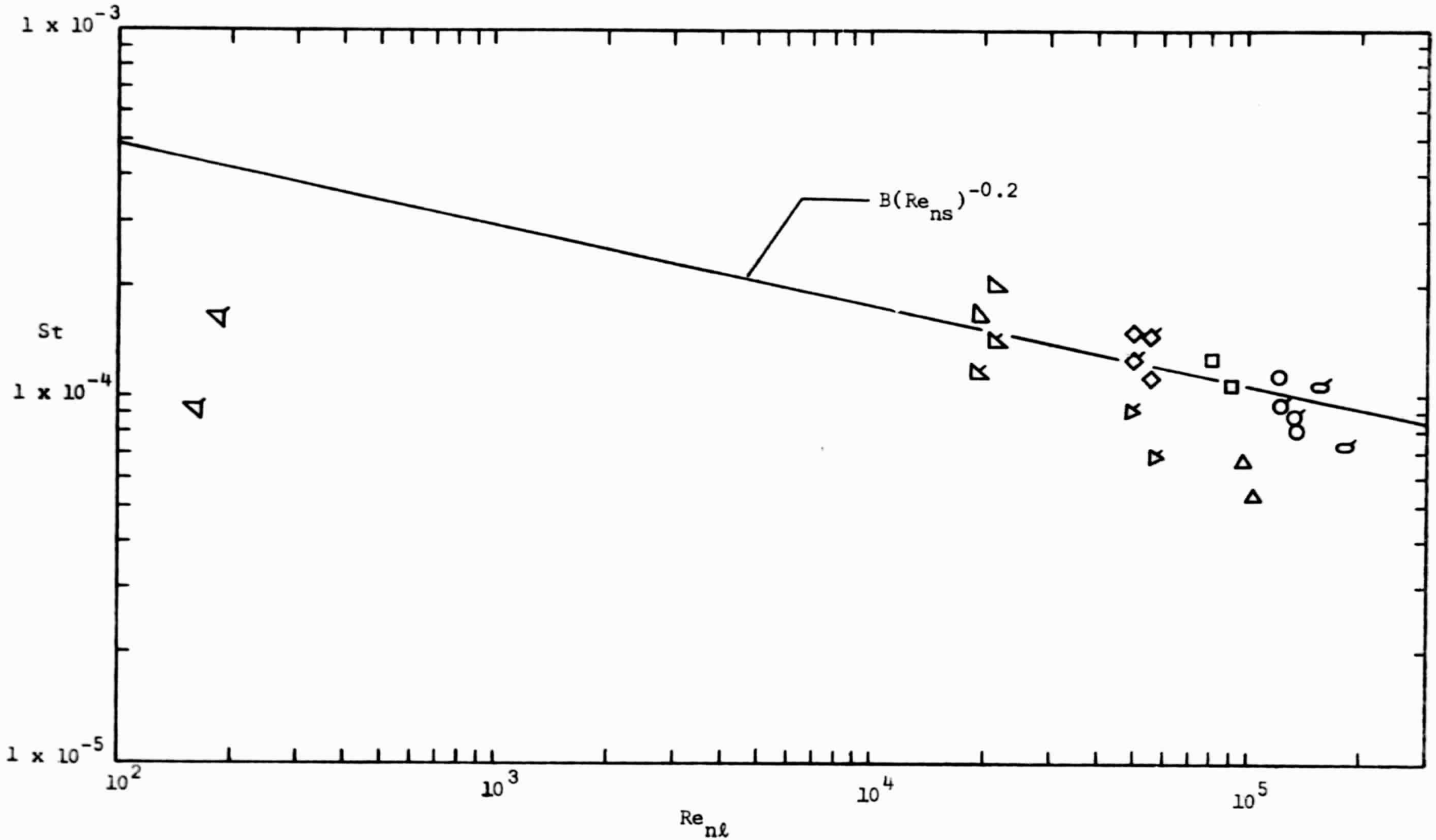

Figure 59. - The heat-transfer data from the leeward pitch-plane ($S < -1.5R$) of the Apollo entry configuration, $\alpha = 33°$.